

The Pennsylvania State University
The Graduate School
College of Earth and Mineral Sciences

**DEVELOPMENT OF A KNOWLEDGE BASE OF Ti-ALLOYS
FROM FIRST-PRINCIPLES AND COMPUTATIONAL
THERMODYNAMICS**

A Dissertation in
Materials Science and Engineering
by
Cassie Marker

© 2017 Cassie Marker

Submitted in Partial Fulfillment
of the Requirements
for the Degree of

Doctor of Philosophy

August 2017

The dissertation of Cassie Marker was reviewed and approved* by the following:

Zi-Kui Liu

Professor of Materials Science and Engineering

Thesis Advisor, Chair of Committee

Allison Beese

Assistant Professor of Materials Science and Engineering

Kristen Fichthorn

Merrell Fenskey Professor of Chemical Engineering and Professor of Physics

Michael Manley

Senior Researcher, Oak Ridge National Laboratory, Materials Science & Technology Division

Special Member

Susan Sinnott

Department Head and Professor of Materials Science and Engineering

*Signatures are on file in the Graduate School.

Abstract

An aging population with an active lifestyle requires the development of better load-bearing implants, which have high levels of biocompatibility and a low elastic modulus. Titanium alloys, in the body centered cubic phase, are great implant candidates, due to their mechanical properties and biocompatibility. The present work aims at investigating the thermodynamic and elastic properties of bcc Ti-alloys, using the integrated first-principles based on Density Functional Theory (DFT) and the CALculation of PHase Diagrams (CALPHAD) method. The use of integrated first-principles based on DFT and CALPHAD modeling has greatly reduced the need for trial and error metallurgy, which is ineffective and costly. The phase stability of Ti-alloys has been shown to greatly affect their elastic properties. Traditionally, CALPHAD modeling has been used to predict the equilibrium phase formation, but in the case of Ti-alloys, predicting the formation of two metastable phases ω and α'' is of great importance as these phases also drastically effect the elastic properties. To build a knowledge base of Ti-alloys, for biomedical load-bearing implants, the Ti-Mo-Nb-Sn-Ta-Zr system were studied because of the biocompatibility and the bcc stabilizing effects of some of the elements.

With the focus on bcc Ti-rich alloys, a database of thermodynamic descriptions of each phase for the pure elements, binary and Ti-rich ternary alloys was developed in the present work. Previous thermodynamic descriptions for the pure elements were adopted from the widely used SGTE database for global compatibility. The previous binary and ternary models from the literature were evaluated for accuracy and new thermodynamic descriptions were applied when necessary. The models were evaluated using available experimental data, as well as the enthalpy of formation of the bcc phase calculated from first-principles based on DFT. The thermodynamic descriptions were combined into a database ensuring that the sublattice models are compatible with each other.

For subsystems, such as the Sn-Ta system, where no thermodynamic description had been evaluated and minimal experimental data was available, first-principles based on DFT was used. The Sn-Ta system has two intermetallic phases, TaSn_2 and Ta_3Sn , with three solution phases: bcc, body centered tetragonal (bct) and diamond. First-principles calculations were done on the intermetallic and solution phases. Special quasirandom structures (SQS) were used to obtain information about the solution phases across the entire composition range. The Debye-Grüneisen approach, as well as the quasiharmonic phonon method were used to obtain the finite-temperature data. Results from first-principles calculations and experiments were used to complete the thermodynamic description. The resulting phase diagram reproduced the first-principles calculations and experimental data accurately.

In order to determine the effect of alloying on the elastic properties, first-principles based on DFT were systematically done on the pure elements, five Ti-X binary systems and Ti-X-Y ternary systems ($X \neq Y = \text{Mo, Nb, Sn, Ta, Zr}$) in the bcc phase. The first-principles calculations predicted the single crystal elastic stiffness constants c_{ij} 's. Correspondingly, the polycrystalline aggregate properties were also estimated from the c_{ij} 's, including bulk modulus B , shear modulus G and Young's modulus E . The calculated results showed good agreement with experimental results. The CALPHAD method was then adapted to assist in the database development of the elastic properties as a function of composition. On average, the database predicted the elastic properties of higher order Ti-alloys within 5 GPa of the experimental results.

Finally, the metastable phase formation, ω and α'' was studied in the Ti-Ta and Ti-Nb systems. The formation energy of these phases, calculated from first-principles at 0 °K, shows that these phases must be stabilized by entropy. A new theoretic framework was introduced that allows the prediction of the increase in entropy due to the competition between the metastable and stable phase. Using this approach, the phase fraction of the phases were predicted for the Ti-Nb system. The predicted phase fractions were used to calculate the mixed force constants to obtain the phonon density of states. Results from inelastic neutron scattering experiments were compared to the predicted phase fractions and phonon density of states for accuracy. Then the predicted phase fractions were used to calculate the elastic properties using the rule of mixtures. The predicted elastic properties were compared with available experimental data.

This thesis provides a knowledge base of the thermodynamic and elastic properties of Ti-alloys from computational thermodynamics. The databases created will

impact research focused on Ti-alloys and specifically efforts focused on Ti-alloys for biomedical applications.

Table of Contents

List of Figures	x
List of Tables	xix
Acknowledgments	xxiii
Chapter 1	
Introduction	1
1.1 Motivation	1
1.2 Overview	2
1.2.1 Equilibrium Phases	2
1.2.2 Metastable Phases	3
Chapter 2	
Methodology	10
2.1 First-Principles Calculations	10
2.1.1 Density Functional Theory at 0 °K	12
2.1.2 Finite-temperature thermodynamics	13
2.1.3 Elastic stiffness calculations	15
2.1.4 Special quasirandom structures (SQS)	17
2.1.5 High-throughput partition function	17
2.1.6 First-principles calculation error	18
2.2 CALPHAD method	19
2.2.1 Solution phases	19
2.2.2 Stoichiometric compounds	21
2.2.3 Elastic Properties	21
2.3 Experimental	22
2.3.1 Ti-Nb sample preparation	22
2.3.2 Neutron Scattering	22
2.3.2.1 ARCS	22

2.3.2.2 Data Analysis	23
---------------------------------	----

Chapter 3

Ti-Mo-Nb-Sn-Ta-Zr

Thermodynamic Database	25
3.1 Introduction	25
3.2 Computational details	26
3.2.1 Sn binaries and ternaries	27
3.3 Pure element calculation results	27
3.4 Enthalpy of formation of bcc phase from first-principles	28
3.5 Thermodynamic modeling of the ten binary systems	29
3.5.1 Mo-Nb, Mo-Ta, Nb-Ta	29
3.5.2 Mo-Zr, Nb-Zr and Ta-Zr	30
3.5.3 Ti-Mo	31
3.5.4 Ti-Nb	32
3.5.5 Ti-Ta	32
3.5.6 Ti-Zr	33
3.6 Thermodynamic modeling of six Ti-containing ternary systems	34
3.6.1 Ti-Mo-Nb	34
3.6.2 Ti-Mo-Ta	35
3.6.3 Ti-Mo-Zr	35
3.6.4 Ti-Nb-Ta	36
3.6.5 Ti-Nb-Zr	37
3.6.6 Ti-Ta-Zr	37
3.7 Conclusion	38

Chapter 4

First-principles aided thermodynamic modeling of the Sn-Ta system

63	
4.1 Introduction	63
4.2 Literature Review	64
4.3 Modeling and Calculations	65
4.3.1 First-principles details	65
4.3.2 CALPHAD	66
4.4 Results and discussion	66
4.4.1 First-principles	66
4.4.2 CALPHAD	68
4.5 Conclusion	70

Chapter 5	
Effects of alloying elements on the elastic properties of bcc Ti-X alloys	86
5.1 Introduction	86
5.2 Modeling and Calculations	87
5.2.1 Calculation details	87
5.2.2 Modeling details	87
5.3 Results and discussion	88
5.3.1 Evaluation of calculation settings	88
5.3.2 Calculations of the Ti-X elastic properties	88
5.3.3 Extrapolation to ternary and higher ordered systems	92
5.4 Conclusion	93
Chapter 6	
Effects of alloying elements on the elastic properties of bcc ternary and higher ordered Ti-alloys	110
6.1 Introduction	110
6.2 Modeling and Calculations	111
6.2.1 Calculation details	111
6.2.2 Modeling details	111
6.3 Results and discussion	112
6.3.1 Elastic calculation results	112
6.3.2 Extrapolation to higher ordered systems	117
6.4 Conclusion	118
Chapter 7	
Phase stability and elastic properties study of the Ti-Ta and Ti-Nb systems	142
7.1 Introduction	142
7.2 Modeling and Calculations	143
7.2.1 Computational details	143
7.2.2 Modeling details	143
7.3 Results and discussion	144
7.3.1 First-principles calculations at 0 K	144
7.3.2 Elastic properties	144
7.3.3 Neutron scattering results	147
7.3.3.1 Phonon density of states at 300 K	147
7.3.3.2 Diffraction patterns at 300 K	147
7.3.4 Partition function approach results	148
7.4 Conclusion	148

Chapter 8	
Conclusions and Future Work	172
8.1 Conclusions	172
8.2 Future Work	175
Appendix A	
Ti-Mo-Nb-Ta-Zr Database	177
Appendix B	
Sn-Ta Database	194
Appendix C	
Mathematica	
Interaction Parameter Fitting	202
Appendix D	
Ti Elastic Database	204
Appendix E	
Pycalphad script	211
Appendix F	
Ti-Nb Experimental Elastic Data	221
Bibliography	223

List of Figures

1.1	Comparison of first-principles calculations [1, 2] and experimental measurements of the Young's modulus of Ti-Ta alloys [3–5]. The purple box refers to the composition range when the calculations and experimentally determined E do not match up due to the formation of two metastable phases ω and α''	8
1.2	Comparison of the present first-principles calculations and experimental measurements of the Young's modulus of Ti-Nb alloys [6–10]. The purple box refers to the composition range when the calculations and experimentally determined E do not match up due to the formation of two metastable phases ω and α''	9
3.1	Previously modeled thermodynamic descriptions of the Mo-Nb (a) [11], Mo-Ta (b) [11] and Nb-Ta (c) [11] binary systems in comparison with available liquidus and solidus phase boundary experimental data to ensure accuracy as detailed in [11].	47
3.2	Previously modeled thermodynamic descriptions of the Mo-Zr [12] system is plotted with phase boundary, reaction, single phase and two phase experimental data. The previously modeled Nb-Zr [13, 14] system is plotted with solidus, hcp solvus and bcc solvus experimental data. The previously modeled Ta-Zr [15] system is plotted with single-phase, two-phase, phase boundary and solidus experimental data (detailed in the mentioned references).	48
3.3	Previously modeled thermodynamic description of the Ti-Mo system versus available phase boundary and solidus experimental data to ensure accuracy [16, 17] (a), and enthalpy of formation of the bcc phase predicted by the previous thermodynamic modeling (solid line) at 300 °K versus the present first-principles calculations (circles) at 0 °K and compared with the enthalpy of formation of the bcc phase obtained from experiments [18] (b).	49

3.4 Previously modeled thermodynamic description of the Ti-Nb system versus available phase boundary and solidus experimental data to ensure accuracy [19–21][20,48] (a), and enthalpy of formation of the bcc phase predicted by the previous thermodynamic modeling (solid line) at 300 °K versus the present first-principles calculations (circles) at 0 °K compared with the enthalpy of formation of the bcc phase obtained from experiments [18] (b).	50
3.5 Previously modeled thermodynamic description of the Ti-Ta system versus available phase boundary and solidus experimental data to ensure accuracy [16, 22] (a), and enthalpy of formation of the bcc phase predicted by the previous thermodynamic modeling (solid line) at 300 °K versus the present first-principles calculations (circles) at 0 °K (b).	51
3.6 Previously modeled thermodynamic description of the Ti-Zr system versus available phase boundary and solidus experimental data to ensure accuracy [21] (a), and enthalpy of formation of the bcc phase predicted by the previous thermodynamic modeling (solid line) at 300 °K versus the present first-principles calculations (circles) at 0 °K (b).	52
3.7 Binary interpolation of the isothermal section of the Ti-Mo-Nb system plotted at 873 °K (a), and enthalpy of formation of the bcc phase predicted by the binary interpolation of the thermodynamic modeling (solid line) at 300 °K versus the present first-principles calculations (circles) at 0 °K (b).	53
3.8 Binary interpolation of the isothermal section of the Ti-Mo-Ta system plotted at 873 °K (a), and enthalpy of formation of the bcc phase predicted by the previous thermodynamic modeling (solid line) at 300 °K and the ternary assessed thermodynamic modeling (red dotted line) versus the present first-principles calculations (circles) at 0 °K (b).	54
3.9 Ternary assessed isothermal section of the Ti-Mo-Ta system plotted at 873 °K (a), and zoomed in ternary assessed isothermal section at 873 °K with the phase boundary and two-phase region experimental data [23] (b) to ensure accuracy of the ternary assessment.	55
3.10 Binary interpolation of the isothermal section of the Ti-Mo-Zr system plotted at 1273 °K compared with experimental phase boundary data [24,25] (a), and enthalpy of formation of the bcc phase predicted by the previous thermodynamic modeling (solid line) at 300 °K versus the present first-principles calculations (circles) at 0 °K (b).	56

3.11	Binary interpolation of the isothermal section of the Ti-Nb-Ta system plotted at 673 °K compared with experimental phase boundary data [26] (a), and binary interpolation of the isothermal section of the Ti-Nb-Ta system plotted at 823 °K compared with experimental phase boundary data [26] (b).	57
3.12	Enthalpy of formation of the bcc phase predicted by the previous thermodynamic modeling (solid line) at 300 °K and the ternary assessed thermodynamic modeling (red dotted line) versus the present first-principles calculations (circles) at 0 °K.	58
3.13	Ternary assessed isothermal section of the Ti-Nb-Ta system plotted at 673 °K compared with experimental phase boundary data [26] to ensure accuracy of the ternary assessment (a), and ternary assessed isothermal section at 823 °K compared with experimental phase boundary data [26] to ensure accuracy of the ternary assessment (b).	59
3.14	Binary interpolation of the isothermal section of the Ti-Nb-Zr system plotted at 843 °K compared with experimental phase boundary and two-phase region data [27] (a), and enthalpy of formation of the bcc phase predicted by the previous thermodynamic modeling (solid line) at 300 °K versus the present first-principles calculations (circles) at 0 °K (b).	60
3.15	Binary interpolation of the isothermal section of the Ti-Ta-Zr system plotted at 1273 °K compared with experimental phase boundary data [28, 29] (a), and binary interpolation of the isothermal section of the Ti-Ta-Zr system plotted at 1773 °K compared with compared with experimental single phase and two-phase region data [28, 29] (b).	61
3.16	Enthalpy of formation of the bcc phase predicted by the previous thermodynamic modeling (solid line) at 300 °K versus the present first-principles calculations (circles) at 0 °K.	62
4.1	Calculated phonon dispersion curve of bcc-Ta, compared with neutron diffraction experiments (\circ) [30] along with the phonon DOS.	75
4.2	Calculated phonon dispersion curve of bct-Sn on the left and phonon DOS on the right. The open squares (\square) are the LO and TO modes from Raman [31] and the filled squares the theoretical prediction of the LO and TO modes at the M point [31].	76
4.3	Calculated phonon dispersion curve for $TaSn_2$ at 0 °K and the phonon DOS.	77
4.4	Calculated phonon dispersion curve of Ta_3Sn at 0 °K on the left and the phonon DOS on the right.	78

4.5	Comparison of the enthalpy and entropy of bcc-Ta from the Debye model (solid line) and the quasiharmonic phonon calculations (red dotted line) to the SGTE data (blue dashed line) [32].	79
4.6	Comparison of the Gibbs energy of bct-Sn from the Debye model (solid line) and the quasiharmonic phonon calculations (red dotted line) to the SGTE data (blue dashed line) [32].	80
4.7	Heat capacity, enthalpy and entropy of TaSn_2 using the Debye model (solid line) and the quasiharmonic phonon calculation (red dotted line) from first-principles calculations, compared with those from the current CALPHAD modeling (blue dashed line).	81
4.8	Heat capacity, enthalpy and entropy of Ta_3Sn using the Debye model (solid line) and the quasiharmonic phonon calculation (red dotted line) compared with those from the current CALPHAD modeling (blue dashed line).	82
4.9	Enthalpy of formation of the bcc phase of the Sn-Ta system as a function of composition at 298 °K and ambient pressure from the current CALPHAD modeling (solid line) and from the first-principles calculations (dots), showing asymmetric behavior. This was compared with data of the Nb-Sn system from Toffolon et al. [33] (dashed red line) which was modeled using experimental data, showing similar asymmetric behavior.	83
4.10	Calculated Sn-Ta phase diagram using the present thermodynamic description.	84
4.11	Enthalpy of mixing of the liquid phase as a function of composition at 298 °K and ambient pressure in the Sn-Ta system.	85
5.1	Elastic stiffness constants of the bcc Ti-Ta binary system calculated with the GGA and PBE exchange correction functions, respectively.	99
5.2	Elastic stiffness constants for the bcc Ti-Mo binary system calculated with strains, ± 0.01 , ± 0.03 and ± 0.07 , respectively, showing comparable results.	100
5.3	Young's modulus E of the Ti-X binary systems. The present calculations are plotted as the filled circles with the error bars. The dotted purple line is the Voigt upper Young's modulus bound, the gold dot dashed line is the lower Reuss Young's modulus bound and the black line is the Hill Young's modulus average. The experimental values [1–5, 7, 8, 34–36] are also included for comparison.	101
5.4	Young's modulus calculated from the model parameters (see 5.2) and Eq. 2.30 as a function of composition from bcc Ti to bcc X. . .	102

5.5	Calculated \bar{C}_{11} values (circles) plotted with their errors as well as the pure element extrapolation (red dashed line) and the present modeling (black dashed line) for five Ti-X binary systems (X = Mo, Nb, Ta, Sn, Zr). Ti-Mo, Ti-Nb, and Ti-Ta alloys are compared with previous calculations from Ikehata et al. [2].	103
5.6	Calculated \bar{C}_{12} values (circles) plotted with their errors as well as the pure element extrapolation (red dashed line) and the present modeling (black dashed line) for five Ti-X binary systems (X = Mo, Nb, Ta, Sn, Zr). Ti-Mo, Ti-Nb, and Ti-Ta alloys are compared with previous calculations from Ikehata et al. [2].	104
5.7	Calculated \bar{C}_{44} values (circles) plotted with their errors as well as the pure element extrapolation (red dashed line) and the present modeling (black dashed line) for five Ti-X binary systems (X = Mo, Nb, Ta, Sn, Zr). Ti-Mo, Ti-Nb, and Ti-Ta alloys are compared with previous calculations from Ikehata et al. [2].	105
5.8	Calculated \bar{C}_{11} - \bar{C}_{12} values (circles) plotted with the present modeling (solid lines) for five Ti-X binary systems (X = Mo, Nb, Ta, Sn, Zr). The \bar{C}_{11} - \bar{C}_{12} shows the stability of the bcc phase. When the \bar{C}_{11} - \bar{C}_{12} value is negative the bcc phase is not stable in the corresponding compositions range.	106
5.9	Bulk modulus B of the Ti-X binary systems. The present calculations are plotted as the filled circles with the error bars. The dotted purple line is the Voigt upper bulk modulus bound, the gold dot dashed line is the lower Reuss bulk modulus bound and the black line is the Hill bulk modulus average.	107
5.10	Shear modulus G of the Ti-X binary systems. The present calculations are plotted as the filled circles with the error bars. The dotted purple line is the Voigt upper shear modulus bound, the gold dot dashed line is the lower Reuss shear modulus bound and the black line is the Hill shear modulus average.	108
5.11	Young's moduli values of multicomponent bcc Ti alloys measured experimentally plotted against the predicted Young's moduli from the pure elements and binary interaction parameters with the black diagonal line showing the exact correlation between the experimental and calculated values. Error bars in the experiments and the bounds from Reuss and Voigt approximations are plotted as vertical and horizontal lines, respectively. The variance in the first calculations from Eq. 2.18-Eq. 2.20 was averaged and plotted as the grey region to show the variance in the first-principles calculations. More information on the alloys is in Table 5.4 [37–39]	109

6.1	Calculated \bar{C}_{11} values (circles) plotted with their errors as well as the interpolation from the binary interaction parameters (red dashed line) and the ternary fitting (black dashed line) for five of the Ti-X-Y binary systems from a 50-50 mixture of the alloying elements X and Y to Ti ($X \neq Y = Mo, Nb, Ta, Sn, Zr$)	126
6.2	Calculated \bar{C}_{11} values (circles) plotted with their errors as well as the interpolation from the binary interaction parameters (red dashed line) and the ternary fitting (black dashed line) for five of the Ti-X-Y binary systems from a 50-50 mixture of the alloying elements X and Y to Ti ($X \neq Y = Mo, Nb, Ta, Sn, Zr$)	127
6.3	Calculated \bar{C}_{12} values (circles) plotted with their errors as well as the interpolation from the binary interaction parameters (red dashed line) and the ternary fitting (black dashed line) for five of the Ti-X-Y binary systems from a 50-50 mixture of the alloying elements X and Y to Ti ($X \neq Y = Mo, Nb, Ta, Sn, Zr$)	128
6.4	Calculated \bar{C}_{12} values (circles) plotted with their errors as well as the interpolation from the binary interaction parameters (red dashed line) and the ternary fitting (black dashed line) for five of the Ti-X-Y binary systems from a 50-50 mixture of the alloying elements X and Y to Ti ($X \neq Y = Mo, Nb, Ta, Sn, Zr$)	129
6.5	Calculated \bar{C}_{44} values (circles) plotted with their errors as well as the interpolation from the binary interaction parameters (red dashed line) and the ternary fitting (black dashed line) for five of the Ti-X-Y binary systems from a 50-50 mixture of the alloying elements X and Y to Ti ($X \neq Y = Mo, Nb, Ta, Sn, Zr$)	130
6.6	Calculated \bar{C}_{44} values (circles) plotted with their errors as well as the interpolation from the binary interaction parameters (red dashed line) and the ternary fitting (black dashed line) for five of the Ti-X-Y binary systems from a 50-50 mixture of the alloying elements X and Y to Ti ($X \neq Y = Mo, Nb, Ta, Sn, Zr$)	131
6.7	Calculated \bar{C}_{11} - \bar{C}_{12} values (circles) plotted with the present modeling (solid lines) for the Ti-X-Y ternary systems ($X \neq Y = Mo, Nb, Ta, Sn, Zr$). The \bar{C}_{11} - \bar{C}_{12} shows the stability of the bcc phase, when the value is negative the bcc phase is not stable in the corresponding composition ranges	132

6.8	<i>E</i> of five of the Ti-X-Y ternary systems are plotted from a 50-50 mixture of the alloying elements to Ti in the bcc phase. The present calculations are plotted as filled circles with the error bars. The red dotted line is the extrapolation for the pure elements and binary interaction parameters only. The dotted purple line is the Voigt upper <i>E</i> bound, the gold dot dashed line is the lower Reuss <i>E</i> bound and the black line is the Hill <i>E</i> average. Experimental values are include for comparison [38–41].	133
6.9	<i>E</i> of five of the Ti-X-Y ternary systems are plotted from a 50-50 mixture of the alloying elements to Ti in the bcc phase. The present calculations are plotted as filled circles with the error bars. The red dotted line is the extrapolation for the pure elements and binary interaction parameters only. The dotted purple line is the Voigt upper <i>E</i> bound, the gold dot dashed line is the lower Reuss <i>E</i> bound and the black line is the Hill <i>E</i> average. Experimental values are include for comparison [38–41].	134
6.10	The Young's modulus is mapped as a function of composition in GPa for the Ti-Mo-Nb, Ti-Mo-Sn, Ti-Mo-Ta, Ti-Mo-Zr and Ti-Nb-Sn alloy systems using pycalphad [42].	135
6.11	The Young's modulus is mapped as a function of composition in GPa for the Ti-Mo-Nb, Ti-Mo-Sn, Ti-Mo-Ta, Ti-Mo-Zr and Ti-Nb-Sn alloy systems using pycalphad [42].	136
6.12	<i>B</i> calculations of five of the Ti-X-Y ternary systems ($X \neq Y = Mo, Nb, Ta, Sn, Zr$). The present calculations are plotted as the filled circles with error bars as well as the interpolation from the binary interaction parameters (red dashed line). The dotted purple line is the Voigt upper bulk modulus bound, the gold dashed line is the lower Reuss bulk modulus bound and the black line is the Hill bulk modulus average plotted from a 50-50 mixture of the alloying elements X and Y to Ti.	137
6.13	<i>B</i> calculations of five of the Ti-X-Y ternary systems ($X \neq Y = Mo, Nb, Ta, Sn, Zr$). The present calculations are plotted as the filled circles with error bars as well as the interpolation from the binary interaction parameters (red dashed line). The dotted purple line is the Voigt upper bulk modulus bound, the gold dashed line is the lower Reuss bulk modulus bound and the black line is the Hill bulk modulus average plotted from a 50-50 mixture of the alloying elements X and Y to Ti.	138

6.14	<i>G</i> calculations of five of the Ti-X-Y ternary systems ($X \neq Y = Mo, Nb, Ta, Sn, Zr$). The present calculations are plotted as the filled circles with error bars as well as the interpolation from the binary interaction parameters (red dashed line). The dotted purple line is the Voigt upper shear modulus bound, the gold dashed line is the lower Reuss shear modulus bound and the black line is the Hill shear modulus average plotted from a 50-50 mixture of the alloying elements X and Y to Ti.	139
6.15	<i>G</i> calculations of five of the Ti-X-Y ternary systems ($X \neq Y = Mo, Nb, Ta, Sn, Zr$). The present calculations are plotted as the filled circles with error bars as well as the interpolation from the binary interaction parameters (red dashed line). The dotted purple line is the Voigt upper shear modulus bound, the gold dashed line is the lower Reuss shear modulus bound and the black line is the Hill shear modulus average plotted from a 50-50 mixture of the alloying elements X and Y to Ti.	140
6.16	<i>E</i> of multicomponent bcc Ti alloys predicted from the database are compared with measured experimental results. Error bars plotted are from the variation in experimentally determined Young's moduli values for the specific multi-component alloy. The grey region refers to the error in the first-principles calculations. More information on the alloys is Table 6.4 [37–39].	141
7.1	Relative energy of the bcc, hcp, ω , α'' phases in the Ti-Nb system are plotted from 100 at. % Ti to 100 at. % Nb.	155
7.2	Relative energy of the bcc, hcp, ω , α'' phases in the Ti-Ta system are plotted from 100 at. % Ti to 100 at. % Ta.	156
7.3	Martensitic transformation temperature is plotted versus the Ti-Nb composition.	157
7.4	Calculated C_{11} , C_{12} , C_{13} , and C_{22} values (circles) plotted as well as the pure element extrapolation (red dashed line) and the present modeling (black dashed line) for five of the elastic stiffness constants of Ti-Nb in the α'' phase.	158
7.5	Calculated C_{23} , C_{33} , C_{44} , C_{55} , and C_{66} values (circles) plotted as well as the pure element extrapolation (red dashed line) and the present modeling (black dashed line) for four of the elastic stiffness constants of Ti-Nb in the α'' phase.	159

7.6	Calculated C_{11} , C_{12} , C_{13} , C_{33} , and C_{44} values (circles) plotted as well as the pure element extrapolation (red dashed line) and the present modeling (black dashed line) for the elastic stiffness constants of Ti-Nb in the ω phase.	160
7.7	Calculated C_{11} , C_{12} , C_{13} , C_{33} , and C_{44} values (circles) plotted as well as the pure element extrapolation (red dashed line) and the present modeling (black dashed line) for the elastic stiffness constants of Ti-Nb in the hcp phase.	161
7.8	Elastic properties of the bcc, hcp, ω , α'' phases in the Ti-Nb system calculated from first-principles based on DFT are plotted as symbols. The CALPHAD fitting are plotted as the dashed lines. The figure is plotted from 100 at. % Ti to 100 at. % Nb.	162
7.9	Phonon density of states is plotted for the TiNb alloy at 20 at. % Nb. The dashed line represents the slow cooled sample while the solid line represents the quenched sample.	163
7.10	Phonon density of states is plotted for the TiNb alloy at 18 at. % Nb. The dashed line represents the slow cooled sample while the solid line represents the quenched sample.	164
7.11	Phonon density of states is plotted for the TiNb alloy at 12 at. % Nb. The dashed line represents the slow cooled sample while the solid line represents the quenched sample.	165
7.12	Phonon density of states is plotted for the TiNb alloy at 10 at. % Nb. The dashed line represents the slow cooled sample while the solid line represents the quenched sample.	166
7.13	Entropy difference between the Ti-Nb alloys with the same alloy composition is plotted as a function of temperature.	167
7.14	Diffraction pattern of the Ti-Nb alloy at 20 at. % Nb. The dashed line represents the slow cooled sample while the solid line represents the quenched sample.	168
7.15	Diffraction pattern of the Ti-Nb alloy at 18 at. % Nb. The dashed line represents the slow cooled sample while the solid line represents the quenched sample.	169
7.16	Diffraction pattern of the Ti-Nb alloy at 12 at. % Nb. The dashed line represents the slow cooled sample while the solid line represents the quenched sample.	170
7.17	Diffraction pattern of the Ti-Nb alloy at 10 at. % Nb. The dashed line represents the slow cooled sample while the solid line represents the quenched sample.	171
C.1	203

List of Tables

1.1	Young's moduli of common implant materials compared with the Young's modulus of bone [43].	7
3.1	Equilibrium properties of volume V_0 , energy E_0 , bulk modulus B and the first derivative of bulk modulus with respect to pressure B' from the first-principles calculations for each pure elements in their SER state. The sv and pv refer to the electrons chosen as valance according to the VASP recommendations. The presently calculated results are also compared with available experimental data.	39
3.2	First-principles results at 0 °K for the enthalpy of formation (H_{Form}) of the bcc phase for different mole fraction (x) of alloying element X in the Ti-X binary systems (X = Mo, Nb, Ta, Zr).	40
3.3	First-principles results at 0 °K for the enthalpy of formation (H_{Form}) of the bcc phase for different mole fraction (x) of Ti in the Ti-X-Y ternary systems (X ≠ Y = Mo, Nb, Ta, Zr).	41
3.4	Modelled binary and ternary thermodynamic parameters for the Ti-Mo-Nb-Ta-Zr system. The thermodynamic description of pure elements is not included. The pure element functions, such as GFCCTI, describe the Gibbs energy (G) of the phase (FCC) for the element (TI) were adopted from the SGTE database [32] are listed in the Supplementary TDB (thermodynamic database) file.	42
3.4	Modelled binary and ternary thermodynamic parameters for the Ti-Mo-Nb-Ta-Zr system. The thermodynamic description of pure elements is not included. The pure element functions, such as GFCCTI, describe the Gibbs energy (G) of the phase (FCC) for the element (TI) were adopted from the SGTE database [32] are listed in the Supplementary TDB (thermodynamic database) file.	43

3.4	Modelled binary and ternary thermodynamic parameters for the Ti-Mo-Nb-Ta-Zr system. The thermodynamic description of pure elements is not included. The pure element functions, such as GFCCTI, describe the Gibbs energy (G) of the phase (FCC) for the element (TI) were adopted from the SGTE database [32] are listed in the Supplementary TDB (thermodynamic database) file.	44
3.4	Modelled binary and ternary thermodynamic parameters for the Ti-Mo-Nb-Ta-Zr system. The thermodynamic description of pure elements is not included. The pure element functions, such as GFCCTI, describe the Gibbs energy (G) of the phase (FCC) for the element (TI) were adopted from the SGTE database [32] are listed in the Supplementary TDB (thermodynamic database) file.	45
3.4	Modelled binary and ternary thermodynamic parameters for the Ti-Mo-Nb-Ta-Zr system. The thermodynamic description of pure elements is not included. The pure element functions, such as GFCCTI, describe the Gibbs energy (G) of the phase (FCC) for the element (TI) were adopted from the SGTE database [32] are listed in the Supplementary TDB (thermodynamic database) file.	46
4.1	Lattice parameters from first-principles calculations compared with experimental values.	71
4.2	Equilibrium volume V_0 , bulk modulus B , and the first derivative of bulk modulus with respect to pressure B' , from fitted equilibrium properties from the EOS at 0 °K compared to experimental work and previous DFT studies.	72
4.3	Elastic stiffness constants and elastic properties predicted using the Hill approach and the scaling factors used in the Debye model, calculated from the Poisson ratio, see Eq. 2.12. To ensure the accuracy of the calculated scaling factor, the bulk modulus (B) calculated from the elastic constants was compared to the B_{EOS} calculated from the EOS fitting Eq. 2.6.	73
4.4	Modeled parameters in SI units in the present work for the phases in the Sn-Ta binary system. These parameters were incorporated with the SGTE data for the pure elements [32].	74
5.1	Calculated pure element elastic stiffness constants and the bulk modulus B (in GPa) by X-C functional of PBE are compared with the previous first-principles calculations (FP) by X-C functional PW91 and experiments (Expt). Sv, pv and d refereeing to the s, p, and d states being treated as valance, respectively.	94

5.2	Evaluated interaction parameters L_0 and L_1 using the R-K polynomial Eq. 2.38 for the elastic stiffness constants for the Ti-X binary systems.	95
5.3	First-principles calculations of the elastic stiffness constants, bulk modulus B , shear modulus G , and Young's modulus E in GPa for different atomic percent compositions of the bcc Ti-X binary systems at 0 °K. As well as experimental data for the Young's modulus obtained at 300 °K by the reference stated.	96
5.3	First-principles calculations of the elastic stiffness constants, bulk modulus B , shear modulus G , and Young's modulus E in GPa for different atomic percent compositions of the bcc Ti-X binary systems at 0 °K. As well as experimental data for the Young's modulus obtained at 300 °K by the reference stated.	97
5.4	Predicted Young's modulus (in GPa) of higher order alloys in the bcc phase compared to experimental values found with both the weight percent and atomic percent listed.	98
6.1	First-principles calculations of the elastic stiffness constants	120
6.1	First-principles calculations of the elastic stiffness constants	121
6.2	First-principles calculations of the bulk modulus B , shear modulus G , and Young's modulus E in GPa for different atomic percent compositions of the bcc Ti-X-Y ternary systems at 0 °K as well as experimental data obtained for the Young's modulus at 300 °K by the references stated.	122
6.2	First-principles calculations of the bulk modulus B , shear modulus G , and Young's modulus E in GPa for different atomic percent compositions of the bcc Ti-X-Y ternary systems at 0 °K as well as experimental data obtained for the Young's modulus at 300 °K by the references stated.	123
6.3	Evaluated interactions parameters (L_2 , Eq. 2.30) for the elastic stiffness constants of the Ti-containing ternary alloys.	124
6.4	Predicted Young's moduli (E) (in GPa) of higher order alloys using the binary and ternary interaction parameters in the bcc phase compared to the predicted Young's moduli (E_{BIN}) using just the binary interaction parameters and the experimental values found with both the weight percent and atomic percent listed.	125
7.1	First-principles calculations of the elastic stiffness constants in GPa for different atomic percent compositions in the α'' , bcc, hcp, and ω phases in the Ti-Nb system at 0 °K.	150

7.1	First-principles calculations of the elastic stiffness constants in GPa for different atomic percent compositions in the α'' , bcc, hcp, and ω phases in the Ti-Nb system at 0 °K.	151
7.2	Evaluated interaction parameters L_0 and L_1 , using Eq. 2.38, for the elastic stiffness constants of the bcc, hcp, α'' and ω phases in the Ti-Nb systems.	152
7.3	Phase fractions and experimentally determined E compared with the predicted E using the rule of mixtures and interaction parameters in Table 7.2 for the Ti-Nb system.	153
7.4	Phase fractions determined from the diffraction patterns for the Ti-Nb alloys.	154

Acknowledgments

Dedication

Chapter 1

Introduction

1.1 Motivation

Titanium (Ti) and its alloys have been used in biomedical applications for many years because of their biocompatibility and corrosion resistance properties [43]. In recent years, there has been an increasing interest in developing better materials for load-bearing implants, due to the increase in total knee and hip replacements. Krutz et al. predicted that the total number of hip and knee replacements would increase by 174% and 673%, respectively, from 2005 to 2030, leading to 572,000 hip and 3.48 million knee procedures in the United States in 2030 [44]. Two of the driving factors for this situation involve the increasing number of younger individuals requiring replacements and the fact that the average life of these implants is only about 7-12 years [45]. These factors contribute significantly to the necessity for better implant materials. The primary considerations for biomedical implants, such as load-bearing knee and hip implants, are biocompatibility, corrosion resistance, fatigue strength, and Young's modulus (E) [43]. In previous years, the most common implants for these applications have been Ti-6Al-4V, stainless steels, and MoCoCr alloys [40, 46]. However, there have been issues with these materials, such as cytotoxicity that has been observed with alloys containing aluminum and vanadium [47]. Another important impediment concerning the common implant materials is stress shielding, which can lead to implant failure. Stress shielding occurs when the E of the implant is higher than that of bone. Due to the difference in E , load applications to the joint result in the implant material absorbing all of the stress and causing the bone surrounding the implant to atrophy, which leads to a loss in bone density, and can

result in implant loosening and failure [43]. Table 1.1 summarizes the comparison of the E of common implant materials (> 100 GPa) to bone (10-40 GPa) [43] and shows the extreme elasticity mismatch between the various materials. Using computational thermodynamics to develop a knowledge base of Ti and its alloys is an extremely useful tool in overcoming these challenges.

This work focused on investigating the thermodynamic and elastic properties of the biocompatible Ti-Mo-Nb-Sn-Ta-Zr system. The thermodynamic and elastic properties were calculated using first-principles based on Density Functional Theory (DFT). The parametrization of the properties was completed using the CALPHAD modeling approach. The combination of these two methodologies has been shown to eliminate the need for trial-and-error metallurgy, thus saving time, money and resources. A new computational methodology to predict the metastable phase formation was presented and verified by neutron scattering experiments. The culmination of this work provides a fundamental understanding of the thermodynamics and elastic properties for the Ti-Mo-Nb-Sn-Ta-Zr system.

1.2 Overview

1.2.1 Equilibrium Phases

The phase stability of Ti alloys has been shown to greatly affect the mechanical properties of these materials, so predicting and understanding this aspect of a Ti alloy will greatly impact its effectiveness as a biomedical implant. Titanium is stable in the α (hexagonal close packed, hcp) phase (space group P6₃/mmc) under standard temperature and pressure. However, at temperatures above 1155 °K, Ti is stable in the β (body centered cubic, bcc) phase (space group Im $\bar{3}$ m). The bcc phase can also be stabilized by alloying and such bcc Ti alloys have received much attention because of their low E values. Ti in the hcp phase has a E of 105 GPa while, Ti-6Al-4V which is a two phase mixture of hcp and bcc has an E of 110 and the Ti-35Nb-5Ta-7Zr alloy in the bcc phase has a E of 55 GPa which is more comparable to that of bone (10-40 GPa) [43, 48–51]. Bcc phase alloys having lower Young’s moduli has been seen for many other alloys as well, such as Ti-13Nb-13Zr, Ti-35Nb-5Ta-7Zr-0.4O, Ti-29Nb-Ta-Zr, and Ti-25Nb-Ta-Zr which are all bcc alloys that have a E of between 71 and 57 GPa [37, 43, 52]. With phase stability playing

an important role in the alloy selection for load-bearing implants, it is important to study how to stabilize the bcc phase at low temperature (<1155 °K). Mo, Nb and Ta were all chosen to be studied because they are biocompatible elements and strong β -stabilizers, while Zr is a bio-compatible weak β -stabilizer individually but strong stabilizer when in combination with other elements, such as Mo, Nb, and Ta [43]. In conjunction with their biocompatibility, studies have shown excellent Mo, Nb, Ta and Zr have excellent corrosion resistance and no allergy problems [52]. Recently, Sn has also been studied for use in Ti-alloys, due to its low cost [40] and in small concentrations, Sn does not effect the biocompatibility of the alloy.

When many bcc Ti-alloys have been shown to have a E more closely matching that of bone, in some cases a bcc Ti-alloy can miss the mark and not have a E that comes close to matching bone. Such an example is Ti-16Nb-13Ta-4Mo which has E of 110 GPa [38]. So, while understanding the thermodynamics of the system will help to target the bcc phase, also being able to predict the elastic properties before attempting to develop alloys for biomedical implants will reduce the need for trial and error and narrow the scope of alloys being selected. Therefore, the present study focused on determining the effects of alloying Ti with Mo, Nb, Sn, Ta and Zr on the thermodynamic and elastic properties. The combined DFT and CALPHAD approach was used to evaluate previous models and build new models for the binary and ternary alloys in the Ti-Mo-Nb-Sn-Ta-Zr system to build a completed database describing the thermodynamic and elastic properties of the system.

1.2.2 Metastable Phases

The completed thermodynamic database predicts the formation of the equilibrium phases, hcp and bcc. Based on the predictions, alloys that are in the bcc phase can be targeted and their elastic properties predicted. However, Ti and its alloys can form two metastable phases, α'' and ω . α'' is an orthorhombic martensitic phase (space group Cmcm). The martensitic transformation is displacive [53, 54]. Thermodynamically the martensitic transformation is first-order and initiated by supercooling defined by $T_0 - M_S$, where T_0 is the temperature where bcc transforms to hcp and M_S is the temperature where the martensitic transformation begins. An applied stress can also contribute to the driving force for a martensitic transformation. Kinetically the martensitic transformation propagates in an athermal manner

which suggests that the velocity of the interface and the force causing its movement contain an instability. The ω phase is a metastable hexagonal phase (space group P6/mmm) of Ti that has lattice parameters closely matching that of bcc Ti. The ω phase has been seen to form athermally when Ti is alloyed with β stabilizing elements such as Mo, Nb and Ta. It has been shown that different cooling techniques of alloys at certain compositions in the Ti-Mo, Ti-Nb and Ti-Ta systems cause either the α'' phase or the ω phase to form with a matrix of untransformed bcc phase. Quenching the samples leads to the formation of α'' , while slow cooling the samples leads to the formation of ω phase. The formation of these phases causes variations to the predicted elastic properties as seen in Figure 1.1 and 1.2, where the closed symbols represent the calculated E and the open symbols represent the experimentally determined E from the literature. The calculations and experiments agree well on the Ti-rich and Ta-rich sides but in the region marked by the purple box, the experiments show a higher E than predicted by calculations. This is due to the formation of α'' and ω . While the formation of the metastable phases greatly effects the properties of the Ti-alloys, there is no current way to predict their formation. In this dissertation, a new theoretical framework was proposed to predict the formation. To introduce the theoretical framework and ensure the accuracy, the phase stability and effect on the elastic properties of the α'' and ω phases were studied for the Ti-Nb and Ti-Ta systems. Initially, the ground state energy and elastic properties of multiple structures in the α'' , ω , bcc and hcp were calculated, across all compositions, for the Ti-Ta and Ti-Nb systems. The new theoretic framework predicts the concentrations and phases fractions where the metastable phases form. The predicted phase fractions were then used to predict the E using the rule of mixtures and mixed force constants are used to obtain the phonon density of states (DOS). The results from inelastic neutron scattering were then used to determine diffraction patterns and phonon density of states. By looking at the diffraction patterns obtained at 300 °K, the phase fractions were obtained and compared to the predicted phase fractions. The phonon DOS obtained from neutron scattering experiments at 300 °K was compared with the mixed force constant first-principles phonon DOS. In order to study what type of transformation takes place for these metastable phases to form, the temperature dependence of the phonon DOS was analyzed. The predicted E using the rule of mixtures was compared with experimental E from literature.

This completed thesis consists of the following main tasks:

1. The thermodynamics of the Ti-Mo-Nb-Sn-Ta-Zr system was investigated using first-principles calculations based on DFT and the CALPHAD method.
 - (a) Previous binary models were evaluated with the available experimental data as well as calculated enthalpy of formation of the bcc phase
 - (b) The thermodynamic description of the Sn-Ta binary alloy was modeled
 - (c) The thermodynamic descriptions of the Ti-containing ternary alloys were modeled
2. The elastic properties of the Ti-Mo-Nb-Sn-Ta-Zr system in the bcc phase were systematically calculated using first-principles based on DFT. The results were used to obtain interaction parameters, following the CALPHAD method, to predict the elastic properties as a function of composition.
3. The metastable phase formation in Ti alloys was investigated by first-principles calculations and experiments done on the Ti-Nb and Ti-Ta systems
 - (a) The ground state energies and elastic properties of the Ti-Nb and Ti-Ta systems in the hcp, bcc, ω and α'' were predicted using first-principles calculations
 - (b) From first-principles calculations:
 - i. The new theoretic framework was used to predict the phase fractions
 - ii. The phase fractions were used in a rule of mixtures to plot the phonon density of states and elastic properties
 - (c) From neutron scattering:
 - i. The phase fractions were determined and compared to the calculated predictions
 - ii. The phonon density of states, at 300 °K, was compared to the mixed force constant predicted phonon density of states

iii. The temperature dependent phonon density of states was used to study the transformation that occurs when these metastable phases form

Table 1.1. Young's moduli of common implant materials compared with the Young's modulus of bone [43].

Alloy	Young's Modulus (GPa)
Bone	10-40
cp-Ti*	105
Ti-6Al-4V	110
Stainless Steel	200
CoCrMo	200-230

*cp-commercially pure titanium

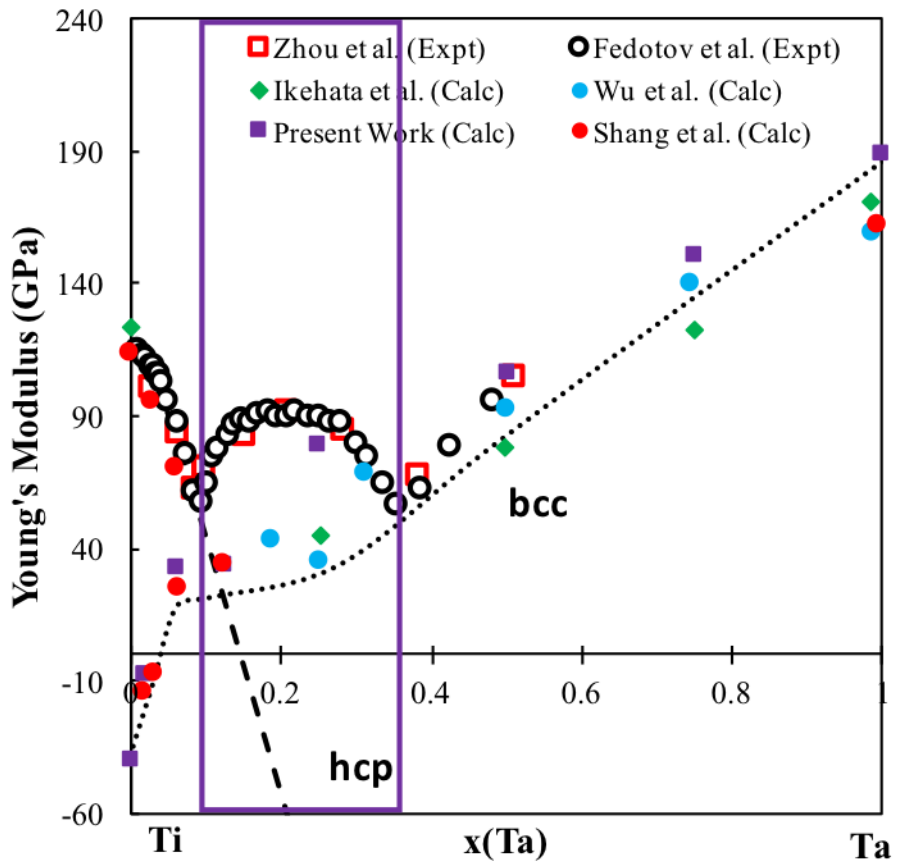


Figure 1.1. Comparison of first-principles calculations [1, 2] and experimental measurements of the Young's modulus of Ti-Ta alloys [3–5]. The purple box refers to the composition range when the calculations and experimentally determined E do not match up due to the formation of two metastable phases ω and α''

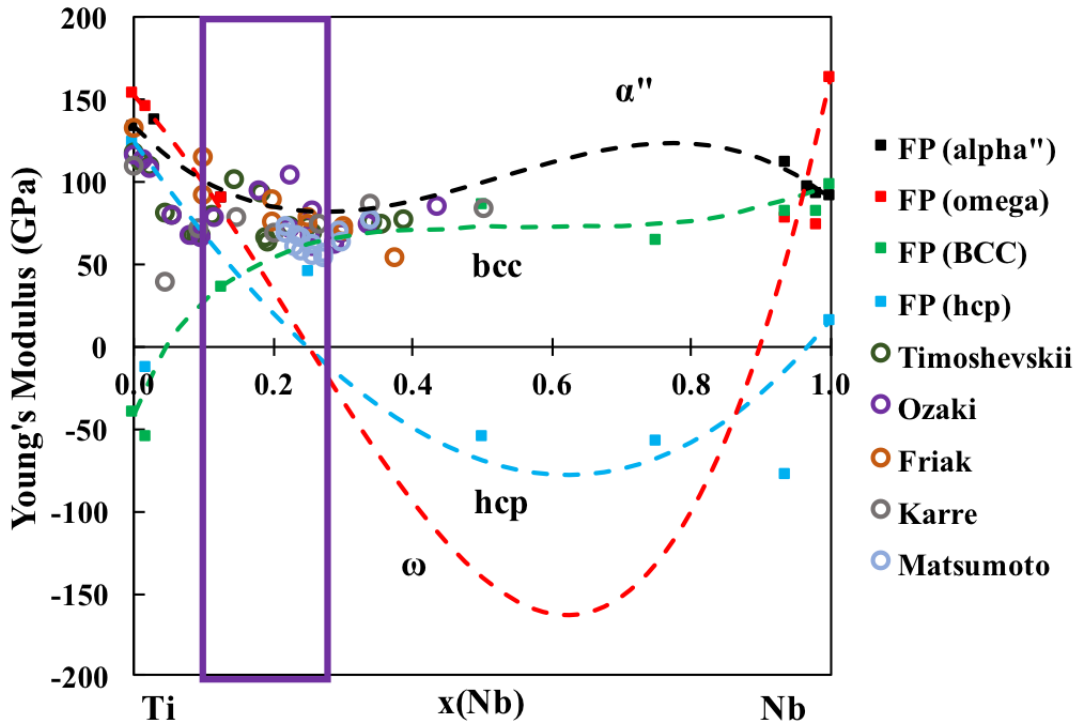


Figure 1.2. Comparison of the present first-principles calculations and experimental measurements of the Young's modulus of Ti-Nb alloys [6–10]. The purple box refers to the composition range when the calculations and experimentally determined E do not match up due to the formation of two metastable phases ω and α''

Chapter 2

Methodology

2.1 First-Principles Calculations

In this dissertation, the ground state energy structures, thermodynamic properties and mechanical properties of Ti and Ti-alloys were calculated using first-principles based on Density Functional Theory. The first-principles refers to the calculations originating from "first-principles", meaning that the inputs were the atomic coordinates and atomic numbers. The first-principles method computes the interactions between atoms in a periodic supercell. This was determined using quantum mechanical electronic theory that is based on the electronic charge density and does not rely on any empirical data. This section provides a description of the DFT methodology.

Schrödinger's time-independent non-relativistic equation is a solution to the many-body problem of calculating the interactions of positively charged nuclei and negatively charged electrons. The Schrödinger equation is:

$$\left[\sum_{i=1}^N \left(-\frac{\hbar^2}{2m} \nabla_i^2 + V_{ext}(r_i) \right) + \sum_{i < j} U(r_i, r_j) \right] \Psi = E_s \Psi \quad (2.1)$$

where the first bracketed part represents the Hamiltonian (\hat{H}), Ψ describes the wave function of electrons, and E_s describes the systems energy. The \hat{H} of the system is described by three parts, the first part represents the kinetic energy with N being the total number of electrons in the system, \hbar being Planck's constant and m the mass of an electron. The second term V_{ext} is the external potential and U is the potential of the electron-electron repulsion.

Eq. 2.1 can be solved for Ψ assuming the nuclei-nuclei interactions can be neglected due to the Born-Oppenheimer approximation. The Born-Oppenheimer approximation allows the assumption the nuclei are stationary and ignore the motion of the nuclei on the electronic timescale, due to the mass difference, with the nuclei being $\sim 10^3$ to 10^5 larger than electrons. However, even with this approximation solving Eq. 2.1 is difficult due to the electron-electron Columb interactions making the electronic motion correlated and the fact that the many-body problem results in too many variables because there are $3N$ degrees of freedom.

Hohenberg-Kohn formulated two theorems to simplify this problem [55]. The first theorem states that the external potential is a unique functional of the electron density. The second theorem states that the density that minimizes the total energy is the exact ground state density and thus the ground state is obtained variationaly. With these theorems, Kohn-Sham proved that the problem can be solved as if the electrons are not interacting and still obtain the density as if they were, by [56]:

$$\left[-\frac{\hbar^2}{2m} \nabla^2 + V_{ext}(r) + V_{Hartree}(r) + V_{XC}(r) \right] \phi_1(r) = \epsilon_i \psi_i(r) \quad (2.2)$$

where $V_{ext}(r)$ describes the electron-nuclei interaction similar as in Eq. 2.1:

$$V_{ext} = -e^2 \sum_a \frac{Z_a}{|r_i - R_a|} \quad (2.3)$$

where r_i represents the position of electron i and R_a represents the position of nucleus a with a charge valance of Z_a . The electron-electron interactions are represented by $V_{Hartree}$:

$$V_{Hartree}(r) = e^2 \int \frac{\rho(r)}{|r - r_j|} d^3r \quad (2.4)$$

where r and r_j represent the electrons and $\rho(r)$ is described by :

$$\rho(r) = \sum_i^N |\psi_i(r)|^2 \quad (2.5)$$

The final term, V_{xc} , is the exchange correlation potential that is described in terms of an exchange-correlation energy. While there is no exact solution to the exchange-correlation (X-C) energy available, there are multiple different approximations. Each approximation is done to account for different things. In the present work,

the generalized gradient approximation by Perdew and Wang (PW91) [57] and the generalized gradient approximation by Perdew, Burke and Ernzerhoff (PBE) [58] were used. The generalized gradient approach improves the total energies and atomization energies compared to other methods such as the local density approximation [59] but can over-correct for the expansion and softening of bonds. The generalized gradient approximation (GGA) is favored for inhomogeneous densities. Based on previous research by Perdew et al. [58], GGA's are considered to be adequate approximations for calculating metals. The use of PW91 vs PBE was compared for the elastic results of the Ti-Ta system. The results are discussed in detail in Chapter 5 but based on the results and the fact that PW91 X-C functional was designed to satisfy as many exact conditions as possible and thus has some issues. Perdew introduced the PBE X-C functional as an improvement to PW91 to satisfy less exact conditions and only looked at the ones that were energetically significant for metals. Therefore, the PBE X-C functional was chosen in the present thesis work. By implementing the theorems and the Kohn-Sham equation, the energy of the system can thus be calculated.

2.1.1 Density Functional Theory at 0 °K

The ground state energy at 0 °K without the contribution of zero-point vibrational energy was calculated by using the equation of states (EOS) fitting for the relationship between the energy and volume of the structure. The EOS fitting was achieved through an energy-volume ($E_0 - V$) curve of 5 or more relaxed volumes and using the four-parameter Birch-Murnaghan (BM4) EOS [60]:

$$E_0(V) = a + bV^{\frac{-2}{3}} + cV^{-43} + dV^{-2} \quad (2.6)$$

where a , b , c and d are fitting parameters. From this equation the equilibrium properties of a structure can be obtained such as, volume V_0 , ground state energy E_0 , bulk modulus B , and first derivative with respect to pressure B' can be calculated.

From the ground state energies, the energy of formation and enthalpy of formation at 0 °K was calculated by:

$$H_{Form} = H_{X_s Y_r} - (sH_X^{SER} + rH_Y^{SER}) \quad (2.7)$$

where $H_{X_sY_r}$ is the enthalpy of a specific structure at a specific composition of X_sY_r in the specific phase, bcc phase in this case, s and r are the mole fractions of elements X and Y , respectively. H_X^{SER} and H_Y^{SER} are the enthalpies of the pure elements X and Y in their standard element reference (SER) at standard temperature and pressure. The SER states of the pure elements are hcp Ti, bcc Mo, bcc Nb, bcc Ta, and hcp Zr. The valance configuration for each element was selected based on the Vienna Ab-initio Software Package (VASP) recommendations [61]. The p electrons were treated as valance electrons for the Mo and Ta, the d electrons were treated as valance electrons for Sn and the s electrons were treated as valance electrons for Ti, Nb, and Zr [61, 62].

2.1.2 Finite-temperature thermodynamics

The Helmholtz energy, $F(V, T)$, was calulated, as a function of temperature T and volume V using first-principles based on DFT:

$$F(V, T) = E_0(V) + F_{vib}(V, T) + F_{T-el}(V, T) \quad (2.8)$$

where E_0 is the static contribution at 0 °K calculated from Eq. 2.6, F_{vib} is the temperature-dependent vibrational contribution, and F_{T-el} is the thermal electronic contribution. At ambient pressure, the Helmholtz energy of the system is equal to the Gibbs energy, which is used in the CALPHAD modeling. The vibrational contribution was obtained through the phonon quasiharmonic supercell (phonon approach) or the Debye-Grüneisen method (Debye). The phonon approach is a more accurate approach than the Debye model but it is also more computationally expensive. In the present work, both the phonon and Debye models are used in different sections. The vibrational contribution obtained through phonon calculations of at least five different volumes is expressed by [63]:

$$F_{vib}(V, T) = k_b T \int_0^\infty \ln \left[2 \sinh \frac{\hbar \varrho}{2k_B T} \right] g(\varrho) d\varrho \quad (2.9)$$

where $g(\varrho)$ is the phonon density of states as a function of phonon frequency ϱ at volume V . ϱ is normally expressed in the literature as ω , however, due to the extensive discussion of the ω phase in this work the phonon frequency is expressed as ϱ to avoid confusion. In addition, the Debye model is used to estimate the

vibrational contribution [60]:

$$F_{vib}(V, T) = \frac{9}{8}k_b\theta_D(V) + k_B T \left[3\ln \left(1 - e^{-\frac{\theta_D}{T}} \right) - D \left(\frac{\theta_D}{T} \right) \right] \quad (2.10)$$

where θ_D is the Debye temperature, T is the temperature, and $D \left(\frac{\theta_D}{T} \right)$ is the Debye function. θ_D is calculated through:

$$\theta_D = s \frac{(6\pi^2)^{\frac{1}{3}}\hbar}{k_B} V_0^{\frac{1}{6}} \left(\frac{B}{M} \right)^{\frac{1}{2}} \left(\frac{V_0}{V} \right)^\gamma \quad (2.11)$$

where s is the Debye temperature scaling factor, γ is the Grüneisen parameter determined by the pressure derivative of the bulk modulus (B'), B is the bulk modulus, M is the atomic mass, and V_0 is the equilibrium volume. Here the V_0 , B , and B' are estimated from the EOS of Eq. 2.6. The Debye temperature scaling factor was determined by Moruzzi et al. [64] to be 0.617 for nonmagnetic metals. However, this value has been shown to be less accurate for all materials. Liu et al. extensively studied the Debye scaling factor and how to calculate the scaling factor based on the Poisson's ratio of a material [65]. The methodology by Liu et al. [65] was used for the present work to calculate the scaling factor:

$$s(\nu) = 3^{\frac{5}{6}} \left[4\sqrt{2} \left(\frac{1+\nu}{1-\nu} \right)^{\frac{3}{2}} + \left(\frac{1+\nu}{1-\nu} \right)^{-\frac{1}{3}} \right] \quad (2.12)$$

where ν is the Poisson's ratio, which can be calculated from the elastic stiffness constants.

The thermal electronic contribution is based on the electronic density of states and calculated with the Fermi-Dirac statistics [60, 66]:

$$F_{T-el} = E_{T-el} - TS_{T-el} \quad (2.13)$$

The E_{T-el} and S_{T-el} represent the energy and entropy of the thermal electron excitations, respectively. The E_{T-el} is expressed by:

$$E_{T-el}(V, T) = \int n(\epsilon, V) f(\epsilon, T) \epsilon d\epsilon - \int^{\epsilon_f} n(\epsilon) \epsilon d\epsilon \quad (2.14)$$

and the entropy S_{T-el} is expressed by:

$$S_{T-el}(V, T) = -k_B \int n(\epsilon, V) [ln f(\epsilon, T) + (1 - f(\epsilon, T)) ln(1 - f(\epsilon, T))] d\epsilon \quad (2.15)$$

where $n(\epsilon, V)$ is the electronic density of states (DOS) at energy ϵ , $f(\epsilon, T)$ is the Fermi-Dirac distribution, ϵ_f is the Fermi energy level and k_B is Boltzmann's constant. The Fermi-Dirac distribution $f(\epsilon, T)$ is expressed by:

$$f(\epsilon, T) = \left[\exp \left(\frac{\epsilon - \mu}{k_B T} \right) + 1 \right]^{-1} \quad (2.16)$$

and μ is the chemical potential of the electrons.

2.1.3 Elastic stiffness calculations

The single crystal elastic stiffness constants ($c_{ij}'s$) were calculated from the ground state energy structure using a stress-strain method developed by Shang et al. [67]. With this method, a set of independent strains $\varepsilon = (\varepsilon_1, \varepsilon_2, \varepsilon_3, \varepsilon_4, \varepsilon_5, \varepsilon_6)$ were imposed on the crystal lattice, where ε_1 , ε_2 , and ε_3 are the normal strains, ε_4 , ε_5 , and ε_6 are the shear strains, generating a set of stresses $\sigma = (\sigma_1, \sigma_2, \sigma_3, \sigma_4, \sigma_5, \sigma_6)$. Hooke's law is then used to calculate the elastic stiffness constants:

$$\begin{pmatrix} c_{11} & c_{12} & c_{13} & 0 & 0 & 0 \\ c_{12} & c_{22} & c_{23} & 0 & 0 & 0 \\ c_{13} & c_{23} & c_{33} & 0 & 0 & 0 \\ 0 & 0 & 0 & c_{44} & 0 & 0 \\ 0 & 0 & 0 & 0 & c_{55} & 0 \\ 0 & 0 & 0 & 0 & 0 & c_{66} \end{pmatrix} = \begin{pmatrix} \varepsilon_{1,1} & \varepsilon_{1,n} \\ \varepsilon_{2,1} & \varepsilon_{2,n} \\ \varepsilon_{3,1} & \dots & \varepsilon_{3,n} \\ \varepsilon_{4,1} & \varepsilon_{4,n} \\ \varepsilon_{5,1} & \varepsilon_{5,n} \\ \varepsilon_{6,1} & \varepsilon_{6,n} \end{pmatrix}^{-1} \begin{pmatrix} \sigma_{1,1} & \sigma_{1,n} \\ \sigma_{2,1} & \sigma_{2,n} \\ \sigma_{3,1} & \dots & \sigma_{3,n} \\ \sigma_{4,1} & \sigma_{4,n} \\ \sigma_{5,1} & \sigma_{5,n} \\ \sigma_{6,1} & \sigma_{6,n} \end{pmatrix} \quad (2.17)$$

where "-1" represents the pseudo-inverse. Due to symmetry, the bcc structure has only three independent elastic stiffness constants. However, with a lack of bcc stability for some of the calculations, all of the elastic stiffness constants were calculated and the average \bar{C}_{11} , \bar{C}_{12} and \bar{C}_{44} values were used:

$$\bar{C}_{11} = \frac{(c_{11} + c_{12} + c_{44})}{3} \quad (2.18)$$

$$\bar{C}_{12} = \frac{(c_{12} + c_{13} + c_{23})}{3} \quad (2.19)$$

$$\bar{C}_{44} = \frac{(c_{44} + c_{55} + c_{66})}{3} \quad (2.20)$$

This case is for the unstable bcc elastic calculations to mimic the behavior of a cubic structure. The largest variance between the similar elastic stiffness constants, when calculating the average, was used to show the deviation from the bcc symmetry in the calculations, shown as error bars. The stable bcc structures show no variance and thus no error bars. To examine the effects of different strain on the elastic properties, three groups of non-zero strain magnitudes, ± 0.01 , ± 0.03 , and ± 0.07 , were tested and the results are discussed in chapter 5. After testing, the ± 0.01 was used for all the calculations. The polycrystalline elastic properties including bulk (B), shear (G), and E modulus were calculated from the elastic stiffness constants, based on the Voigt-Reuss-Hill approach [68]. The Voigt gives the upper elastic bound due to the assumption of constant strain in all grains, the Reuss gives the lower elastic bound due to the assumption of constant stress in all grains, and the Hill approach is the average of Voigt and Reuss and is closer to real values [69, 70]. The Hill approach is hence what is listed in the results section. The Voigt and Reuss bounds were also plotted in the figures to give the bounds of the moduli values.

In order to fully investigate the effects of the alloying elements on the Ti-alloys, the mechanical stability of the bcc phase was studied. The mechanical stability is given by Born's criteria for a cubic crystal [71, 72]:

$$\bar{C}_{11} - |\bar{C}_{12}| > 0 \quad (2.21)$$

$$\bar{C}_{11} + 2\bar{C}_{12} > 0 \quad (2.22)$$

$$\bar{C}_{44} > 0 \quad (2.23)$$

Based on Born's criteria, when $\bar{C}_{11} - \bar{C}_{12}$ becomes negative then the phase, bcc in this case, loses its mechanical stability and thus $\bar{C}_{11} - \bar{C}_{12}$ is plotted in the results section.

2.1.4 Special quasirandom structures (SQS)

To calculate the energies, enthalpies of formation and elastic properties across the entire binary and ternary composition range, varying compositions of special quasirandom structures (SQS) were used. The SQS are small supercells used to mimic randomly substituted structures in terms of correlation functions. The binary and ternary bcc SQS, used in the present work, were previously generated by Jiang et al. [73, 74]. The relaxation of these SQS structures is complicated because local atomic relaxations can cause the structure to lose the desired lattice symmetry which is far from the original bcc lattice. To preserve symmetry, the calculations were carried out with three different relaxation schemes: 1) the cell volume, cell shape, and ionic positions are simultaneously relaxed, 2) the cell volume and shape are simultaneously relaxed, and 3) only the cell volume is relaxed. The relaxed structure with the lowest energy that preserved the bcc symmetry was used. There are two ways to verify that whether the SQS is still bcc or not after the relaxations. The first is to merge different elements into one element for the SQS structure, and then, use codes available to check the symmetry or space group (such as VASP [62] and phonopy [75]). The second is to visualize the structure directly using a visualization software and compare the symmetry to the unrelaxed bcc structure. For the present work, the relaxed structures were plotted in visualization software using and compared to the unrelaxed structure. After the relaxation, at least five different volume structures were generated and the ions were allowed to relax. This yields the different volumes needed for the EOS fitting described above, which allows a better prediction of the different properties as a function of composition.

2.1.5 High-throughput partition function

This section introduces a theoretic framework to predict the formation of a solid with a mixture of multiple microstates. Our theoretic framework implies that the competition of stable and metastable microstates, results in an increase of entropy as a function of temperature. The increased entropy is what stabilizes the formation of the metastable phases similarly to how entropy stabilizes Ti in the bcc phase. The combined helmholtz energy can be expressed by [76]:

$$F_c = -k_B T \left(\sum \frac{Z_i}{Z_c} \ln Z_i - \sum \frac{Z_i}{Z_c} \ln \frac{Z_i}{Z_c} \right) \quad (2.24)$$

where Z_i represents the partition function of a state expressed by:

$$Z_i = e^{-\frac{F_i}{k_B T}} = \sum_k e^{-\frac{E_{ik}}{k_B T}} \quad (2.25)$$

where F_i is the helmholtz energy of state i and E_{ik} is the energy eigenvalues of microstate k in the i state. Z_c represents the combined system expressed by:

$$Z_c = e^{-\frac{F_c}{k_B T}} = \sum_j e^{-\frac{E_{cj}}{k_B T}} \quad (2.26)$$

where F_c is the Helmholtz energy of the system and E_{cj} is the energy eigenvalues of microstate j in the combined state, c . Another way to write the combined helmholtz energy, based on these equations, is:

$$F_c = \sum p_i F_i - TS_{SCE} \quad (2.27)$$

where p_i is:

$$p_i = \frac{Z_i}{Z_c} \quad (2.28)$$

S_{SCE} is the state configurational entropy. The S_{SCE} is what stabilizes the phase formation and is predicted by:

$$S_{SCE} = -k_B \sum p_i \ln p_i \quad (2.29)$$

This entropy takes into account the statistical competition between the states making the combined helmholz energy more accurate.

2.1.6 First-principles calculation error

The error between the previous results (experimental or calculation) and present results was calculated using:

$$\sqrt{\frac{\sum [(A_{calc} - A_{ref})]^2}{\kappa}} = Difference \quad (2.30)$$

where A_{calc} is from the present calculation and A_{ref} is from the previous experiment or calculation, and κ is the total number of data points.

2.2 CALPHAD method

The CALPHAD method evaluates parameters to represent the Gibbs energy of individual phases as a function of temperature, pressure and composition. Thermochemical and phase boundary data obtained from experiments and first-principles calculations were used in the PARROT module of Thermo-Calc to evaluate the thermodynamic interaction parameters [77]. The Gibbs free energy is described by enthalpy H , temperature T and entropy S as follows:

$$G = H - TS \quad (2.31)$$

The Gibbs energy is then parameterized and expressed by:

$$G - H^{SER} = a + bT + cT\ln T + dT^2 + \sum_2^n e_n T^n \quad (2.32)$$

where H^{SER} refers to the elemental enthalpy in the SER state and a, b, c, d, e are coefficients. Other thermodynamic properties such as enthalpy, entropy and heat capacity can be derived from this equation. The parameterized equations for the pure elements have been determined and widely adopted from the SGTE to ensure global compatibility between different databases [32].

2.2.1 Solution phases

The databases were built upon the pure elements and then the effects of the binary and ternary interactions are modeled. Normally, the effects of alloying are modeled as solution phases or stoichiometric phases. The solution phases with one sublattice are described by:

$$G_m^\phi = \sum x_A^0 G_A^\phi + RT \sum x_A \ln x_A + {}^{x_S} G_m^\phi \quad (2.33)$$

where x_A is the mole fraction of element A and ${}^0 G_A^\phi$ is the molar Gibbs energy of pure element A in the specific phase (ϕ) being modeled and this is summed

for all elements in the alloy system of interest. The second term describes the ideal interaction between elements and is again summed for every element in the alloy system of interest. The last term represents the excess mixing energy, representing the non-ideal interactions between different species A and B . The non-ideal interactions are modeled between every set of binary and ternary elements in the system of interest. The excess mixing energy can be expressed by the Redlich-Kister polynomial as [78]:

$${}^{XS}G_m^\phi = \sum x_A x_B \sum_{k=0}^k L_{A,B}^\phi (x_A - x_B)^k \quad (2.34)$$

where ${}^k L_{A,B}^\phi$ represents the interaction parameter for elements A and B in phase ϕ described by:

$$L_{A,B}^\phi = {}^k a + {}^k bT \quad (2.35)$$

where ${}^k a$ and ${}^k b$ are evaluated model parameters. Eq. 2.34 can be extended to multi-component systems as:

$$\begin{aligned} {}^{XS}G_m^\phi = & \sum x_A x_B \sum_{k=0}^k L_{A,B}^\phi (x_A - x_B)^k + \sum x_A x_B x_C \\ & \left[{}^0 L_{A,B,C}^\phi (x_A + \delta_{A,B,C}) + {}^1 L_{A,B,C}^\phi (x_B + \delta_{A,B,C}) + {}^2 L_{A,B,C}^\phi (x_C + \delta_{A,B,C}) \right] \end{aligned} \quad (2.36)$$

where the ternary interaction parameters $L_{A,B,C}^\phi$ are described the same as the binary interaction parameters in Eq. 2.35 and $\delta_{A,B,C}$ is defined as $\delta_{A,B,C} = (1 - x_A - x_B - x_C)/3$.

Many alloys go through a disorder to order transition within a phase which requires modeling both the ordered and disordered part. For example, at low temperatures in many of the Ti-containing binary alloys, the randomly substituted bcc phase goes through a second order transition to become the ordered bcc#2 phase (CsCl-type). In the present work no modeling is done for the ordered bcc#2 phase. However, previous modeling of the bcc#2 phase is incorporated in to the database. The modeling of ordered phases was discussed extensively by Ansara [16].

2.2.2 Stoichiometric compounds

The Gibbs energy of stoichiometric compounds was modeled in per mole unit formula. For the stoichiometric compound, A_pB_q , the Gibbs energy is expressed by [79]:

$${}^0G_m^{A_pB_q} = a + bT + p * {}^0G_A^{SER} + q * {}^0G_B^{SER} \quad (2.37)$$

where a and b are the evaluated parameters, ${}^0G_A^{SER}$ is the Gibbs energy of pure element A in the SER phase, ${}^0G_B^{SER}$ is the Gibbs energy of pure element B in the SER phase, p is the number of atoms per unit formula of element A , and q is the number of atoms per unit formula of element B .

2.2.3 Elastic Properties

To obtain the elastic properties as a function of composition, the CALPHAD modeling approach was adopted and the Redlich-Kister polynomial was used to describe the elastic stiffness constants by [78, 80]:

$$E(x) = \sum x_A E_A^\phi + \sum x_A x_B^k L_{A,B}^\phi + \sum x_A x_B x_C^0 L_{A,B,C}^\phi \quad (2.38)$$

where similar to Eq. 2.34 and 2.36 the x_A , x_B , and x_C refer to the mole fraction of element A , B , and C respectively, E_A is the elastic property of element A , ${}^kL_{A,B}^\phi$ and ${}^kL_{A,B,C}^\phi$ are the binary and ternary interaction parameters, respectively. The binary and ternary interaction parameters were described in terms of Eq. 2.35 but with solely an a coefficient. For the binary modeling, the addition of one or two interaction parameters were studied to ensure the best fit. For the ternary systems, only one interaction parameter is needed [81–83]. The fittings of the binary and ternary interaction parameters were completed using the Mathematica code in appendix C. The binary interaction parameters were fitted using the difference between the pure elements extrapolation and the first-principles results for each Ti-X (X= Mo, Nb, Sn, Ta, Zr) composition. The ternary interaction parameters were fitted using the difference between the interpolaiton calculated from the pure elements and binary interaction parameters and the first-principles based on DFT results. The interaction parameters determined to describe the elastic stiffness constants were incorporated into a database. Pycalphad [42] was then

used to calculate the moduli values as a function of composition based on the Voigt-Reuss-Hill approach.

2.3 Experimental

2.3.1 Ti-Nb sample preparation

To study the effect of the metastable phase formation, two sets of Ti-Nb alloy samples at 0.1, 0.12, 0.18, and 0.2 mole fraction of Nb using pieces of Ti (99.8 % Ti Alfa Aesar, Stock No. 00241 for set one, and 99.8 % Sigma Aldrich, Stock No. 305812 HELP) and Nb (99.8 % Sigma Aldrich, HELP, for set one and set two). Two different titanium pieces were used because the Alfa Aesar titanium pieces were out of stock but they both had the same purity and thus should not lead to any issues with the data analysis. The alloyed samples were arc melted (MAM1, Edmund Buhler GmbH, Germany) under argon atmosphere. The alloys were machined into a cylindrical shape (0.7 inches in diameter and 0.7 inches in thickness). The samples were then heat treated using a Lindberg 59544 tube furnace. The tube was made of Al_2O_3 and was under vacuum. The samples were annealed at 1273 °K for 24 hours. The samples from set 1 were quenched in water to form the α'' phase. The samples in set 2 were slow cooled to form the ω phase.

2.3.2 Neutron Scattering

2.3.2.1 ARCS

The inelastic neutron scattering measurements were carried out using the Wide Angular-Range Chopper Spectrometer (ARCS) at the Spallation Neutron Source (SNS) at Oak Ridge National Laboratory. ARCS is a time-of-flight spectrometer meaning that the neutron beam's original position and energy are fixed and the ARCS detectors measure the neutrons final position and the time elapse. From this information, the data output on ARCS is a plot of the momentum and energy of the neutrons. The measurements were taken with the samples loaded in a customized vanadium sample holder. The holder was mounted into the furnace and kept under vacuum throughout all measurements. Two incident neutron energies, $E_i = 25\text{meV}$ and $E_i = 50\text{meV}$, were used at each temperature (300, 500, 700, 900, 1110 K).

Vanadium was chosen for the sample holders because vanadium has a very low coherent scattering length for neutrons and would not interact with the samples at the high temperatures being measured. The empty vanadium sample holder was measured at the same conditions at each temperature. The output of momentum and energy of the neutrons was corrected for the empty can scattering as well as the ARCS background.

2.3.2.2 Data Analysis

From the corrected momentum and energy plots of the samples, the diffraction patterns and phonon density of states can be obtained.

Diffraction is prominently an elastic scattering process. So the intensities of neutrons, with no change in energy, at each momenta are calculated and modeled as a Guassian function [84,85]. In the present work, each alloy sample contained some combination of the bcc, hcp, α'' and ω phases. In order to obtain the phase fractions, diffraction patterns, from the literature, of Ti and Nb in each of the individual phases are combined and fit to the diffraction pattern of the alloy in question. In order to do the fitting, the distance between scattering planes is taken into account for each phase. By fitting the literature diffraction patternsto the diffraction pattern of the alloy being studied the phase fractions are obtained.

From the energy vs momentum plots the phonon DOS of states can be obtained in a few different ways. In the present work an iterative method is used to remove the elastic and multi-phonon contributions to the phonon DOS and thus plot just the one-phonon DOS [86,87]. In order to obtain the one-phonon DOS, an iterative process was done that approximates the multi-phonon contribution and subtracts that and the elastic contribution from the total scattering to obtain the single-phonon DOS. First, a trial phonon DOS from the momenta vs energy plots was used to calculate the time dependent self-correlation function ($G(t)$) and the mean square atomic displacement $\langle u^2 \rangle$. $G(t)$ was expressed by [88,89]:

$$G(t) = \int_{-\infty}^{\infty} d\varrho \frac{Z(\varrho)}{\varrho} n(\varrho) e^{-i\varrho t} \quad (2.39)$$

where $Z(\varrho)$ is the phonon density of states as a function of phonon frequency ϱ and $n(\varrho)$ is the thermal occupancy factor. From $G(t)$ the dynamic structure factor from the incoherent scattering was calculated by [88,89]:

$$\bar{S}_{total}^{inc}(\varrho) = \sum_{\theta} \frac{1}{2\pi\hbar} e^{-Q^2(\theta,\varrho)\langle u^2 \rangle} \int_{-\infty}^{\infty} dt e^{-i\varrho t} e^{\hbar^2 Q^2(\theta,\varrho)G(t)/2M} \left[e^{\frac{-t^2}{2} \left(\frac{\Delta E(\varrho)}{2\hbar} \right)^2} \right] \quad (2.40)$$

where $e^{-Q^2(\theta,\varrho)\langle u^2 \rangle}$ is the Debye-Waller factor described the mean square atomic displacement [87]. The anisotropy in the Debye-Waller factor was neglected because the resulting errors were negligible [88]. M is the mass of a neutron, \hbar is Planck's constant and the bracked area has the ΔE which is the Gaussian instrument energy resolution of variable width. Q is defined by [88,89]:

$$Q(\theta, \varrho) = \sqrt{\frac{2M}{\hbar^2} \left(2E - \hbar\varrho - 2E\sqrt{1 - \frac{\hbar\varrho}{E}} \cos(2\theta) \right)} \quad (2.41)$$

From $G(t)$, the incoherent one-phonon \bar{S}_1^{inc} and elastic scattering \bar{S}_0^{inc} were determined and the multi-phonon incoherent scattering (S_m^{inc})contribution can be calculated by [88,89]:

$$\bar{S}_m^{inc} = \bar{S}_{total}^{inc} - \bar{S}_0^{inc} - \bar{S}_1^{inc} \quad (2.42)$$

The calculated \bar{S}_m^{inc} is then a good approximation for the multiphonon coherent scattering contribution as well. The elastic contribution was then total dynamical structure factor was scaled to match the incoherent dynamical structure factor and the elastic contribution was subtracted. From there the multiphonon contribution was subtacted leaving the new one-phonon DOS. This new one-phonon DOS was used to recalculate the multiphonon contribution. The procedure was repeated three times to converge the phonon DOS based on previous recommendations that showed three iterations were enough to converge within statistical errors [88,89].

Chapter 3 |

Ti-Mo-Nb-Sn-Ta-Zr

Thermodynamic Database

3.1 Introduction

The design of Ti-alloys for biomedical applications necessitates a completed thermodynamic database that will facilitate the prediction of phase compositions and fractions as a function of composition and temperature. However, there is no completed thermodynamic database for the Ti-Mo-Nb-Sn-Ta-Zr system and thus the present work aims at building a complete database with special focus on the Ti-rich alloys and bcc phase models. With this in mind the pure elements have been extensively studied and are widely adopted from the SGTE database [32]. The modeling of the binary systems has been widely documented with the exception of the Ta-Sn and Mo-Sn systems, while experimental phase boundary data is available for the ternary systems but little to no modeling has been completed. The Mo-Sn and Sn-Ta subsystems have high melting temperatures and little to no experimental data. In these cases, first-principles calculations based on DFT can be used to aid in modeling and supplement the lack of experimental data. The complete modeling of the Ta-Sn system is discussed in Chapter 4. In the present chapter, the thermodynamic descriptions of the Ti-Mo-Nb-Sn-Ta-Zr system are described.

While many of the alloys in this Ti system have been studied experimentally, yielding phase equilibrium data, only limited calorimetry data is available. With the present work focuses on bcc Ti-rich alloys, first-principles calculations based on DFT of the enthalpy of formation of the bcc phase were calculated. The thermodynamic

descriptions were built or evaluated using available experimental phase boundary data and present calculated thermochemical data. This work looks at evaluating new and previous models for the binary and Ti-containing ternary systems.

3.2 Computational details

First-principles results based on Density Functional Theory (DFT) are used to predict the enthalpy of formation of specific phases. In the present work, the enthalpy of formation of the bcc phase was calculated for the Ti-X and Ti-X-Y ($X \neq Y = Mo, Nb, Sn, Ta, Zr$) using the calculated energy of the pure elements in their SER states. For each binary system, 3 special quasirandom structures at different compositions, Ti_4X_{12} , Ti_8X_8 , $Ti_{12}X_4$, were calculated where ($X = Mo, Nb, Sn, Ta, Zr$). The SQS were each 16-atom supercells that were previously generated and relaxed according to the methodology chapter [73]. For each binary system other dilute compositions were calculated, i.e. Ti-Mo 4 dilute structures ($Mo_{53}Ti$ 54-atoms, $Mo_{15}Ti$ 16-atoms, Ti_7Mo 8-atoms, $Ti_{15}Mo$ 16-atoms), Ti-Nb 4 dilute structures ($Nb_{53}Ti$ 54-atoms, $Nb_{15}Ti$ 16-atoms, Ti_7Nb 8-atoms, $Ti_{53}Nb$ 54-atoms), Ti-Sn 1 dilute structure ($Ti_{15}Sn$ 16-atoms), Ti-Ta 5 dilute structures ($Ta_{53}Ti$ 54-atoms, $Ta_{15}Ti$ 16-atoms, Ti_7Ta 8-atoms, $Ti_{15}Ta$ 16-atoms, $Ti_{53}Ta$ 54-atoms), and Ti-Zr 2 dilute structures ($Zr_{15}Ti$ 16-atoms, $Ti_{53}Zr$ 54-atoms). For the Ti-X-Y ($X \neq Y = Mo, Nb, Sn, Ta, Zr$) ternary systems, three SQS calculations were completed at the compositions $Ti_{12}X_{12}Y_{12}$ (36-atom), $Ti_{16}X_8Y_8$ (32-atom), $Ti_{48}X_8Y_8$ (64-atom). The ternary SQS were previously generated and also relaxed according to the details outlined in the methodology chapter [74]. The DFT calculations are completed using VASP (Vienna ab-initio Simulation Package) [61]. The ion-electron interactions were described using the projector augmented wave (PAW) [62, 90] method. Based on the work of comparing X-C functionals (Figure 5.1) the exchange-correlation functional of the generalized gradient approach depicted by Perdew, Burke, and Ernzerhof (PBE) was employed [58]. For consistency, a 310 eV energy cutoff was adopted for all calculations, which is roughly 1.3 times higher than the default values suggested by VASP for the elements Ti, Mo, Nb, Sn, Ta, and Zr. The energy convergence criterion was 10^{-6} eV/atom, and the Monkhorst-Pack scheme is used for Brillouin zone sampling [61, 91]. The k-points grid for each calculation are listed in appendix c.

3.2.1 Sn binaries and ternaries

The thermodynamic description of the Mo-Sn system has never been modeled and there is little to no experimental data available. With this fact, first-principles calculations can be used to fill in the missing data points. However, this is not a hugely important sub-system and the modeling will be part of the future work. The Ta-Sn system is modeled in chapter 4. For the Sn-Zr system, the thermodynamic description was previously modeled. However, these models do not use compatible sublattice modeling with the current database, for the hcp phase. While the, Sn-Nb and Ti-Sn binary systems have been previously modeled, Sn will only be included in small percentages to the overall Ti-based alloy so until the rest of Sn binaries are modeled Sn will not be included in the database.

3.3 Pure element calculation results

In order to build the Ti-Mo-Nb-Ta-Zr thermodynamic database, thermodynamic descriptions for all the binary systems are evaluated first for accuracy and model compatibility and incorporated into the database (see Chapter 2). In the present work, only thermodynamic descriptions for the Ti-containing ternary systems are generated, Ti-X-Y ($X \neq Y = \text{Mo, Nb, Ta, Zr}$). When applicable the previous thermodynamic descriptions of the non Ti-containing ternary systems are incorporated into the database. The only case of a thermodynamic description of a non Ti-containing ternary, from this system, available in literature is the Mo-Nb-Ta system [11], and it is incorporated here.

Table 3.1 shows the equilibrium properties, volume V_0 , energy E_0 , bulk modulus B , and the derivative of bulk modulus B' obtained from Eq. 2.6 at 0 °K. The energy E_0 and bulk modulus B are compared with previous first-principles calculations at 0 °K. The energy values between the present calculations and previous calculations vary by 0 to 0.1 eV/atom. The B results from the present calculations and previous calculations vary by at most 3 GPa. The variances between the E_0 and B are small and due to the fact that the previous calculations used slightly different input parameters such as a different exchange correlation functional (PBE vs PW91) and higher energy cutoff values. Overall, the results are comparable. The B results from the present calculations at 0 °K are then compared with experimental values

from literature. The variance between the B from the calculations and the B from experiments is also 3 GPa or less. This variance is attributed to the difference in temperature between the calculations and experiments. Based on the small variances shown in Table 3.1, the present calculations are deemed accurate.

3.4 Enthalpy of formation of bcc phase from first-principles

The enthalpies of formation of the bcc phase ($\text{bcc-}H_{Form}$) for the binary and ternary systems are presented in Table 3.2 and Table 3.3, respectively. As discussed in the methodology chapter, the $\text{bcc-}H_{Form}$ is calculated by Eq. 2.7. It is seen that Table 3.2 shows the first-principles results for $\text{bcc-}H_{Form}$ for the Ti-Mo system go from positive to negative to positive indicating the formation of a bcc miscibility gap. The first-principles results of the $\text{bcc-}H_{Form}$, for the Ti-Nb, Ti-Ta, and Ti-Zr systems, are positive across the entire composition range. Table 3.3 shows the values of the first-principles calculated $\text{bcc-}H_{Form}$. It is seen that the $\text{bcc-}H_{Form}$ values, for the Ti-Mo-Nb, Ti-Mo-Ta and Ti-Nb-Ta systems, go from positive at 100 at. % Ti to negative at 0 at. % Ti at the $X_{50}Y_{50}$ composition. The $\text{bcc-}H_{Form}$ values remain positive from 100 at. % Ti to 0 at. % Ti at the $X_{50}Y_{50}$ composition for the Ti-Mo-Zr, Ti-Nb-Zr, and Ti-Ta-Zr systems. For each system that the $\text{bcc-}H_{Form}$ is calculated, the values are compared with the CALPHAD modeling predictions and in some cases, are compared with experimentally obtained results. For some of the systems, when comparing the first-principles results of the $\text{bcc-}H_{Form}$ and the CALPAHD modeling prediction of the $\text{bcc-}H_{Form}$, no large discrepancies are seen and thus no new modeling is completed. In other cases, comparing the first-principles results of the $\text{bcc-}H_{Form}$ and the CALPAHD modeling prediction of the $\text{bcc-}H_{Form}$ showed larger discrepancies and then the first-principles $\text{bcc-}H_{Form}$ values are used to introduce new bcc interaction parameters. Each binary and Ti-containing ternary system is discussed in detail in the next sub sections below.

3.5 Thermodynamic modeling of the ten binary systems

3.5.1 Mo-Nb, Mo-Ta, Nb-Ta

Figure 3.1 shows the calculated phase diagrams for the Mo-Nb, Mo-Ta, and Nb-Ta systems from thermodynamic descriptions in the literature in comparison with experiments. The Mo-Nb, Mo-Ta and Nb-Ta descriptions are adopted from the modeling completed by Xiong et al. [11]. Xiong et al. [11] modeled these three binary systems and the ternary system, Mo-Nb-Ta. Binary interaction parameters were introduced for the liquid and bcc solution phases. The thermodynamic description, for the Mo-Nb system, was completed using differential thermal analysis experiments that measured both the liquidus and solidus temperatures [11]. Xiong et al. [11] decided to only use the experiments (shown in Figure 3.1 as X and +) that estimated the pure elements melting temperatures reasonably well when evaluating the binary interaction parameters. Xiong et al. [11] discussed, that after evaluating the binary interaction parameters for the Mo-Nb system, the experiments, shown by \circ , \triangle , \square , agreed well with the predicted phase diagram. Even though, the remaining experimental data points (\diamond , *) were quite low as compared to the predicted phase diagram, they were also quite low compared to all the other experiments [11] and were considered inaccurate. Thus Xiong et al. [11] concluded that the thermodynamic description generated is adequate at predicting the experimental data.

The thermodynamic description, for the Mo-Ta system, was completed using two sets of experimental data (\triangle , *, \diamond , \square) [11]. These particular experimental data points were chosen because they accurately measured the melting temperatures of Mo and Ta. The predicted phase diagram accurately reproduced the experimental data, with the exception of the experimental data [11] shown as " \circ ". This set of experimental data was 70 °K higher than all other experimental data. So as discussed by Xiong et. al. [11] the data were not thought to be accurate and were ignored.

For the Nb-Ta system, the thermodynamic description was completed using the experimental liquidus data [11] depicted in the figure by \circ , \triangle , and \square , because it predicts the melting temperatures of Nb and Ta accurately. The experimental

work which measured the solidus temperature (*) was not used because the melting temperatures of Nb and Ta showed discrepancy. The predicted phase diagram reproduces the experimental data well with the exception of the experimental work depicted by \diamond . This data was ignored because the values were 343 °K higher than the experimental values and thus it was determined by Xiong et al. [11] to be inaccurate. The present work agrees with the conclusion reached by Xiong et al. [11] and agrees that the phase diagrams reproduce the experimental data accurately. The sublattice models used by Xiong et al. [11] are compatible with the working database and the binary descriptions are incorporated without any changes. The interaction parameters for the binary systems incorporated into the database are listed in Table 3.4.

3.5.2 Mo-Zr, Nb-Zr and Ta-Zr

Figure 3.2 shows the predicted phase diagrams for the Mo-Zr, Nb-Zr, and Ta-Zr systems. For the Mo-Zr system, there are multiple previous thermodynamic descriptions and experimental results available. In the present work, the evaluation by Perez et al. [12] is chosen to be incorporated due to the fact that their model was also incorporated into the Ti-Mo-Zr ternary modeling found in the literature. The experimental data that is plotted determined the single-phase region, two-phase region, phase boundaries, and peritectic and eutectoid reactions. Perez et al. [12] went into more details on the available experimental data and discussing what was included in their evaluation. Perez et al. [12] introduced interaction parameters for the liquid, bcc, hcp, and Laves_C15 phases. The thermodynamic description generally reproduces all experimental data accurately.

The thermodynamic description, for the Nb-Zr system, was previously evaluated by Guillermet [13] in the literature. Figure 3.2 plots the predicted phase diagram with the solidus experimental data (\diamond , *) as well as the hcp solvus (Y, \circ) and bcc miscibility gap (\triangle , \square , +) data [13, 14, 21]. The description includes interaction parameters for the liquid, bcc, and hcp solution phases and accurately reproduces the experimental data.

For the Ta-Zr system, the thermodynamic description was also evaluated by Guillermet [15]. As discussed by Guillermet [15], there is quite a lot of experimental data, phase boundary results from at least five different papers and thermodynamic

results from three different papers [15]. Figure 3.2 plots the single-phase, two-phase, phase boundary, and solidus experimental data. Interaction parameters were introduced for the bcc, hcp, and liquid phases. The predicted phase diagram reproduces the data fairly well.

The thermodynamic descriptions of the three binary systems Mo-Zr, Nb-Zr, and Ta-Zr are determined to be accurate and the sublattice modeling used is compatible with the working database. Thus, the thermodynamic descriptions are incorporated into the database. The interaction parameters for the binary systems incorporated into the database are listed in Table 3.4.

3.5.3 Ti-Mo

The thermodynamic description in the COST 507 database, modeled by Saunders, [16] is looked at for the Ti-Mo system. This model is chosen because it is the model incorporated into the Ti-Mo-Zr thermodynamic modeling [24]. Interaction parameters were evaluated for the liquid, fcc, hcp, bcc (ordered bcc#1 and disordered bcc#2), AlM_D019, AlM-D022, and the AlTi-L10 phases. Figure 3.3a plots the predicted phase diagram [16] with the available experimental phase boundary data [17]. The phase boundary data is reproduced accurately. Figure 3.3b plots the predicted enthalpy of formation of the bcc phase (solid line) versus the results from the present first-principles calculations (circles) and are compared to the enthalpies of formation of the bcc phase obtained experimentally (red squares) [18]. The experimental bcc- H_{Form} values and the prediction from the model are at 300 °K while the first-principles results are at 0 °K. The experimental values of bcc- H_{Form} compare well with the calculations but get more negative closer to the Mo-rich side which can be attributed to the temperature difference. The enthalpy of formation of the bcc phase predicted varies from the first-principles calculations drastically between 20 and 80 at.% Mo. This discrepancy is due to the disagreement on the existence of a bcc miscibility gap. Previous experimental research, including the values plotted here, have shown an equilibrium bcc miscibility gap which would fit what is seen in the first-principles calculations [18, 92, 93]. While there is an interaction parameter for the bcc order and disorder, Saunders [16] did not model the bcc miscibility gap as being an equilibrium phase. While there are previous thermodynamic descriptions that model the bcc miscibility gap, Kar et al. [24]

showed that the experimental data from higher-component systems fit better with the description containing no miscibility gap. Based on this and the fact that the sublattice modeling is compatible with the working database, the thermodynamic description by Saunders [16] is adopted with no changes. The interaction parameters for the binary system incorporated into the database are listed in Table 3.4.

3.5.4 Ti-Nb

For the Ti-Nb system, its thermodynamic description is taken from Zhang et al. [19]. Originally the thermodynamic description by Kumar et al. [20, 21] was evaluated because it was used in the modeling of the Ti-Nb-Zr system. However, new experimental phase boundary data on the Nb rich side (Δ) showed the need to switch to the Zhang et al. [19] thermodynamic description. Zhang et al. [19] introduced interaction parameters for the Liquid, bcc, hcp and omega phases. Figure 3.4a plots the predicted phase diagram from Zhang et al. [19] versus solidus data (\square), hcp and bcc solvus data (\circ) [20, 21] and the new Nb-rich bcc solvus data (Δ) [19]. Figure 3.4b plots the predicted enthalpy of formation (solid line) versus the present first-principles calculations (circles) and are compared to the enthalpies of formation of the bcc phase obtained experimentally (red squares) [18]. The experimental bcc- H_{Form} values and the prediction from the model are at 300 °K while the first-principles results are at 0 °K. The experimental bcc- H_{Form} values compare well with the calculations and any variance can be attributed to the temperature difference. There is an average variance of 0.17 kJ/mol-atom between the DFT and CALPHAD predictions of th bcc- H_{Form} which is also attributed to the temperature difference. However, even with the variance, the CALPHAD prediction compares well with the DFT results and the phase diagram reproduces the experimental data accurately. The sublattice models are compatible and the thermodynamic description from Zhang et al. [19] is incorporated into the present database with no alterations. The interaction parameters for the binary system incorporated into the database are listed in Table 3.4.

3.5.5 Ti-Ta

The thermodynamic description, for the Ti-Ta system, is taken from the COST 507 database [16]. The predicted phase diagram is plotted in Figure 3.5a, with

the experimental liquidus and solidus data (\diamond and Y) as well as bcc and hcp solvus data (\triangle , \square , and \circ) for comparison. The evaluation includes interaction parameters for the fcc, hcp, liquid, AlM-D019, AlM-D022, AlTi-L10, and the bcc (ordered bcc#1, disordered bcc#2) phases [22]. The thermodynamic description reproduces the experimental data accurately. The enthalpy of formation of the bcc phase predicted by the CALPHAD modeling (solid line) is plotted with the first-principles results (circles) in Figure 3.5b. The CALPHAD prediction of the bcc- H_{Form} reproduces the results from first-principles reasonably well on the Ti-rich and Ta-rich sides. The first-principles results vary on an average by 0.17 kJ/mol-atom. However, the CALPHAD prediction is at 300 °K and the first-principles are at 0 °K which explains the variance. Based on these conclusions the thermodynamic description is deemed accurate and since the sublattice modeling is compatible, the thermodynamic description is incorporated into the database and not altered. The interaction parameters for the binary system incorporated into the database are listed in Table 3.4.

3.5.6 Ti-Zr

The thermodynamic description, of the Ti-Zr system, evaluated by Kumar et al. [21] is used in the present work. The model by Kumar et al. is chosen because it was used in the ternary modeling of the Ti-Mo-Zr and Ti-Nb-Zr systems. The evaluation introduces interaction parameters for the liquid, bcc, and hcp solution phases. Figure 3.6a plots the predicted phase diagram compared with phase boundary data for the bcc to hcp (\circ) phase transformation and solidus (\triangle). The thermodynamic description accurately reproduces the phase boundary data. When doing the evaluation, heat of transformation data was also used and was discussed by Kumar et al. [21]. Figure 3.6b plots the present first-principles results (circles) versus the CALPHAD prediction (solid line) for the bcc- H_{Form} . The first-principles results and CALPHAD modeling vary on average by 1.2 kJ/mol-atom. The variance is larger than the other binary alloys due to the instability of the bcc phase at both 0 °K and 300 °K for the Ti-Zr alloy but the calculations and CALPHAD prediction follow the same trend. Based on the agreement between the experimental data, no alterations were made to the thermodynamic description and with the sublattice modeling compatibility, it was incorporated into the database. The interaction

parameters for the binary system incorporated into the database are listed in Table 3.4.

3.6 Thermodynamic modeling of six Ti-containing ternary systems

3.6.1 Ti-Mo-Nb

A thermodynamic description, for the Ti-Mo-Nb system, has never been evaluated in the literature. Two experimental investigations were done on the Ti-Mo-Nb system at 873 °K and 1373 °K [25, 94]. While both investigations agree that the isothermal section at 1373 °K is solely the bcc phase, the investigations differed on the phase boundary at 873 °K. It is suspected that at such a low temperature the samples did not reach equilibrium which accounts for the discrepancy. Based on this, the binary interpolation of the isothermal sections at 1373 °K and 873 °K are plotted. The predicted phase diagram at 1373 °K agreed with the experimentally determined phase diagram to be solely the bcc phase. The phase diagram at 873 °K is plotted in Figure 3.7a. The discrepancy, at 873 °K, is the existence of the bcc miscibility gaps as well as what compositions the phase boundary lines lie at. The enthalpy of formation of the bcc phase is predicted using an interpolation of the binary interaction parameters (solid line) and plotted with the first-principles results, in Figure 3.7b, starting from a 50-50 mixture of the alloying elements ($\text{Mo}_{50}\text{Nb}_{50}$) to 100 at.% Ti. While the first-principles calculations are at 0 °K and the binary interpolation is at 300 °K, the calculation results are reproduced with the CALPHAD prediction. The prediction varies by less than 1.5 kJ/mol-atom for all the calculations except at $\text{Mo}_{50}\text{Nb}_{50}$. While the calculation varies substantially from the prediction at $\text{Mo}_{50}\text{Nb}_{50}$, in order to improve this, the Mo-Nb binary system would have to be adjusted. In the present work, no thermochemical data was used to ensure the accuracy of the non Ti-containing binary systems but the previous binary models were able to reproduce the phase boundary data as discussed above. Based on the discrepancy between the experimental data and the fact that the first-principles thermochemical calculations are reproduced well by the binary interpolation, no ternary interaction parameters are evaluated.

3.6.2 Ti-Mo-Ta

The thermodynamic description, of the Ti-Mo-Ta system, has not been previously modeled. The binary interpolation of the Ti-Mo-Ta alloy is plotted in Figure 3.8a at 873 °K. At 873 °K, the Ti-Mo-Ta alloy has the bcc and hcp solution phases with a tie triangle showing a three-phase region of bcc#1, bcc#2, and hcp. The experimental data agreed with the two-phase bcc-hcp region in the Ti-rich corner, but did not see a bcc miscibility gap or tie triangle [23]. Figure 3.8b shows the present first-principles calculations (circles) of the bcc- H_{Form} compared with the binary interpolation from the CALPHAD prediction (solid black line). The first-principles calculations line up fairly well with the CALPHAD prediction. However, due to the discrepancy of the experimental data ternary interaction parameters are investigated for the hcp and bcc phases using the first-principles results and experimental phase boundary data. The evaluated interaction parameters are listed in Table 3.4. After assessing the ternary interaction parameters, the isothermal section at 873 °K is again plotted and compared with experimental data in Figure 3.9a and zoomed in for Figure 3.9b. The enthalpy of formation of the newly assessed bcc phase is plotted as a red dashed line in Figure 3.8b. The assessment reproduces the first-principles results accurately. With the introduction of the interaction parameters the isothermal section fits with the experimental data [23]. The work by Nikitin [23] determined hcp phase boundary data plotted as \circ and two phase experimental data as \bullet . The two phase experimental data is reproduced by the present model. The hcp phase boundary data are not reproduced. However, reliable solid phase boundary data are difficult to obtain at such a low temperature and if the evaluation is altered to fit the data; it then over fits and stabilizes non-equilibrium phases.

3.6.3 Ti-Mo-Zr

The thermodynamic description of the Ti-Mo-Zr system was previously modeled by Kar et al. [24]. The same binary phases used in the modeling by Kar et al. are included in the present database. The phases in this ternary system are liquid, bcc, hcp, and Laves_C15. After interpolating the ternary system from the binary models and comparing to two sets of available experimental data, Kar et al. [24] introduced interaction parameters for the Laves_C15 phase. As discussed by Kar et al. [24],

there is phase boundary data at 1273 °K, from two papers [24]. The phase boundary data conflicts on how far out the two-phase region should extend toward the Ti-rich corner and whether there is a bcc miscibility gap. Due to the discrepancy, Kar et al. [24] decided not to introduce any bcc, liquid or hcp interaction parameters. The prediction of the phase diagram at 1273 °K by Kar et al. [24] is plotted in Figure 3.10a and compared with one set of phase boundary data [24]. The phase boundary data fits well on the Zr-Mo binary side but extends further in the Ti-rich corner. This is where the discrepancy lies, the other set of phase boundary data, not shown here, stops shorter than the prediction. The predicted enthalpy of formation of the bcc phase is plotted with the present first-principles results in Figure 3.10b. The first-principles results vary by 1.5 kJ/mol-atom from the CALPHAD prediction but the largest variance is seen at Mo₅₀Zr₅₀ which would only be improved by adjusting the binary Mo-Zr interaction parameters. Based on the available experimental data [24], the present first-principles calculations, and the conclusions from Kar et al. [24], the present work agrees with the introduction of the ternary Laves_C15 interaction parameters and lack of liquid, bcc and hcp ternary interaction parameters. The ternary Laves_C15 interaction parameters are listed in Table 3.4.

3.6.4 Ti-Nb-Ta

A thermodynamic description of the Ti-Nb-Ta system had not previously been evaluated in the literature but different isothermal sections had been estimated by Na et al. [26] using phase boundary data. The phase boundary data was obtained through x-ray diffraction. Na et al. [26] looked at samples at 823 °K and 673 °K. The authors [26] discussed that it is likely that the alloys at 673 °K never reach equilibrium conditions. The experimental results [26] were plotted on the binary interpolation in Figure 3.11a and Figure 3.11b. The bcc phase boundary data do not match with the binary interpolation. Figure 3.12 plots the enthalpy of formation of the bcc phase predicted by the binary interpolation (solid line) and the first-principles results (circles). The first-principles results vary from the binary interpolation. Due to the variance, ternary interaction parameters for the bcc and hcp phases are investigated. The evaluation was done using the 823 °K experimental data and the present first-principles calculations and the 673 °K data

was neglected. The evaluated ternary interaction parameters are listed in Table 3.4. After evaluation, the ternary isothermal sections are plotted with the phase boundary data in Figure 3.13a and Figure 3.13b. The isothermal sections at both 673 and 823 °K reproduce the experimental data [26] well. The assessed prediction (red dashed line in Figure 3.12) of the enthalpy of formation of the bcc phase also improves to accurately match the first-principles results.

3.6.5 Ti-Nb-Zr

The thermodynamic description, of the Ti-Nb-Zr system, was previously evaluated by multiple authors [21, 27]. In the present work, the binary interpolation of the ternary isothermal section at multiple temperatures are compared with experimental data [21, 27]. Figure 3.14a plots the isothermal section at 843 °K compared with the two-phase equilibria data and the tie-triangle phase boundary data [27]. The binary interpolation reproduced the data accurately. The enthalpy of formation of the bcc phase is plotted in Figure 3.14b. The CALPHAD prediction (solid line) of the bcc- H_{Form} varies on an average by 1.34 kJ/mol-atom from the first-principles results (circles). While there is some variance, it can be attributed to the temperature difference and overall the variance isn't large. So, the conclusion is reached to not introduce ternary interaction parameters.

3.6.6 Ti-Ta-Zr

For the Ti-Ta-Zr system, Lin et al. [28] calculated the isothermal sections using binary interpolations and introduced no interaction parameters. The isothermal sections at 1273 and 1773 °K are plotted in Figure 3.15a and Figure 3.15b, respectively. Experimental phase boundary data along the bcc miscibility gap at 1273 °K and single phase • and two phase region ● data using x-ray diffraction at 1773 ° are plotted to compare with the binary interpolations [28, 29]. The phase boundary data is reproduced accurately. Figure 3.16 plots the binary interpolation prediction (solid line) of the bcc- H_{Form} compared to the present first-principles calculations (circles). On average the first-principles varies by 3.69 kJ/mol-atom attributed partially to the temperature difference. While the variance is larger for the enthalpy of formation, the experimental data points [28] are reproduced and thus no ternary interaction parameters are evaluated

It is worth mentioning that all the interaction parameters for the Ti-Mo-Nb-Ta-Zr system are listed in Table 3.4 and combined into a single thermodynamic database (TDB) file in Appendix A.

3.7 Conclusion

The present work builds a compatible thermodynamic database for the Ti-Mo-Nb-Sn-Ta-Zr system using descriptions of five pure elements, ten binary systems, and nine Ti-containing ternary systems. The thermodynamic descriptions of the pure elements are adopted from the SGTE database [32]. All of the binary systems had previous thermodynamic descriptions available in literature except Mo-Sn and Ta-Sn. A previous model was evaluated for accuracy when available for the binary systems. The Sn-Ta system was modeled in chapter 4. After evaluation the thermodynamic descriptions were incorporated into the present database. The binary interpolations of the Ti-containing ternary systems were plotted and compared with the available experimental data as well as the enthalpy of formation of the bcc phase calculated from first-principles based on DFT. The Ti-Sn-X systems ($X = \text{Mo, Nb, Ta, Zr}$) will be modeled in the future work with a thermodynamci description of the Mo-Sn system. The binary interpolations of the Ti-Nb-Zr and Ti-Ta-Zr systems had previously been plotted but no interaction parameters had been introduced. The present evaluation agreed with the previous evaluations and no ternary interaction parameters were introduced. The Ti-Mo-Zr system had previously been modeled and the present work agreed with the evaluation. The Ti-Mo-Nb, Ti-Mo-Ta and Ti-Nb-Ta systems had never previously been modeled. The present work evaluated interaction parameters for the Ti-Mo-Ta and Ti-Nb-Ta systems but didn't introduce any interaction parameters for the Ti-Mo-Nb system. The thermodynamic descriptions were all incorporated into a complete database that accurately predicts the phase stability of the Ti-Mo-Nb-Sn-Ta-Zr systems.

Table 3.1. Equilibrium properties of volume V_0 , energy E_0 , bulk modulus B and the first derivative of bulk modulus with respect to pressure B' from the first-principles calculations for each pure elements in their SER state. The sv and pv refer to the electrons chosen as valance according to the VASP recommendations. The presently calculated results are also compared with available experimental data.

Phase	V_0 ($\text{\AA}^3/\text{atom}$)	E_0 (eV/atom)	B (GPa)	B'	Reference
hcp-Ti_sv	17.37	-7.80	113	3.54	This work
		-7.89	113		Calc 0 °K [95, 96]
			110		Expt 300 °K [97]
bcc-Mo_pv	15.91	-10.84	262	4.37	This work
		-10.86	262		Calc 0 °K [96, 98]
			261		Expt 300 °K [99]
bcc-Nb_sv	18.14	-10.22	171	3.78	This work
		-10.12	174		Calc 0 °K [96, 100]
			172		Expt 300 °K [99]
bcc-Ta_pv	18.32	-11.85	196	4.32	This work
		-11.85	194		Calc 0 °K [96, 101]
			196		Expt 300 °K [99]
hcp-Zr_sv	23.44	-8.51	94	3.13	This work
		-8.55	94		Calc 0 °K [96, 102–104]

Table 3.2. First-principles results at 0 °K for the enthalpy of formation (H_{Form}) of the bcc phase for different mole fraction (x) of alloying element X in the Ti-X binary systems (X = Mo, Nb, Ta, Zr).

Structure	Type of Calc	x(X)	H_{Form} (kJ/mol-atom)
Ti	Elemental	0.000	7.29
Ti ₁₅ Mo	Dilute	0.063	3.08
Ti ₇ Mo	Dilute	0.125	2.82
Ti ₇₅ Mo ₂₅	SQS	0.250	1.12
Ti ₅₀ Mo ₅₀	SQS	0.500	-3.67
Ti ₂₅ Mo ₇₅	SQS	0.750	-5.18
TiMo ₁₅	Dilute	0.937	1.79
TiMo ₅₃	Dilute	0.981	5.82
Mo	Elemental	1.000	0.00
Ti ₅₃ Nb	Dilute	0.019	6.92
Ti ₇ Nb	Dilute	0.125	5.88
Ti ₇₅ Nb ₂₅	SQS	0.250	7.57
Ti ₅₀ Nb ₅₀	SQS	0.500	8.54
Ti ₂₅ Nb ₇₅	SQS	0.750	1.15
TiNb ₁₅	Dilute	0.938	0.59
TiNb ₅₃	Dilute	0.981	0.20
Nb	Elemental	1.000	0.00
Ti ₅₃ Ta	Dilute	0.019	7.21
Ti ₁₅ Ta	Dilute	0.063	7.04
Ti ₇ Ta	Dilute	0.125	9.28
Ti ₇₅ Ta ₂₅	SQS	0.250	4.89
Ti ₅₀ Ta ₅₀	SQS	0.500	3.94
Ti ₂₅ Ta ₇₅	SQS	0.750	3.10
TiTa ₁₅	Dilute	0.938	0.94
TiTa ₅₃	Dilute	0.981	0.28
Ta	Elemental	1.000	0.00
Ti ₅₃ Zr	Dilute	0.019	5.49
Ti ₇₅ Zr ₂₅	SQS	0.250	4.59
Ti ₅₀ Zr ₅₀	SQS	0.500	1.94
Ti ₂₅ Zr ₇₅	SQS	0.750	3.50
TiZr ₁₅	Dilute	0.938	5.72
Zr	Elemental	1.000	8.19

Table 3.3. First-principles results at 0 °K for the enthalpy of formation (H_{Form}) of the bcc phase for different mole fraction (x) of Ti in the Ti-X-Y ternary systems (X ≠ Y = Mo, Nb, Ta, Zr).

Structure	Type of Calc	x(Ti)	H_{Form} (kJ/mol-atom)
Mo ₅₀ Nb ₅₀	SQS	0.000	-38.69
TiMoNb	SQS	0.333	5.08
Ti ₂ MoNb	SQS	0.500	-2.10
Ti ₆ MoNb	SQS	0.750	2.18
Mo ₅₀ Ta ₅₀	SQS	0.000	-15.64
TiMoTa	SQS	0.333	-5.34
Ti ₂ MoTa	SQS	0.500	-1.82
Ti ₆ MoTa	SQS	0.750	2.77
Mo ₅₀ Zr ₅₀	SQS	0.000	10.31
TiMoZr	SQS	0.333	8.36
Ti ₂ MoZr	SQS	0.500	7.73
Ti ₆ MoZr	SQS	0.750	6.82
Nb ₅₀ Ta ₅₀	SQS	0.000	-0.41
TiNbTa	SQS	0.333	1.82
Ti ₂ NbTa	SQS	0.500	3.80
Ti ₆ NbTa	SQS	0.750	5.59
Nb ₅₀ Zr ₅₀	SQS	0.000	6.21
TiNbZr	SQS	0.333	9.82
Ti ₂ NbZr	SQS	0.500	10.06
Ti ₆ NbZr	SQS	0.750	8.75
Ta ₅₀ Zr ₅₀	SQS	0.000	5.75
TiTaZr	SQS	0.333	2.98
Ti ₂ TaZr	SQS	0.500	2.79
Ti ₆ TaZr	SQS	0.750	0.79

Table 3.4: Modelled binary and ternary thermodynamic parameters for the Ti-Mo-Nb-Ta-Zr system. The thermodynamic description of pure elements is not included. The pure element functions, such as GFCCTI, describe the Gibbs energy (G) of the phase (FCC) for the element (Ti) were adopted from the SGTE database [32] are listed in the Supplementary TDB (thermodynamic database) file.

Phase	Reference	Interaction Parameter
Liquid	[16]	$0_{Ti,Mo}^L = -9000.0 + 2.00 * T$
	[19]	$0_{Ti,Nb}^L = 7406.1$
	[16]	$0_{Ti,Ta}^L = 1000.0$
	[16]	$0_{Ti,Ta}^L = -7000.0$
	[21]	$0_{Ti,Zr}^L = -967.7$
	[11]	$0_{Mo,Nb}^L = 15253.7$
	[11]	$1_{Mo,Nb}^L = 10594.2$
	[11]	$0_{Mo,Ta}^L = 13978.9$
	[12]	$0_{Mo,Zr}^L = -24055.1 + 8.146 * T$
	[12]	$1_{Mo,Zr}^L = -5132.17 + 4.804 * T$
	[13]	$0_{Nb,Zr}^L = 10311.0$
	[13]	$1_{Nb,Zr}^L = 6709.0$
	[15]	$0_{Ta,Zr}^L = 13832.1$
	[15]	$1_{Ta,Zr}^L = -7150$
	[16]	$0_{Ti,Mo}^L = 2000.0$
	[16]	$1_{Ti,Mo}^L = -2000.0$
	[19]	$0_{Ti,Nb}^L = 13045.3$
	[16]	$0_{Ti,Ta}^L = 12000.0$
	[16]	$1_{Ti,Ta}^L = -2500.0$
	[21]	$0_{Ti,Zr}^L = -4346.2 + 5.49 * T$
	[11]	$0_{Mo,Nb}^L = -68202.6 + 29.86 * T$
	[11]	$1_{Mo,Nb}^L = 8201.3$
	[11]	$0_{Mo,Ta}^L = -75129.2 + 30.00 * T$
	[11]	$1_{Mo,Ta}^L = 6039.2$
	[12]	$0_{Mo,Zr}^L = 17936.0 + 3.10 * T$
	[12]	$1_{Mo,Zr}^L = -991.0 + 4.30 * T$
	[11]	$0_{Nb,Ta}^L = 1298.0$

Table 3.4: Modelled binary and ternary thermodynamic parameters for the Ti-Mo-Nb-Ta-Zr system. The thermodynamic description of pure elements is not included. The pure element functions, such as GFCCTI, describe the Gibbs energy (G) of the phase (FCC) for the element (Ti) were adopted from the SGTE database [32] are listed in the Supplementary TDB (thermodynamic database) file.

Phase	Reference	Interaction Parameter
hcp	[13]	$0_{Nb,Zr}^L = 15911.0 + 3.35 * T$
	[13]	$1_{Nb,Zr}^L = 3919.0 - 1.09 * T$
	[15]	$0_{Ta,Zr}^L = 29499.6 + 2.67 * T$
	[15]	$1_{Ta,Zr}^L = -4396.2 + 4.43 * T$
	[15]	$2_{Ta,Zr}^L = -6353.3 + 4.91 * T$
	This work	$0_{Ti,Mo,Ta}^L = -154731.2$
	This work	$0_{Nb,Ta,Ti}^L = -136603.3$
	This work	$1_{Nb,Ta,Ti}^L = -136602.7$
	[16]	$0_{Ti,Mo}^L = 22760.0 - 6.00 * T$
	[19]	$0_{Ti,Nb}^L = 11742.4$
fcc	[16]	$0_{Ti,Ta}^L = 8500.0$
	[21]	$0_{Ti,Zr}^L = 5133.0$
	[12]	$0_{Mo,Zr}^L = 26753.8 + 4.56 * T$
	[13]	$0_{Nb,Zr}^L = 24411.0$
Al3M_D022	[15]	$0_{Ta,Zr}^L = 30051.7$
	[16]	$0_{Ti,Mo}^L = 16500.0$
	[16]	$0_{Ti,Ta}^L = 8500.0$
	[16]	$0_{Ti:Ti}^L = 4 * GFCCTI$
AlM_D019	[16]	$0_{Mo:Mo}^L = 4 * GFCCMO$
	[16]	$0_{Ti:Mo}^L = GFCCMO + 3.0 * GFCCTI$
	[16]	$0_{Mo:Ti}^L = 3.0 * GFCCMO + GFCCTI$
	[16]	$0_{Ti:Ta}^L = GFCCTA + 3.0 * GFCCTI$
	[16]	$0_{Ti:Ti}^L = 4.0 + 4.0 * GHserti$
	[16]	$0_{Mo:Mo}^L = 4.0 * GHCPMO$
	[16]	$0_{Ta:Ta}^L = 4.0 * GHCPТА$
	[16]	$0_{Ti:Mo}^L = 17072.0 - 4.5 * T + GHCPMO + 3.0 * GHserti$
	[16]	$0_{Mo:Ti}^L = 17072.0 - 4.5 * T + 3.0 * GHCPMO + GHserti$

Table 3.4: Modelled binary and ternary thermodynamic parameters for the Ti-Mo-Nb-Ta-Zr system. The thermodynamic description of pure elements is not included. The pure element functions, such as GFCCTI, describe the Gibbs energy (G) of the phase (FCC) for the element (Ti) were adopted from the SGTE database [32] are listed in the Supplementary TDB (thermodynamic database) file.

Phase	Reference	Interaction Parameter
[16]	[16]	$0_{Ti:Ta}^L = 6376.0 + GHCPA + 3.0 * GHSERTI$
	[16]	$0_{Ta:Ti}^L = 6376.0 + 3.0 * GHCPA + GHSERTI$
	[16]	$0_{Ti:Mo}^L = 51212.0 - 13.5 * T$
	[16]	$0_{Mo,Ti:Ti}^L = 51212.0 - 13.5 * T$
	[16]	$0_{Mo:Mo,Ti}^L = 5692.0 - 1.5 * T$
	[16]	$0_{Ti:Ti,Mo}^L = 5692.0 - 1.5 * T$
	[16]	$0_{Ta,Ti:Ta}^L = 19128.0$
	[16]	$0_{Ta,Ti:Ti}^L = 19128.0$
	[16]	$0_{Ta:Ta,Ti}^L = 2128.0$
	[16]	$0_{Ti:Ta,Ti}^L = 2128.0$
AlTi	[16]	$0_{Ti:Ti}^L = 2.0 * GFCCCTI$
	[16]	$0_{Mo:Mo}^L = 2.0 * GFCCMO$
	[16]	$0_{Ta:Ta}^L = 2.0 * GFCCTA$
	[16]	$0_{Ti:Mo}^L = 8250.0 + GFCCMO + GFCCCTI$
	[16]	$0_{Mo:Ti}^L = 8250.0 + GFCCMO + GFCCCTI$
	[16]	$0_{Ti:Ta}^L = 4250.0 + GFCCTA + GFCCCTI$
	[16]	$0_{Ta:Ti}^L = 4250.0 + GFCCTA + GFCCCTI$
	[16]	$0_{Mo,Ti:Mo}^L = 8250.0$
	[16]	$0_{Mo,Ti:Ti}^L = 8250.0$
	[16]	$0_{Mo:Mo,Ti}^L = 8250.0$
bcc#2	[16]	$0_{Ti:Mo}^L = 10000.0$
	[16]	$0_{Mo:Ti}^L = 10000.0$

Table 3.4: Modelled binary and ternary thermodynamic parameters for the Ti-Mo-Nb-Ta-Zr system. The thermodynamic description of pure elements is not included. The pure element functions, such as GFCCTI, describe the Gibbs energy (G) of the phase (FCC) for the element (Ti) were adopted from the SGTE database [32] are listed in the Supplementary TDB (thermodynamic database) file.

Phase	Reference	Interaction Parameter
Laves_C15	[16]	$0_{Ti:Ta}^L = 5000.0$
	[16]	$0_{Ta:Ti}^L = 5000.0$
	[24]	$0_{Ti:Ti}^L = 15000.0 + 3.0 * GHSERTI$
	[12]	$0_{Mo:Mo}^L = 15000.0 + 3.0 * GHSERMO$
	[12]	$0_{Zr:Zr}^L = 15000.0 + 3.0 * GHSERZR$
	[24]	$0_{Ti:Mo}^L = 15000.0 + GHSERMO$ + $2.0 * GHSERTI$
	[24]	$0_{Mo:Ti}^L = 15000.0$ + $2.0 * GHSERMO + GHSERTI$
	[24]	$0_{Ti:Zr}^L = 9000.0$ + $GHSERZR + 2.0 * GHSERTI$
	[24]	$0_{Zr:Ti}^L = 15000.0 + 2.0 * GHSERZR + GHSERTI$
	[12]	$0_{Mo:Zr}^L = -21734.8 + 0.14 * T$ + $GHSERZR + 2.0 * GHSERMO$
omega	[12]	$0_{Zr:Mo}^L = 21734.8 - 0.14 * T$ + $2.0 * GHSERZR + GHSERMO$
	[12]	$0_{Mo:Mo,Zr}^L = 60000.0$
	[12]	$0_{Zr:Mo,Zr}^L = 60000.0$
	[12]	$0_{Mo,Zr:Mo}^L = 100000.0$
	[12]	$0_{Mo,Zr:Zr}^L = 100000.0$
	[24]	$0_{Ti:Mo,Zr}^L = 60000.0$
	[24]	$0_{Mo,Zr:Ti}^L = 100000.0$
	[19]	$0_{Ti}^L = 1886.7 - 0.15 * T + GHSERTI$
	[19]	$0_{Nb}^L = 15000.0 + 2.4 * T + GHSERNB$
	[32]	$0_{Zr}^L = -8878.082 + 144.432234 * T$ - $26.8556 * T * LN(T) - .002799446 * T2 + 38376 * T - 1$
		$298.15 < T < 2128$

Table 3.4: Modelled binary and ternary thermodynamic parameters for the Ti-Mo-Nb-Ta-Zr system. The thermodynamic description of pure elements is not included. The pure element functions, such as GFCCTI, describe the Gibbs energy (G) of the phase (FCC) for the element (Ti) were adopted from the SGTE database [32] are listed in the Supplementary TDB (thermodynamic database) file.

Phase	Reference	Interaction Parameter
	[19]	$-29500.524 + 265.290858 * T - 42.144 * T * LN(T)$ $+ 7.17445E + 31 * T - 9$ $2128 < T < 6000$ $0LTi, Nb = -3775.9$

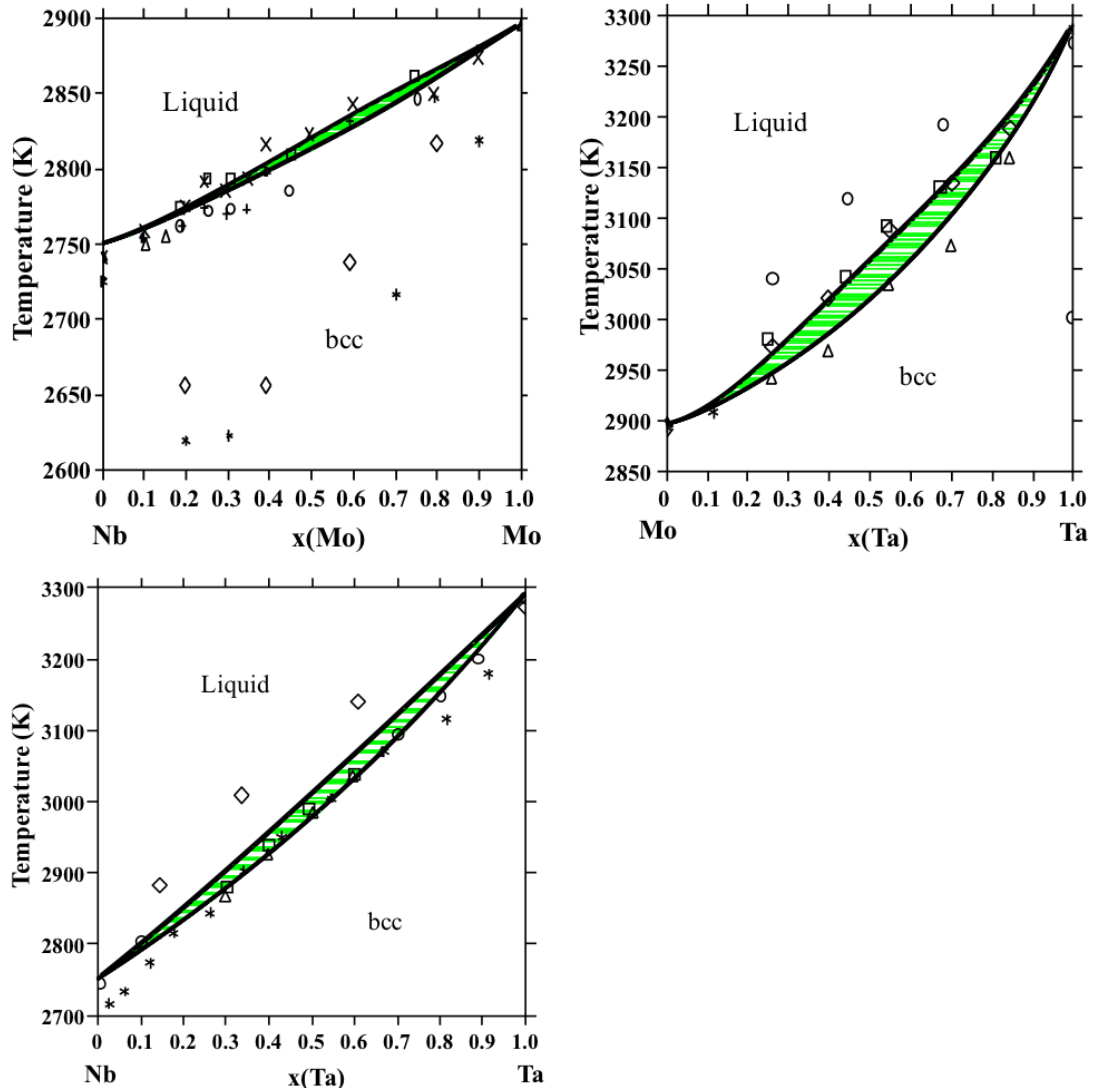


Figure 3.1. Previously modeled thermodynamic descriptions of the Mo-Nb (a) [11], Mo-Ta (b) [11] and Nb-Ta (c) [11] binary systems in comparison with available liquidus and solidus phase boundary experimental data to ensure accuracy as detailed in [11].

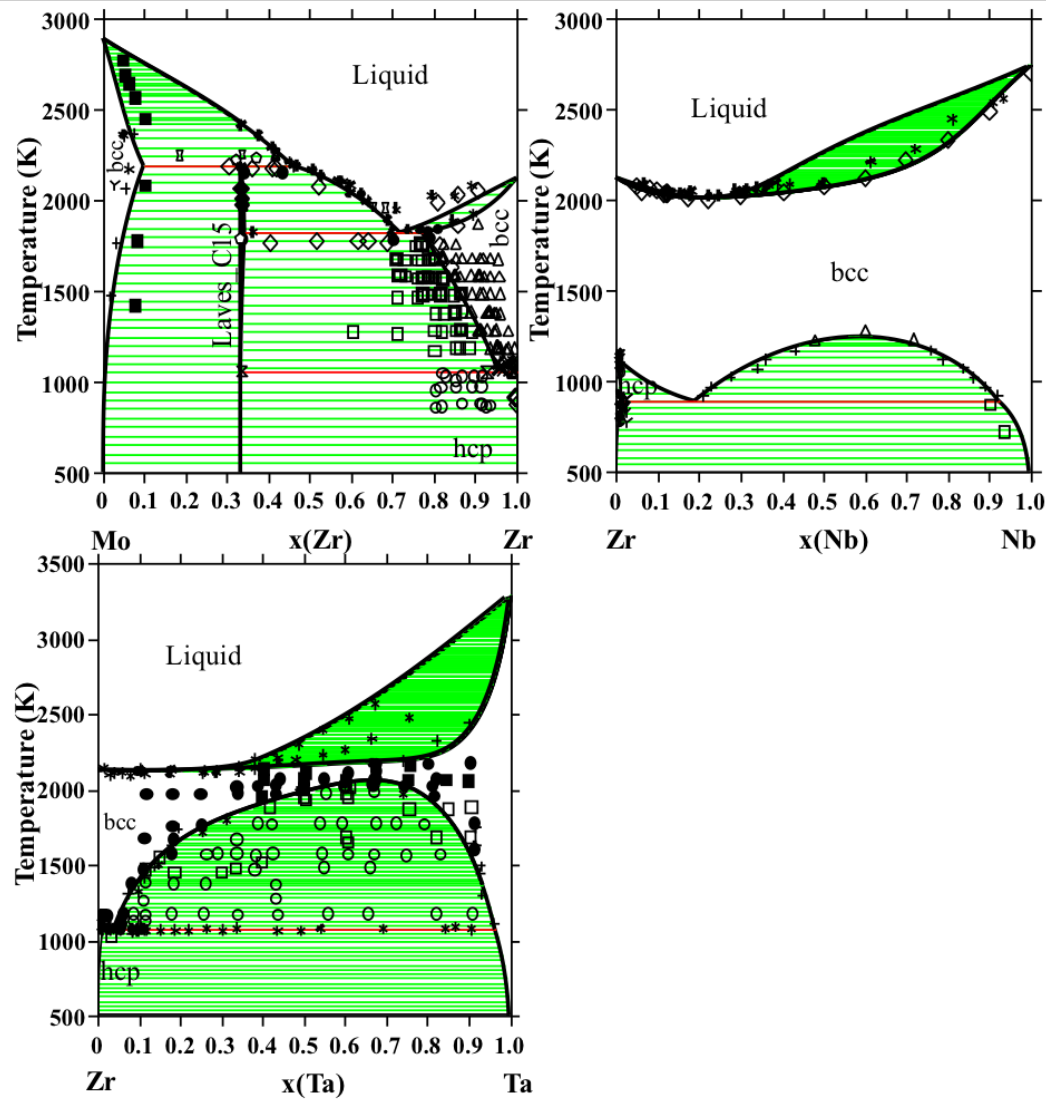


Figure 3.2. Previously modeled thermodynamic descriptions of the Mo-Zr [12] system is plotted with phase boundary, reaction, single phase and two phase experimental data. The previously modeled Nb-Zr [13, 14] system is plotted with solidus, hcp solvus and bcc solvus experimental data. The previously modeled Ta-Zr [15] system is plotted with single-phase, two-phase, phase boundary and solidus experimental data (detailed in the mentioned references).

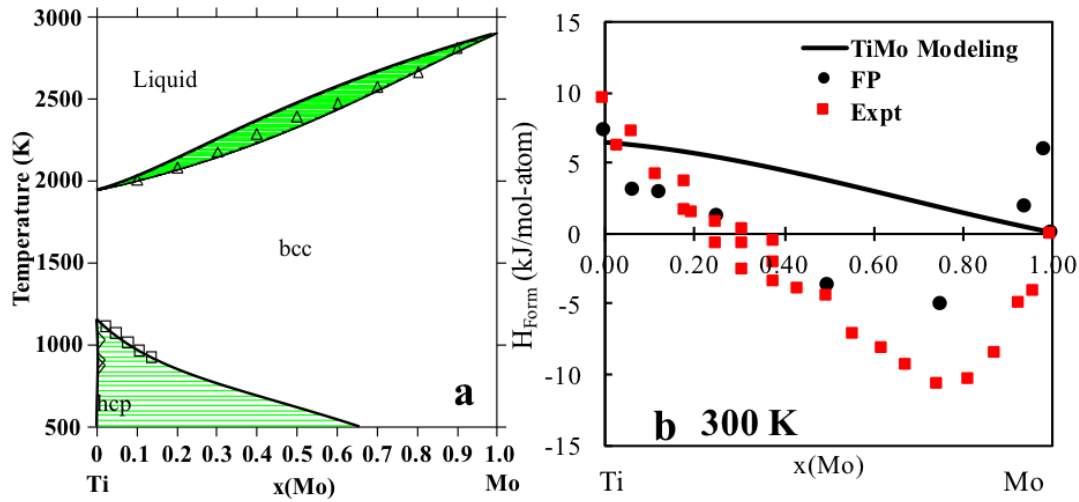


Figure 3.3. Previously modeled thermodynamic description of the Ti-Mo system versus available phase boundary and solidus experimental data to ensure accuracy [16, 17] (a), and enthalpy of formation of the bcc phase predicted by the previous thermodynamic modeling (solid line) at 300 °K versus the present first-principles calculations (circles) at 0 °K and compared with the enthalpy of formation of the bcc phase obtained from experiments [18] (b).

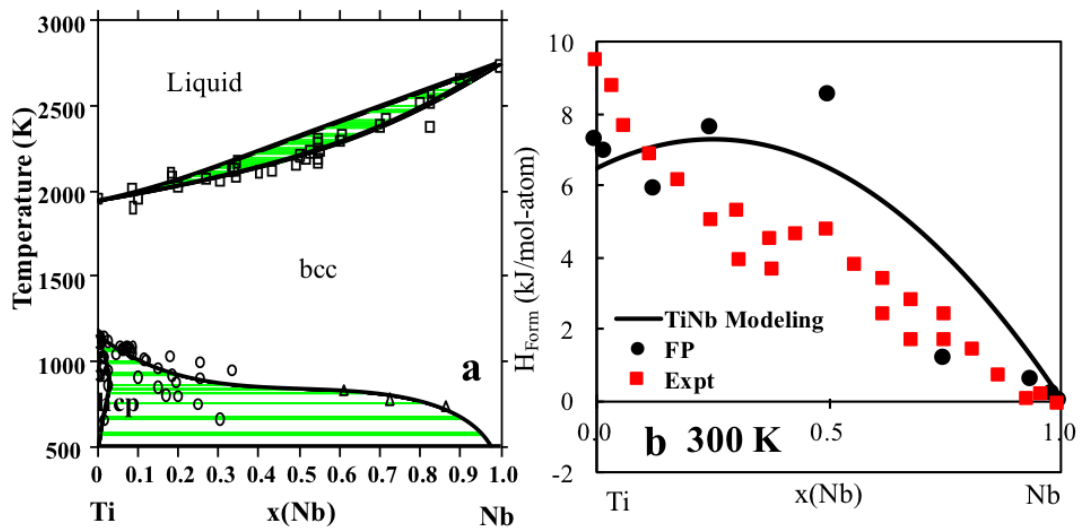


Figure 3.4. Previously modeled thermodynamic description of the Ti-Nb system versus available phase boundary and solidus experimental data to ensure accuracy [19–21][20,48] (a), and enthalpy of formation of the bcc phase predicted by the previous thermodynamic modeling (solid line) at 300 °K versus the present first-principles calculations (circles) at 0 °K compared with the enthalpy of formation of the bcc phase obtained from experiments [18] (b).

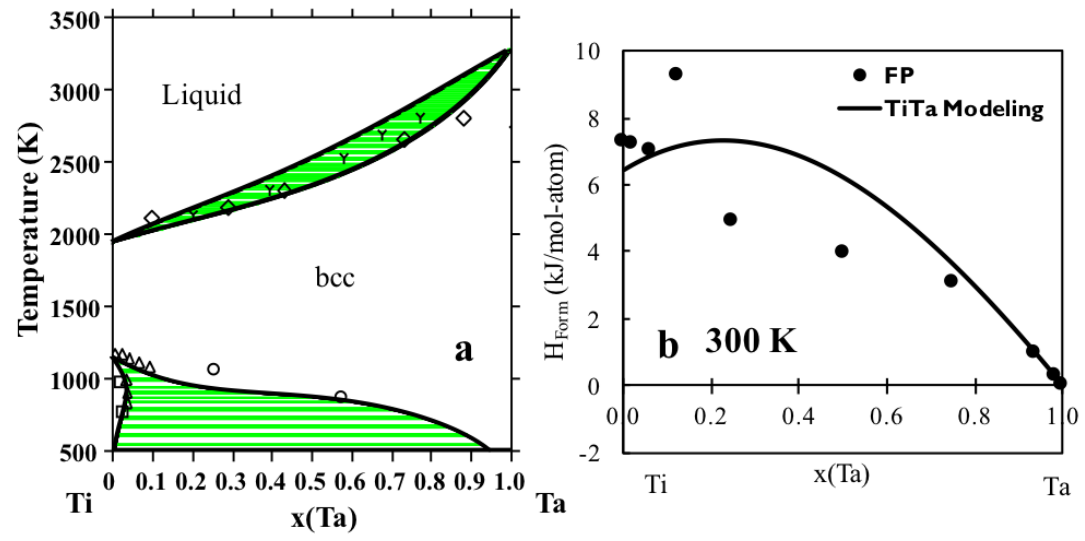


Figure 3.5. Previously modeled thermodynamic description of the Ti-Ta system versus available phase boundary and solidus experimental data to ensure accuracy [16, 22] (a), and enthalpy of formation of the bcc phase predicted by the previous thermodynamic modeling (solid line) at 300 °K versus the present first-principles calculations (circles) at 0 °K (b).

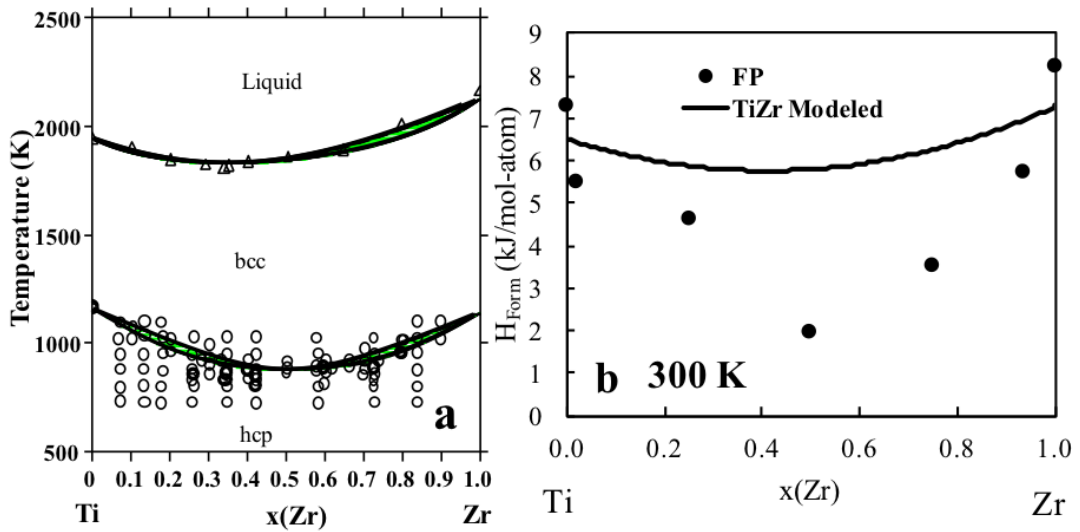


Figure 3.6. Previously modeled thermodynamic description of the Ti-Zr system versus available phase boundary and solidus experimental data to ensure accuracy [21] (a), and enthalpy of formation of the bcc phase predicted by the previous thermodynamic modeling (solid line) at 300 °K versus the present first-principles calculations (circles) at 0 °K (b).

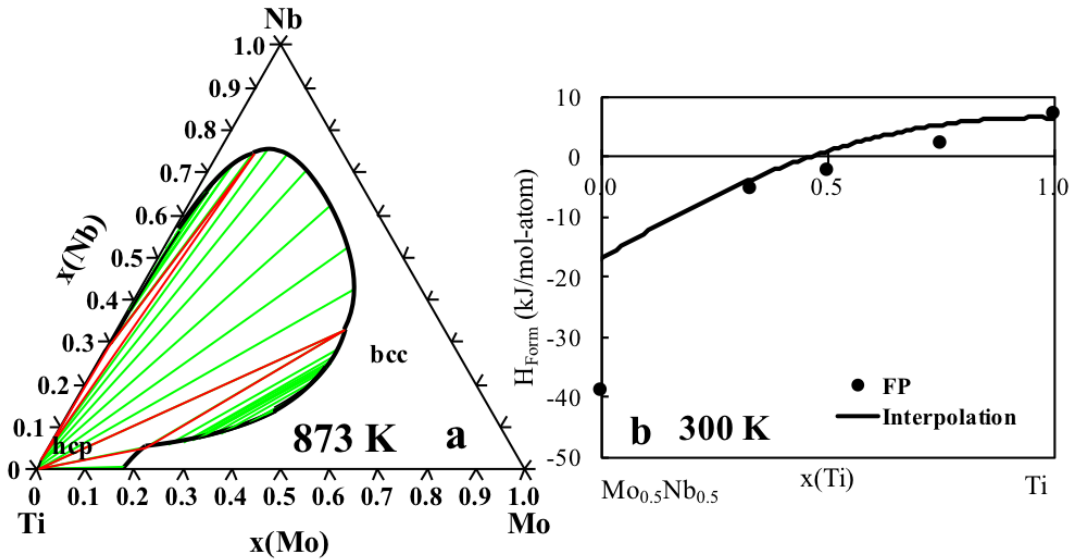


Figure 3.7. Binary interpolation of the isothermal section of the Ti-Mo-Nb system plotted at 873 °K (a), and enthalpy of formation of the bcc phase predicted by the binary interpolation of the thermodynamic modeling (solid line) at 300 °K versus the present first-principles calculations (circles) at 0 °K (b).

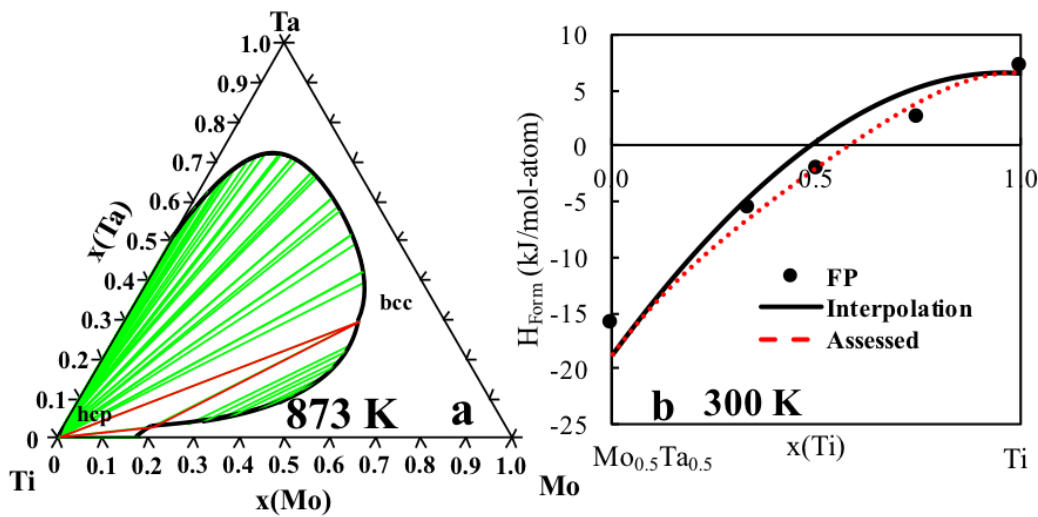


Figure 3.8. Binary interpolation of the isothermal section of the Ti-Mo-Ta system plotted at 873 °K (a), and enthalpy of formation of the bcc phase predicted by the previous thermodynamic modeling (solid line) at 300 °K and the ternary assessed thermodynamic modeling (red dotted line) versus the present first-principles calculations (circles) at 0 °K (b).

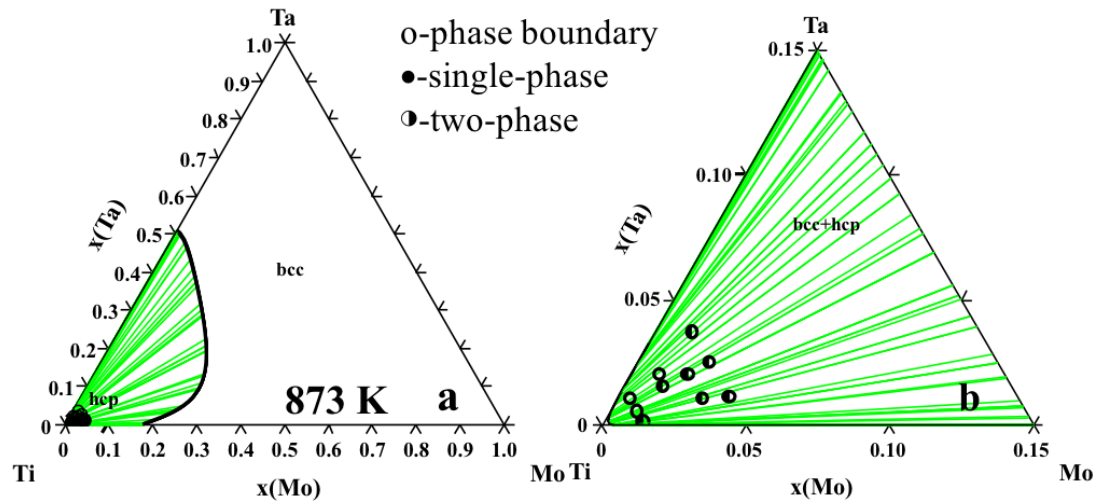


Figure 3.9. Ternary assessed isothermal section of the Ti-Mo-Ta system plotted at 873 °K (a), and zoomed in ternary assessed isothermal section at 873 °K with the phase boundary and two-phase region experimental data [23] (b) to ensure accuracy of the ternary assessment.

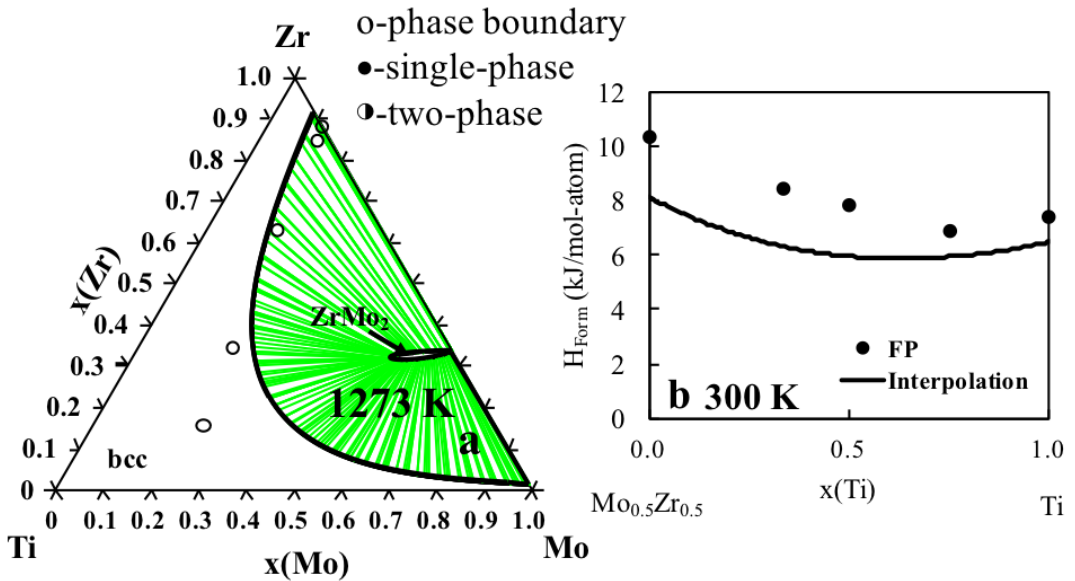


Figure 3.10. Binary interpolation of the isothermal section of the Ti-Mo-Zr system plotted at 1273 °K compared with experimental phase boundary data [24, 25] (a), and enthalpy of formation of the bcc phase predicted by the previous thermodynamic modeling (solid line) at 300 °K versus the present first-principles calculations (circles) at 0 °K (b).

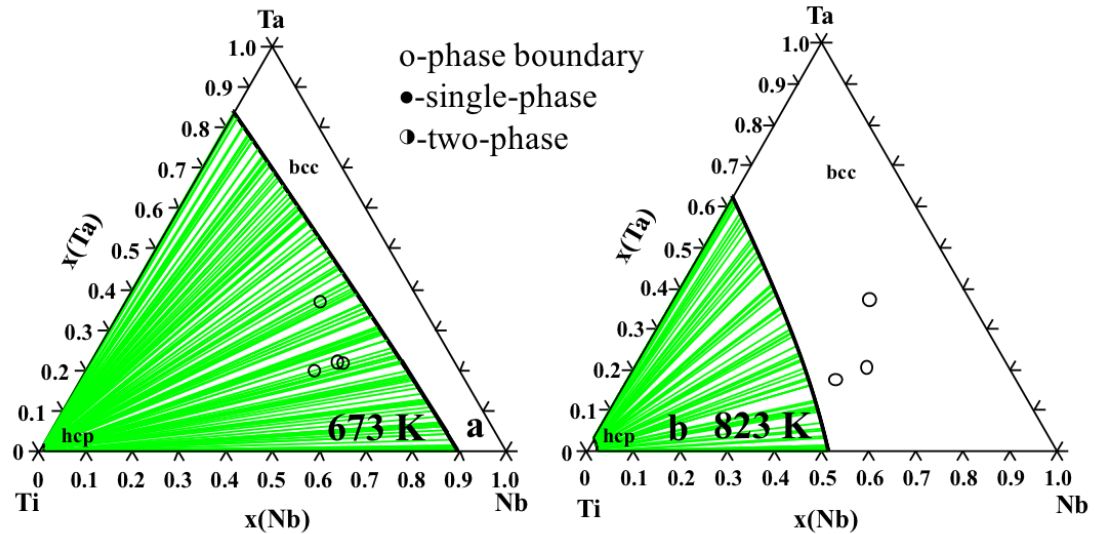


Figure 3.11. Binary interpolation of the isothermal section of the Ti-Nb-Ta system plotted at 673 °K compared with experimental phase boundary data [26] (a), and binary interpolation of the isothermal section of the Ti-Nb-Ta system plotted at 823 °K compared with experimental phase boundary data [26] (b).

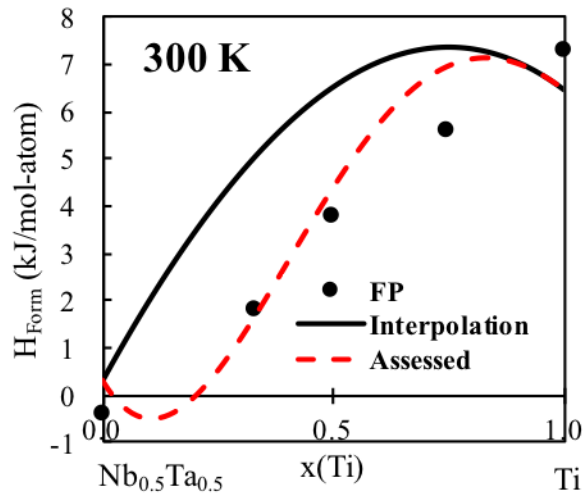


Figure 3.12. Enthalpy of formation of the bcc phase predicted by the previous thermodynamic modeling (solid line) at 300 °K and the ternary assessed thermodynamic modeling (red dotted line) versus the present first-principles calculations (circles) at 0 °K.

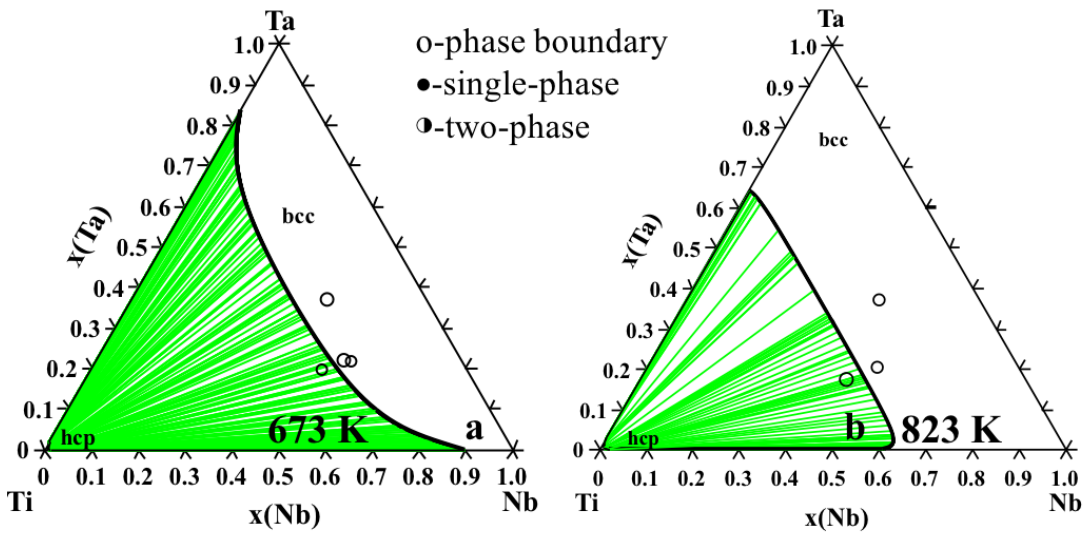


Figure 3.13. Ternary assessed isothermal section of the Ti-Nb-Ta system plotted at 673 °K compared with experimental phase boundary data [26] to ensure accuracy of the ternary assessment (a), and ternary assessed isothermal section at 823 °K compared with experimental phase boundary data [26] to ensure accuracy of the ternary assessment (b).

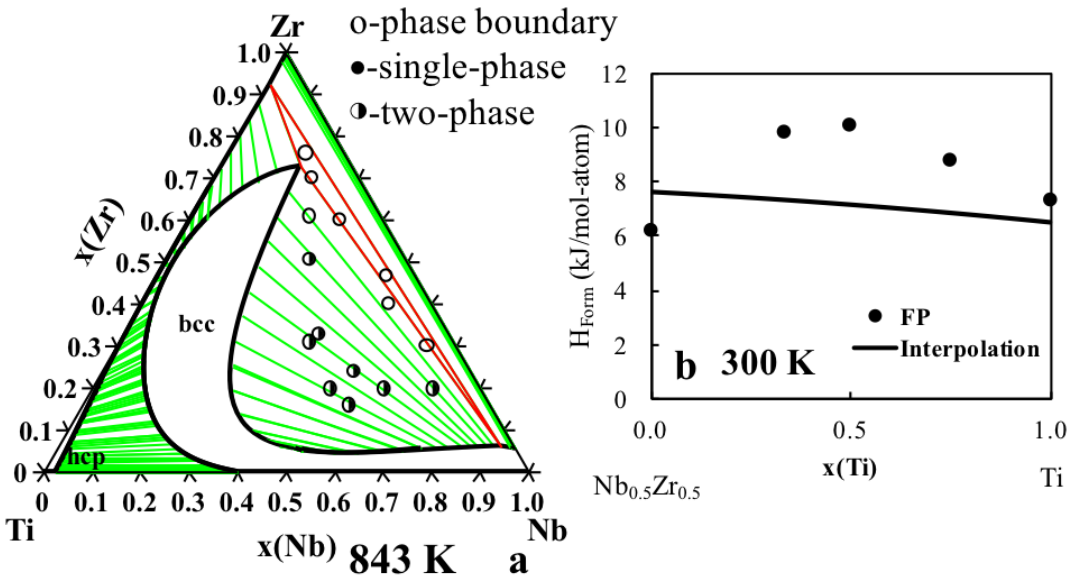


Figure 3.14. Binary interpolation of the isothermal section of the Ti-Nb-Zr system plotted at 843 °K compared with experimental phase boundary and two-phase region data [27] (a), and enthalpy of formation of the bcc phase predicted by the previous thermodynamic modeling (solid line) at 300 °K versus the present first-principles calculations (circles) at 0 °K (b).

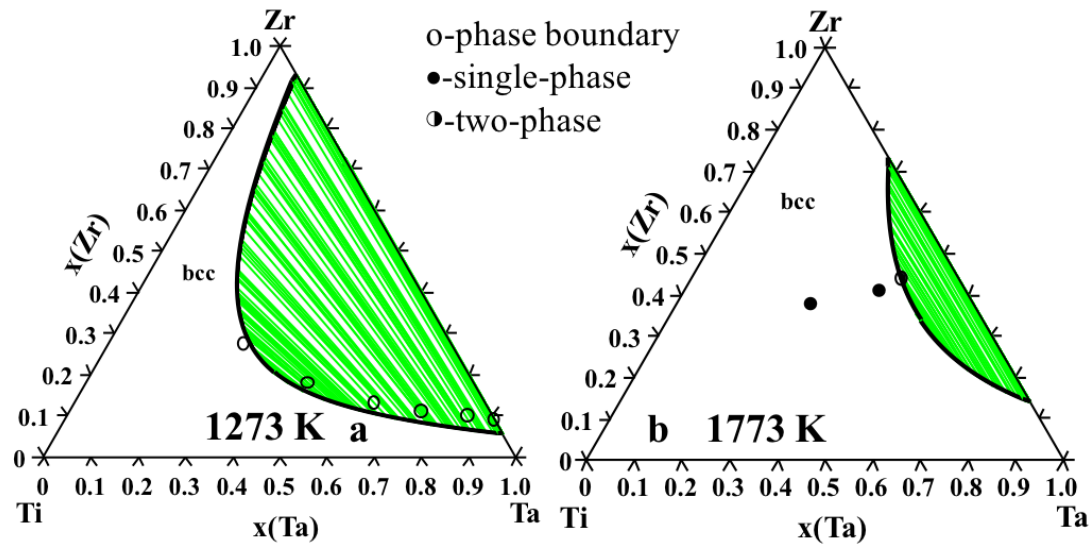


Figure 3.15. Binary interpolation of the isothermal section of the Ti-Ta-Zr system plotted at 1273 °K compared with experimental phase boundary data [28,29] (a), and binary interpolation of the isothermal section of the Ti-Ta-Zr system plotted at 1773 °K compared with compared with experimental single phase and two-phase region data [28,29] (b).

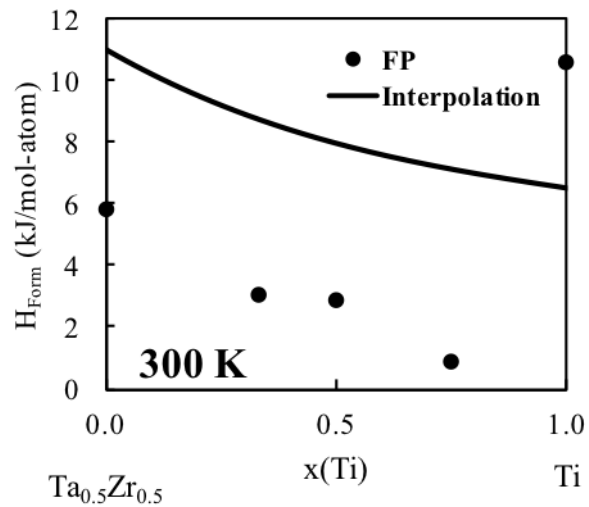


Figure 3.16. Enthalpy of formation of the bcc phase predicted by the previous thermodynamic modeling (solid line) at 300 °K versus the present first-principles calculations (circles) at 0 °K.

Chapter 4

First-principles aided thermodynamic modeling of the Sn-Ta system

4.1 Introduction

Currently, the biomaterial implant research of Ti alloys is focused on biocompatible elements that stabilize the body centered cubic (bcc, β) phase of Ti and help to lower its elastic modulus. Tantalum (Ta) is a biocompatible element and is considered to be a strong -stabilizers [51]. Recently, tin (Sn) has also been researched for use in Ti-alloys due to its biocompatibility and low cost [40]. Kuroba et al. [105] studied various Ti-alloys such as Ti-29-Nb-13Ta-2Sn (weight percentage, and similarly hereinafter unless specified otherwise), Ti-29Nb-13Ta-4Mo, and Ti-29Nb-13Ta-6Sn for use as biocompatible implant materials. Kuroba and Hagiwara [106] also studied new Ti-Cu-Ni-Sn-Ta alloys for the artificial materials used in orthopedic surgeries. The Sn-Ta system is thus an important sub-system for this purpose [107]. A complete knowledge base of the thermodynamic description of Sn-Ta can be used to examine the effects of temperature and composition on phase stability for higher order systems and help to tailor experimental alloy selections to viable options. The CALPHAD technique, in combination with first-principles and phonon calculations based on the DFT, has been proven to provide valuable data to model the thermodynamic properties of binary such as Ta-Sn that lack sufficient experimental data [81]. The Sn-Ta system has three solid solution phases and two

intermetallic compounds, i.e. the bcc, body centered tetragonal (bct), and diamond solution phases, and the intermetallic compounds Ta_3Sn with space group $Pm\bar{3}n$ and $TaSn_2$ ($Ta_{1.2}Sn_{1.8}$) with space group $Fddd$ [108].

In the present work, thermodynamic data was predicted using first-principles calculations for the two intermetallics and for the bcc, bct and diamond solution phases. The finite temperature properties of the phases were obtained using the Debye-Grüneisen model [60] and phonon calculations based on the supercell approach [63]. The DFT data was used to model the parameters of the Gibbs energy of each phase using the CALPHAD technique.

4.2 Literature Review

The Sn-Ta binary system was studied by Okamoto [108], Studnitzky and Schmid-Fetzer [109], and Basile [110]. Both of the intermetallic phases, Ta_3Sn and $TaSn_2$, were shown to have a very narrow homogeneity range. Basile [110] observed that $TaSn_2$ is located around $Ta_{1.2}Sn_{1.8}$ which was then designated as Ta_2Sn_3 by Okamoto [108]. It seems that $TaSn_2$ is a more compatible description of the stoichiometric compound based on the descriptions of similar systems (V-Sn, and Nb-Sn) [33, 111, 112], and thus will be used in the present work. Basile [110] determined $TaSn_2$ has a peritectic reaction at 595 °C and used X-ray diffraction (XRD) to elucidate the lattice parameters of $TaSn_2$.

Studnitzky and Schmid-Fetzer [109] used powder samples to study the Ta_3Sn and $TaSn_2$ intermetallic phases and verified the results previously reported by Basile [110]. They cold pressed the pure element powders at 600 MPa and then heated the pellets at 1000 °C for up to 48 hours. The resulting pellet was then cold pressed at 600 MPa again. Under these conditions $TaSn_2$ was observed at 400 °C, but was not present as the temperature increased to 600 °C. In the work by Courtney et al. [113], Ta_3Sn was studied to see how the temperature affects the long-range ordering parameter. In Courtney et al.'s work, Ta_3Sn powder samples were sintered at 600, 700, 950, 1200, and 1450 °C for 2, 4, 7, and 16 days, respectively. Each sample was then studied using x-ray diffraction at room temperature to examine the phases present and the long-range ordering. They concluded that the transition temperature of superconductivity for Ta_3Sn varied by a maximum of 4 °K based on heat treatment and sintering times due to long-range ordering that occurred.

Courtney et al. also measured the lattice parameter of each sample and reported the average value of this cubic phase being 5.285 Å.

4.3 Modeling and Calculations

4.3.1 First-principles details

In the present work, the Vienna ab-initio Simulation Package (VASP) was used to perform the first-principles calculations [61]. The projector augmented-wave (PAW) [62, 90] method was used to describe the electron-ion interactions. Based on the work of comparing X-C functionals (Figure 5.1) the exchange-correlation functional of the generalized gradient approach depicted by Perdew, Burke, and Ernzerhof (PBE) was employed [58]. A sigma value of 0.2 eV and a plane wave energy cutoff of 1.3 times higher than the highest default cutoff was adopted. The Brillouin zone sampling was done with Blöchl corrections [90] using a gamma centered Monkhorst-Pack (MP) scheme [91]. The k-points grid for diamond-Sn, bcc-Ta, TaSn₂, and bcc-Sn were 4x4x4, 6x6x6, 10x10x5, and 6x6x6 respectively. The k-point grids for the bct-Sn, Ta₃Sn and bcc SQS calculations used an automated k-point mesh generator in VASP with the length of the subdivisions specified as 80. The energy convergence criterion of the electronic self-consistency is set as 10⁻⁴ eV/atom and 10⁻⁴ eV/A was set as the stopping criteria for the ionic relaxation loop for all of the calculations.

To calculate the enthalpy of formation of the bcc phase across the entire composition range, the enthalpy of formation of Ta and Sn in the bcc phase were calculated with five different compositions of Ta_{1-x}Sn_x, where x=0.0185 (Ta₅₃Sn, 54 atoms), 0.25, 0.5, 0.75, and 0.9815 (TaSn₅₃, 54 atoms). For x=0.0185 and 0.9815, calculations were performed on a diluted 54 atom cell where all atoms but one was Sn or Ta (Ta₅₃Sn and TaSn₅₃). For x=0.25, 0.5, and 0.75, 16-atom special quasirandom structures (SQS) in the bcc phase developed by Jiang et al. [73] were used to mimic the behavior of random structures. The relaxation of these structures is complicated and discussed in the methodology section. The enthalpy of formation was plotted as a function of composition and then used for the modeling.

4.3.2 CALPHAD

The Gibbs energy functions of the pure elements were adopted from the SGTE (SSUB) database [32]. In the present work, the bcc and liquid phases were modeled in conjunction with the two intermetallics Ta_3Sn and $TaSn_2$. Dilute first-principles calculations of Ta in Sn were done for the diamond and bct phases. However, there is little solubility of Ta in these phases and there is no description of pure Ta in these phases available in SGTE. So, no binary interaction parameters were introduced in the modeling similar to other Sn systems such as Nb-Sn and V-Sn [111, 112]. The interaction parameters of the liquid and bcc solution phases were modeled using Eq. 2.33 and 2.34, while Ta_3Sn and $TaSn_2$ were modeled according to Eq. 2.37.

4.4 Results and discussion

4.4.1 First-principles

To evaluate the accuracy of phonon calculations for the present system, both the dispersion curves and the phonon DOS are plotted for bcc-Ta, bct-Sn, $TaSn_2$, and Ta_3Sn in Figure 4.1, 4.2, 4.3, and 4.4, respectively. The bcc-Ta phonon dispersion curve in Figure 4.1 is compared with values obtained by Taioli et al. [30] using neutron scattering, showing good agreement. The longitudinal modes (LO) and the transverse modes (TO) measured by Raman spectroscopy [31] (open square) along with the previous theoretical predictions at the M point (filled square) for bct-Sn are compared with the calculated phonon dispersion curve in Figure 4.2. The substantial difference for the LO mode may be due to the temperature and pressure differences as pointed out by Olijnyk [31]. No imaginary phonon frequencies are obtained in the phonon DOS plots for bcc-Ta, bct-Sn, $TaSn_2$, Ta_3Sn , indicating that they are all mechanically and dynamically stable at 0 °K.

The calculated lattice parameters at 0 °K from the EOS fitting and with the Debye and phonon models at 298 °K are compared to available experimental and previous DFT results in Table 4.1. The lattice parameters of Ta are compared with the experimental lattice parameters by Predmore and Arsenault [114] at room temperature and the previous 0 °K DFT results by Shang et al. [115] who used the GGA-PW91 exchange correlation functional. The Sn lattice parameters are

compared to experimental work by Allen et al. [116] at 298 °K and calculations by Arróyave et al. [117]. The properties of the TaSn₂ and Ta₃Sn intermetallics are compared to experimental values by Calvert et al. [118] and Courtney et al. [113], respectively. The results show a less than 0.5% difference when compared with other DFT results at 0 °K. There is a less than 2% difference between the DFT 0 °K results and the experiments, which are listed in Table 4.1. The variance is due to the fact that the calculations are at 0 °K and the experiments are at a higher temperature. When comparing the calculated lattice parameters at 298 °K to the experiments, all of the predictions improve to show a less than 1% difference with the exception of Sn, which shows a less than 2% difference.

Table 4.2 shows the equilibrium volume, V_0 , bulk modulus, B , and the derivative of bulk modulus B' obtained by the EOS E-V fitting of the first-principles data at 0 °K. The Sn and Ta calculations are compared with previous first-principles calculations and available experiments. The volume shows a less than 0.5% difference between the previous DFT results and current DFT results for both Sn and Ta [114, 119]. The comparison of the DFT results at 0 °K and the experimental results at 298 °K for volume show a slightly higher variance of less than 5 % due to the difference in temperature [115, 119]. The B comparison of previous 0 °K DFT results and the present 0 °K DFT results show a less than 7 GPa difference and the DFT results at 0 °K vary by less than 11 GPa from the experimental results at 298 °K [114, 115, 119]. The difference between the current calculations and the previous values may be due to many reasons; e.g. the different choices in input parameters used by Peltzer et al. [119] and different exchange correlation functionals. Another reason is due to the temperature difference 0 °K (calculations) versus 298 °K (experiments). Figure 4.5 shows the enthalpy and entropy of Ta from the Debye and phonon approaches in comparison with the data from the SGTE pure element database [32]. Figure 4.6 shows the comparison of the enthalpy and entropy calculated for Sn from the phonon and Debye model to the SGTE pure element database [32]. Both show excellent agreement.

The elastic stiffness constants and polycrystalline elastic properties calculated by the Hill approach and the scaling factors for the Debye model are shown in Table 4.3. To ensure the accuracy of the scaling factor, the elastic stiffness constants and moduli are compared with previous first-principles results [96, 103, 104, 120, 121]. The previous calculation results and present calculation results only vary slightly

for the TaSn_2 structure. The present work calculated the elastic stiffness constants for the Ta_3Sn structure at 2 different atom sizes and compared the results with previous calculations by the Materials Project [96, 103, 104, 120, 121]. The present elastic stiffness results are quite similar. There is a larger variance between the present results and the Materials Project results. This can be attributed to the different input parameters and exchange correlation functional used (PBE in the present work and GGA-PW91 in Materials Project). B calculated from the c_{ij} methodology (designated as B_{cij}) is compared with the B obtained from the EOS fitting (designated as B_{EOS}), showing a difference of less than 3%. Since the B_{EOS} from the EOS fitting is already compared to experiments, the elastic calculations and the scaling factor for the Debye model are thus deemed accurate.

4.4.2 CALPHAD

The PARROT module in the Thermo-Calc software [77] is used to optimize the parameters of the Gibbs energy function of the TaSn_2 and Ta_3Sn intermetallics as well as the binary interaction parameters for the bcc and liquid phases. The Gibbs energy parameters of the intermetallics are first estimated from the thermodynamic properties obtained by the phonon supercell method because the phonon calculations are regarded as more accurate than the Debye model. While the decomposition temperature of the TaSn_2 intermetallic is known to be 868 °K from experiments, the decomposition of the Ta_3Sn intermetallic has not been reported in the literature. It is noted that both the Nb-Sn and V-Sn systems, which are quite similar to the Ta-Sn system, have the X_3Sn phase forming through a peritectic reaction of $\text{bcc} + \text{Liquid} \rightarrow \text{X}_3\text{Sn}$ [33, 111, 112]. Based on the assumption from similar works that Ta_3Sn is also formed through a peritectic reaction, the Ta_3Sn parameters are adjusted and the parameters for the liquid phase are evaluated. The evaluation of the Gibbs parameters along with the results from the Debye model and the phonon quasiharmonic approach for TaSn_2 and Ta_3Sn are plotted in Figure 4.7 and Figure 4.8, respectively. As seen in both figures, the data from the phonon method correlates well with the current CALPHAD modeling. This is to be expected since this data was used to evaluate the parameters. It is noted in Figure 4.7, that the heat capacity and entropy of TaSn_2 from the current CALPHAD modeling is higher than those from the first-principles calculations. This is due to the fact that the

enthalpy and entropy values from DFT were adjusted with the experimental data of the peritectic temperature.

The bct and diamond phases are treated as ideal due to the little solubility. As previously stated, the enthalpies of formation of the bcc phase for five different Sn-Ta compositions are calculated and plotted in Figure 4.9, showing asymmetrical behavior. There is a discrepancy between the first-principles value and the CALPHAD modeling for the lattice stability of bcc-Sn. The first-principles predicts a value of 15.48 kJ/mol-atom and the CALPHAD model gives 4.42 kJ/mol-atom. This difference is expected to be due to the instability of Sn in the bcc phase. Wang et al. [122] concluded and discussed the same discrepancy when comparing first-principles DFT results to SGTE data for Os and Ru. Wang et al. calculated the lattice stability of bcc and fcc (face centered cubic) structure for Os and Ru, both stable in the hexagonal close packed phase at standard temperature and pressure, and concluded a difference of approximately 40 and 60 kJ/mol for Ru and Os, respectively. Wang et al. attributed this difference to the fact that when using first-principles calculations of unstable structures, frequencies of some of the phonon modes would become imaginary and thus the results would be less accurate. On the other hand, the CALPHAD technique can extrapolate lattice stabilities from binary solutions for which an alloying element has stabilized the otherwise unstable structure. These enthalpies of formation calculated from the SQS first-principles calculations are used to evaluate the bcc binary interaction parameters in the present CALPHAD modeling. The enthalpy of formation of the bcc phase is negative at the Ta rich side and becomes positive at the Sn rich side. This is common for X-Sn systems [111, 112], such as the Nb-Sn system [112] shown in Figure 4.9. It should be noted that Toffolon et al. [33, 112] used experimental data on the Sn-rich bcc phase to evaluate the Nb-Sn system's bcc interaction parameters. Due to the asymmetry of enthalpy of formation for the bcc phase, a subregular 1L interaction parameters is introduced.

The interaction parameters obtained in the present work are listed in Table 4.4. Based on these model parameters, the phase diagram is calculated and shown in Figure 4.10. The melting temperature of Ta_3Sn is predicted to be 2884 °K. Both the intermetallics decompose incongruently similar to those in the Nb-Sn and V-Sn systems. As seen in Table 4.4, both intermetallic phases have a negative enthalpy of formation and a negative entropy of formation. This goes along with previous

predictions by Arroyave and Liu [123] where they showed that the enthalpy and entropy of formation have the same sign. The calculated enthalpy of mixing of the liquid phase is plotted in Figure 4.11. The interaction parameter for the liquid phase allows for an accurate representation of the phase stability in Figure 4.10 but may need to be slightly adjusted if experimental data would come available.

4.5 Conclusion

The present work incorporates the thermodynamic data from DFT-based first-principles calculations and the available experimental data in the literature to model the Gibbs energies for the bcc and liquid solution phases and the stoichiometric Ta_3Sn and TaSn_2 phases of the Sn-Ta system. First-principles calculations are used to predict the enthalpy of formation of the bcc phase for the evaluation of interaction parameters in the phase. The decomposition temperature of Ta_3Sn is predicted to be 2884 °K. The completed thermodynamic description is compiled into a tdb file. The tdb file and raw data from the first-principles calculations are in appendix b.

Table 4.1. Lattice parameters from first-principles calculations compared with experimental values.

Phase	Space Group	<i>a</i> (Å)	<i>b</i> (Å)	<i>c</i> (Å)	Reference
bcc-Ta	Im $\bar{3}$ m	3.316			This work (0 °K)
		3.328			This work phonon (298 °K)
		3.330			This work Debye (298 °K)
		3.30			Expt. [114]
		3.32			DFT (0 °K) [115]
bct-Sn	I4 ₁ /amd	5.939	3.214		This work (0 °K)
		5.959	3.236		This work phonon (298 °K)
		5.954	3.222		This work Debye (298 °K)
		5.83	3.18		Expt. [116]
		5.93	3.23		DFT (0 °K) [117]
TaSn ₂	Fd ³ d	5.641	9.766	19.200	This work (0 °K)
		5.652	9.786	19.238	This work phonon (298 °K)
		5.652	9.785	19.238	This work Debye (298 °K)
		5.63	9.80	19.18	Expt. [118]
Ta ₃ Sn	Pm $\bar{3}$ n	5.304			This work (0 °K)
		5.319			This work phonon (298 °K)
		5.319			This work Debye (298 °K)
		5.29			Expt. [113]

Table 4.2. Equilibrium volume V_0 , bulk modulus B , and the first derivative of bulk modulus with respect to pressure B' , from fitted equilibrium properties from the EOS at 0 °K compared to experimental work and previous DFT studies.

Phase	V_0 (Å ³ /atom)	B (GPa)	B'	Reference
bcc-Ta	18.241	193.7	3.84	This work
	17.9685	200		Expt. [114]
	18.313	195.3	3.82	DFT [115]
bct-Sn	28.431	47.7	4.61	This work
	27.055	58.0		Expt. [119]
	28.396	54.0		DFT [119]
TaSn ₂	22.631	104.3	4.80	This work
Ta ₃ Sn	18.668	182.4	4.27	This work

Table 4.3. Elastic stiffness constants and elastic properties predicted using the Hill approach and the scaling factors used in the Debye model, calculated from the Poisson ratio, see Eq. 2.12. To ensure the accuracy of the calculated scaling factor, the bulk modulus (B) calculated from the elastic constants was compared to the B_{EOS} calculated from the EOS fitting Eq. 2.6.

	TaSn ₂		Ta ₃ Sn		
	This Work	FP	This Work	This Work	FP
		[96, 103, 104, 120]	8 atoms	32 atoms	[96, 103, 104, 121]
C ₁₁ (GPa)	166	161	297	310	226
C ₁₂ (GPa)	79	78	127	131	155
C ₁₃ (GPa)	62	57			
C ₂₂ (GPa)	189	182			
C ₂₃ (GPa)	68	68			
C ₃₃ (GPa)	187	183			
C ₄₄ (GPa)	37	35	65	68	22
C ₅₅ (GPa)	59	55			
C ₆₆ (GPa)	61	60			
E (GPa)	135		210	202	
G (GPa)	53	51	80	76	27
Poisson Ratio	0.288	0.29	0.32	0.32	0.43
Scaling factor	0.789		0.71	0.71	
B _{cij} (GPa)	107	107	184	190	179
B _{EOS} (GPa)	104		182		

Table 4.4. Modeled parameters in SI units in the present work for the phases in the Sn-Ta binary system. These parameters were incorporated with the SGTE data for the pure elements [32].

Phase (model)	Modeled Paramters
bcc (Sn,Ta)	${}^0L_{Ta,Sn}^b cc = + 70451$
	${}^1L_{Ta,Sn}^b cc = + 112237$
Liquid (Sn,Ta)	${}^0L_{Ta,Sn}^L iq = 17118$
TaSn ₂	$G^{TaSn_2} = {}^0G_{Sn}^{bct} + {}^0G_{Ta}^{bcc} - 29678 - 4.202T$
Ta ₃ Sn	$G^{Ta_3Sn} = {}^0G_{Sn}^{bct} + 3{}^0G_{Ta}^{bcc} - 68844 - 6.000T$

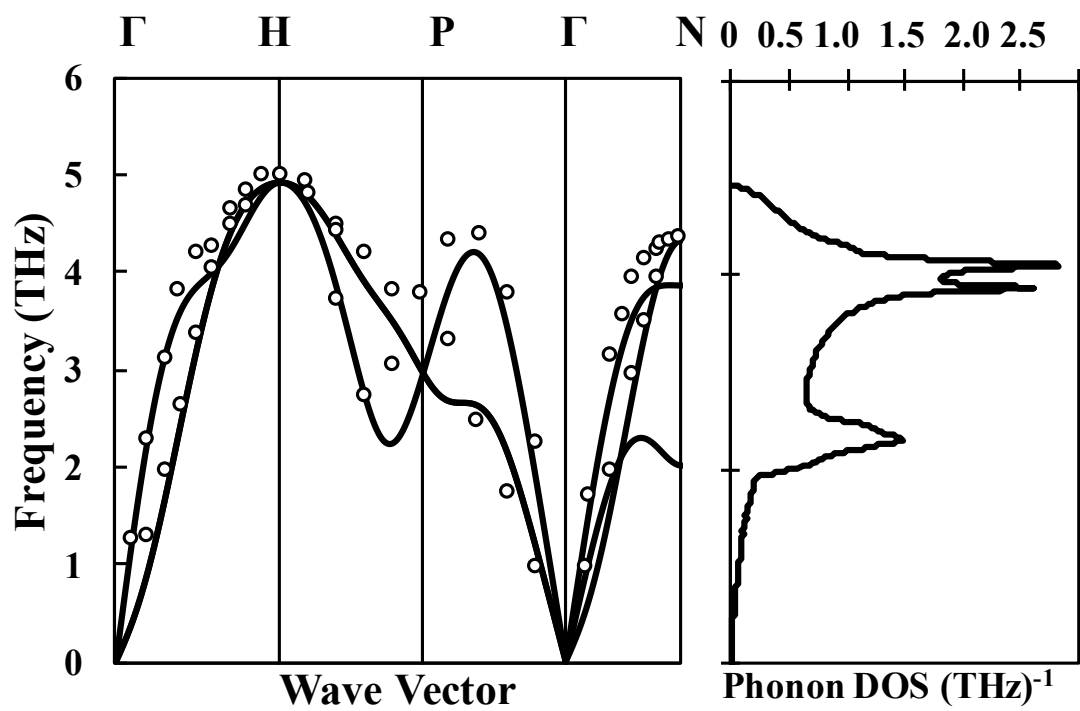


Figure 4.1. Calculated phonon dispersion curve of bcc-Ta, compared with neutron diffraction experiments (\circ) [30] along with the phonon DOS.

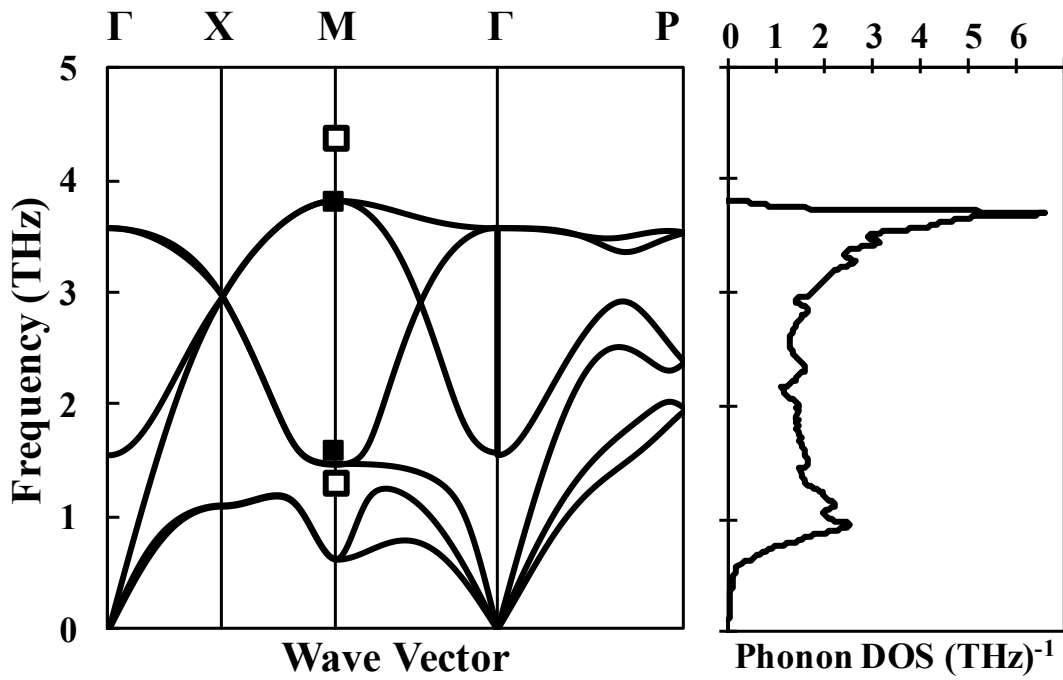


Figure 4.2. Calculated phonon dispersion curve of bct-Sn on the left and phonon DOS on the right. The open squares (\square) are the LO and TO modes from Raman [31] and the filled squares the theoretical prediction of the LO and TO modes at the M point [31].

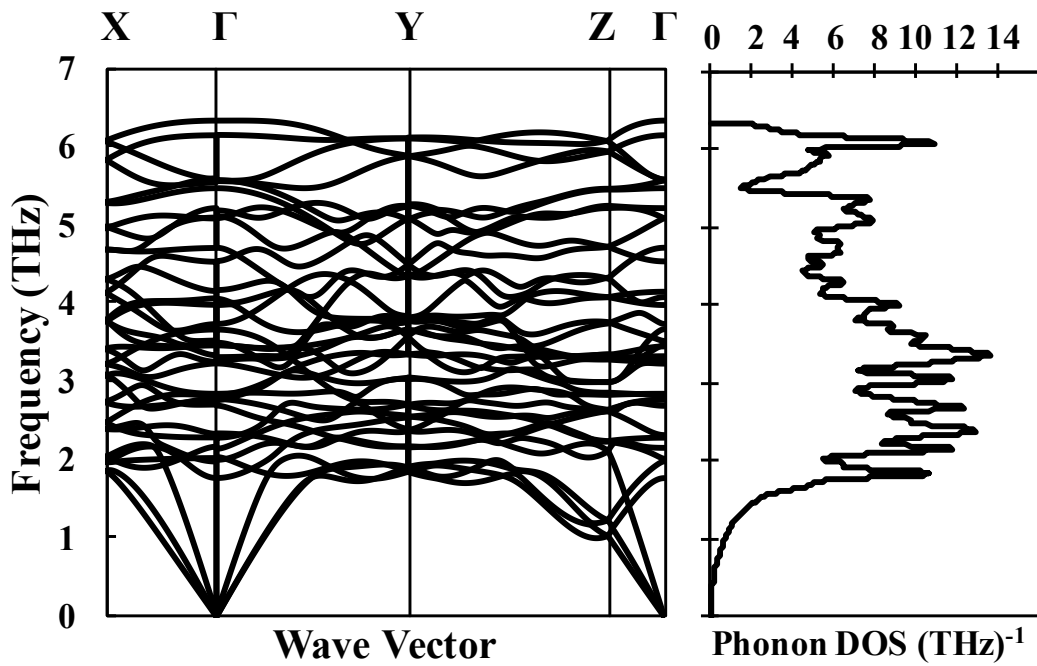


Figure 4.3. Calculated phonon dispersion curve for TaSn_2 at 0 °K and the phonon DOS.

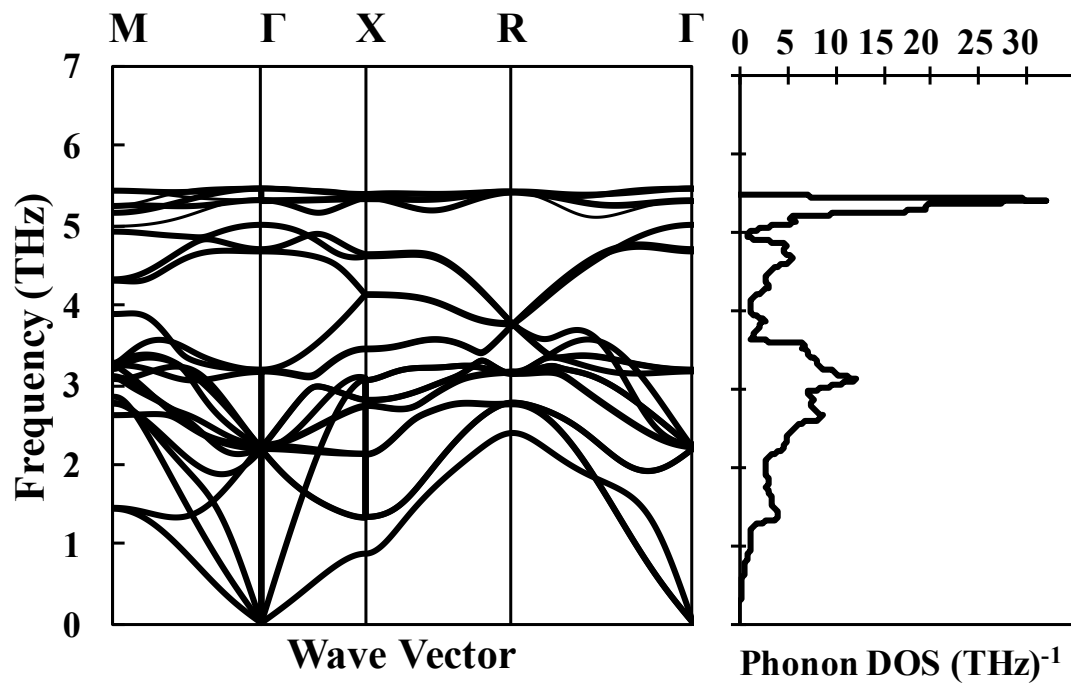


Figure 4.4. Calculated phonon dispersion curve of Ta_3Sn at $0\text{ }^{\circ}\text{K}$ on the left and the phonon DOS on the right.

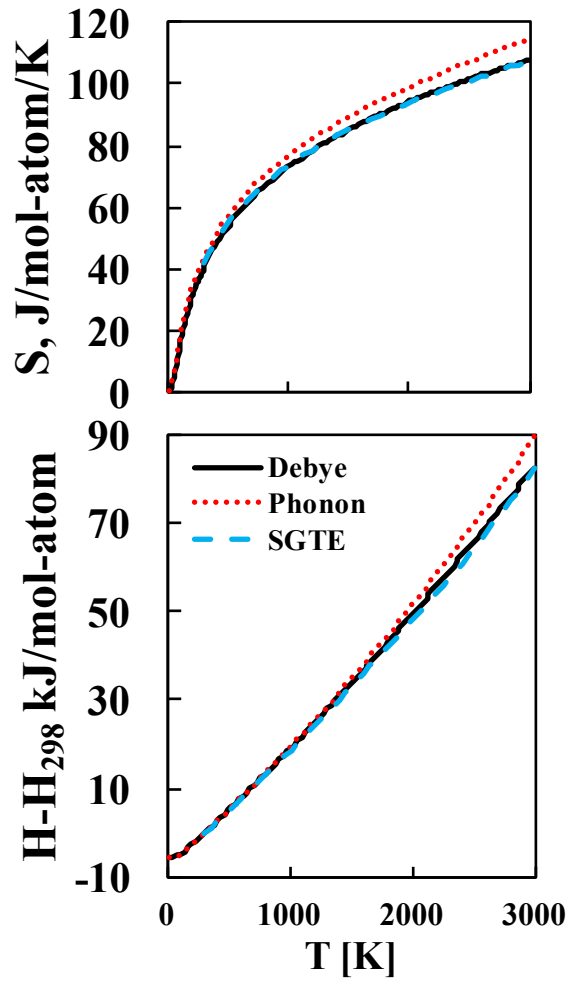


Figure 4.5. Comparison of the enthalpy and entropy of bcc-Ta from the Debye model (solid line) and the quasiharmonic phonon calculations (red dotted line) to the SGTE data (blue dashed line) [32].

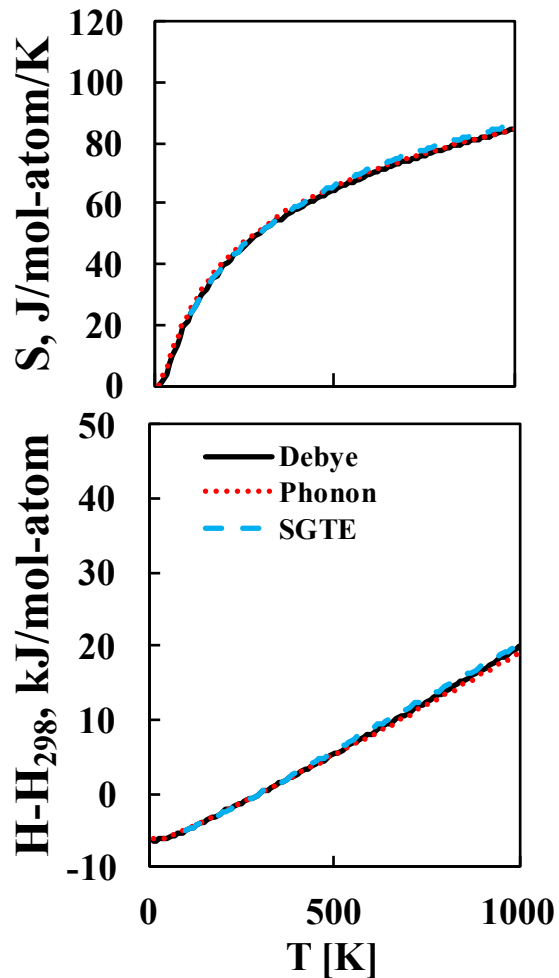


Figure 4.6. Comparison of the Gibbs energy of bct-Sn from the Debye model (solid line) and the quasiharmonic phonon calculations (red dotted line) to the SGTE data (blue dashed line) [32].

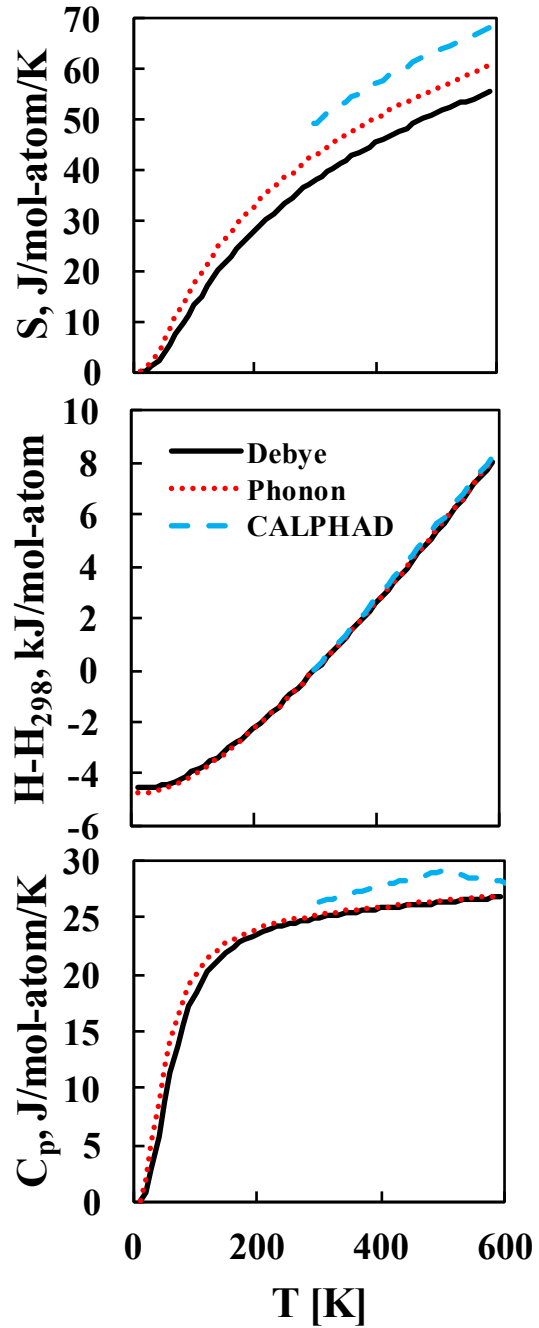


Figure 4.7. Heat capacity, enthalpy and entropy of TaSn_2 using the Debye model (solid line) and the quasiharmonic phonon calculation (red dotted line) from first-principles calculations, compared with those from the current CALPHAD modeling (blue dashed line).

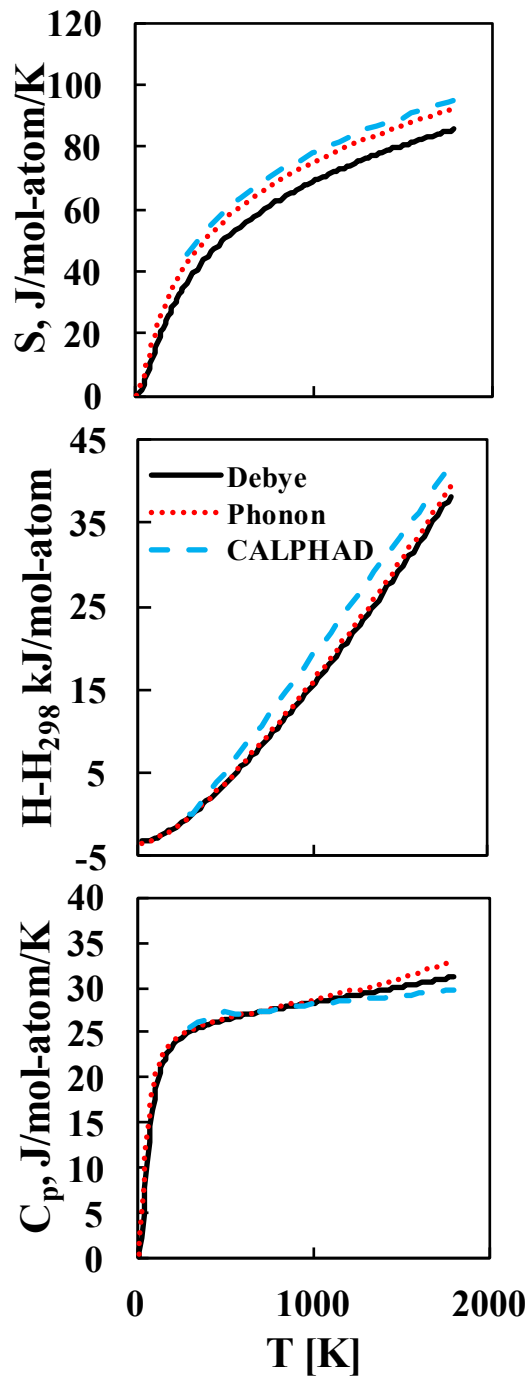


Figure 4.8. Heat capacity, enthalpy and entropy of Ta_3Sn using the Debye model (solid line) and the quasiharmonic phonon calculation (red dotted line) compared with those from the current CALPHAD modeling (blue dashed line).

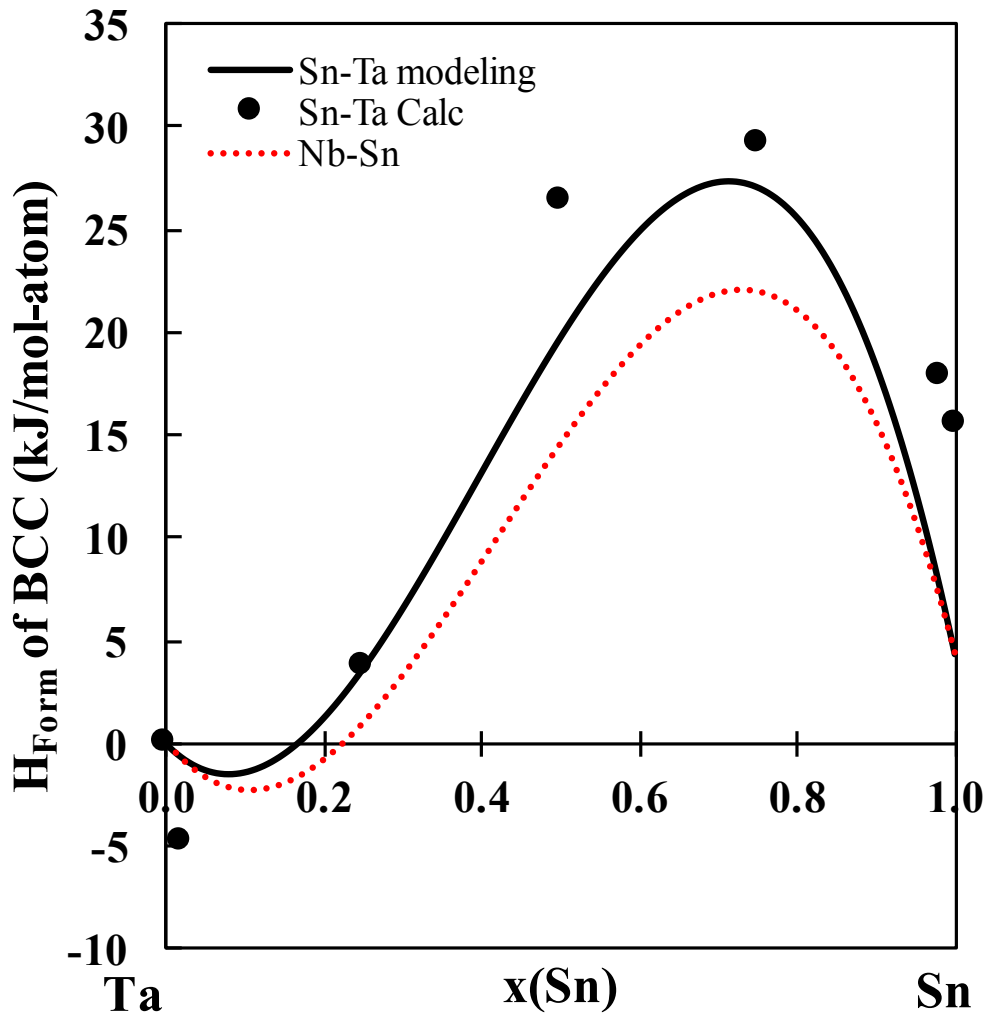


Figure 4.9. Enthalpy of formation of the bcc phase of the Sn-Ta system as a function of composition at 298 °K and ambient pressure from the current CALPHAD modeling (solid line) and from the first-principles calculations (dots), showing asymmetric behavior. This was compared with data of the Nb-Sn system from Toffolon et al. [33] (dashed red line) which was modeled using experimental data, showing similar asymmetric behavior.

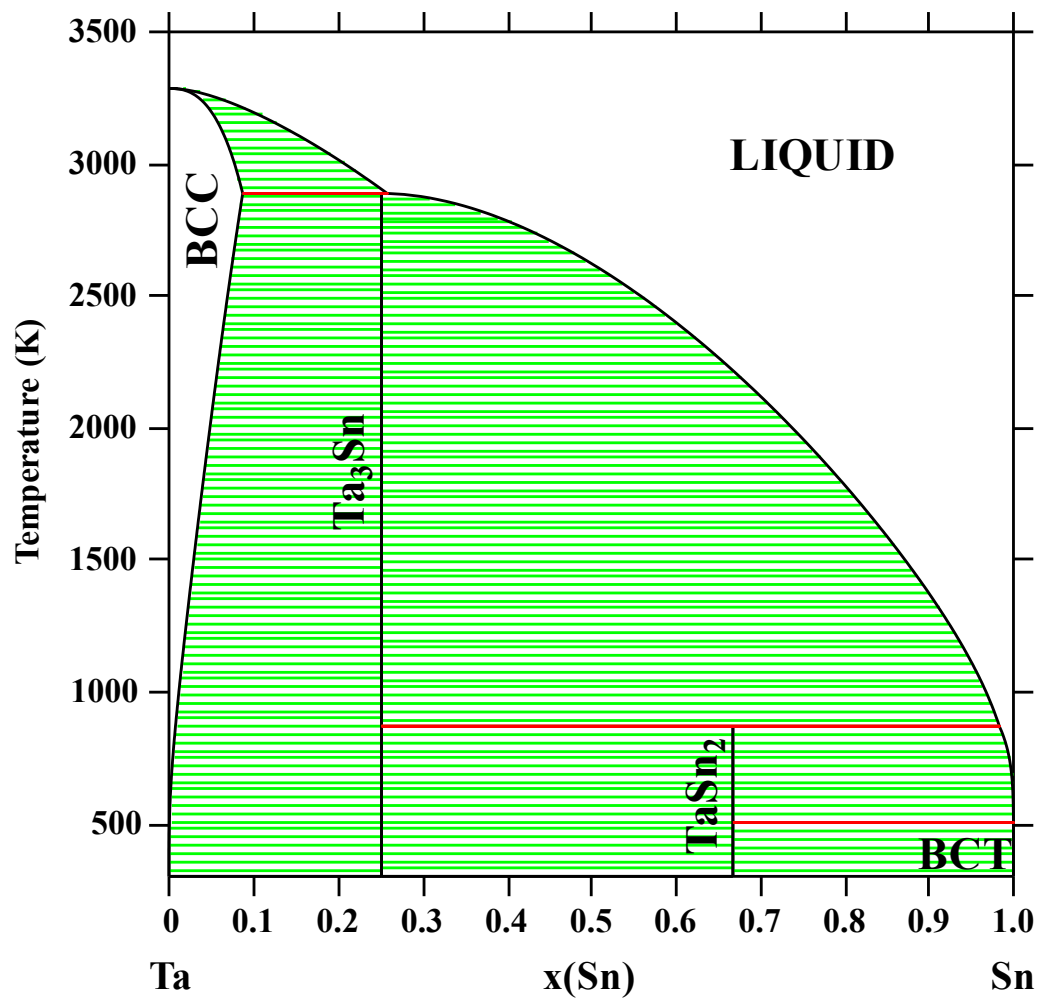


Figure 4.10. Calculated Sn-Ta phase diagram using the present thermodynamic description.

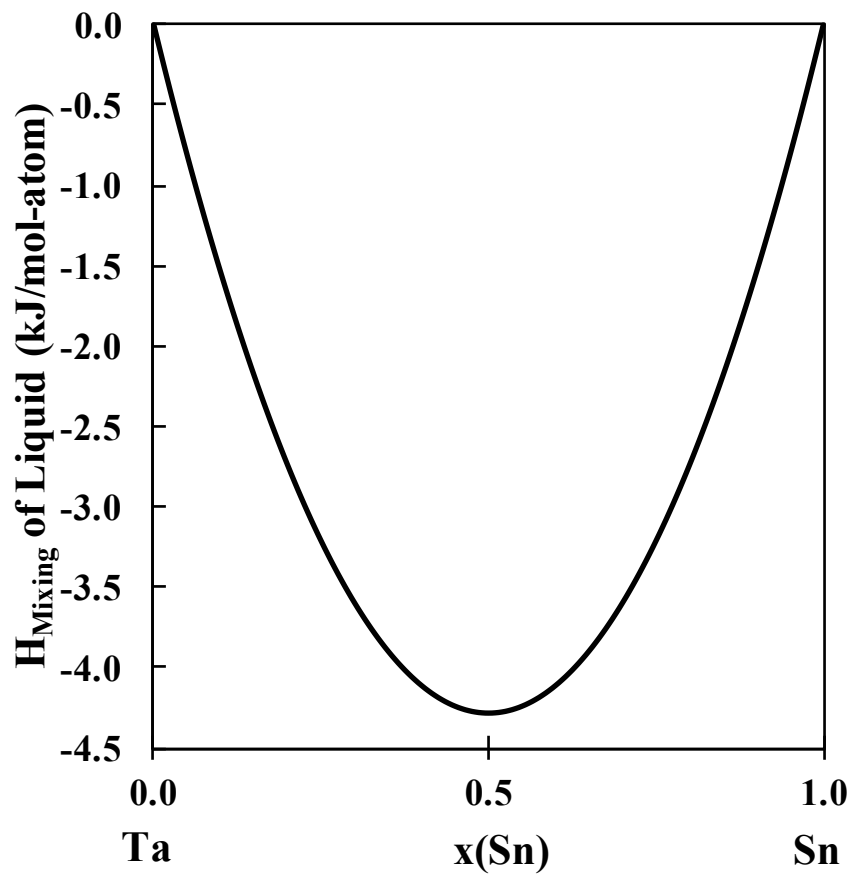


Figure 4.11. Enthalpy of mixing of the liquid phase as a function of composition at 298 °K and ambient pressure in the Sn-Ta system.

Chapter 5 |

Effects of alloying elements on the elastic properties of bcc Ti- X alloys

5.1 Introduction

The present chapter is aimed at studying the effects of alloying elements on the mechanical properties of Ti-alloys as well as completing a database to calculate the elastic properties as a function of composition. This is accomplished by systematically studying the single crystal elastic stiffness constants (c_{ij} 's) and polycrystalline aggregate properties of bcc Ti-X (X = Mo, Nb, Ta, Sn, Zr) alloys. The elastic properties are calculated using first-principles calculations based on density functional theory (DFT). The composition dependence of elastic properties of Ti-X alloys is explored through the dilute solutions and special quasirandom structures (SQS) [73] for concentrated solutions using the methodologies outlined in the methodology chapter. The obtained elastic properties are then fit using the CALPHAD method and extrapolated to higher order Ti-alloys.

5.2 Modeling and Calculations

5.2.1 Calculation details

In the present work the Vienna ab-initio Simulation Package (VASP) [61] was employed to calculate the elastic properties of pure elements and Ti-containing binary systems in the bcc phase. The ion-electron interactions were described using the projector augmented wave (PAW) [62, 90] method. As discussed previously, the use of two X-C functionals were compared in this chapter and based on the results the generalized gradient approach depicted by Perdew, Burke, and Ernzerhof (PBE-GGA) was employed [58]. For consistency, a 310 eV energy cutoff was adopted for all calculations, which is roughly 1.3 times higher than the default value. The energy convergence criterion was 10^{-6} eV/atom, and the Monkhorst-Pack scheme is used for Brillouin zone sampling [61, 91]. The k-points grid for each calculation are listed in Appendix D.

For the Ti-X binary systems, calculations for both dilute and SQS solutions were carried out. Three SQS cells with mole fractions of X atoms at 0.25, 0.5, and 0.75 were employed. Five dilute solutions were calculated for each Ti-X binary alloy using supercell sizes, i.e., Ti_{53}X (54-atom), Ti_{15}X (16-atom), Ti_7X (8-atom), X_{15}Ti (16-atom), and X_{53}Ti (54-atom). The interaction parameters for the elastic stiffness constants were then determined according to the methodology laid out in chapter 2.

5.2.2 Modeling details

The first-principles results were then used to model the elastic stiffness constants. The modeling was completed by calculating the difference between the first-principles calculations and a linear extrapolation between pure elements. The differences were then used to fit to the interaction parameters. Due to the limitations within the PARROT module, a mathematica script was used to fit the interaction parameters. The mathematica script is appended in appendix C. With the focus being Ti-rich alloys, the first-principles results with 70 at. % Ti or higher were weighted heavier (x_6 , according to the authors' practices) than the other points for the fittings. The best fit was found by comparing the fittings obtained with one interaction parameter or with two interaction parameters. The moduli

values were than calculated from the elastic stiffness constants according to the methodology chapter.

5.3 Results and discussion

5.3.1 Evaluation of calculation settings

The X-C functionals of PW91 and PBE were tested on the Ti-Ta binary system. The results are plotted in Figure 5.1. It is shown that the c_{44} values of Ti-Ta alloys consistently differ around 10 GPa or less between the PW91 and PBE calculations. The c_{11} and c_{12} calculations differ less than 5 GPa. The c_{11} and c_{12} values with 25 at.% Ta from SQS calculations vary by 26 GPa and 13 GPa, respectively. Since overall the values vary by an error of less than 0.2 (calculated with Eq. 2.30), it is concluded that the X-C functional choice does not make a significant difference in the results. The PBE functional was created after PW91 and meant to be an improvement on the PW91, discussed in more detail in Chapter 2, and was chosen for the present work.

Three magnitudes of strain were tested on the Ti-Mo binary system and plotted in 5.2. The results show that the different strain magnitudes do not affect the results. For example, the data calculated using ± 0.01 , ± 0.013 , and ± 0.007 strains at Mo_{15}Ti for c_{11} was 451 GPa, 450 GPa, and 450 GPa, respectively, varying within 1 GPa ($< 1\%$), similar to the variance in the c_{12} and c_{44} results. Overall, the variance in the c_{11} and c_{12} is less than 0.02 (Eq. 2.30). The largest variance is seen in the $\text{Ti}_{50}\text{Mo}_{50}$, the c_{44} values are 42 GPa, 42 GPa, and 65 GPa calculated with ± 0.01 , ± 0.013 , and ± 0.007 strains, respectively. Overall, the strain magnitude does not seem to affect the calculated results, and the ± 0.01 strain magnitude is thus used for all the calculations.

5.3.2 Calculations of the Ti-X elastic properties

The elastic stiffness constants and bulk modulus B are calculated from c_{ij} of pure elements in the bcc structure and reported in 5.1. The results in the present work were all obtained at 0 °K without considering the effect of zero-point vibrational energy as discussed in the section of methodology. The results for Mo, Nb and

Ta, which are stable in the bcc structure at low temperatures, are compared with experimental data at temperatures specified in the table 5.1 [99, 124]. The error (Eq. 2.30) between the present results and previous results for Mo, Nb and Ta are 0.0261, 0.075, and 0.0425, respectively [68, 99, 124]. This discrepancy is partially due to the experimental values being obtained at higher temperatures than the calculations at 0 °K.

Ti and Zr are stable in the hcp structure at low temperatures, and Sn is stable in the body centered tetragonal and diamond structures at low temperatures. Due to the instability of Ti, Sn and Zr in the bcc structure at low temperatures, their elastic stiffness coefficients are compared with previous first-principles calculations at 0 °K [115] used the PW91 functional, and the errors are 0.024, 0.528 and 0.051, respectively. The differences are related to the instability of the bcc structure, the different exchange correlation functionals and the different input parameters chosen. Due to the bcc instability, multiple relaxation schemes were run in the present work to find the lowest energy structure retaining the bcc symmetry, making the results the most accurate representation of the bcc pure elements.

Figure 5.3 summarizes the present Young's modulus results for each Ti-X binary system (circles). The solid lines are from the Voigt-Reuss-Hill approach with the elastic coefficients from the current modeling using Eq. 2.30 and the model parameters shown in Table 5.2. The Hill average is plotted as a solid black line while the Voigt (high bound) and Reuss (low bound) are plotted as dotted lines and dashed lines, respectively. When the structures are stable the Voigt and Reuss do not vary drastically but when the structures are unstable the Voigt and Reuss show the high and low bounds of the modulus calculations with the Hill average being what the database will predict. The results calculated for the Ti-Mo, Ti-Nb, and Ti-Ta systems are compared with previous calculated results from Ikehata et al. [2], and the difference is due to the different input parameters and structures used at each composition. Ikehata et al. used the s electrons as the valance electrons for Ti and used the B2 structure for their $\text{Ti}_{0.5}\text{X}_{0.5}$ with Ti at the body centered site and X at the corner site. For the $\text{Ti}_{0.25}\text{X}_{0.75}$ and $\text{Ti}_{0.75}\text{X}_{0.25}$ structures they used the DO_3 structure with space group $Fm\bar{3}m$, as opposed to the BCC space group of $Im\bar{3}m$. While the present work used the p electrons as valance for Ti based on updated work and new recommendations by VASP and 16-atom SQS structures from Jiang et al. [73]. The SQS structures mimic the random substitution

of elements that represent the atomic structures of solution phases better. The Ti-Mo, Ti-Nb and Ti-Ta alloy results are also compared with available experimental results [3–5, 7, 34–36] in Table 5.3.

Figure 5.3a compares the present results for the Ti-Mo alloy system with experimental data from Zhang et al. [34], Collings et al. [35], and Sung et al. [36]. It can be seen that the Young's modulus increases from pure Ti to pure Mo. The results from Sung et al. [36] differ by about 60 GPa from the present work. However, during the x-ray diffraction and transmission electron microscopy investigations by Sung et al, one of the metastable phases, α'' and ω , in addition to the bcc phase was observed in the samples. The ω phase is a hexagonal phase (space group P6/mmm) with lattice parameters closely matching those of the bcc phase, and the α'' phase is a martensitic orthorhombic phase (space group Cmcm). The formation of the α'' and ω phases causes variations in the mechanical properties and thus the mechanical properties are expected to vary from the elastic properties of the single bcc phase. Zhang et al. [34] and Collings et al. [35] did not observe the formation of either metastable phase. The Young's modulus determined by Zhang et al. and Collings et al. are predicted with the present Voigt-Reuss bounds but have an error of 0.39 (Eq. 2.30) from the Hill average Young's modulus.

The present Young's moduli of the Ti-Nb alloy system are compared with data from Ozaki et al. [7] and Collings et al. [35] in Figure 5.3b, showing an increase in Young's modulus with an increase in Nb concentration. The analyses of the samples from the work by Ozaki et al. and Collings et al. showed that the alloys all contained the single bcc phase. The Young's modulus from the present first-principles calculations show an error of 0.09 (Eq. 2.30) from the Young's modulus determined by Ozaki et al. and Collings et al.

Figure 5.3d shows the Young's modulus calculation results for the Ti-Ta alloy system and compares them to the experimental Young's modulus values determined by Fedotov et al. [5] and Zhou et al. [3, 4]. The Young's modulus in the Ti-Ta system increases from pure Ti to pure Ta, and the calculated Yougn's moduli have an error of 0.19 (Eq. 2.30) compared to the experimental Young's moduli [3–5].

The error between the experimentally determined Young's moduli and the calculated Young's moduli is expected due to the temperature difference (calculations at 0 °K and experiments at 298 °K). The experimentally determined Young's moduli fit well within the Voigt and Reuss bounds and the present calculations provide

good prediction of the elastic properties of the Ti-Mo, Ti-Nb and Ti-Ta alloys as a function of composition.

The calculated Young's moduli for the Ti-Sn (Figure 5.3c) and Ti-Zr (Figure 5.3e) systems cannot be compared to experimental data because the bcc phase is not stable in these systems at low temperatures. For the Ti-Sn alloy system the Young's modulus increases from 0 to 35 at. % Sn and then decreases from 35 to 100 at. % Sn. The Young's modulus data, for the Ti-Zr alloy system, increases from 0 to 40 at. % Zr, and then decreases from 40 to 100 at. % Zr. Figure 5.4 plots the Young's modulus as a function of composition from pure Ti in the bcc structure to the alloying element ($X = \text{Mo, Nb, Sn, Ta, Zr}$) and compares the effects of each alloying element on the Young's modulus.

Figure 5.5 to Figure 5.7 plots the calculated elastic stiffness constants, \bar{C}_{11} , \bar{C}_{12} , \bar{C}_{44} (circles) and compares them with the elastic stiffness constants fitting (solid line) and linear extrapolation between the pure elements for each binary alloy, Ti-Mo, Ti-Nb, Ti-Sn, Ti-Ta, and Ti-Zr. The previous results from Ikehata et al. [2] are plotted for comparison for the Ti-Mo, Ti-Nb, and Ti-Ta alloys. It can be seen that Mo, Nb, and Ta effect the elastic stiffness constants in a similar fashion. As shown in Figure 5.5a, 5.5b and 5.5d the \bar{C}_{11} increases from Ti to X (Mo, Nb, Ta). Figure 5.7a, 5.7b and 5.7d show that the \bar{C}_{44} values first decrease and then increase with the addition of the alloying element X ($X = \text{Mo, Nb, and Ta}$). The calculated \bar{C}_{12} increases by the addition of Mo or Ta (Figure 5.6a and Figure 5.6d, respectively), and the \bar{C}_{12} first decreases and then increases by the addition of Nb (Figure 5.6b). A similar trend is shown in the \bar{C}_{11} and \bar{C}_{12} data for the Ti-Sn system (Figure 5.5 and Figure 5.6c). The \bar{C}_{11} and \bar{C}_{12} values first increase and then decrease from pure Ti to pure Sn. As seen in Figure 5.7c, the \bar{C}_{44} first increases, then decreases, and then increases again from pure Ti to pure Sn. In the Ti-Zr system, the \bar{C}_{11} and \bar{C}_{44} values first increase and then decrease with increasing Zr concentration (Figure 5.5e and Figure 5.7e). For the Ti-Zr system, the calculated \bar{C}_{12} values first decrease and then increase, as shown in Figure 5.6e.

As discussed in the methodology (chapter 2), the instability of the bcc phase can be determined by Born's criteria (Eq. 2.21-2.23). The look at the bcc stability the $\bar{C}_{11} - \bar{C}_{12}$ values from the first-principles calculations and modeling are plotted in Figure 5.8. When the $\bar{C}_{11} - \bar{C}_{12}$ is positive the bcc phase is mechanically stable and when the $\bar{C}_{11} - \bar{C}_{12}$ is negative the bcc phase is mechanically unstable. The

bcc phase is mechanically unstable at Mo, Nb, Sn, Ta, and Zr concentrations of less than 5.5, 11.5, 51.5, 9.5 and 4.0 at. %, respectively. Figure 5.9 and Figure 5.10 show the shear (G) and bulk moduli (B) of the Ti-X (X = Mo, Nb, Sn, Ta, Zr) systems, with the present results (circles), the Hill average (solid black line), and Voigt (purple dashed line) and Reuss (yellow dashed line) bounds plotted. Similar trends in the B and G data are seen for the Ti-Mo, Ti-Nb and Ti-Ta systems. The B and G increase with increasing Mo, Nb and Ta concentration, as shown in Figure 5.9 and Figure 5.10, respectively. The bulk and shear moduli values increase and then decrease from pure Ti to pure Sn in the Ti-Sn system (Figure 5.9c and Figure 5.10c). In the Ti-Zr system, the B decreases from pure Ti to pure Zr (Figure 5.9e) and the G first increases and then decreases from pure Ti to pure Zr (Figure 5.10e).

5.3.3 Extrapolation to ternary and higher ordered systems

The interaction parameters in Table 5.2 can be used to predict the elastic stiffness constants of higher order Ti-alloys by summing the interaction parameters of each binary alloy contained in the multi-component alloy from Eq. 2.38. The predicted elastic stiffness constants of the multi-component alloys can be used to calculate the Young's modulus as a function of composition, as shown in Figure 5.4. The Hill average is plotted as a solid line while the Voigt and Reuss bounds are plotted as dotted and dashed lines, respectively. The accuracy of prediction of the elastic properties of higher ordered Ti alloys are evaluated by comparing the predicted results with previous experimental results [37–40] as shown in Figure 5.11 and Table 5.4. The black diagonal line represents a perfect correlation between the predicted and experimental Young's modulus. The grey region is the error (3 GPa) in the first-principles calculations, which is the average variance in \overline{C}_{11} , \overline{C}_{12} and \overline{C}_{44} from Eq. 2.18-2.20.

It can be seen that, the difference between experimental E at the same composition from Niinomi et al. [40], Geetha et al. [38], Tane et al. [37] and Mohammad et al. [39] varies from 2 GPa to 46 GPa, based on the heat treatments and measuring techniques. The scattering in the Young's moduli among experimental measurements is denoted by the vertical error bars in Figure 5.11. The horizontal error bars show the Reuss and Voigt Young's moduli ranges with the Hill average marked by the circle. The experimental Young's moduli deviate from the present predictions

by 0.69 to 14 GPa. This difference is due to the temperature difference between the first-principles data and the experimental results. Considering the fact that the experimental results from the literature at the same composition vary drastically, the present first-principles calculations give a good representation of the elastic properties of higher order Ti-alloys. Introducing the binary interaction parameters of non-Ti containing alloys in the system and the ternary interaction parameters can further improve the database predictions.

5.4 Conclusion

The effects of five alloying elements on the elastic properties of bcc Ti-X (X = Mo, Nb, Sn, Ta, Zr) alloys, including the elastic stiffness constants, bulk modulus, shear modulus, and Young's modulus, were systematically studied using first-principles calculations. The CALPAHD methodology was used to evaluate interaction parameters to predict the elastic properties as a function of composition. The present calculations show that 5.5, 11.5, 51.5, 9.5, and 4.0 at. % of Mo, Nb, Sn, Ta and Zr, respectively, are required to stabilize the bcc phase according to the Born criteria. The trends observed were summarized for each Ti-X (X= Mo, Nb, Sn, Ta, Zr) binary system. Alloying with Mo, Nb, and Ta results in similar trends, which is probably because Mo, Nb, and Ta are strong bcc stabilizers and stable in the bcc structure at room temperature. The interaction parameters determined in the current work were used to predict the elastic properties of higher order alloys. The accuracy of database predictions of the YoungâŽs modulus was evaluated by comparing the calculated and experimental Young's moduli. Overall, the database provides good predictions of the elastic properties of Ti-alloys in the bcc phase as a function of composition.

Table 5.1. Calculated pure element elastic stiffness constants and the bulk modulus B (in GPa) by X-C functional of PBE are compared with the previous first-principles calculations (FP) by X-C functional PW91 and experiments (Expt). Sv, pv and d refereeing to the s, p, and d states being treated as valance, respectively.

Pure Elements			\bar{C}_{11}	\bar{C}_{11}	\bar{C}_{11}	B
Ti_sv	This work 0 K	93	115	41	108	
	Calc 0 K [115]	96	116	40	107	
Mo_pv	This work 0 K	475	164	108	268	
	Expt 73 K [68]	473	156	111		
	Expt 300 K [124]	473	160	109	261	
Nb_sv	This work 0 K	245	144	27	178	
	Expt 4 K [68]	253	133	31		
	Expt 300 K [99]	247	135	29	172	
Sn_d	This work 0 K	50	52	29	51	
	Calc 0 K [115]	30	60	18	48	
Ta_pv	This work 0 K	278	164	81	202	
	Expt 0 K [68]	266	158	87		
	Expt 300 K [99]	267	161	83	196	
Zr_sv	This work 0 K	86	91	32	89	
	Calc 0 K [115]	82	94	30	90	

Table 5.2. Evaluated interaction parameters L_0 and L_1 using the R-K polynomial Eq. 2.38 for the elastic stiffness constants for the Ti-X binary systems.

Alloy	Interaction Parameter	Ti-Mo	Ti-Nb	Ti-Sn	Ti-Ta	Ti-Zr
\bar{C}_{11}	L_0	-22.16	40.46	119.46	83.65	246.97
	L_1	0	0	0	-67.76	-135.95
\bar{C}_{12}	L_0	-36.40	-32.39	15.90	38.05	-110.53
	L_1	0	0	-146.80	0	78.00
\bar{C}_{44}	L_0	-142.9	-41.54	59.79	-51.96	70.06
	L_1	0	-41.95	-94.38	0	0

Table 5.3: First-principles calculations of the elastic stiffness constants, bulk modulus B , shear modulus G , and Young's modulus E in GPa for different atomic percent compositions of the bcc Ti-X binary systems at 0 °K. As well as experimental data for the Young's modulus obtained at 300 °K by the reference stated.

Reference	$\text{Ti}_{100-b}\text{X}_b$	\bar{C}_{11}	\bar{C}_{12}	\bar{C}_{44}	B	G	E
This work	Ti	93	115	41	108	-12.91	-40.34
This work	$\text{TiMo}_{6.3}$	124	111	38	115	20	54
This work	$\text{TiMo}_{12.5}$	146	113	29	124	23	65
This work	TiMo_{25}	178 ± 3	123 ± 15	32 ± 11	141 ± 15	30 ± 15	84 ± 15
This work	TiMo_{50}	268 ± 9	136 ± 19	42 ± 9	180 ± 19	51 ± 19	138 ± 19
This work	TiMo_{75}	385 ± 9	146 ± 6	66 ± 6	226 ± 9	84 ± 9	224 ± 9
This work	$\text{TiMo}_{93.8}$	451	158	96	256	114	397
This work	$\text{TiMo}_{98.1}$	464	163	100	263	118	308
This work	Mo	475	164	108	268	125	325
Expt 300 K [34]	TiMo_8						83
Expt 300 K [34]	TiMo_{12}						90
Expt 300 K [35]	TiMo_8						84
Expt 300 K [35]	TiMo_{11}						89
Expt 300 K [35]	TiMo_{18}						101
This work	$\text{TiNb}_{1.9}$	93	115	35	108	-18	-56
This work	$\text{TiNb}_{12.5}$	116	116	37	116	11	31
This work	TiNb_{25}	140 ± 11	116 ± 13	34 ± 10	124 ± 13	22 ± 13	63 ± 13
This work	TiNb_{50}	181 ± 9	121 ± 2	31 ± 10	141 ± 9	31 ± 10	86 ± 10
This work	TiNb_{75}	208 ± 3	130 ± 4	15 ± 10	156 ± 4	22 ± 10	64 ± 10
This work	$\text{TiNb}_{93.8}$	242	134	18	170	28	81
This work	$\text{TiNb}_{98.1}$	242	134	18	170	28	81
This work	Nb	245	144	27	178	35	98
Expt 300 K [7]	TiNb_{29}						67
Expt 300 K [7]	TiNb_{34}						74
Expt 300 K [7]	TiNb_{44}						84
Expt 300 K [35]	TiNb_{26}						64
Expt 300 K [35]	TiNb_{30}						65
Expt 300 K [35]	TiNb_{34}						73

Table 5.3: First-principles calculations of the elastic stiffness constants, bulk modulus B , shear modulus G , and Young's modulus E in GPa for different atomic percent compositions of the bcc Ti-X binary systems at 0 °K. As well as experimental data for the Young's modulus obtained at 300 °K by the reference stated.

Reference	$\text{Ti}_{100-b}\text{X}_b$	\bar{C}_{11}	\bar{C}_{12}	\bar{C}_{44}	B	G	E
Expt 300 K [35]	TiNb ₄₄						83
This work	TiSn _{6.3}	100	122	46	115	-10	-30
This work	TiSn ₂₅	105 ±5	114 ±2	60 ±4	111 ±5	11 ±5	31 ±5
This work	TiSn ₅₀	88 ±9	93 ±9	46 ±4	91 ±9	10 ±9	29 ±9
This work	TiSn ₇₅	92 ±9	55 ±7	35 ±8	67 ±9	27 ±9	72 ±9
This work	Sn	50	52	29	51	7	21
This work	TiTa _{1.9}	100	115	39	110	-3	-9
This work	TiTa _{6.3}	116	113	30	114	11	32
This work	TiTa _{12.5}	120	121	39	121	11	32
This work	TiTa ₂₅	167 ±1	140 ±3	45	149 ±3	28 ±3	78 ±3
This work	TiTa ₅₀	208 ±1	159	51 ±3	175 ±1	38 ±3	106 ±3
This work	TiTa ₇₅	239 ±7	143 ±5	62 ±3	175 ±7	56 ±7	152 ±7
This work	TiTa _{93.8}	257	158	72	191	62	168
This work	TiTa _{98.1}	264	163	72	197	62	169
This work	Ta	278	164	81	202	70	189
Expt 300 K [5]	TiTa ₃₈						62
Expt 300 K [5]	TiTa ₄₂						79
Expt 300 K [5]	TiTa ₄₈						95
Expt 300 K [3]	TiTa ₃₈						67
Expt 300 K [3]	TiTa ₅₁						105
This work	TiZr _{1.9}	112	106	43	108	17	48
This work	TiZr ₂₅	148 ±14	82 ±7	54 ±7	104 ±14	44 ±14	116 ±14
This work	TiZr ₅₀	152 ±17	76 ±12	48 ±12	101 ±17	44 ±17	115 ±17
This work	TiZr ₇₅	126 ±12	82 ±3	45 ±3	97 ±12	34 ±12	91 ±12
This work	TiZr _{93.8}	89	90	34	90	9	27
This work	Zr	86	91	32	89	6	16

Table 5.4. Predicted Young's modulus (in GPa) of higher order alloys in the bcc phase compared to experimental values found with both the weight percent and atomic percent listed.

Alloy Name (%wt)	at %	Calc E	Expt E
Ti-35Nb-7Zr-5Ta [38]	Ti-24Nb-5Zr-2Ta	81	80
Ti-29Nb-13Ta-4.6Zr [38]	Ti-20Nb-5Ta-3Zr	76	75
Ti-29Nb-13Ta-6Sn [38]	Ti-21Nb-5Ta-3Sn	68	74
Ti-29Nb-13Ta-4.6Sn [38]	Ti-20Nb-5Ta-3Sn	67	66
Ti-29Nb-13Ta-4.5Zr [38]	Ti-20Nb-5Ta-3Zr	76	65
Ti-29Nb-13Ta-4.6Zr [37]	Ti-21Nb-5Ta-3Zr	76	64
Ti-30Nb-10Ta-5Zr [37]	Ti-23Nb-4Ta-3Zr	77	64
Ti-35Nb-10Ta-5Zr [37]	Ti-25Nb-4Ta-4Zr	80	65
Ti-24Nb-4Zr-7.9Sn [39]	Ti-15Nb-3Zr-4Sn	65	54
Ti ₃₅ Nb ₂ Ta ₃ Zr [39]	Ti-23Nb-1Ta-2Zr	69	61
Ti-29Nb-11Ta-5Zr [39]	Ti-20Nb-6Ta-2Zr	74	60
Ti-10Zr-5Ta-5Nb [39]	Ti-6Zr-1Ta-3Nb	64	52
Ti-29Nb-13Ta-2Sn [39]	Ti-20Nb-5Ta-1Sn	66	62

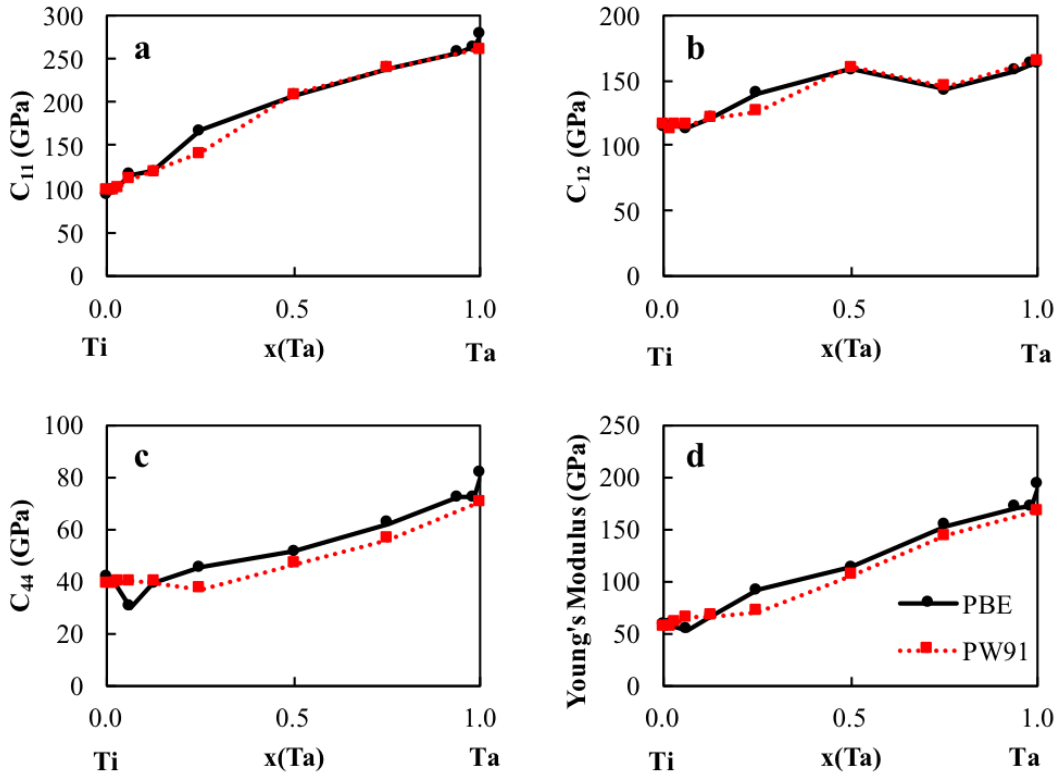


Figure 5.1. Elastic stiffness constants of the bcc Ti-Ta binary system calculated with the GGA and PBE exchange correction functions, respectively.

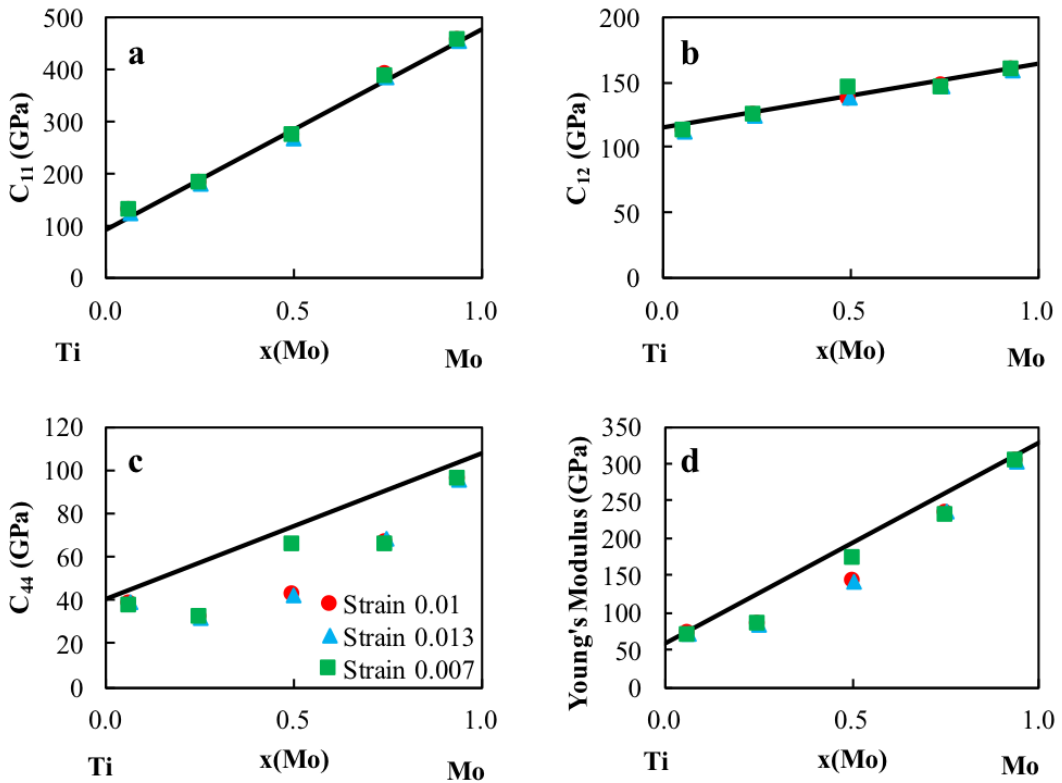


Figure 5.2. Elastic stiffness constants for the bcc Ti-Mo binary system calculated with strains, ± 0.01 , ± 0.03 and ± 0.07 , respectively, showing comparable results.

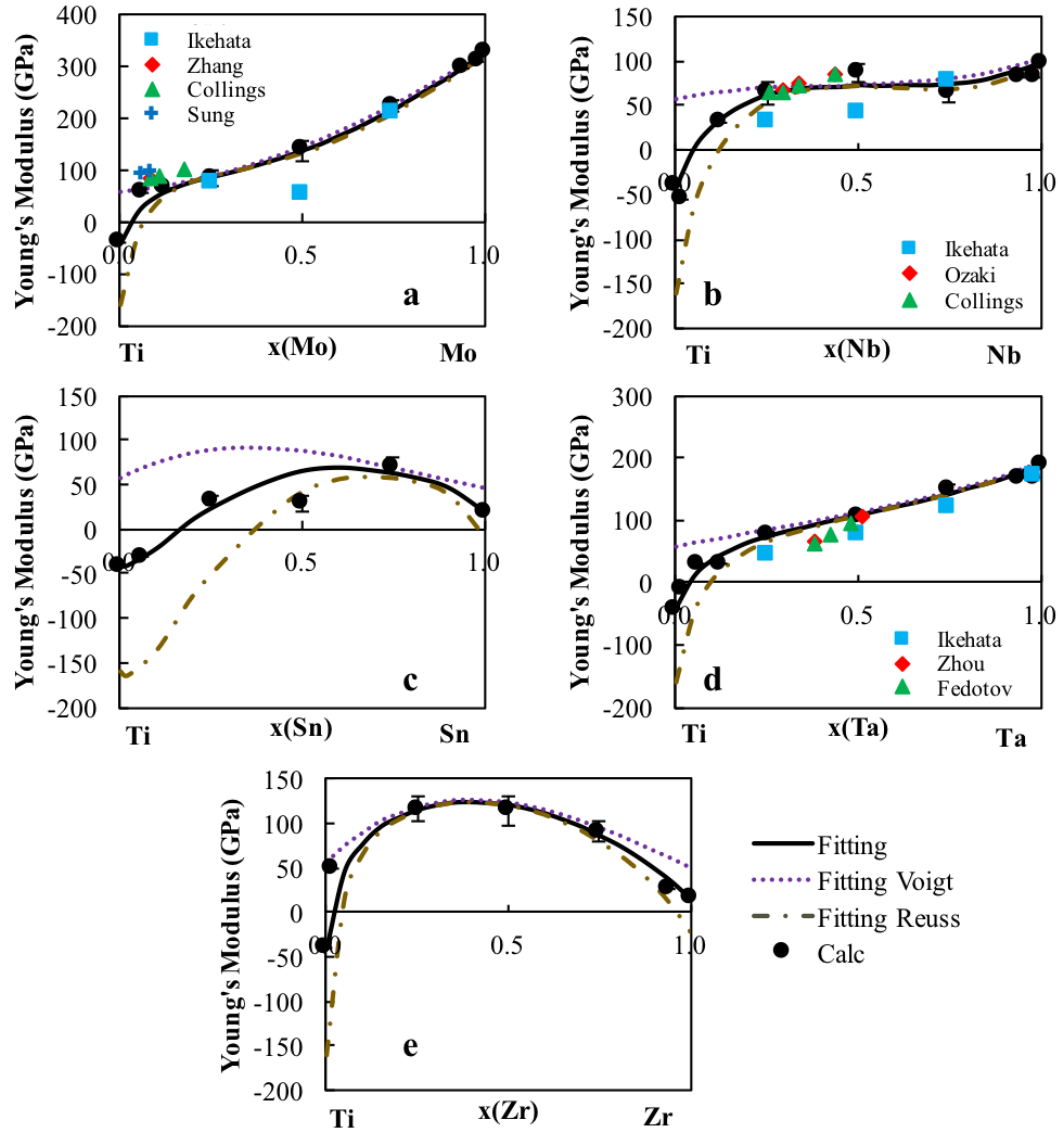


Figure 5.3. Young's modulus E of the Ti-X binary systems. The present calculations are plotted as the filled circles with the error bars. The dotted purple line is the Voigt upper Young's modulus bound, the gold dot dashed line is the lower Reuss Young's modulus bound and the black line is the Hill Young's modulus average. The experimental values [1–5, 7, 8, 34–36] are also included for comparison.

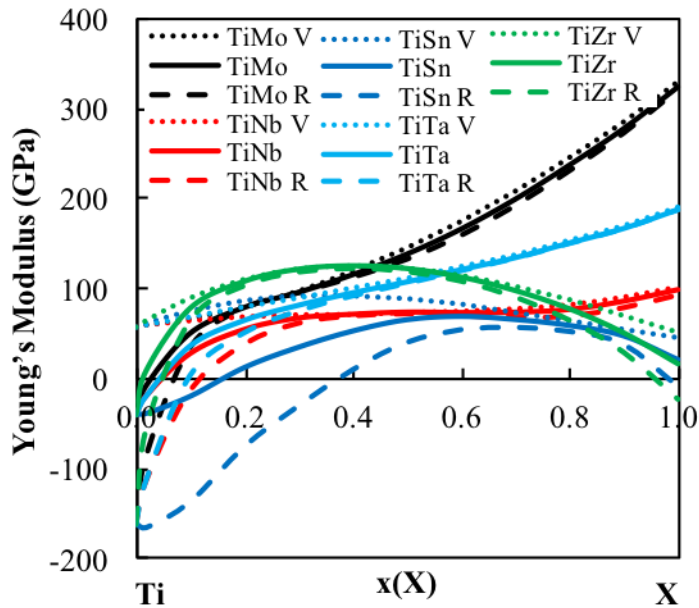


Figure 5.4. Young's modulus calculated from the model parameters (see 5.2) and Eq. 2.30 as a function of composition from bcc Ti to bcc X.

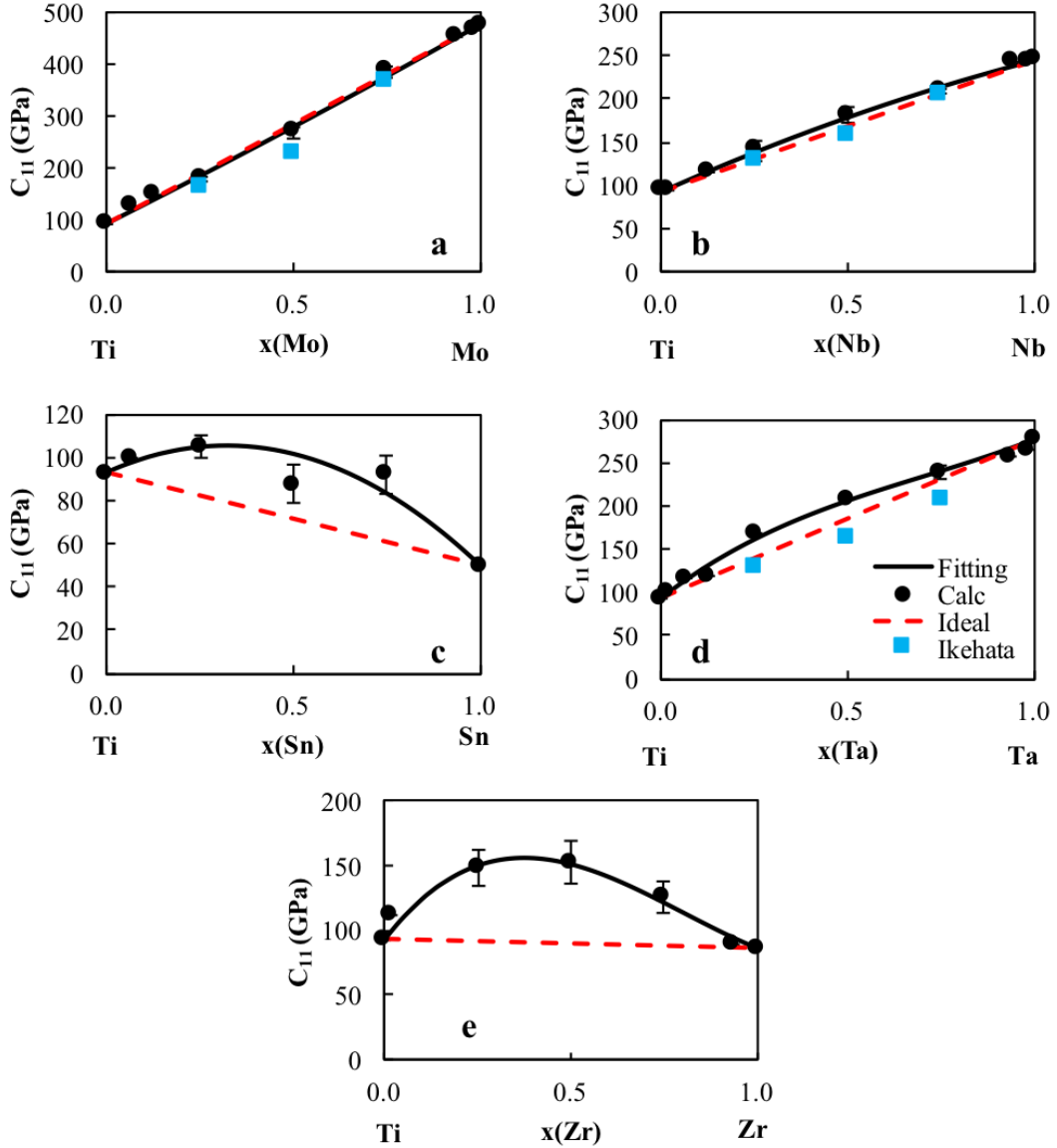


Figure 5.5. Calculated \bar{C}_{11} values (circles) plotted with their errors as well as the pure element extrapolation (red dashed line) and the present modeling (black dashed line) for five Ti-X binary systems ($X = \text{Mo}, \text{Nb}, \text{Ta}, \text{Sn}, \text{Zr}$). Ti-Mo, Ti-Nb, and Ti-Ta alloys are compared with previous calculations from Ikehata et al. [2].

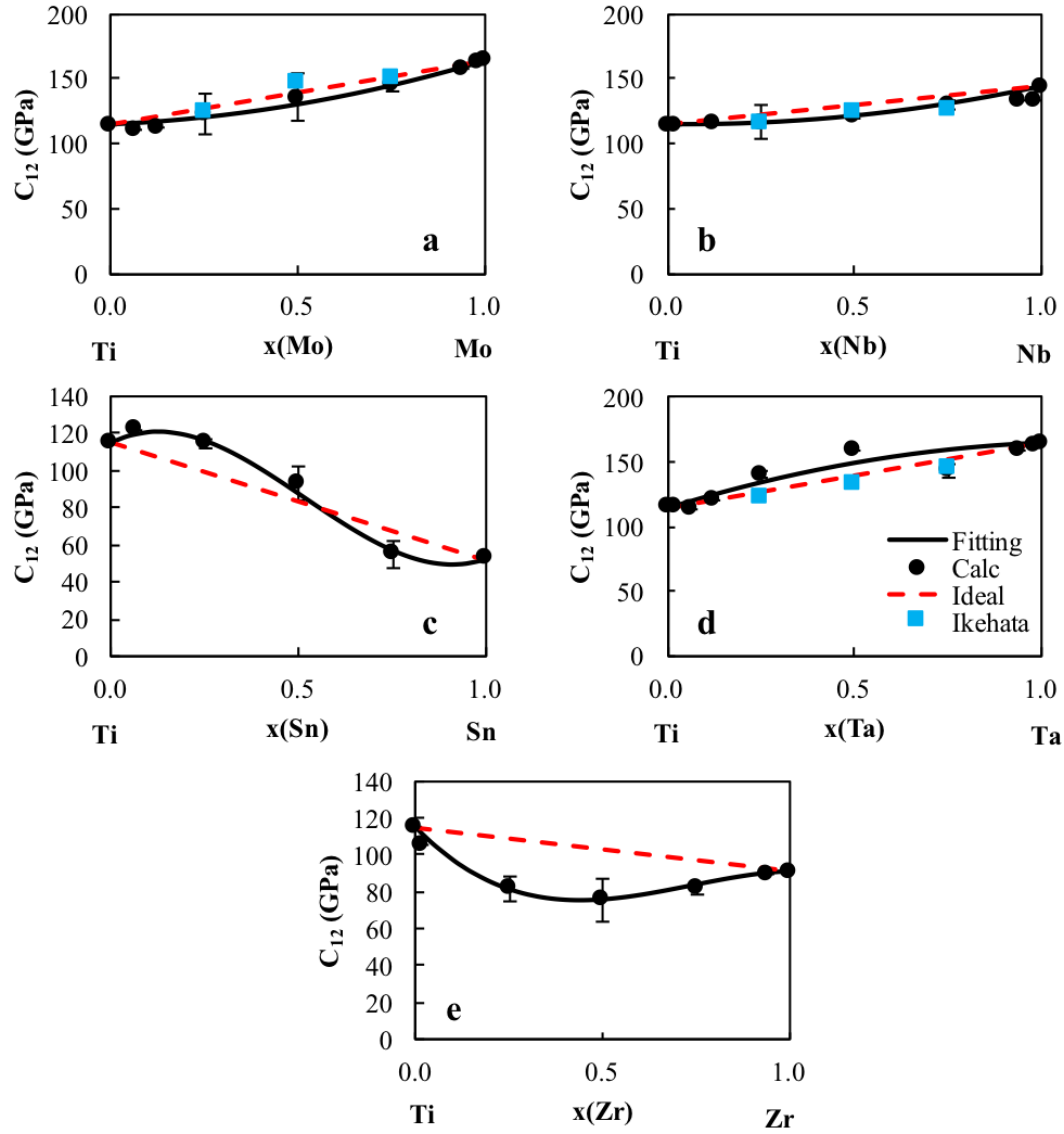


Figure 5.6. Calculated \bar{C}_{12} values (circles) plotted with their errors as well as the pure element extrapolation (red dashed line) and the present modeling (black dashed line) for five Ti-X binary systems ($X = \text{Mo}, \text{Nb}, \text{Ta}, \text{Sn}, \text{Zr}$). Ti-Mo, Ti-Nb, and Ti-Ta alloys are compared with previous calculations from Ikehata et al. [2].

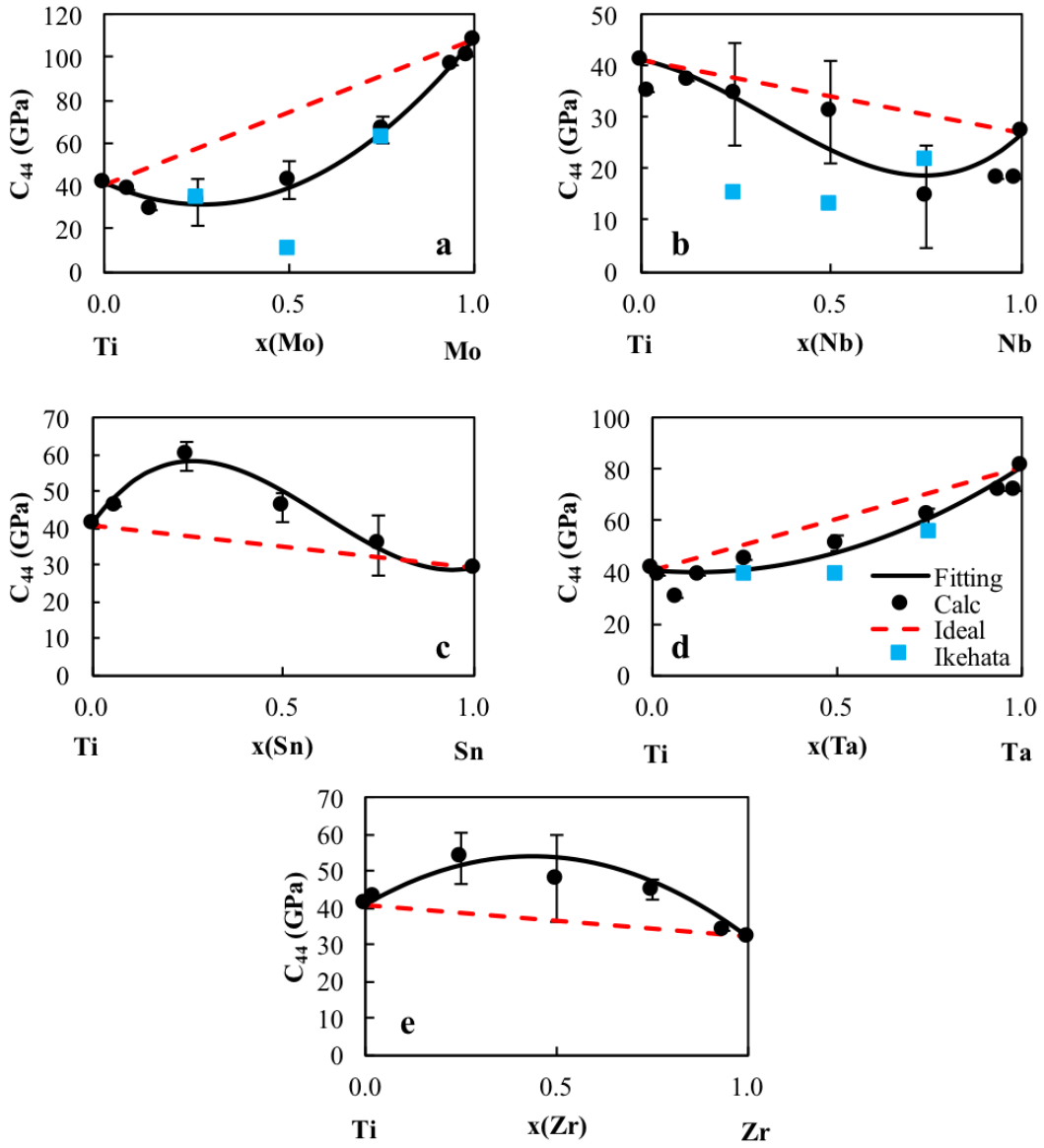


Figure 5.7. Calculated \bar{C}_{44} values (circles) plotted with their errors as well as the pure element extrapolation (red dashed line) and the present modeling (black dashed line) for five Ti-X binary systems ($X = \text{Mo}, \text{Nb}, \text{Ta}, \text{Sn}, \text{Zr}$). Ti-Mo, Ti-Nb, and Ti-Ta alloys are compared with previous calculations from Ikehata et al. [2].

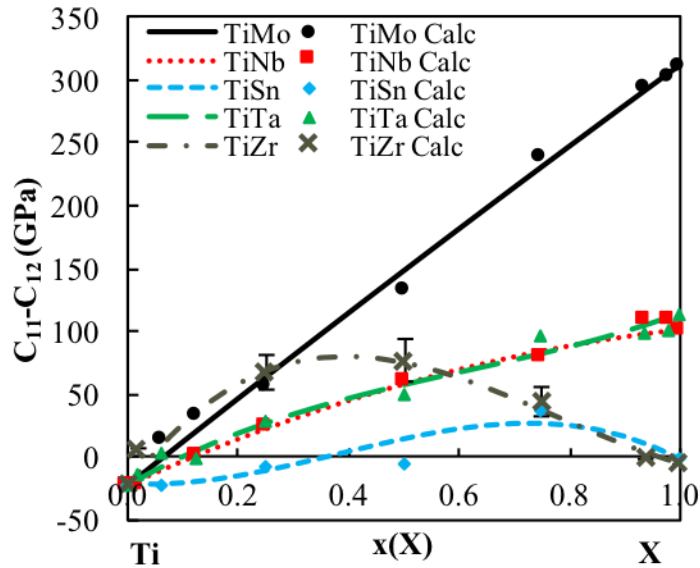


Figure 5.8. Calculated $\bar{C}_{11}-\bar{C}_{12}$ values (circles) plotted with the present modeling (solid lines) for five Ti-X binary systems ($X = \text{Mo, Nb, Ta, Sn, Zr}$). The $\bar{C}_{11}-\bar{C}_{12}$ shows the stability of the bcc phase. When the $\bar{C}_{11}-\bar{C}_{12}$ value is negative the bcc phase is not stable in the corresponding compositions range.

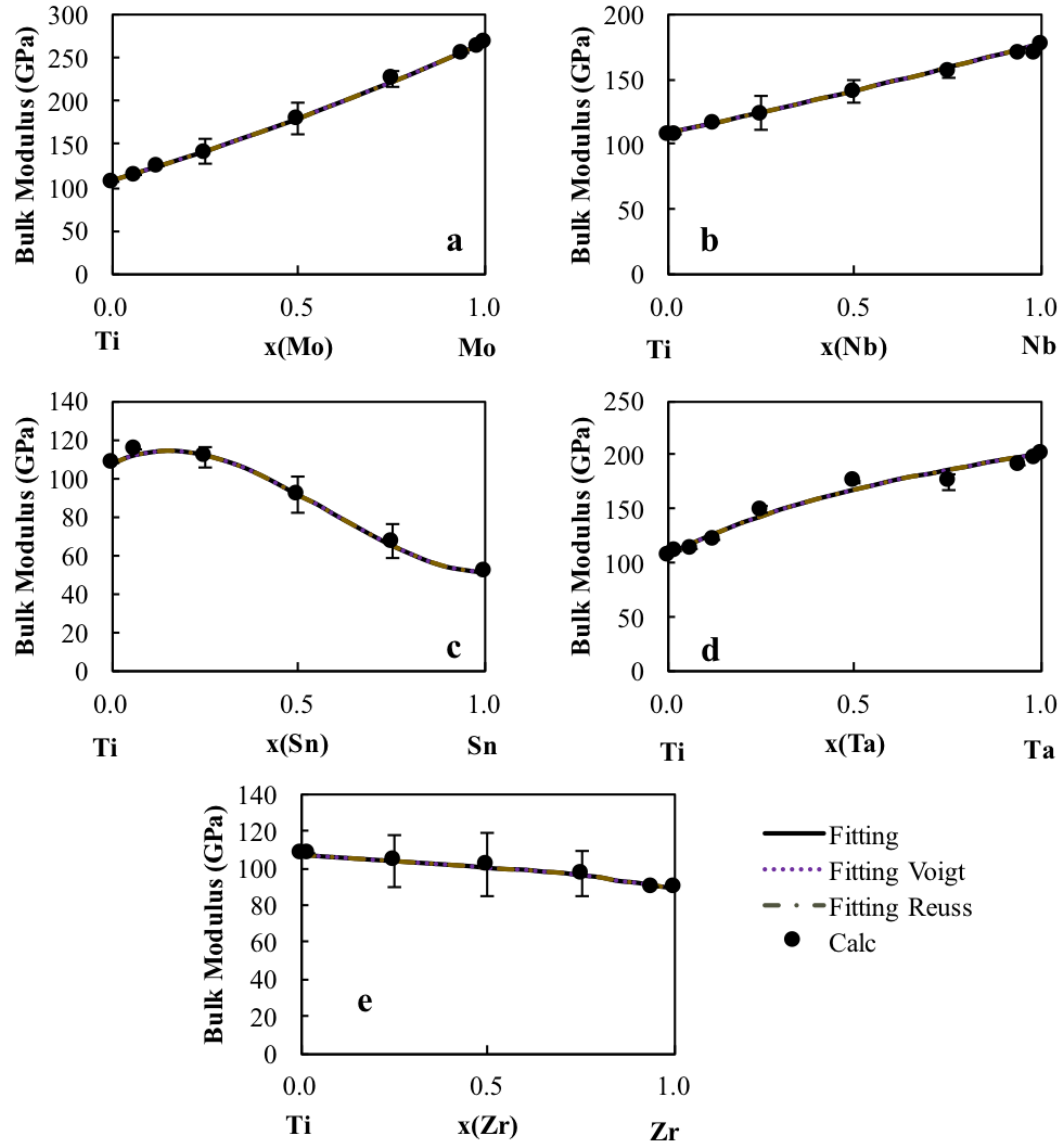


Figure 5.9. Bulk modulus B of the Ti-X binary systems. The present calculations are plotted as the filled circles with the error bars. The dotted purple line is the Voigt upper bulk modulus bound, the gold dot dashed line is the lower Reuss bulk modulus bound and the black line is the Hill bulk modulus average.

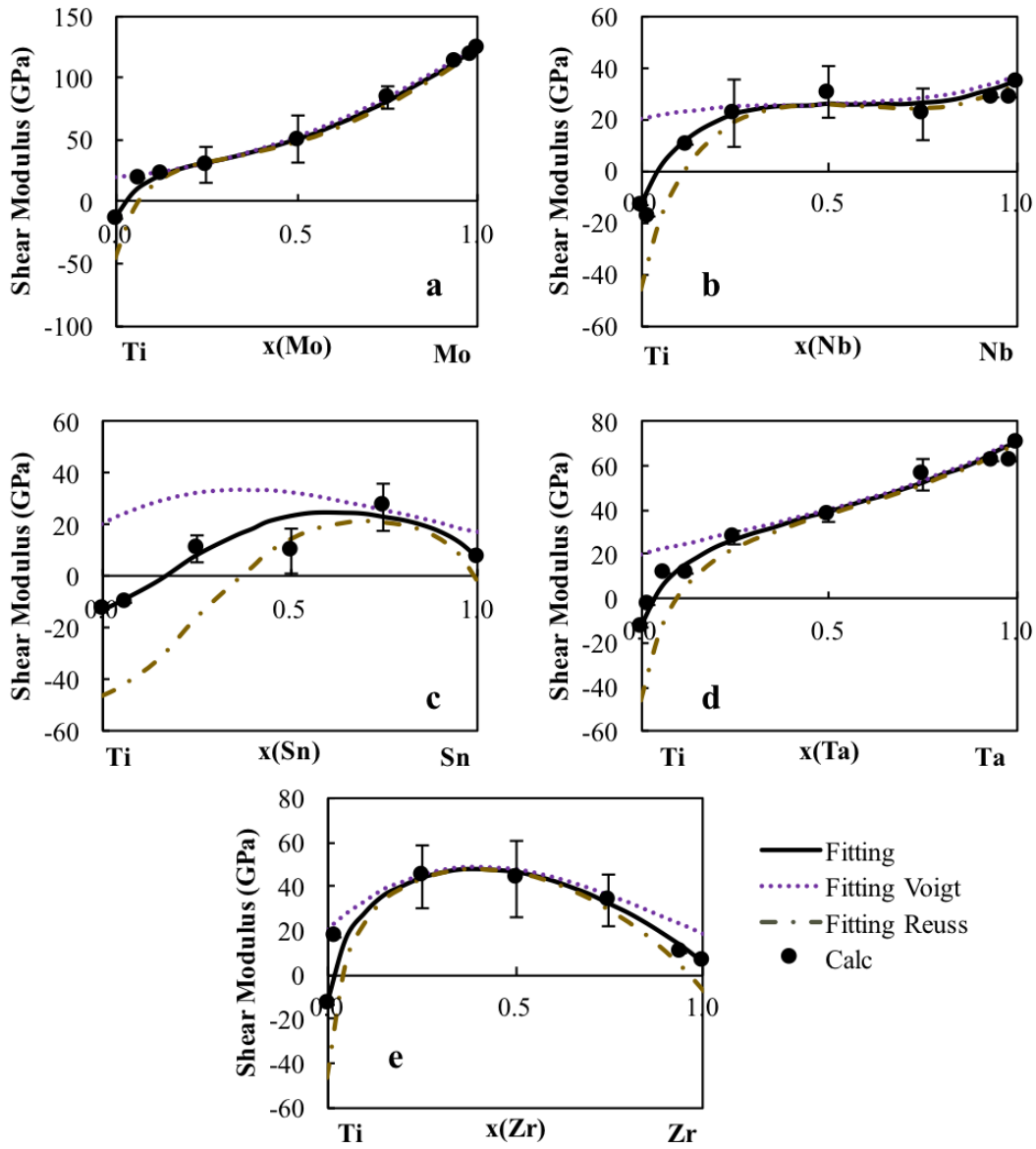


Figure 5.10. Shear modulus G of the Ti-X binary systems. The present calculations are plotted as the filled circles with the error bars. The dotted purple line is the Voigt upper shear modulus bound, the gold dot dashed line is the lower Reuss shear modulus bound and the black line is the Hill shear modulus average.

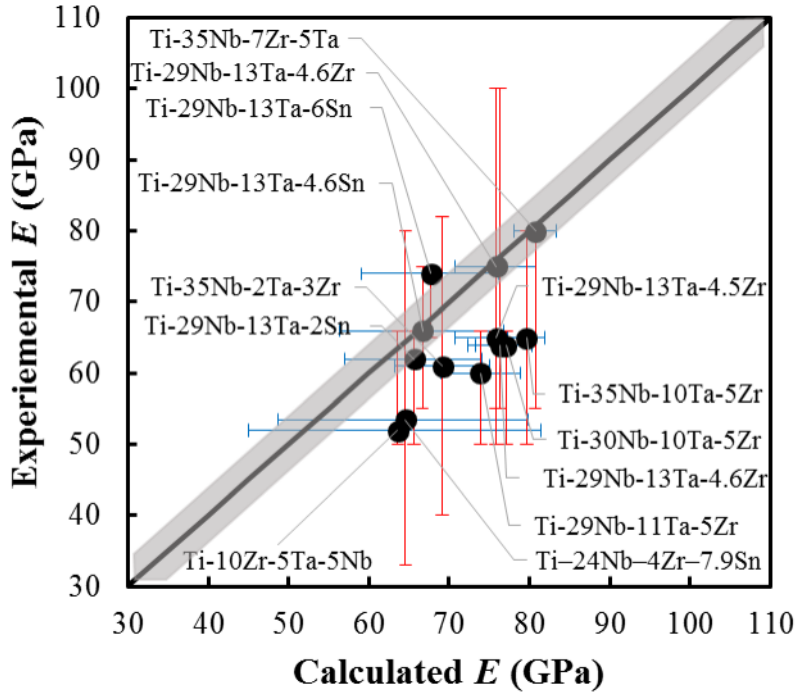


Figure 5.11. Young's moduli values of multicomponent bcc Ti alloys measured experimentally plotted against the predicted Young's moduli from the pure elements and binary interaction parameters with the black diagonal line showing the exact correlation between the experimental and calculated values. Error bars in the experiments and the bounds from Reuss and Voigt approximations are plotted as vertical and horizontal lines, respectively. The variance in the first calculations from Eq. 2.18-Eq. 2.20 was averaged and plotted as the grey region to show the variance in the first-principles calculations. More information on the alloys is in Table 5.4 [37–39]

Chapter 6 |

Effects of alloying elements on the elastic properties of bcc ternary and higher ordered Ti-alloys

6.1 Introduction

In order to develop a better understanding about alloying effect on the elastic properties of Ti alloys, the present work is developing an elastic database for the Ti-Mo-Nb-Sn-Ta-Zr system. With the focus being on bcc Ti-alloys, the effects of alloying elements on the pure elements and Ti-X binary alloys in the bcc phase were calculated in chapter 5. After extrapolating to higher order systems, it was hypothesized that studying the effects of alloying on the elastic properties of ternary alloys would improve the database. The present work focuses on studying the elastic properties of the Ti-X-Y ($X \neq Y = Mo, Nb, Ta, Sn, and Zr$) ternary alloys in the bcc phase. The single crystal elastic stiffness constants (c_{ij} 's) and polycrystalline aggregate properties are predicted across the composition range using Density Functional Theory (DFT) at 0 °K outlined in the methodology chapter. Based on the DFT results, the CALPHAD approach outlined in the methodology is used to evaluate ternary interaction parameters. The interaction parameters are then incorporated into the database and the database accuracy is again tested similarly to the testing in chapter 5. The completed database is used to map the elastic modulus as a function of composition.

6.2 Modeling and Calculations

6.2.1 Calculation details

To study the elastic properties of the ternary bcc Ti alloys in the Ti-Mo-Nb-Sn-Ta-Zr system, DFT-based first-principles calculations were employed using the VASP (Vienna ab-initio simulation package) [61, 62]. Four kinds of calculations were performed for each ternary alloy Ti-X-Y, with the varying compositions of $X_{50}Y_{50}$ (16-atom supercell), $TiXY$ (36 atoms), Ti_2XY (32 atoms), Ti_6XY (64 atoms). The relaxation and use of SQS are discussed extensively in the methodology (chapter 2). The SQS used in this chapter were generated by Jiang et al. [73, 74]. The projector augmented wave (PAW) method was used to describe the ion-electron interaction. Based on our previous work done in chapter 5 (Figure 5.1), the X-C functional of the generalized gradient approximation depicted by Perdew, Burke, and Ernzerhof (PBE-GGA) [58] was employed. An energy cutoff roughly 1.3 times higher than the default values among all elements (i.e., 310 eV) was used for all calculations. The Brillouin zone sampling was done using the γ -centered Monkhorst-Pack scheme [91]. The k-point grids used for the ternary SQS were 4x4x4 and the k-point grids used for the binary $X_{50}Y_{50}$ SQS structures were an automated k-point mesh generator in VASP with the length of the subdivision specified at 80. The elastic calculations were completed using a strain magnitude of ± 0.01 based on the study done in chapter 5 and the results seen in Figure 5.2.

6.2.2 Modeling details

The first-principles results were then used to model the ternary interaction parameters of the elastic stiffness constants. The modeling was completed by plotting the binary interpolation from the working database build in chapter 5. The plots started at a 50-50 mixture ($X_{50}Y_{50}$) of the alloying elements ($X \neq Y = Mo, Nb, Sn, Ta, and Zr$) and plotted to pure Ti. The elastic stiffness constants of the pure elements and the binary interaction parameters from Table 5.2 were used to plot the binary interpolation. The differences between the ternary first-principles calculations and the binary interpolation were then used to obtain a single fitting parameter using the mathematica code in appendix C. With the focus being Ti-rich alloys and wanting to follow the same modeling technique used on the binary alloys,

the first-principles results with 70 at.% Ti or higher were weighted heavier (x6, according to the authors' practices) than the other points for the fittings. The best fit was found and the ternary interaction parameters were incorporated into the database. The databases was then used to predict the moduli values of the ternary and higher order alloys.

6.3 Results and discussion

6.3.1 Elastic calculation results

The elastic stiffness constants \bar{C}_{11} , \bar{C}_{12} , and \bar{C}_{44} are plotted in Figure 6.1 to Figure 6.6 for Ti-X-Y alloys ($X \neq Y = Mo, Nb, Sn, Ta, Zr$). The plots start from a 50-50 mixture of the alloying elements $X_{50}Y_{50}$ to Ti. The calculations are plotted as circles, the interpolation from the pure elements and binary interaction parameters is plotted as a red dashed line. The difference between the calculations and binary interpolation was used to fit the ternary interaction parameters. The ternary fitting is plotted as a solid black line. The calculated elastic stiffness constants and moduli values are listed in Table 6.2 together with experimental values [38–41] for comparison.

The \bar{C}_{11} values, for most of the Ti-X-Y systems, decrease from $X_{50}Y_{50}$ to Ti (see Figure 6.1 and Figure 6.2). However, the Ti-Sn-Zr and Ti-Ta-Zr system differ. The values, for the Ti-Sn-Zr (Figure 6.2d), first increase from $Sn_{50}Zr_{50}$ to 60 at.% Ti and then decrease from 60 to 100 at.% Ti. The values, in the Ti-Ta-Zr system (Figure 6.2e), first increase from $Ta_{50}Zr_{50}$ to 35 at.% Ti and then decrease from 35 to 100 at.% Ti. The \bar{C}_{12} results are plotted in Figure 6.3 and Figure 6.4. The \bar{C}_{12} values decrease from $X_{50}Y_{50}$ to Ti, for the Ti-Mo-Nb, Ti-Mo-Ta and Ti-Nb-Ta systems. The \bar{C}_{12} values, for the Ti-Mo-Sn and Ti-Nb-Sn systems, first decrease from $X_{50}Y_{50}$ to 15 at.% Ti then increase from 15 to 85 at.% Ti and then decrease from 85 to 100 at.% Ti. The Ti-Mo-Zr and Ti-Nb-Zr systems show a decrease in \bar{C}_{12} value from $X_{50}Y_{50}$ to 60 at.% Ti and then an increase from 60 to 100 at.% Ti. The \bar{C}_{12} values increase from $X_{50}Y_{50}$ to 70 at.% Ti and then decrease from 70 to 100 at.% Ti for the Ti-Sn-Ta system. For the Ti-Sn-Zr system, the \bar{C}_{12} values increase from 0 to 100 at.% Ti and the \bar{C}_{12} values, for the Ti-Ta-Zr system, first decrease from 0 to 70 at.% Ti and then increase from 70 to 100 at.% Ti. The \bar{C}_{44} results are

plotted in Figure 6.5 and Figure 6.6. The \bar{C}_{44} values decrease from $X_{50}Y_{50}$ to Ti, for the Ti-Mo-Sn and Ti-Ta-Zr systems. For the Ti-Mo-Zr and Ti-Mo-Ta systems, the \bar{C}_{44} values first decrease from 0 to 80 at.% Ti and then increase from 80 to 100 at.% Ti. The \bar{C}_{44} values, for the Ti-Mo-Nb and Ti-Nb-Ta systems, first decrease from $X_{50}Y_{50}$ to 65 at.% Ti and then increase from 65 to 100 at.% Ti. The \bar{C}_{44} values first increase from 0 to 80 at.% Ti and then decrease from 80 to 100 at.% Ti for the Ti-Nb-Sn and Ti-Nb-Zr systems. For the Ti-Sn-Ta system (Figure 6.6c), the \bar{C}_{44} values decrease from 0 until 20 at.% Ti, then increase from 20 to 50 at.% Ti and then decrease from 50 to 100 at.% Ti. The \bar{C}_{44} values, for the Ti-Sn-Zr system, first increase from $X_{50}Y_{50}$ to 60 at.% Ti and then decrease from 60 to 100 at.% Ti.

The trends in the ternary elastic stiffness constants can be summarized and explained by looking at the elastic stiffness calculations done on the pure elements and Ti-X ($X = \text{Mo, Nb, Sn, Ta, Zr}$) Chapter 5. The c_{11} and c_{12} of Mo, Nb and Ta are higher than Ti, while Sn and Zr are lower. The c_{44} for Mo and Ta are higher than Ti, while Nb, Sn, and Zr are lower. This can be explained because Mo, Nb and Ta are stable in the bcc structure at low temperatures while Ti, Sn and Zr are not, so the elastic stiffness constants are lower. The similarities of Mo, Nb and Ta are again noticed in the Ti-X data trends. The \bar{C}_{11} , \bar{C}_{12} , and \bar{C}_{44} all follow the same trends for the Ti-Mo, Ti-Nb, and Ti-Ta systems with the \bar{C}_{11} and \bar{C}_{12} increasing in value from 100 to 0 at.% Ti and the \bar{C}_{44} decreases and then increases from 100 to 0 at.% Ti. Based on this information, it is no surprise that the Ti-Mo-Nb, Ti-Mo-Ta and Ti-Nb-Ta systems have the same trends in their c_{ij} data. When Ti-Mo, Ti-Nb, and Ti-Ta are alloyed with Sn in the ternary systems, they show similar trends for the most, not all, of the c_{ij} . The same is true for the Ti-Mo, Ti-Nb, and Ti-Ta systems alloyed with Zr.

Based on the discussion in the methodology, Born's criteria is used to look at the mechanical stability of the bcc phase. When $\bar{C}_{11}-\bar{C}_{12}$ becomes negative then the bcc phase loses mechanical stability and is thus plotted in Figure 6.7. Based on the present results, the bcc phase loses mechanical stability in the Ti-Mo-Nb, Ti-Mo-Ta, Ti-Mo-Zr, Ti-Nb-Zr, Ti-Sn-Zr, and Ti-Ta-Zr systems when the Ti concentration is more than 90 at.%, with the values being 91, 92, 95, 93, 91, and 94 at.% Ti, respectively. The bcc phase loses mechanical stability at Ti concentrations above 87, 77, 89, and 80 at.% Ti for Ti-Mo-Sn, Ti-Nb-Sn, Ti-Nb-Ta and Ti-Sn-Ta systems, respectively. Close to where the bcc phase loses its mechanical stability, the Young's

modulus is reduced and such compositions may be desirable low modulus bcc Ti alloys.

Figure 6.8 and Figure 6.9 plot the Young's moduli (E) calculations (circles) for each Ti-X-Y ternary system ($X \neq Y = \text{Mo, Nb, Sn, Ta, Zr}$) starting from a 50-50 mixture of the two alloying elements to Ti. The red dashed line is the Hill average interpolated from the binary interaction parameters shown in Table 5.2. The Hill average (black solid line), Voigt (purple dotted line), Reuss (gold dotted-dashed line) bounds are plotted using the binary (Table 5.3) and ternary interaction parameters (Table 6.3). The Voigt and Reuss bounds vary more drastically when the bcc structure is unstable as opposed to when the bcc structure is stable. The Hill average with the binary and ternary interaction parameters is employed, which should be closer to the polycrystalline values. The Hill average is what the database predicts because it has been shown to be a more accurate representation of the Young's modulus [70, 111]. Whenever possible experimentally determined Young's moduli [38–41] (data listed in Table 6.2) are plotted for comparison. The difference/error between the previous results (both experimental and from calculations) and the present first-principles results is reported here. The equation is defined in Chapter 2 Eq. 2.30.

The first-principles E , for the Ti-Mo-Nb (Figure 6.8a) system are compared with experimentally obtained E data in the review paper by Niinomi et al. [40]. The experimental E results were obtained using a nanoindenter after solution treatment. The experimental E values are higher than the Hill average calculated values (difference of 71 GPa or an error of 0.65 using Eq. 2.30) and more closely match the Voigt bound (difference of 46 GPa). Niinomi [40] pointed out that Young's moduli obtained from microhardness testing are higher than the polycrystalline Young's moduli value, thus our calculation results should be close to the polycrystalline E values. The present data show that the E decreases in value from 0 to 100 at.% Ti.

In the literature, no bcc Ti-Mo-Sn (Figure 6.8b) experimental E results were found to be compared with the present work. The Voigt-Reuss bounds and the Hill average are quite similar until around 65 at.% Ti when they begin to vary. The E values decrease from 0 to 100 at.% Ti. The calculated E results for the Ti-Mo-Ta alloy system (Figure 6.8c) are compared with experimental data reported by Niinomi et al. [40] and Mohammed et al. [39]. The E values reported by Niinomi et al. [40] were obtained using an ultrasonic measurement after the samples were

solution treated. Niinomi et al. [40] pointed out that the ultrasonic method obtained E values in between the tensile test and microhardness methodology and showed no large error in the experiments. The experimental E fit well with the present Voigt bound (difference of 9 GPa) and had an error of 0.46 (Eq. 2.30) from the Hill average (difference of 33 GPa). The E values decrease from 0 to 100 at.% Ti.

The Young's moduli of the Ti-Mo-Zr alloy system (Figure 6.8d) is compared with experimental values reported by Mohammed et al. [39]. The error in the experiments and methodology was not discussed. The experimental E [39] and the present E (Hill average) vary by less than 6 GPa and the E values decrease from 0 to 100 at.% Ti. Experimentally determined Young's moduli results from Niinomi et al. [40], Mohammed et al. [39], and Nozoe et al. [41] are compared with the present E calculations for the Ti-Nb-Sn alloy system (Figure 6.8e). The experimental E results reported by Niinomi et al. [40] were obtained through tensile testing of samples that were solution treated and cold rolled. Niinomi et al. showed that E results at this specific composition varied by 10 GPa. The E results reported by Niinomi et al. [40] and Mohammed et al. [39] differ from the Hill average by 9 and 15 GPa, respectively (an error of 0.28 using Eq. 2.30). The E results from Nozoe et al. [41] differ by 10, 32 and 78 GPa from the Voigt, Hill and Reuss results, respectively, and have an error of 0.56 (Eq. 2.30). However, Nozoe et al. reported that the samples formed the metastable omega phase. The ω phase is a metastable hexagonal phase (space group P6/mmm) with lattice parameters closely matching those of the bcc phase. Nozoe et al. [41] also discussed how the aging of the Ti-Mo-Sn samples greatly affected the E . So overall the calculations satisfactorily predicted the Young's moduli of the Ti-Mo-Nb, Ti-Mo-Sn, Ti-Mo-Ta, Ti-Mo-Zr and Ti-Nb-Sn systems.

Figure 6.9 continues to plot the E of the Ti-X-Y ternary alloy systems. The first-principles E , for the Ti-Nb-Ta system, are compared with experimentally determined E values reported by Mohammed et al. [39] (Figure [39]a). At this composition, the Voigt and Reuss bounds are very close to the Hill average. Thus, while the experimental E result fits closer to the Reuss bound (difference of 8 GPa), the experimental E result only varies by 15 and 21 GPa from the Hill and Voigt results, respectively and has an error of 0.28 (Eq. 2.30). Niinomi et al. [40] reported the E results of a different composition Ti-Nb-Ta alloy, Ti-29Nb-13Ta as opposed to Ti-25Nb-25Ta. Niinomi et al. [40] showed that the E determined experimentally

for the Ti-Nb-Ta alloy varies by approximately 40 GPa. The E decreases in value from 0 to 100 at.% Ti in the Ti-Nb-Ta ternary system.

The first-principles E results for the Ti-Nb-Zr (Figure 6.9b) system are compared with experimentally determined E results from Geetha et al. [38], Mohammed et al. [39], and Niinomi et al. [40]. The experimental E results reported by Niinomi et al. [40] are for the Ti-13Nb-13Zr and Ti-27Nb-8Zr alloys. The results for the Ti-13Nb-13Zr were obtained using both the ultrasonic and 3-point bending tests and varied by 50 GPa, while the Ti-27Nb-8Zr results were obtained using tensile testing and varied by 50 GPa. The experimentally determined E results varied from the present Voigt, Hill and Reuss results by an average of 9, 2, and 14 GPa, respectively and has an error of 0.08 (Eq. 6.9) from the Hill average. Overall, the E first increases in value from 0 to 70 at.% Ti and then decreases from 70 to 100 at.% Ti for the Ti-Nb-Zr system. The Ti-Sn-Ta, Ti-Sn-Zr and Ti-Ta-Zr alloy systems have experimental data to be compared with and our results are shown in Figure 6.9c, Figure 6.9d, and Figure 6.9e, respectively. For the Ti-Sn-Ta system, the E values decreases in value from 0 to 100 at.% Ti. The E values for the Ti-Sn-Zr system first increases from 0 to 60 at.% Ti and then decreases from 60 to 100 at.% Ti. The E values for the Ti-Ta-Zr system first decreases from 0 to 15 at.% Ti, where the values begin to increase from 15 to 30 at.% Ti and then decreases from 30 to 100 at.% Ti.

It can be seen that there is a large variation in the experimental data depending on the technique used to obtain the data. Also, the first-principles calculations and the CALPHAD fittings are done using data obtained at 0 °K while the experiments are obtained using polycrystalline samples at 300 °K. Considering these facts, the experimental values fit well within the bounds set by Reuss and Voigt, and the Hill average generally reproduces the experimentally determined E data for the Ti-X-Y ternary alloys.

Using the complete database with interaction parameters listed in Table 5.2 and 6.3, the elastic stiffness constants can be predicted and then the moduli values can be calculated and mapped. Figure 6.10 and Figure 6.11 uses the global minimization tools in pycalphad [42] to map the E based on composition for Ti-X-Y ternaries. The maps can point to regions with specific moduli values to be targeted. The pycalphad code used is in appendix E.

The B and G moduli calculated (circles) are plotted in Figure 6.12 to Figure

6.15 for each Ti-X-Y ($X \neq Y = \text{Mo, Nb, Sn, Ta, Zr}$) system starting from a 50-50 mixture of X and Y to Ti. The red dashed line is the Hill average interpolated from the binary interaction parameters shown in Table 5.2. The Hill average (black solid line), Voigt (purple dotted line), Reuss (gold dotted-dashed line) bounds are plotted using the binary and ternary interaction parameters (Table 5.2 and 6.3). The B values, for all the Ti-X-Y ternaries except Ti-Nb-Sn, Ti-Sn-Ta and Ti-Sn-Zr decreases from 0 to 100 at.% Ti, as shown in Figure 6.12 and Figure 6.13. The B values for the Ti-Nb-Sn and Ti-Sn-Ta systems first decrease from 0 to 10 at.% Ti and then increase from 10 to 55 at.% Ti and then decrease from 55 to 100 at.% Ti. For the Ti-Sn-Zr system, the B values first increase from 0 to 85 at.% Ti and then decreases from 85 to 100 at.% Ti. The G values decrease from 0 to 100 at.% Ti for all the ternary systems except Ti-Nb-Sn, Ti-Nb-Zr, Ti-Sn-Zr and Ti-Ta-Zr (Figure 6.14 and Figure 6.15). The G values increase from 0 to 60 at.% Ti and then decrease from 60 to 100 at.% Ti for the Ti-Nb-Sn, Ti-Nb-Zr systems. For the Ti-Sn-Zr system, the G values first increase from 0 to 55 at.% Ti and then decrease from 55 to 100 at.% Ti. The G values increase from 0 to 40 at.% Ti and then decrease from 40 to 100 at.% Ti for the Ti-Ta-Zr system.

Both the G and E are negative when they are close to Ti. This is due to the instability of the bcc phase close to Ti. As discussed by BornâŽs criteria, when $\overline{C}_{11}-\overline{C}_{12}$ is negative the bcc phase loses mechanical stability. The Voigt bound of G_v is expressed by:

$$G_v = (\overline{C}_{11} - \overline{C}_{12} + \overline{C}_{44}) / 5 \quad (6.1)$$

So, when $\overline{C}_{11}-\overline{C}_{12}$ it causes G to be negative. The E is then calculated from the B and G , so when G is negative it can cause E to be negative. This is one of the reasons that finding bcc Ti alloys close to the bcc stability will produce a low E .

6.3.2 Extrapolation to higher ordered systems

The pure element elastic results along with the binary and ternary interaction parameters are combined into a database file in appendix D. The E is predicted and compared with experimental results for higher order Ti alloys and the results are shown in Table 6.4 and Figure 6.16. The same comparison was made in chapter 5 (Table 5.4 and Figure 5.4), but those predictions were made without the ternary

interaction parameters. Figure 6.16 plots the calculated E (Hill average) versus the experimentally determined Young's moduli [37–39]. The black diagonal line would be a perfect correlation between the predictions and experiments. The grey region is the average variance in the first-principles calculations when calculating the average elastic stiffness constants using Eq. 2.18-Eq. 2.20 (3 GPa). The same higher order alloys were picked to compare the effect of introducing the ternary interaction parameters. As discussed previously, the error bars plotted for the experiments come from the variance that was seen when comparing the experimentally determined Young's moduli at the same composition from Niinomi et al. [40], Geetha et al. [38], Tane et al. [37], and Mohammed et al. [39]. The horizontal error bars are the Voigt and Reuss bounds. Previously, without ternary interaction parameters, the predictions and experimental results varied anywhere between 0.69 and 14 GPa and on average by 7 GPa. The calculations are usually larger than the experimental values due to the temperature difference: the computed single crystal elastic stiffness constants are at 0 °K, while the experiments on the polycrystalline samples are usually performed at 300 °K. As discussed, introducing ternary interaction parameters improves the database. The introduction of the ternary interaction parameters improved the predictions to vary anywhere from 0.39 to 13 GPa from the experimental values with an average variance of only 5 GPa. Thus, while the ternary interactions have small effects on the final results, the introduction of Ti-containing ternary interaction parameters still improves the predictions and the database is more accurate to predict the Young's modulus of higher order Ti alloys.

6.4 Conclusion

The present study systematically calculates the elastic properties of the bcc Ti ternary alloys, including the elastic stiffness constants, bulk modulus, shear modulus, and Young's modulus. Five alloying elements, Mo, Nb, Sn, Ta and Zr are studied. The general CALPHAD modeling approach is used to fit ternary interaction parameters. From the elastic stiffness constant data, the Ti-X-Y ($X \neq Y = Mo, Nb, Ta$) show the same trends in the data. This is to be expected because Mo, Nb, and Ta are similar elements that are strong β -stabilizers and stable in the bcc phase at low temperatures. It was also seen that the Ti-X-Sn ($X = Mo, Nb, Ta$)

alloys showed similar trends in the data for most of the elastic stiffness constants, so do the Ti-X-Zr (X = Mo, Nb, Ta) alloys. The present calculations showed that the bcc Ti-alloy was mechanically stabilized at compositions less than 91, 92, 95, 93, 91, 94, 87, 77, 89, and 80 at % Ti for the Ti-Mo-Nb, Ti-Mo-Ta, Ti-Mo-Zr, Ti-Nb-Zr, Ti-Sn-Zr, Ti-Ta-Zr, Ti-Mo-Sn, Ti-Nb-Sn, Ti-Nb-Ta and Ti-Sn-Ta alloys, respectively. As discussed above, Mo, Nb and Ta are strong β -stabilizers and thus the Ti-Mo-Nb, Ti-Mo-Ta, and Ti-Nb-Ta systems stabilize the bcc phase similarly. Also, discussed previously, Zr is a weak β -stabilizer alone but when alloyed with other elements it acts a strong β -stabilizer. This is observed with these results with the Ti-Mo-Zr, Ti-Nb-Zr, Ti-Ta-Zr systems all stabilizing the bcc phase at high Ti concentrations (95, 93, and 94 at.% respectively). Zr is even able to stabilize the Ti-Sn-Zr system at a high Ti concentration of 91 at.% Ti, even with Sn. Sn is not stable in the bcc phase and is not a β -stabilizer. So, when alloyed with Sn, a higher concentration of other alloying elements is needed to stabilize the bcc phase.

The pure element elastic results along with the binary and ternary interaction parameters are combined into a database file in appendix D. The database can be used to map possible alloy compositions to find potential materials with a Young's modulus in the target range for biomedical load-bearing implants using the pycalphd code in appendix e. Overall, the introduction of the ternary interaction parameters improved the database's ability to predict the E of higher order alloys by a small amount. The complete database, however, satisfactorily predicts the elastic properties of higher order Ti-alloys and will help guide future research to develop low-modulus biocompatible Ti alloys.

Table 6.1: First-principles calculations of the elastic stiffness constants

Reference	$Ti_{100-2b}X_bY_b$	\overline{C}_{11}	\overline{C}_{11}	\overline{C}_{11}
This work	Ti	93	115	41
This work	TiMo _{12.5} Nb _{12.5}	155	121 ±4	34 ±4
This work	TiMo _{25.0} Nb _{25.0}	222 ±3	129 ±3	33 ±3
This work	TiMo _{33.3} Nb _{33.3}	269 ±5	134 ±3	42 ±4
This work	Mo ₅₀ Nb ₅₀	414 ±6	165 ±3	68
This work	TiMo _{12.5} Sn _{12.5}	137 ±15	121 ±2	56 ±13
This work	TiMo _{25.0} Sn _{25.0}	160 ±3	130 ±8	71 ±2
This work	TiMo _{33.3} Sn _{33.3}	167 ±8	133 ±6	75 ±2
This work	Mo ₅₀ Sn ₅₀	192 ±28	130 ±36	40 ±31
This work	TiMo _{12.5} Ta _{12.5}	153 ±1	125 ±4	38 ±3
This work	TiMo _{25.0} Ta _{25.0}	222 ±2	136 ±1	45 ±3
This work	TiMo _{33.3} Ta _{33.3}	263 ±4	145 ±6	49 ±4
This work	Mo ₅₀ Ta ₅₀	370 ±13	163 ±4	63 ±4
This work	TiMo _{12.5} Zr _{12.5}	125 ±1	109 ±8	35 ±1
This work	TiMo _{25.0} Zr _{25.0}	160 ±1	116 ±5	34 ±2
This work	TiMo _{33.3} Zr _{33.3}	182 ±1	116 ±2	31 ±8
This work	Mo ₅₀ Zr ₅₀	231 ±7	118 ±5	33 ±8
This work	TiNb _{12.5} Sn _{12.5}	115 ±4	118 ±3	55
This work	TiNb _{25.0} Sn _{25.0}	131 ±9	121 ±6	64 ±3
This work	TiNb _{33.3} Sn _{33.3}	134 ±2	122 ±3	67 ±6
This work	Nb ₅₀ Sn ₅₀	132 ±4	118 ±8	56 ±4
This work	TiNb _{12.5} Ta _{12.5}	130 ±3	124 ±4	37 ±3
This work	TiNb _{25.0} Ta _{25.0}	182 ±1	129 ±4	43 ±6
This work	33.3Ta _{33.3}	208	135 ±1	44 ±1
This work	Nb ₅₀ Ta ₅₀	260 ±2	148 ±3	47 ±3
This work	TiNb _{12.5} Zr _{12.5}	101 ±2	113 ±4	32 ±3
This work	TiNb _{25.0} Zr _{25.0}	122 ±1	113 ±3	28 ±3
This work	TiNb _{33.3} Zr _{33.3}	143 ±2	107 ±5	28 ±3
This work	Nb ₅₀ Zr ₅₀	154 ±5	110 ±3	15 ±2
This work	TiSn _{12.5} Ta _{12.5}	115 ±6	121 ±4	60 ±2
This work	TiSn _{25.0} Ta _{25.0}	138 ±13	125 ±4	75 ±4

Table 6.1: First-principles calculations of the elastic stiffness constants

Reference	$\text{Ti}_{100-2b}\text{X}_b\text{Y}_b$	\overline{C}_{11}	\overline{C}_{11}	\overline{C}_{11}
This work	$\text{TiSn}_{33.3}\text{Ta}_{33.3}$	138 ± 6	131 ± 8	78 ± 1
This work	$\text{Sn}_{50}\text{Ta}_{50}$	133 ± 8	130 ± 4	60 ± 4
This work	$\text{TiSn}_{12.5}\text{Zr}_{12.5}$	97 ± 5	111 ± 4	55 ± 2
This work	$\text{TiSn}_{25.0}\text{Zr}_{25.0}$	99 ± 12	103 ± 4	59 ± 7
This work	$\text{TiSn}_{33.3}\text{Zr}_{33.3}$	96 ± 7	98 ± 3	55 ± 3
This work	$\text{Sn}_{50}\text{Zr}_{50}$	85 ± 7	87 ± 9	42 ± 3
This work	$\text{TiTa}_{12.5}\text{Zr}_{12.5}$	136 ± 36	103 ± 21	44 ± 5
This work	$\text{TiTa}_{25.0}\text{Zr}_{25.0}$	130 ± 3	117 ± 4	42 ± 7
This work	$\text{TiTa}_{33.3}\text{Zr}_{33.3}$	148 ± 1	115 ± 2	44 ± 2
This work	$\text{Ta}_{50}\text{Zr}_{50}$	157 ± 2	123 ± 3	35 ± 3

Table 6.2: First-principles calculations of the bulk modulus B , shear modulus G , and Young's modulus E in GPa for different atomic percent compositions of the bcc Ti-X-Y ternary systems at 0 °K as well as experimental data obtained for the Young's modulus at 300 °K by the references stated.

Reference	$\text{Ti}_{100-2b}\text{X}_b\text{Y}_b$	B	G	E
This work	Ti	108	-12.91	-40.34
This work	$\text{TiMo}_{12.5}\text{Nb}_{12.5}$	132 ± 4	26 ± 4	73 ± 4
This work	$\text{TiMo}_{25.0}\text{Nb}_{25.0}$	160 ± 3	38 ± 3	105 ± 3
This work	$\text{TiMo}_{33.3}\text{Nb}_{33.3}$	179 ± 5	51 ± 5	139 ± 5
This work	$\text{Mo}_{50}\text{Nb}_{50}$	248 ± 6	87 ± 6	233 ± 6
Expt 300 K [40]	TiMo_6Nb_2			110
This work	$\text{TiMo}_{12.5}\text{Sn}_{12.5}$	126 ± 15	27 ± 15	75 ± 15
This work	$\text{TiMo}_{25.0}\text{Sn}_{25.0}$	140 ± 8	39 ± 8	106 ± 8
This work	$\text{TiMo}_{33.3}\text{Sn}_{33.3}$	144 ± 8	42 ± 8	114 ± 8
This work	$\text{Mo}_{50}\text{Sn}_{50}$	151 ± 36	36 ± 36	100 ± 36
This work	$\text{TiMo}_{12.5}\text{Ta}_{12.5}$	134 ± 4	25 ± 4	72 ± 4
This work	$\text{TiMo}_{25.0}\text{Ta}_{25.0}$	165 ± 2	44 ± 3	122 ± 3
This work	$\text{TiMo}_{33.3}\text{Ta}_{33.3}$	184 ± 6	53 ± 6	$145 \pm$
This work	$\text{Mo}_{50}\text{Ta}_{50}$	232 ± 13	77 ± 13	208 ± 13
Expt 300 K [39]	TiMo_7Ta_1			74
Expt 300 K [40]	TiMo_7Ta_1			74
This work	$\text{TiMo}_{12.5}\text{Zr}_{12.5}$	114 ± 8	20 ± 8	55 ± 8
This work	$\text{TiMo}_{25.0}\text{Zr}_{25.0}$	131 ± 5	29 ± 5	80 ± 5
This work	$\text{TiMo}_{33.3}\text{Zr}_{33.3}$	138 ± 2	32 ± 8	89 ± 8
This work	$\text{Mo}_{50}\text{Zr}_{50}$	156 ± 7	41 ± 8	113 ± 8
Expt 300 K [39]	TiMo_7Zr_3			64
This work	$\text{TiNb}_{12.5}\text{Sn}_{12.5}$	117 ± 4	14 ± 4	41 ± 4
This work	$\text{TiNb}_{25.0}\text{Sn}_{25.0}$	124 ± 9	26 ± 9	72 ± 9
This work	$\text{TiNb}_{33.3}\text{Sn}_{33.3}$	126 ± 6	28 ± 6	78 ± 6
This work	$\text{Nb}_{50}\text{Sn}_{50}$	123 ± 8	26 ± 8	72 ± 8
Expt 300 K [39]	$\text{TiNb}_{22}\text{Sn}_2$			44
Expt 300 K [40]	$\text{TiNb}_{22}\text{Sn}_2$			50
Expt 300 K [41]	TiNb_9Sn_3			58

Table 6.2: First-principles calculations of the bulk modulus B , shear modulus G , and Young's modulus E in GPa for different atomic percent compositions of the bcc Ti-X-Y ternary systems at 0 °K as well as experimental data obtained for the Young's modulus at 300 °K by the references stated.

Reference	$\text{Ti}_{100-2b}\text{X}_b\text{Y}_b$	B	G	E
This work	$\text{TiNb}_{12.5}\text{Ta}_{12.5}$	126 ±4	15 ±4	43 ±4
This work	$\text{TiNb}_{25.0}\text{Ta}_{25.0}$	147 ±6	35 ±6	98 ±6
This work	$_{33.3}\text{Ta}_{33.3}$	159 ±1	41 ±1	113 ±1
This work	$\text{Nb}_{50}\text{Ta}_{50}$	185 ±3	50 ±3	140 ±3
Expt 300 K [39]	$\text{TiNb}_{10}\text{Ta}_{19}$			55
This work	$\text{TiNb}_{12.5}\text{Zr}_{12.5}$	109 ±4	-2 ±4	-6 ±4
This work	$\text{TiNb}_{25.0}\text{Zr}_{25.0}$	116 ±3	14 ±3	40 ±3
This work	$\text{TiNb}_{33.3}\text{Zr}_{33.3}$	119 ±5	23 ±5	66 ±5
This work	$\text{Nb}_{50}\text{Zr}_{50}$	125 ±5	17 ±5	50 ±5
Expt 300 K [39]	TiNb_8Zr_8			77
Expt 300 K [39]	$\text{TiNb}_{12}\text{Zr}_9$			14
Expt 300 K [39]	$\text{TiNb}_{11}\text{Zr}_3$			50
Expt 300 K [40]	$\text{TiNb}_{17}\text{Zr}_5$			78
Expt 300 K [38]	TiNb_8Zr_8			81
This work	$\text{TiSn}_{12.5}\text{Ta}_{12.5}$	119 ±6	13 ±6	39 ±6
This work	$\text{TiSn}_{25.0}\text{Ta}_{25.0}$	129 ±13	31 ±13	86 ±13
This work	$\text{TiSn}_{33.3}\text{Ta}_{33.3}$	133 ±8	28 ±8	79 ±8
This work	$\text{Sn}_{50}\text{Ta}_{50}$	131 ±8	20 ±8	57 ±8
This work	$\text{TiSn}_{12.5}\text{Zr}_{12.5}$	106 ±5	4 ±5	13 ±5
This work	$\text{TiSn}_{25.0}\text{Zr}_{25.0}$	102 ±12	15 ±12	42 ±12
This work	$\text{TiSn}_{33.3}\text{Zr}_{33.3}$	97 ±7	15 ±7	43 ±7
This work	$\text{Sn}_{50}\text{Zr}_{50}$	86 ±9	11 ±9	32 ±9
This work	$\text{TiTa}_{12.5}\text{Zr}_{12.5}$	114 ±21	30 ±21	82 ±21
This work	$\text{TiTa}_{25.0}\text{Zr}_{25.0}$	121 ±4	20 ±7	58 ±7
This work	$\text{TiTa}_{33.3}\text{Zr}_{33.3}$	126 ±2	30 ±2	83 ±2
This work	$\text{Ta}_{50}\text{Zr}_{50}$	134 ±3	26 ±3	74 ±3

Table 6.3. Evaluated interactions parameters (L_2 , Eq. 2.30) for the elastic stiffness constants of the Ti-containing ternary alloys.

Alloy	Interaction Parameter	\bar{C}_{11}	\bar{C}_{12}	\bar{C}_{44}
Ti-Mo-Nb	L_2	-29.97	13.97	9.72
Ti-Mo-Sn	L_2	-83.85	31.80	74.73
Ti-Mo-Ta	L_2	-106.53	-12.35	5.27
Ti-Mo-Zr	L_2	-245.27	50.43	-44.96
Ti-Nb-Sn	L_2	-41.52	25.52	67.85
Ti-Nb-Ta	L_2	-93.77	-15.80	4.25
Ti-Nb-Zr	L_2	-220.35	72.10	-55.29
Ti-Sn-Ta	L_2	-95.39	-10.94	67.85
Ti-Sn-Zr	L_2	-155.34	68.86	3.85
Ti-Ta-Zr	L_2	-149.67	-8.91	-23.70

Table 6.4. Predicted Young's moduli (E) (in GPa) of higher order alloys using the binary and ternary interaction parameters in the bcc phase compared to the predicted Young's moduli (E_{BIN}) using just the binary interaction parameters and the experimental values found with both the weight percent and atomic percent listed.

Alloy Name (%wt)	at %	Calc E_{BIN}	Calc E	Expt E
Ti-35Nb-7Zr-5Ta [38]	Ti-24Nb-5Zr-2Ta	81	78	80
Ti-29Nb-13Ta-4.6Zr [38]	Ti-20Nb-5Ta-3Zr	76	73	75
Ti-29Nb-13Ta-6Sn [38]	Ti-21Nb-5Ta-3Sn	68	68	74
Ti-29Nb-13Ta-4.6Sn [38]	Ti-20Nb-5Ta-3Sn	67	66	66
Ti-29Nb-13Ta-4.5Zr [38]	Ti-20Nb-5Ta-3Zr	76	73	65
Ti-29Nb-13Ta-4.6Zr [37]	Ti-21Nb-5Ta-3Zr	76	75	64
Ti-30Nb-10Ta-5Zr [37]	Ti-23Nb-4Ta-3Zr	77	74	64
Ti-35Nb-10Ta-5Zr [37]	Ti-25Nb-4Ta-4Zr	80	78	65
Ti-24Nb-4Zr-7.9Sn [39]	Ti-15Nb-3Zr-4Sn	65	62	54
Ti-35Nb-2Ta-3Zr [39]	Ti-23Nb-1Ta-2Zr	69	68	61
Ti-29Nb-11Ta-5Zr [39]	Ti-20Nb-6Ta-2Zr	74	72	60
Ti-10Zr-5Ta-5Nb [39]	Ti-6Zr-1Ta-3Nb	64	62	52
Ti-29Nb-13Ta-2Sn [39]	Ti-20Nb-5Ta-1Sn	66	65	62

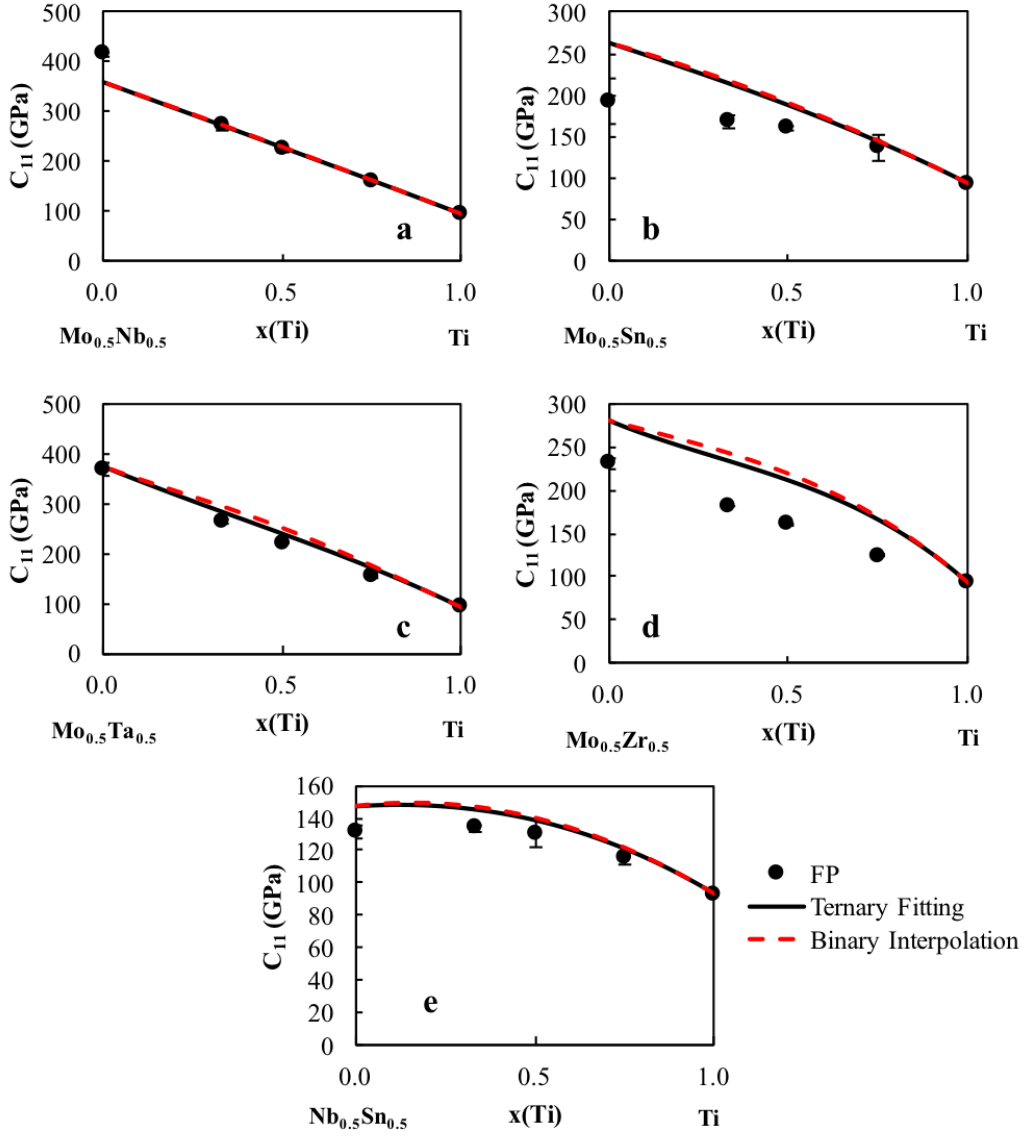


Figure 6.1. Calculated \bar{C}_{11} values (circles) plotted with their errors as well as the interpolation from the binary interaction parameters (red dashed line) and the ternary fitting (black dashed line) for five of the Ti-X-Y binary systems from a 50-50 mixture of the alloying elements X and Y to Ti ($X \neq Y = \text{Mo}, \text{Nb}, \text{Ta}, \text{Sn}, \text{Zr}$).

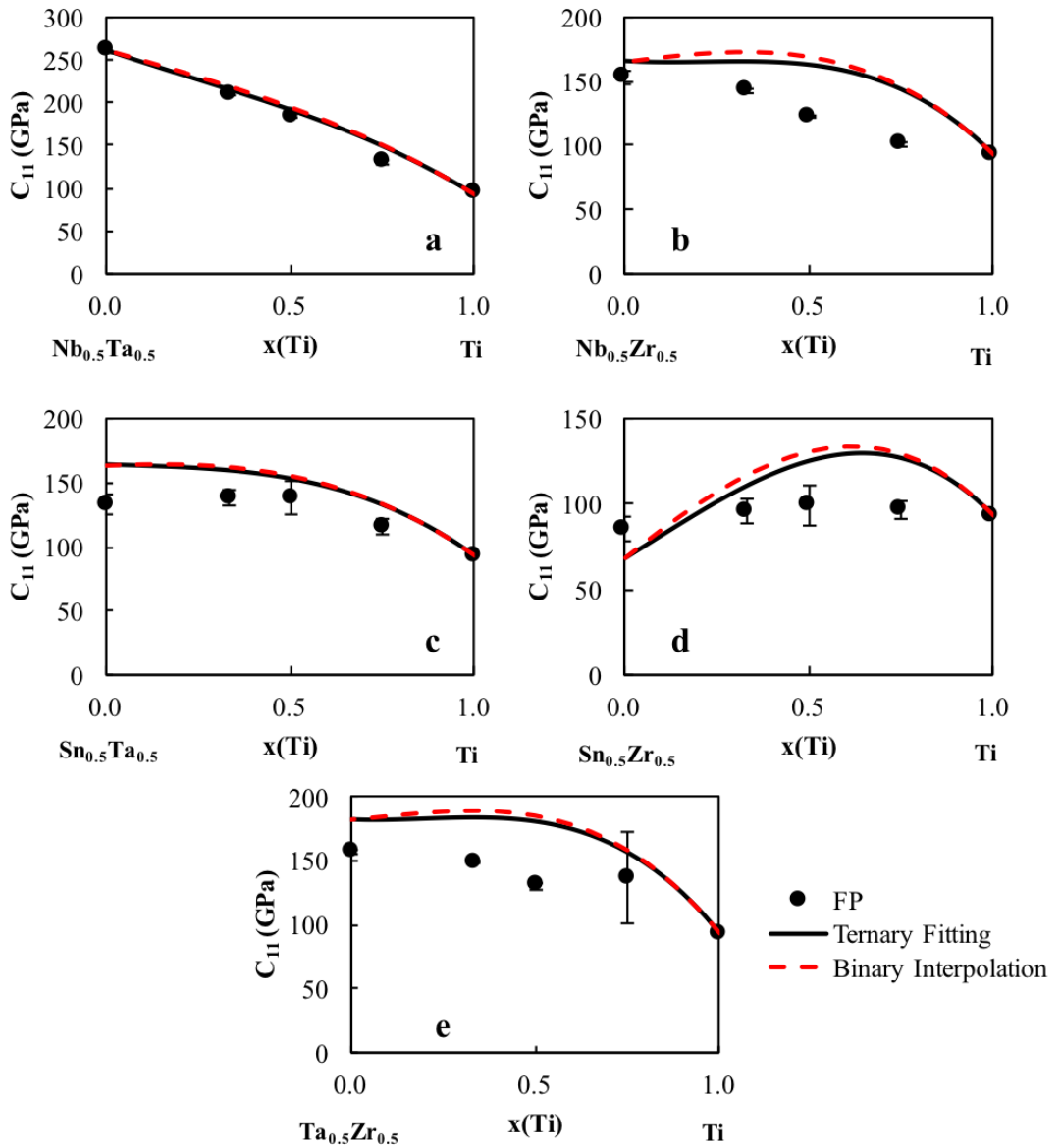


Figure 6.2. Calculated \bar{C}_{11} values (circles) plotted with their errors as well as the interpolation from the binary interaction parameters (red dashed line) and the ternary fitting (black dashed line) for five of the Ti-X-Y binary systems from a 50-50 mixture of the alloying elements X and Y to Ti ($X \neq Y = \text{Mo, Nb, Ta, Sn, Zr}$).

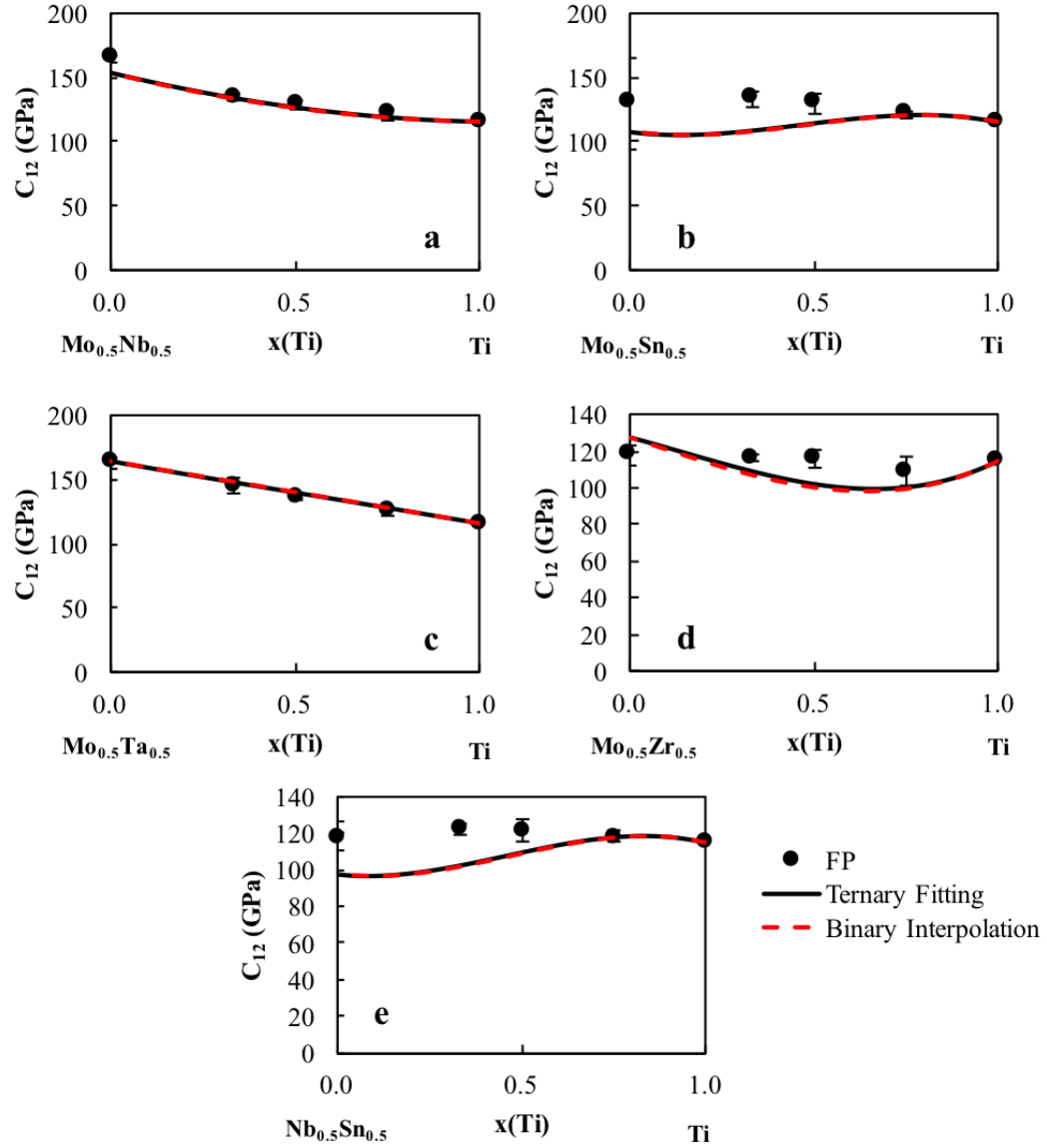


Figure 6.3. Calculated \bar{C}_{12} values (circles) plotted with their errors as well as the interpolation from the binary interaction parameters (red dashed line) and the ternary fitting (black dashed line) for five of the Ti-X-Y binary systems from a 50-50 mixture of the alloying elements X and Y to Ti ($X \neq Y = \text{Mo}, \text{Nb}, \text{Ta}, \text{Sn}, \text{Zr}$).

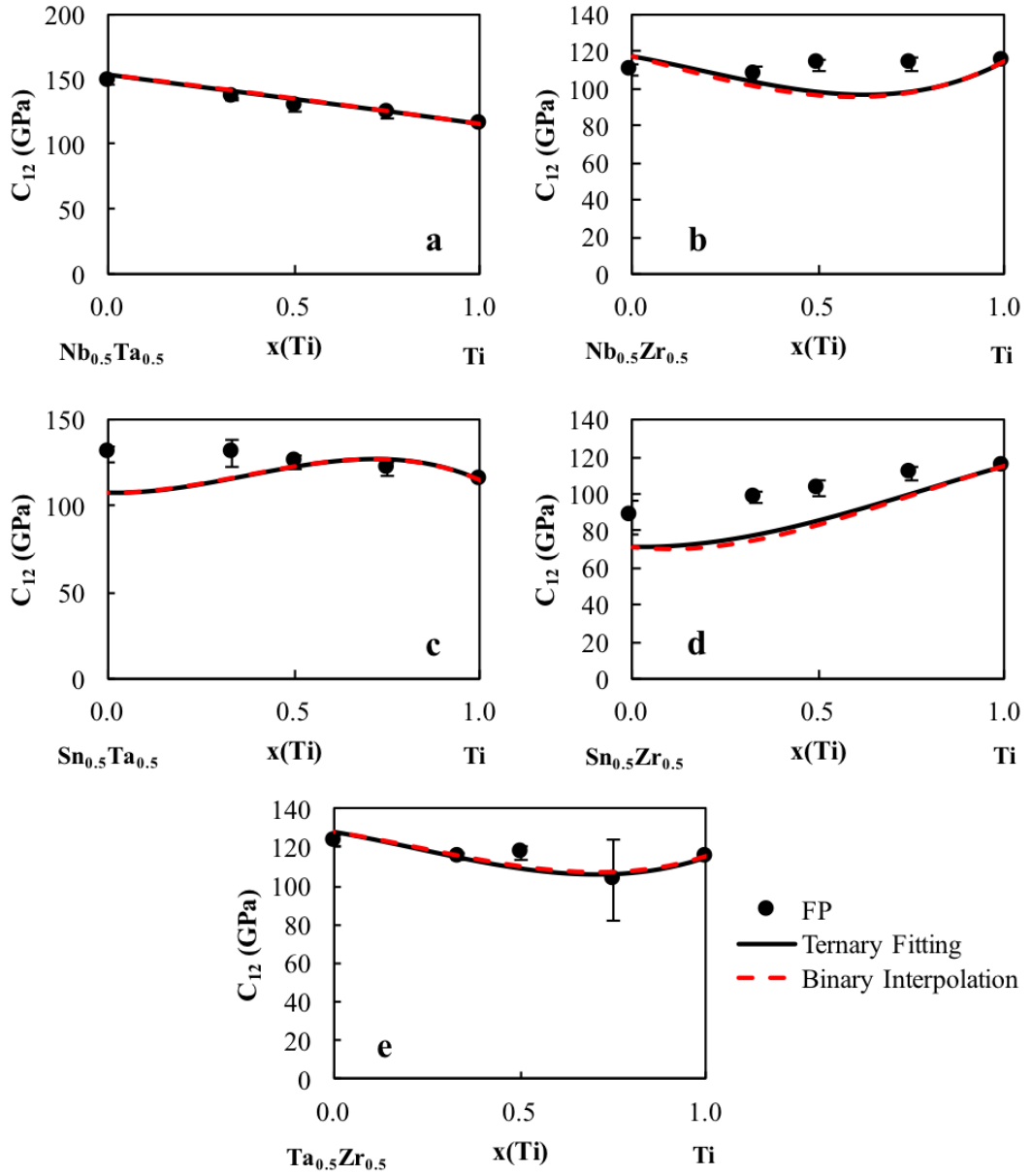


Figure 6.4. Calculated \bar{C}_{12} values (circles) plotted with their errors as well as the interpolation from the binary interaction parameters (red dashed line) and the ternary fitting (black dashed line) for five of the Ti-X-Y binary systems from a 50-50 mixture of the alloying elements X and Y to Ti ($X \neq Y = \text{Mo, Nb, Ta, Sn, Zr}$).

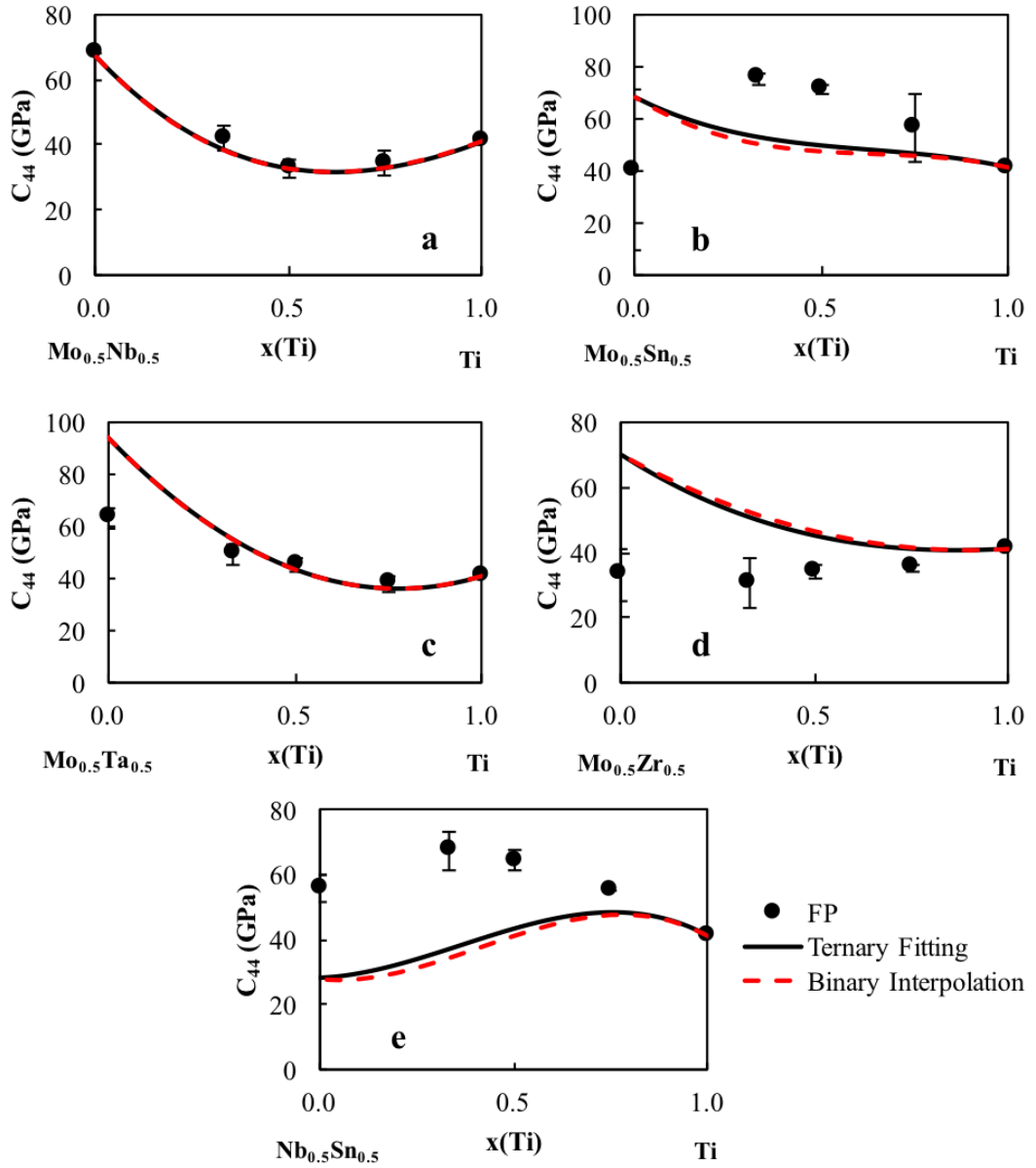


Figure 6.5. Calculated \bar{C}_{44} values (circles) plotted with their errors as well as the interpolation from the binary interaction parameters (red dashed line) and the ternary fitting (black dashed line) for five of the Ti-X-Y binary systems from a 50-50 mixture of the alloying elements X and Y to Ti ($X \neq Y = \text{Mo}, \text{Nb}, \text{Ta}, \text{Sn}, \text{Zr}$).

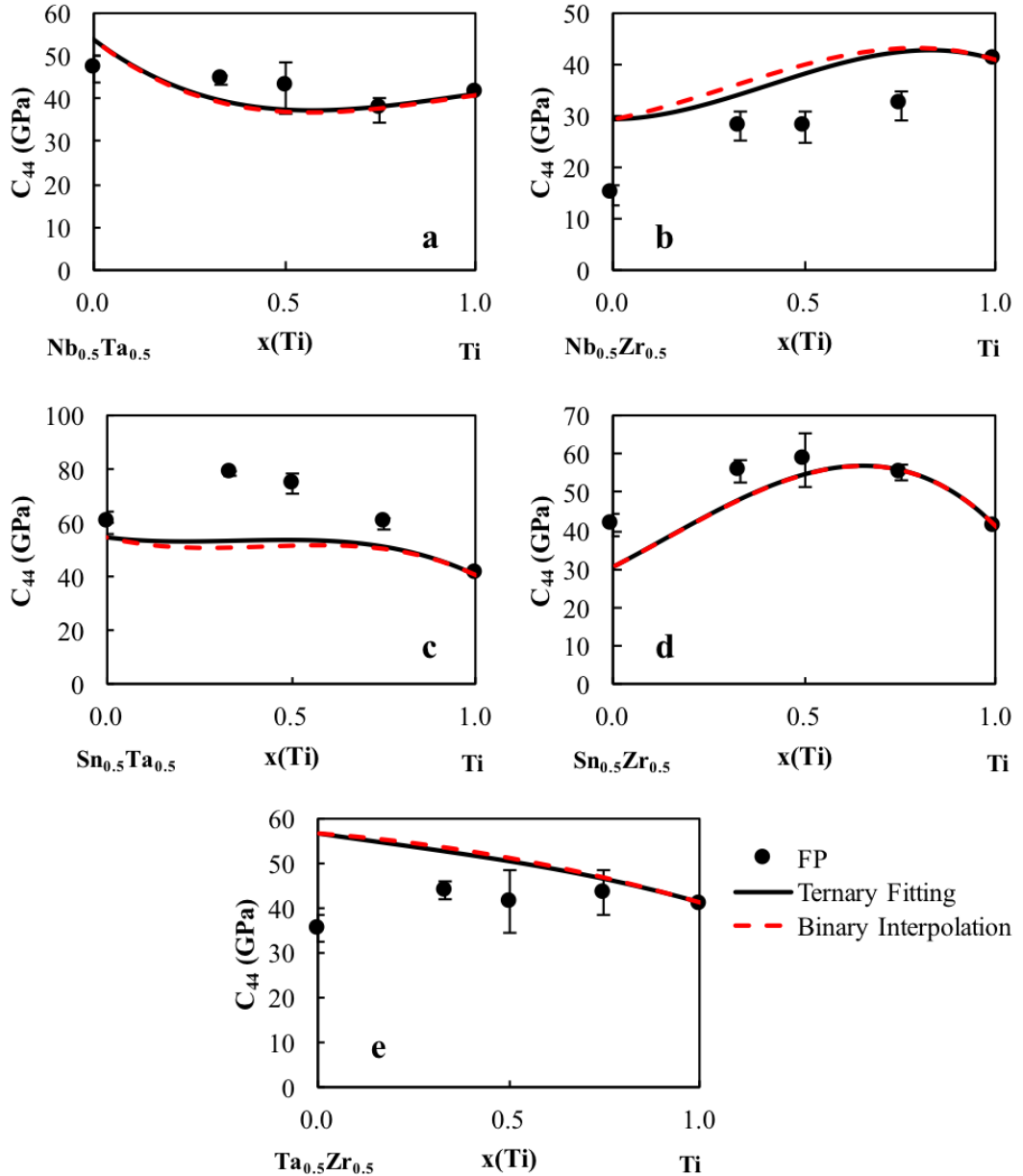


Figure 6.6. Calculated \bar{C}_{44} values (circles) plotted with their errors as well as the interpolation from the binary interaction parameters (red dashed line) and the ternary fitting (black dashed line) for five of the Ti-X-Y binary systems from a 50-50 mixture of the alloying elements X and Y to Ti ($X \neq Y = \text{Mo, Nb, Ta, Sn, Zr}$).

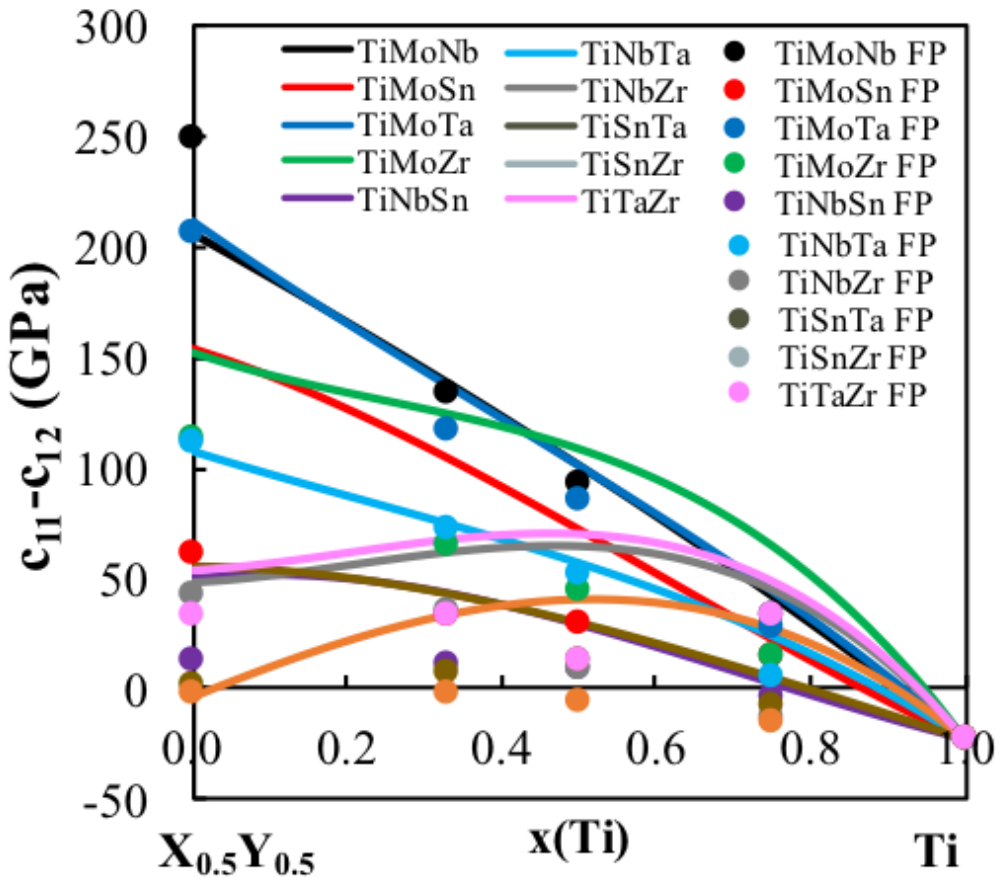


Figure 6.7. Calculated $\bar{C}_{11}-\bar{C}_{12}$ values (circles) plotted with the present modeling (solid lines) for the Ti-X-Y ternary systems ($X \neq Y = \text{Mo, Nb, Ta, Sn, Zr}$). The $\bar{C}_{11}-\bar{C}_{12}$ shows the stability of the bcc phase, when the value is negative the bcc phase is not stable in the corresponding composition ranges.

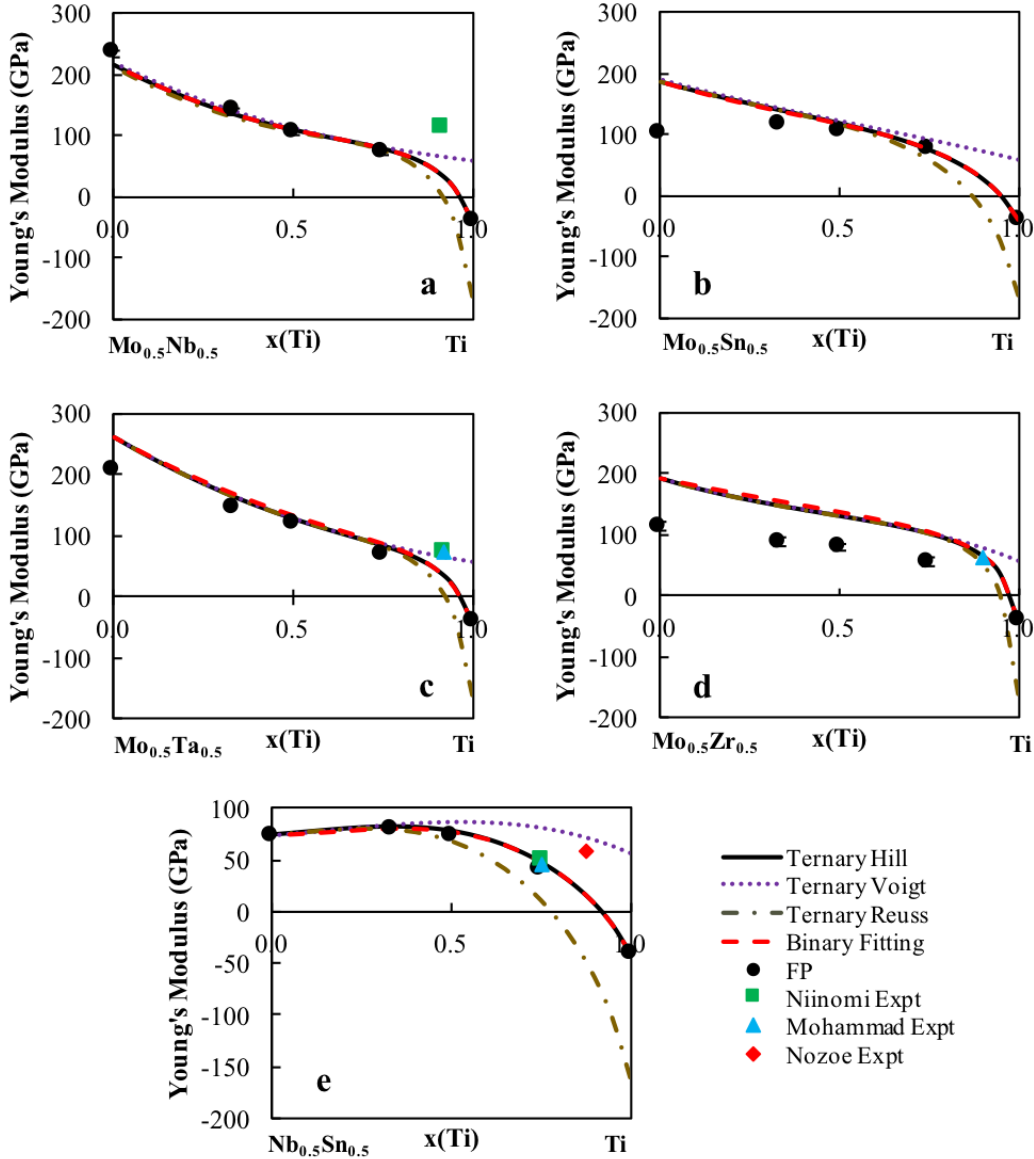


Figure 6.8. E of five of the Ti-X-Y ternary systems are plotted from a 50-50 mixture of the alloying elements to Ti in the bcc phase. The present calculations are plotted as filled circles with the error bars. The red dotted line is the extrapolation for the pure elements and binary interaction parameters only. The dotted purple line is the Voigt upper E bound, the gold dot dashed line is the lower Reuss E bound and the black line is the Hill E average. Experimental values are include for comparison [38–41].

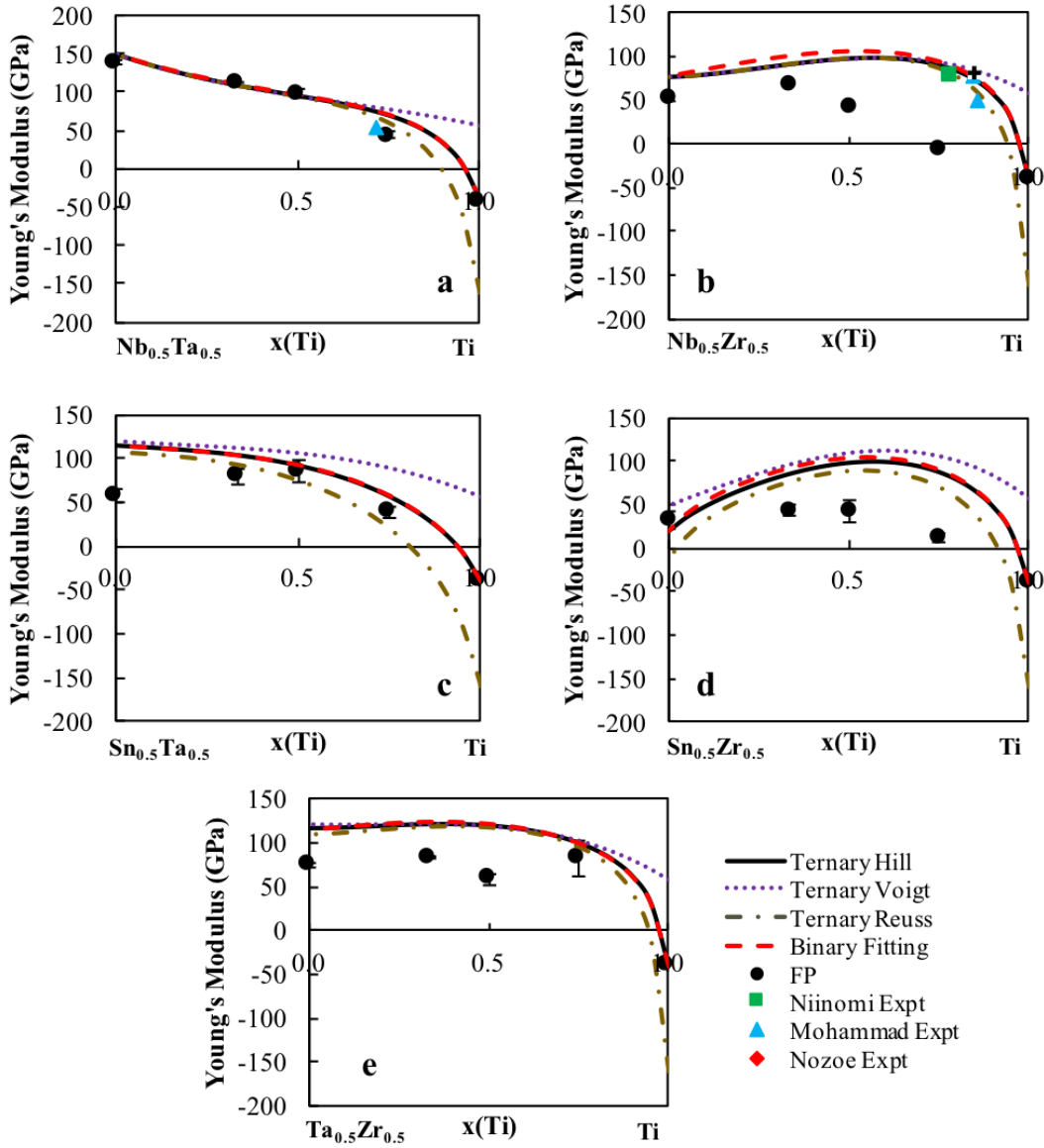


Figure 6.9. E of five of the Ti-X-Y ternary systems are plotted from a 50-50 mixture of the alloying elements to Ti in the bcc phase. The present calculations are plotted as filled circles with the error bars. The red dotted line is the extrapolation for the pure elements and binary interaction parameters only. The dotted purple line is the Voigt upper E bound, the gold dot dashed line is the lower Reuss E bound and the black line is the Hill E average. Experimental values are include for comparison [38–41].

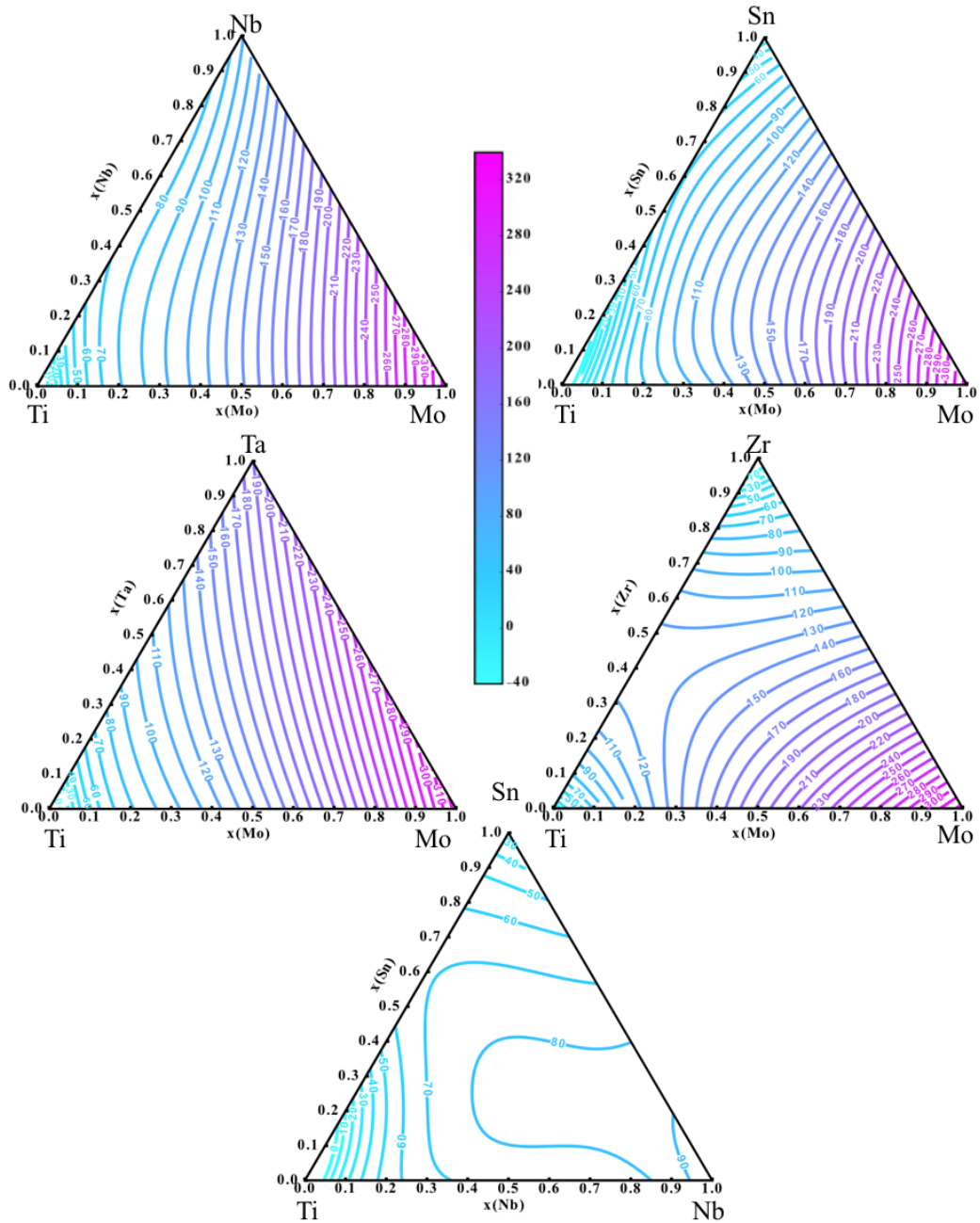


Figure 6.10. The Young's modulus is mapped as a function of composition in GPa for the Ti-Mo-Nb, Ti-Mo-Sn, Ti-Mo-Ta, Ti-Mo-Zr and Ti-Nb-Sn alloy systems using pycalphad [42].

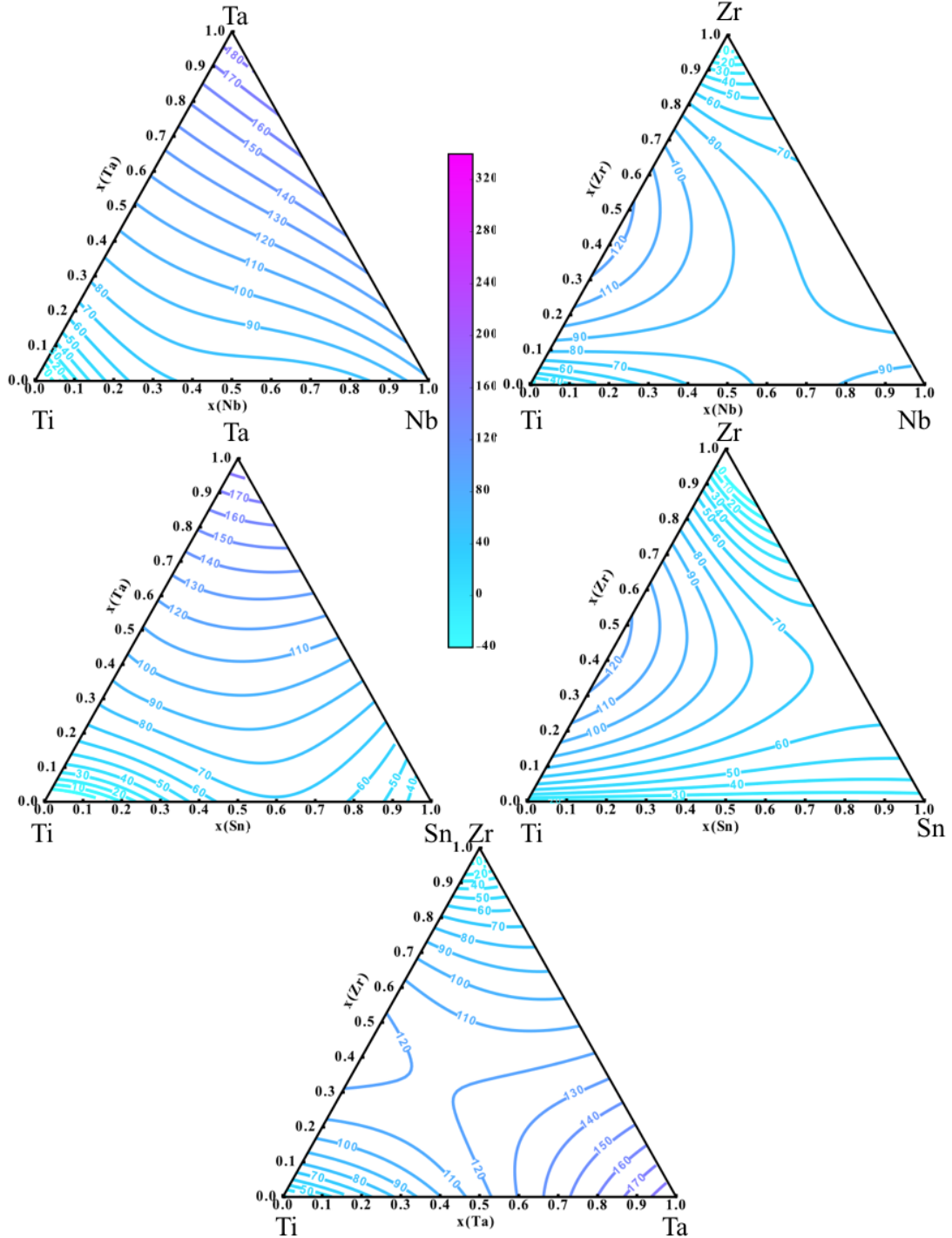


Figure 6.11. The Young's modulus is mapped as a function of composition in GPa for the Ti-Mo-Nb, Ti-Mo-Sn, Ti-Mo-Ta, Ti-Mo-Zr and Ti-Nb-Sn alloy systems using pycalphad [42].

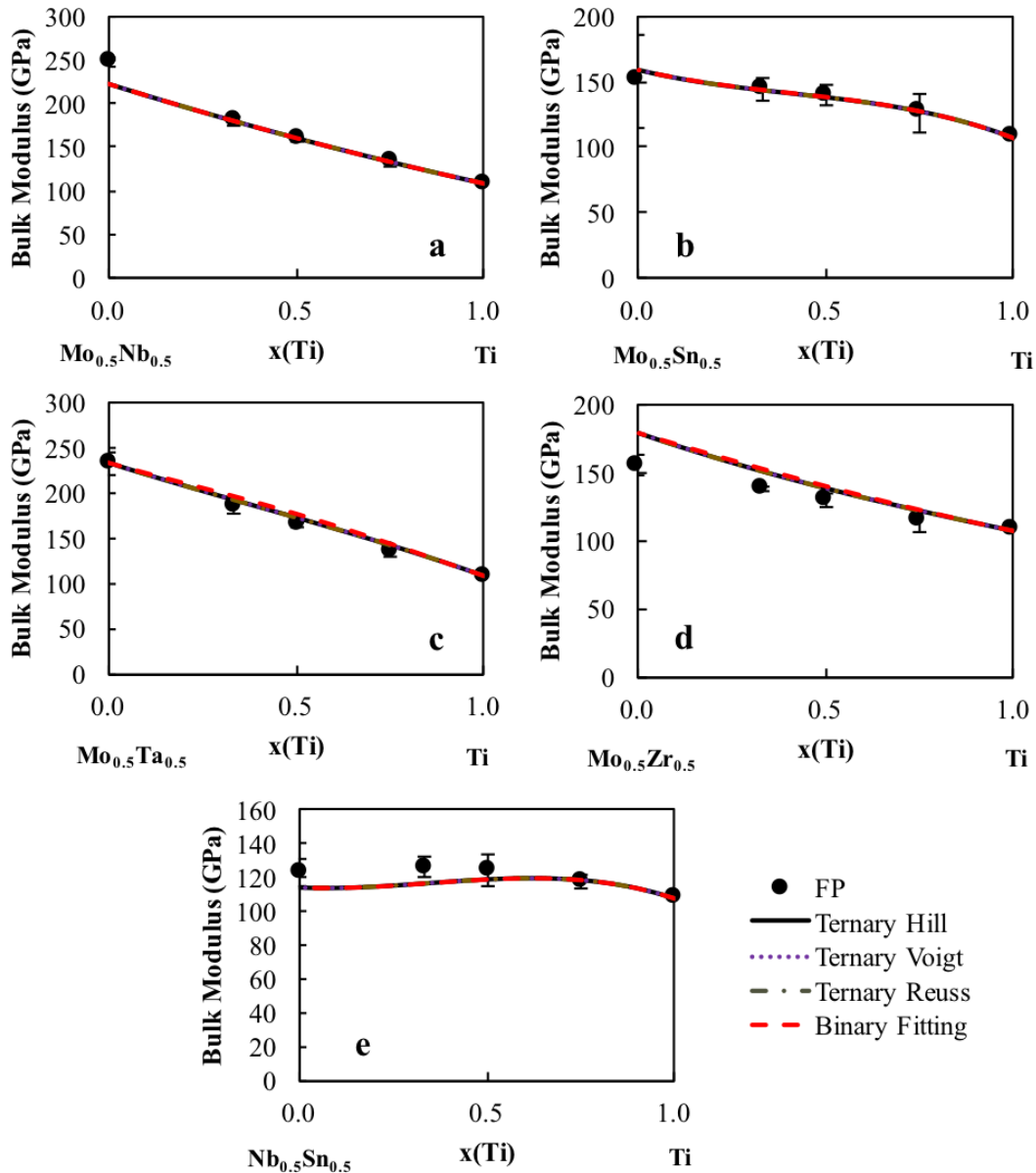


Figure 6.12. B calculations of five of the Ti-X-Y ternary systems ($X \neq Y = \text{Mo, Nb, Ta, Sn, Zr}$). The present calculations are plotted as the filled circles with error bars as well as the interpolation from the binary interaction parameters (red dashed line). The dotted purple line is the Voigt upper bulk modulus bound, the gold dashed line is the lower Reuss bulk modulus bound and the black line is the Hill bulk modulus average plotted from a 50-50 mixture of the alloying elements X and Y to Ti.

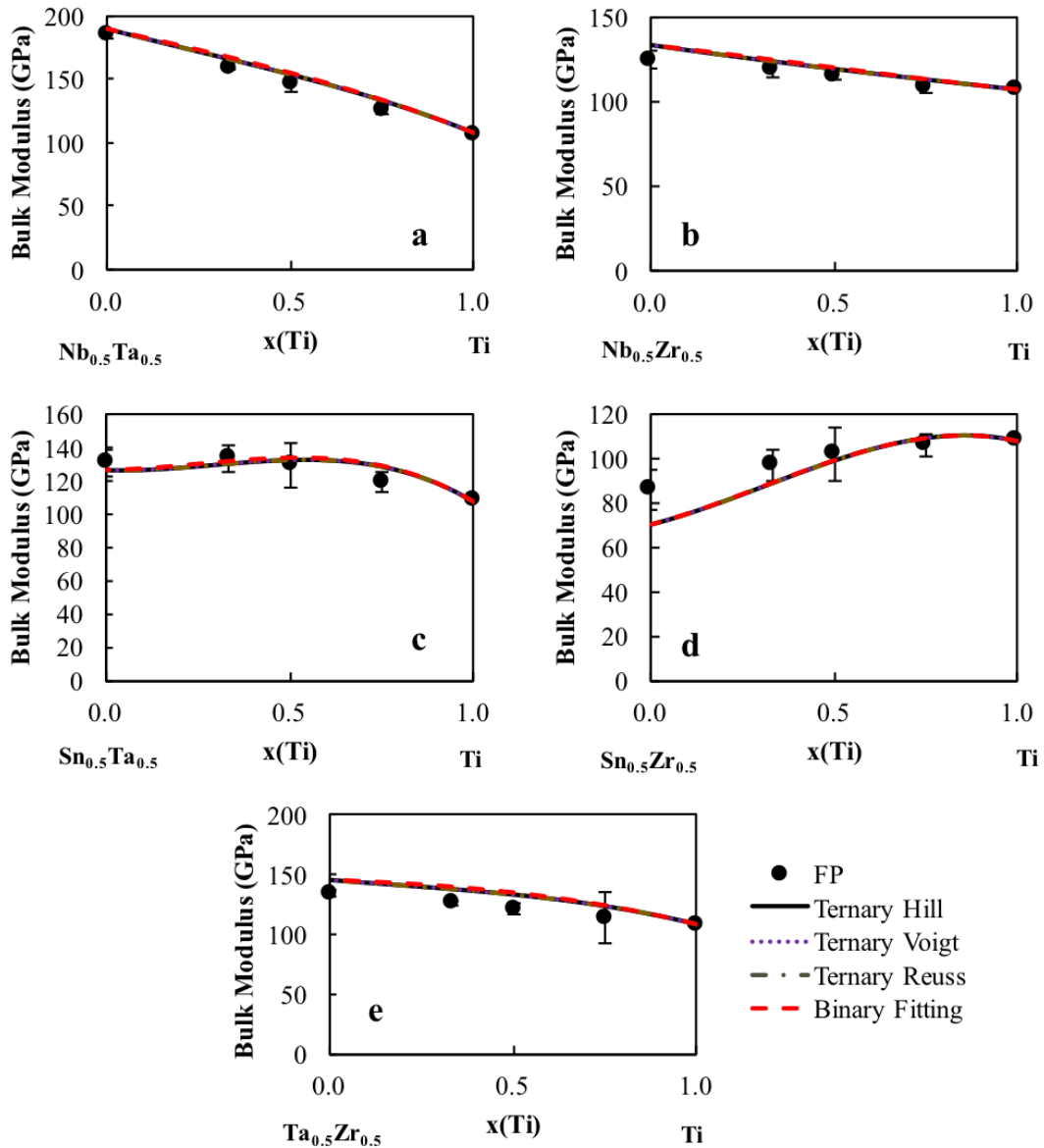


Figure 6.13. B calculations of five of the Ti-X-Y ternary systems ($X \neq Y = \text{Mo, Nb, Ta, Sn, Zr}$). The present calculations are plotted as the filled circles with error bars as well as the interpolation from the binary interaction parameters (red dashed line). The dotted purple line is the Voigt upper bulk modulus bound, the gold dashed line is the lower Reuss bulk modulus bound and the black line is the Hill bulk modulus average plotted from a 50-50 mixture of the alloying elements X and Y to Ti.

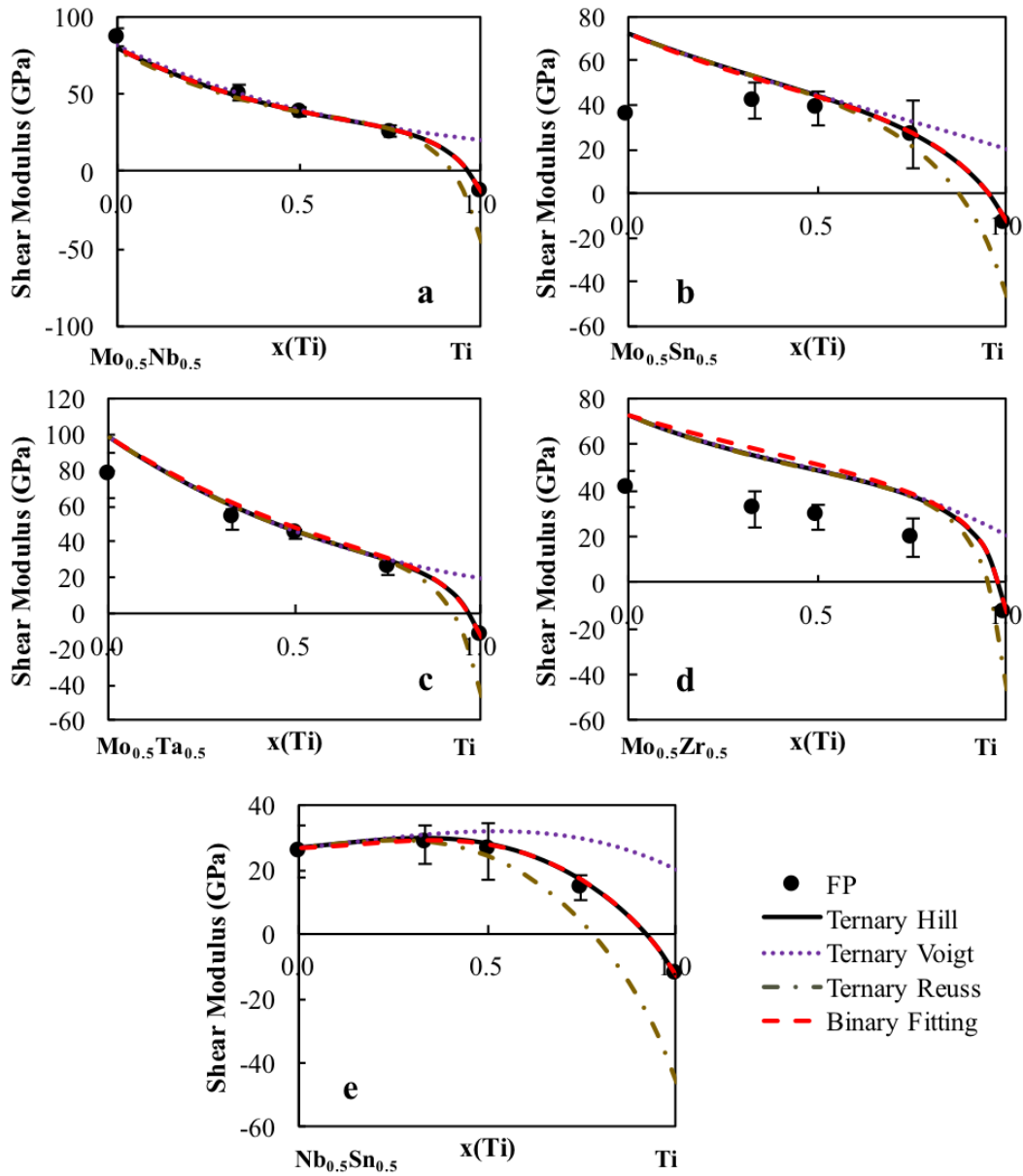


Figure 6.14. G calculations of five of the Ti-X-Y ternary systems ($X \neq Y = \text{Mo}, \text{Nb}, \text{Ta}, \text{Sn}, \text{Zr}$). The present calculations are plotted as the filled circles with error bars as well as the interpolation from the binary interaction parameters (red dashed line). The dotted purple line is the Voigt upper shear modulus bound, the gold dashed line is the lower Reuss shear modulus bound and the black line is the Hill shear modulus average plotted from a 50-50 mixture of the alloying elements X and Y to Ti.

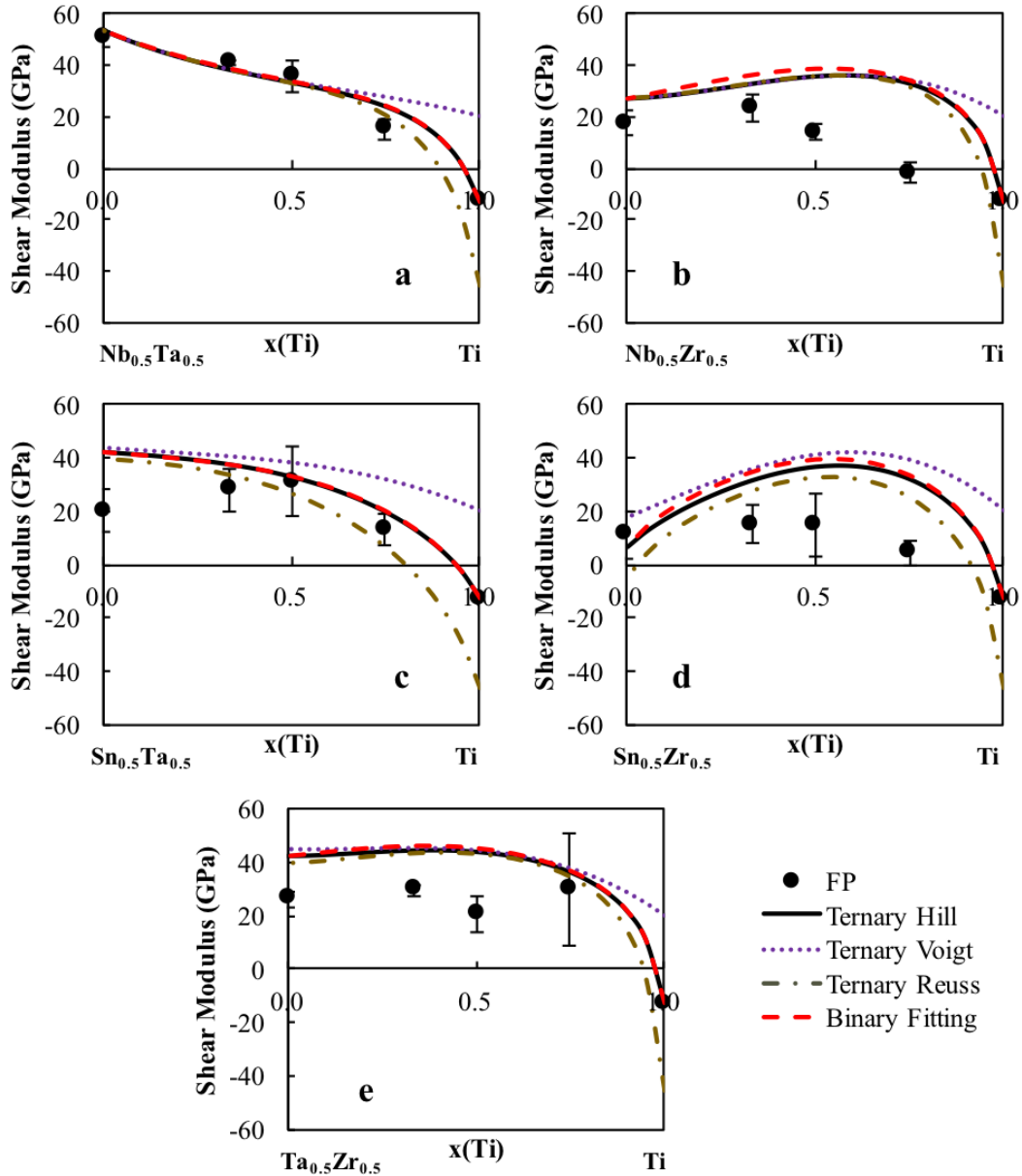


Figure 6.15. G calculations of five of the $\text{Ti}-\text{X}-\text{Y}$ ternary systems ($\text{X} \neq \text{Y} = \text{Mo, Nb, Ta, Sn, Zr}$). The present calculations are plotted as the filled circles with error bars as well as the interpolation from the binary interaction parameters (red dashed line). The dotted purple line is the Voigt upper shear modulus bound, the gold dashed line is the lower Reuss shear modulus bound and the black line is the Hill shear modulus average plotted from a 50-50 mixture of the alloying elements X and Y to Ti .

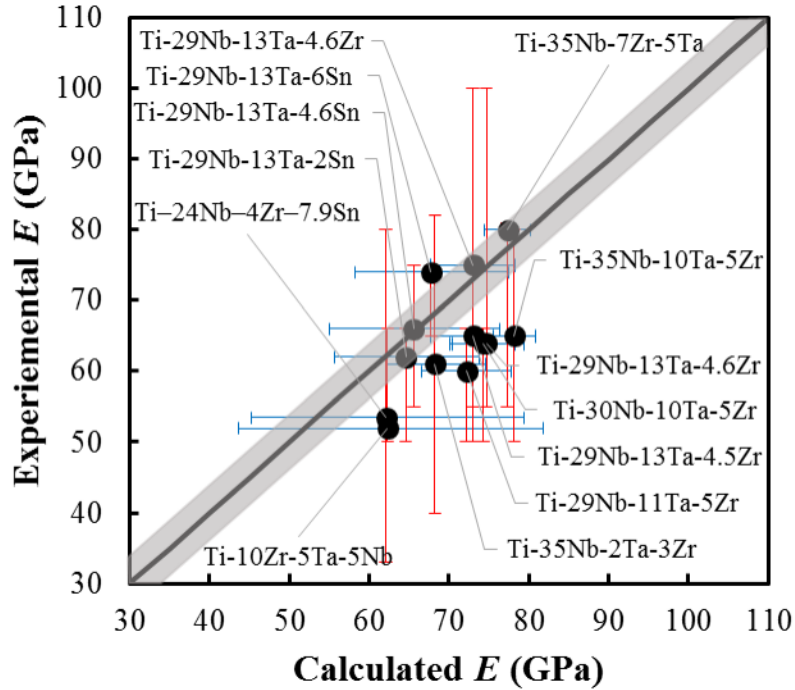


Figure 6.16. E of multicomponent bcc Ti alloys predicted from the database are compared with measured experimental results. Error bars plotted are from the variation in experimentally determined Young's moduli values for the specific multi-component alloy. The grey region refers to the error in the first-principles calculations. More information on the alloys is Table 6.4 [37–39].

Chapter 7 |

Phase stability and elastic properties study of the Ti-Ta and Ti-Nb systems

7.1 Introduction

The present chapter is aimed at studying the formation of the metastable phases ω and α'' . As shown in chapter 1 Figure 1.2 and 1.1, the formation of the α'' and ω phases effects the elastic properties of the implant alloy. Understanding the effect of the metastable phases and at what compositions they form will help with alloy selection and increase the likelihood of finding a suitable alloy for the load-bearing implant application. The stability at 0 °K of the bcc, hcp, *omega*, *alpha''* phases is calculated and discussed for the Ti-Ta and Ti-Nb alloys using multiple structures across the entire composition range. The elastic properties of the four phases are then calculated systematically and interaction parameters are introduced using the CALPHAD method, similar to chapter 5, to be able to predict the elastic properties as a function of composition. With an understanding of how the phases effect the elastic properties, a new theoretical framework was introduced in chapter 2 in order to be able to predict the formation of the metastable phases. This chapter uses the new theoretic framework to study Ti and the Ti-Nb system in the bcc, ω and α'' phases. The theoretic framework is used to predict the phase fractions of the metastable phases and the mixed force constants to plot the phonon density of states. In order to ensure the accuracy of the theroretic framework, neutron

scattering experiments are completed on 4 different Ti-Nb compositions. The data from the experiments is used to determine the phase fractions and phonon density of states. The results from the neutron scattering are compared with the theoretical results. The determined phase fractions are used to predict the elastic properties and compared with experimental values in literature.

7.2 Modeling and Calculations

7.2.1 Computational details

In the present work the Vienna ab-initio Simulation Package (VASP) [61] was employed to calculate the ground state energy and elastic properties of the pure elements and Ti-Nb and Ti-Ta systems in the bcc, hcp, ω , and α'' phases. The ion-electron interactions were described using the projector augmented wave (PAW) [62, 90] method and based on the previous work of comparing X-C functionals (Figure ??) the exchange-correlation functional of the generalized gradient approach depicted by Perdew, Burke, and Ernzerhof (PBE-GGA) was employed [58]. The energy convergence criterion was 10^{-6} eV/atom. The Brillouin zone sampling was done using the γ -centered Monkhorst-Pack scheme [91]. The ground state energy of 330 structures in the bcc phase, across the entire composition range, were calculated using 8x8x8 k-point meshes. The ground state energy of 21 structures in the hcp phase, across the entire composition range, were calculated using 10x10x13 k-point meshes. The ground state energy of 73 structures in the ω phase, across the entire composition range, were calculated using 13x13x7 k-point meshes. The ground state energy of 33 structures in the α'' phase, across the entire composition range, were calculated using 12x11x10 k-point meshes. The elastic properties were then calculated using a ± 0.01 magnitude of strain.

7.2.2 Modeling details

The elastic stiffness constants were modeled using the first-principles based DFT results. The modeling was completed by calculating the difference between the first-principles calculations and a linear extrapolation between pure elements. The differences were then used to fit to the interaction parameters. Due to the limitations

within the PARROT module, a mathematica script was used to fit the interaction parameters. The mathematica script is appended in appendix C. The best fit was found by comparing the fittings obtained with one interaction parameter or with two interaction parameters. The moduli values were then calculated using pycalphad and the code in appendix D and E [42].

7.3 Results and discussion

7.3.1 First-principles calculations at 0 K

The phase stability at 0 °K is calculated as a function of composition for the Ti-Nb and Ti-Ta systems. Figure 7.1 shows the relative energy of the bcc, hcp, ω , and α'' phases from 100 at. % Ti to 100 at. % Nb. The relative energies are calculated similarly to the enthalpy of formation in Eq. 2.7, the ground state energies of the pure elements in the SER state are multiplied by the composition of the specific structure and then subtracted from the ground state energy of the structure being studied. Figure 7.2 is the relative energy of the bcc, hcp, ω , and α'' phases from 100 at. % Ti to 100 at. % Ta. Figure 7.1 and 7.2 are both at 0 °K. The figures show that the bcc and hcp phases are the lowest phases in energy. This shows that the ω and α'' phases are stabilized by entropy.

The Ti-Nb system is chosen to study more in depth due to the experimental work available in the literature which mapped the martensitic transformation temperature for Ti-Nb alloys between the 20 and 30 at. % Nb is shown in Figure 7.3 [125].

7.3.2 Elastic properties

For the Ti-Nb system, the elastic stiffness constants of the bcc, hcp, α'' , and ω phases are calculated. The calculations of the bcc phase were completed and discussed in chapter 5. Figure 7.4 and 7.5 plots the elastic stiffness constants, C_{11} , C_{12} , C_{13} , C_{22} , C_{23} , C_{33} , C_{44} , C_{55} , and C_{66} , for the α'' phase. The C_{11} , C_{22} , C_{23} , C_{55} , and C_{66} values all start off decreasing, then begin to increase in value and finally decrease in value from pure Ti to pure Nb. The C_{12} and C_{13} values all start off increasing, then begin to decrease in value and finally increase in value from

pure Ti to pure Nb. The C_{33} values decrease and then increase in value from pure Ti to pure Nb. The C_{44} values start off increasing and then decrease in value from pure Ti to pure Nb.

Figure 7.6 plots the elastic stiffness constants, C_{11} , C_{12} , C_{13} , C_{33} , and C_{44} , for the ω phase. The C_{11} and C_{33} values all start off increasing and then decreasing from pure Ti to pure Nb. The C_{11} values all start off decreasing and then increase from pure Ti to pure Nb. The C_{12} increases, decreases and then increases in values from pure Ti to pure Nb. The C_{33} values start off decreasing then increase and then decrease again from pure Ti to pure Nb.

Figure 7.7 plots the elastic stiffness constants, C_{11} , C_{12} , C_{13} , C_{33} , and C_{44} , for the hcp phase. The C_{12} , C_{13} and C_{33} values all start off decreasing, then increase and then decrease from pure Ti to pure Nb. The C_{11} values decrease from pure Ti to pure Nb. The C_{44} values increase, decrease and then increase from pure Ti to pure Nb.

The calculated elastic stiffness constants are listed in Table 7.1. From the elastic stiffness constants, the Young's moduli values are calculated as a function of composition and are plotted in Figure 7.8. The dotted lines are the fittings that use the interaction parameters in Table 7.2. The calculations show that the Young's moduli, for the hcp phase, decrease in value until around 80 at. % Nb and then increase from 80 at. % Nb to pure Nb. The Young's moduli, for the omega phase, follows the same trend as the hcp phase. The E values decrease from pure Ti to around 60 at. % Nb and then increase from 60 at. % Nb to pure Nb. The E values, for the bcc phase, increase from pure Ti to pure Nb. The E values, for the α'' phase, decrease from pure Ti to around 20 at. % Nb, then increase from 10 at. % Nb to 70 at. % Nb and then decrease from 70 at. % Nb to pure Nb. The E values for the hcp, ω , and bcc phases all go negative at some point. Based on Born's criteria, a negative Young's modulus can indicate that the phase is not stable at that composition. From Figure 7.8, it can be seen that the E values of the α'' phase are higher than the hcp or bcc phases. This explains why in Figure 1.2 the experimental Young's moduli increase in value with the formation of the metastable.

At least four different authors have experimentally determined the E of various Ti-Nb alloys at different compositions, which are plotted in Figure 1.2, [6, 8, 8, 9]. Ozaki et al. [7] showed the same results discussed earlier that at certain compositions

quenched samples formed bcc and α'' while the cooled samples formed bcc and ω . There was more experimental results for the quenched samples which is why present work reviewed this data and averaged the E values at the same compositions. The full experimental results reviewed are listed in appendix F and the averaged experimental values are listed in Table 7.3. From these experiments, some of the phase fractions were determined [8] and those phase fractions are listed in Table 7.3. For the compositions where the phase fractions were not determined, we extrapolated an estimated phase fractions, those phase fractions are in italics in order to differentiate from a prediction and a measured phase fraction. Based on these phase fractions and the interaction parameters in Table 7.2, the rule of mixtures is used to predict the Young's moduli and compared with the experimentally determined E . The rule of mixtures is expressed by:

$$E_c = x_{p1}E_{p1} + x_{p2}E_{p2} \quad (7.1)$$

where x_{p1} and x_{p2} are the phase fractions of phase 1 and phase 2. E_{p1} and E_{p2} are the elastic modulus of the alloys in phase 1 and phase 2. Based on the data up until 10 at. % Nb the samples are 100 % hcp and the predicted E vary, on average, from the experimental E by 7.7 GPa. From 10 at. % Nb to 30 at. % Nb the α'' and bcc phases formed. The exact phase fraction of the bcc phase was measured by Friak et al. for the 10, 20, 25, and 30 at. % Nb samples. An extrapolation from these values is used for the phase fractions of the remaining alloys in this composition range. Using the phase fractions and rule of mixtures, the predicted E varies, on average, from the experimental E by 0.52 GPa. If the alloys had been assumed to be a bcc and hcp mixture, as the CALPHAD predictions tell us, the predicted E would vary, on average, from the experimental E by 22 GPa. Above 33 at. % Nb the samples are all bcc phase. The predicted E vary, on average, from the experimental E by 7 GPa. Overall, the variances are quite small when compared to the variance seen in the experiments. As seen in appendix F, the experimental E values of pure Ti in the hcp phase vary by 24 GPa. The variance between the predicted E and experimental E can be attributed to the fact that the predicted E are at 0 °K and the experimental E are at 300 °K. Based on the comparison, it is seen that if the phase fraction of the metastable phases can be predicted than the database can be used with the rule of mixtures to accurately predict the elastic properties.

7.3.3 Neutron scattering results

7.3.3.1 Phonon density of states at 300 K

The phonon density of states was obtained at 300 °K for each set of samples at each Nb composition. The phonon density of states are plotted in Figure 7.9, 7.10, 7.11, 7.12. The samples at the same composition are plotted together for comparison. The phonon density of states of the slow cooled samples, that should contain the bcc and ω phases, are plotted with dashed lines and the phonon density of states of the quenched samples, that should contain the bcc and α'' phases, are plotted with solid lines. The fact that the different samples show different phonon DOS means that the quenching versus slow cooling worked and the samples should have different phases. In order to investigate the difference of the phonon DOS further the entropy of each sample was calculated from the phonon DOS ($g(E)$):

$$S_{vib} = 3k_B \int_0^{E_{max}} [(n+1) \ln(n+1) - n \ln(n)] g(E) dE \quad (7.2)$$

where n is the Bose-Einstein occupation factor [126]. The entropy difference between the alloys at the same compositions is plotted in 7.13. The figure shows that the entropy difference increases from 10 mol % Nb to 20 mol % Nb. The increase in entropy with increasing Nb content makes sense when looking at Figure 1.2. The figure and previous research shows that the α'' and ω phases form from approximately 10 mol % to 35 mol % Nb. At 10 mol % Nb, only a small amount of the metastable phases form which is why the experimentally determined elastic properties still line up well with the theoretically obtained elastic properties. This is supported by the lower entropy difference between the two 10 mol % Nb alloys. However, closer to 20 mol % Nb, Figure 7.8 shows that the experimental Young's moduli is higher than computationally determined Young's moduli. Research showed that the phase fractions of the metastable phase is larger at this composition than the three other compositions studied in this work. This is supported by the larger difference in entropy at 20 mol % Nb.

7.3.3.2 Diffraction patterns at 300 K

The diffraction patterns for each alloy are plotted in Figure 7.14, 7.15, 7.16 7.17. The slow cooled samples are plotted as solid lines and the quenched samples are

plotted as dashed lines. The diffraction patterns plot the Q vs. the intensity. Using a different neutron scattering technique or x-ray diffraction would lead to better diffraction patterns and more accurate predictions of the phase stability. The plots are compared with known diffraction patterns of Ti and Nb in the four phases to determine an approximation of the phase fractions. The determined phase fractions of each alloy are listed in Table 7.4. The analysis shows that the quenched samples formed 0.12, 0.20, 0.57 and 0.70 phase fraction of bcc for the 10, 12, 18 and 20 at. % Nb samples, respectively. The slow cooled samples showed 0.2, 0.3, 0.6, 0.7 phase fraction of the bcc phase for the 10, 12, 18, and 20 at. % Nb samples, respectively. The phase fractions for the 10 and 20 at. % Nb quenched samples compares well with the fractions determined by Friak et al. [8] shown in Table 7.3.

7.3.4 Partition function approach results

The implementation of the new theoretical framework is ongoing. Due to the difficulty of implementing the theoretic framework, we began by calculating pure Ti. The energy is being mapped for Ti in the bcc, ω , α'' and hcp phases looking for the energy minima. Quasiharmonic phonon calculations will be completed on the structures at the lowest energy minima points. The helmholtz energy results and eigenvalues from these calcualtions will be used in Eq. 2.24, 2.27, 2.26, and 2.25. Using the calculation of entropy, from the combined helmholtz, this work should more accurately predict Ti in the bcc phase. Once the work has been shown to be accurate for pure Ti, it will be extended to the Ti-Nb binary system and compared to the neutron scattering results.

7.4 Conclusion

The present study systematically calculates the elastic stiffness constants and Young's moduli of the Ti-Nb system in the bcc, hcp, ω , and α'' phases. The general CALPHAD modeling approach is used to fit binary interaction parameters. The E values were similar for the hcp and ω phase which makes sense since they both have hexagonal symmetry. The α'' phase has E values that are higher than the other three phase which explains why when formed the E increases. Experiments showed that up to 10 at. % Nb the samples formed solely the hcp phase and the database

predicts the E values by an average variance of 8 GPa from the experimental E . The samples from 10 at. % Nb to 30 at. % Nb formed both the bcc and α'' or ω phases. If the samples are slow cooled then the samples form the bcc and ω phases. If the samples are quenched they form the bcc and α'' phases. Using experimentally determined phase fractions and the rule of mixtures, the database accurately predicts the E values by an average variance of 0.52 GPa when compared with the experimental E values. At Nb concentrations greater than 30 at. % Nb form solely the bcc phase and the database predicts the E values by an average variance of 7 GPa from the experimental E values. The phonon DOS at 300 °K differences between the slow cooled and quenched samples especially when looking at the entropy difference between the samples. Diffraction patterns from ARCS are difficult to fit but the phase fractions are approximated. The implementation of the new theoretic framework is ongoing but from the results here, if the phase fractions of the metastable phases can be predicted then the elastic database can accurately assess the Young's moduli and elastic stiffness constants.

Table 7.1: First-principles calculations of the elastic stiffness constants in GPa for different atomic percent compositions in the α'' , bcc, hcp, and ω phases in the Ti-Nb system at 0 °K.

$Ti_{1-b}Nb_b$	c_{11}	c_{12}	c_{13}	c_{22}	c_{23}	c_{33}	c_{44}	c_{55}	c_{66}
α''									
Ti	198	69	84	197	84	189	40	40	63
TiNb ₃	106	112	123	152	45	138	25	17	38
TiNb ₁₃	171	88	105	171	67	170	47	13	43
TiNb ₉₄	307	94	119	248	143	214	31	-24	13
TiNb ₉₇	307	88	115	232	124	284	59	-58	8
TiNb ₉₈	293	88	115	232	124	284	59	-58	8
Nb	306	88	125	240	135	284	47	-69	9
bcc									
Ti	93	115	-	-	-	-	41	-	-
TiNb ₂	93	115	-	-	-	-	35	-	-
TiNb ₁₃	116	116	-	-	-	-	37	-	-
TiNb ₂₅	140	116	-	-	-	-	34	-	-
TiNb ₅₀	181	121	-	-	-	-	31	-	-
TiNb ₇₅	208	130	-	-	-	-	15	-	-
TiNb ₉₄	242	134	-	-	-	-	18	-	-
TiNb ₉₈	242	134	-	-	-	-	18	-	-
Nb	245	144	-	-	-	-	27	-	-
hcp									
Ti	175	88	80	-	-	190	41	-	-
TiNb ₂	79	-44	-38	-	-	73	45	-	-
TiNb ₁₃	A	B	C	-	-	D	E	-	-
TiNb ₂₅	156	113	104	-	-	200	13	-	-
TiNb ₅₀	124	151	135	-	-	185	-19	-	-
TiNb ₇₅	76	213	156	-	-	173	-61	-	-
TiNb ₉₄	15	289	177	-	-	163	-104	-	-
TiNb ₉₈	34	280	185	-	-	145	-106	-	-
Nb	24	18	11	-	-	25	-6	-	-
ω									

Table 7.1: First-principles calculations of the elastic stiffness constants in GPa for different atomic percent compositions in the α'' , bcc, hcp, and ω phases in the Ti-Nb system at 0 °K.

Ti _{1-b} Nb _b	c ₁₁	c ₁₂	c ₁₃	c ₂₂	c ₂₃	c ₃₃	c ₄₄	c ₅₅	c ₆₆
Ti	194	87	61	-	-	246	54	-	-
TiNb ₂	187	87	63	-	-	250	50	-	-
TiNb ₁₃	171	89	83	-	-	165	30	-	-
TiNb ₉₄	240	90	142	-	-	234	-22	-	-
TiNb ₉₈	242	88	120	-	-	270	-5	-	-
Nb	243	181	110	-	-	212	-55	-	-

Table 7.2. Evaluated interaction parameters L_0 and L_1 , using Eq. 2.38, for the elastic stiffness constants of the bcc, hcp, α'' and ω phases in the Ti-Nb systems.

Alloy	Interaction Parameter	α''	bcc	hcp	ω
c ₁₁	L_0	-102.443	40.4555	92.0107	-142.979
	L_1	606.748	-	126.357	159.767
c ₁₂	L_0	97.3105	-32.3885	719.463	-888.25
	L_1	-186.214	-	1322.75	-1074.08
c ₁₃	L_0	-11.5368	N/A	541.702	349.337
	L_1	-307.745	N/A	906.397	275.297
c ₂₂	L_0	-100.063	N/A	N/A	N/A
	L_1	355.649	N/A	N/A	N/A
c ₂₃	L_0	-75.1048	N/A	N/A	N/A
	L_1	283.22	N/A	N/A	N/A
c ₃₃	L_0	-468.983	N/A	481.962	-100.909
	L_1	-114.152	N/A	665.306	733.448
c ₄₄	L_0	14.125	-41.5375	-266.658	263.258
	L_1	-	-41.9528	-416.274	475.336
c ₅₅	L_0	204.71	N/A	N/A	N/A
	L_1	479.179	N/A	N/A	N/A
c ₆₆	L_0	-59.1357	N/A	N/A	N/A
	L_1	139.625	N/A	N/A	N/A

Table 7.3. Phase fractions and experimentally determined E compared with the predicted E using the rule of mixtures and interaction parameters in Table 7.2 for the Ti-Nb system.

x(Nb)	Phase Fraction	Expt E	Calc E
0.00	all hcp	118.31	123.8
0.01	all hcp	112.52	117.7
0.02	all hcp	108.33	112.0
0.05	all hcp	79.47	94.9
0.08	all hcp	66.41	78.4
0.09	all hcp	68.73	73.1
0.10	0.06 BCC/0.94 α''	84.64	95.89
0.11	0.15BCC/0.94 α''	78.72	88.19
0.18	0.45BCC/0.94 α''	93.02	70.08
0.19	0.49BCC/0.94 α''	64.26	68.65
0.20	0.60 BCC/0.94 α''	77.62	65.74
0.22	0.63BCC/0.94 α''	70.90	67.44
0.23	0.67BCC/0.94 α''	75.85	67.00
0.24	0.71BCC/0.94 α''	61.11	66.63
0.25	0.81 BCC/0.94 α''	72.52	66.10
0.26	0.80BCC/0.94 α''	66.61	66.23
0.27	0.84BCC/0.94 α''	54.61	66.98
0.29	0.91BCC/0.94 α''	62.13	66.16
0.30	0.90 BCC/0.94 α''	68.11	68.21
0.34	all bcc	77.47	66.69
0.36	all bcc	73.78	69.00
0.39	all bcc	76.62	69.81
0.43	all bcc	84.05	69.77

Table 7.4. Phase fractions determined from the diffraction patterns for the Ti-Nb alloys.

Alloy	x(Nb)	Phase Fraction		
		bcc	ω	α''
Q-TiNb ₁₀	0.10	0.12	-	0.88
Q-TiNb ₁₂	0.12	0.20	-	0.80
Q-TiNb ₁₈	0.18	0.57	-	0.43
Q-TiNb ₂₀	0.20	0.70	-	0.3
SC-TiNb ₁₀	0.10	0.20	0.8	-
SC-TiNb ₁₂	0.12	0.30	0.7	-
SC-TiNb ₁₈	0.18	0.60	0.4	-
SC-TiNb ₂₀	0.20	0.70	0.3	-

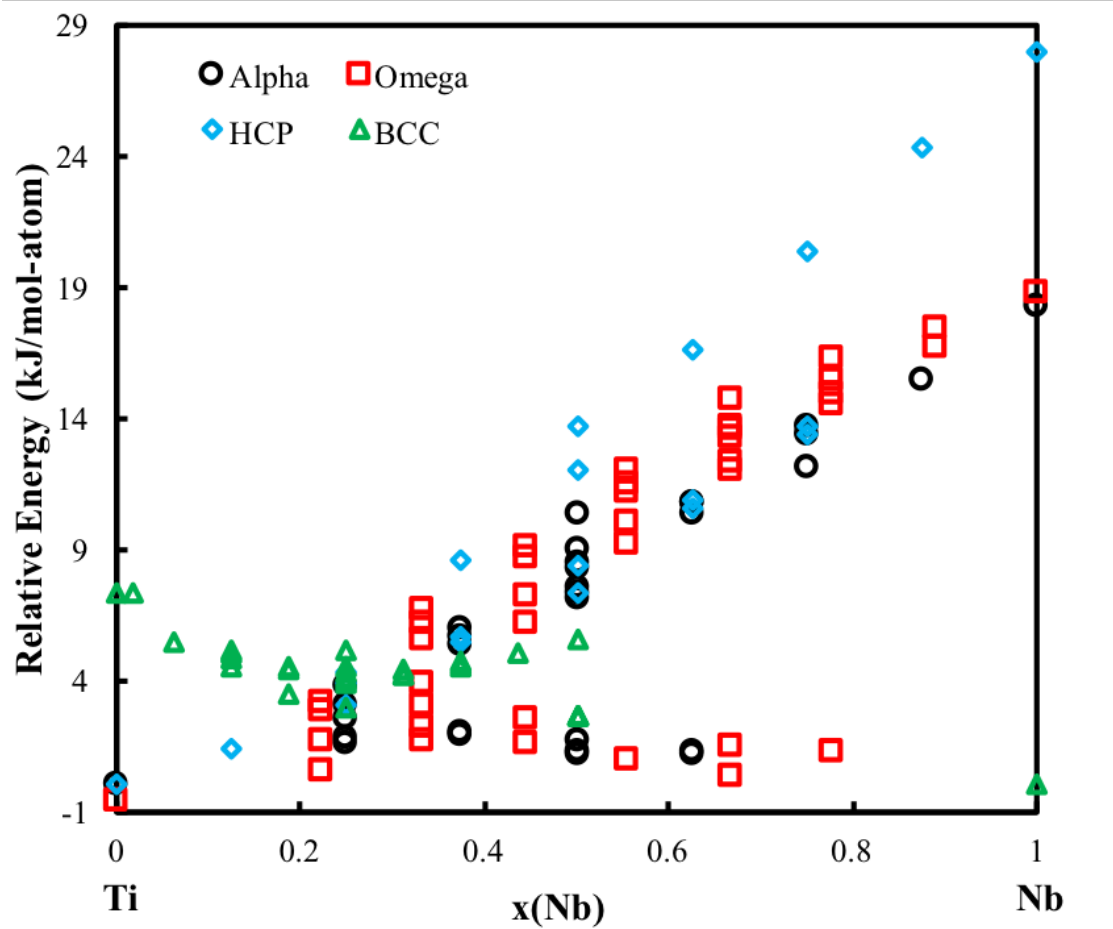


Figure 7.1. Relative energy of the bcc, hcp, ω , α'' phases in the Ti-Nb system are plotted from 100 at. % Ti to 100 at. % Nb.

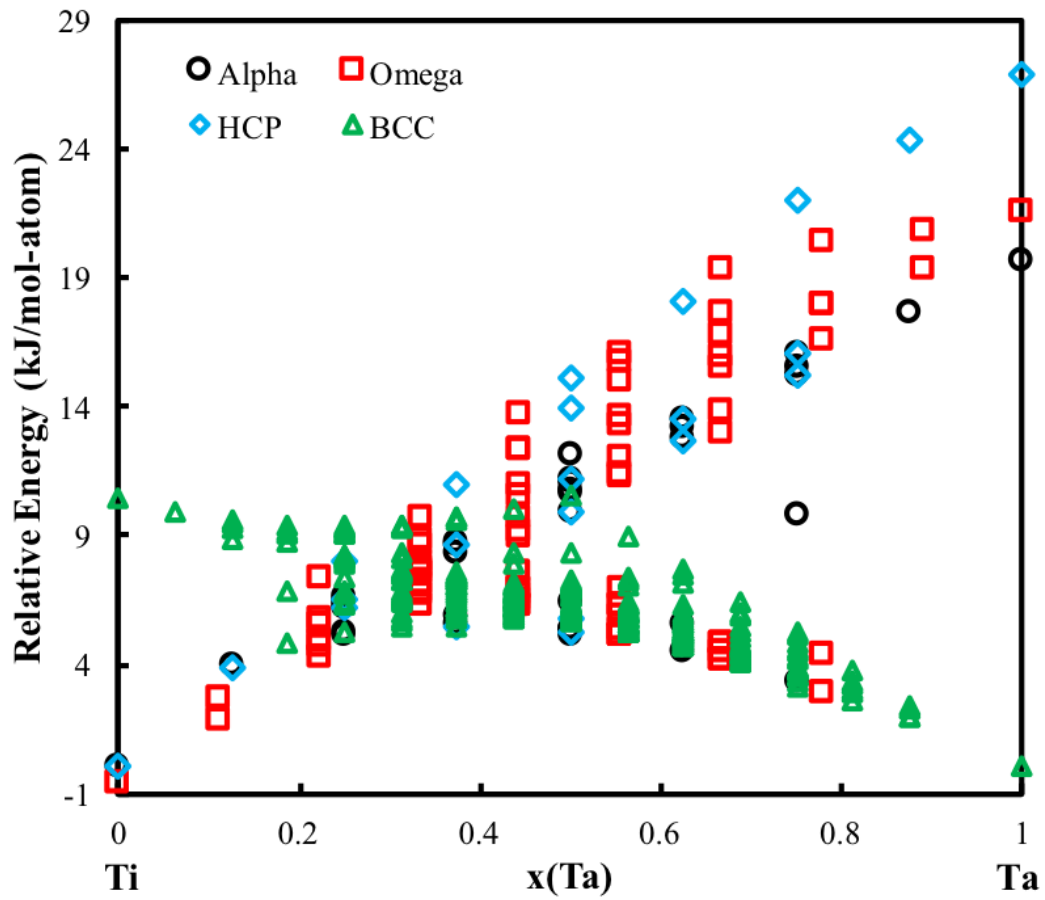


Figure 7.2. Relative energy of the bcc, hcp, ω , α'' phases in the Ti-Ta system are plotted from 100 at. % Ti to 100 at. % Ta.

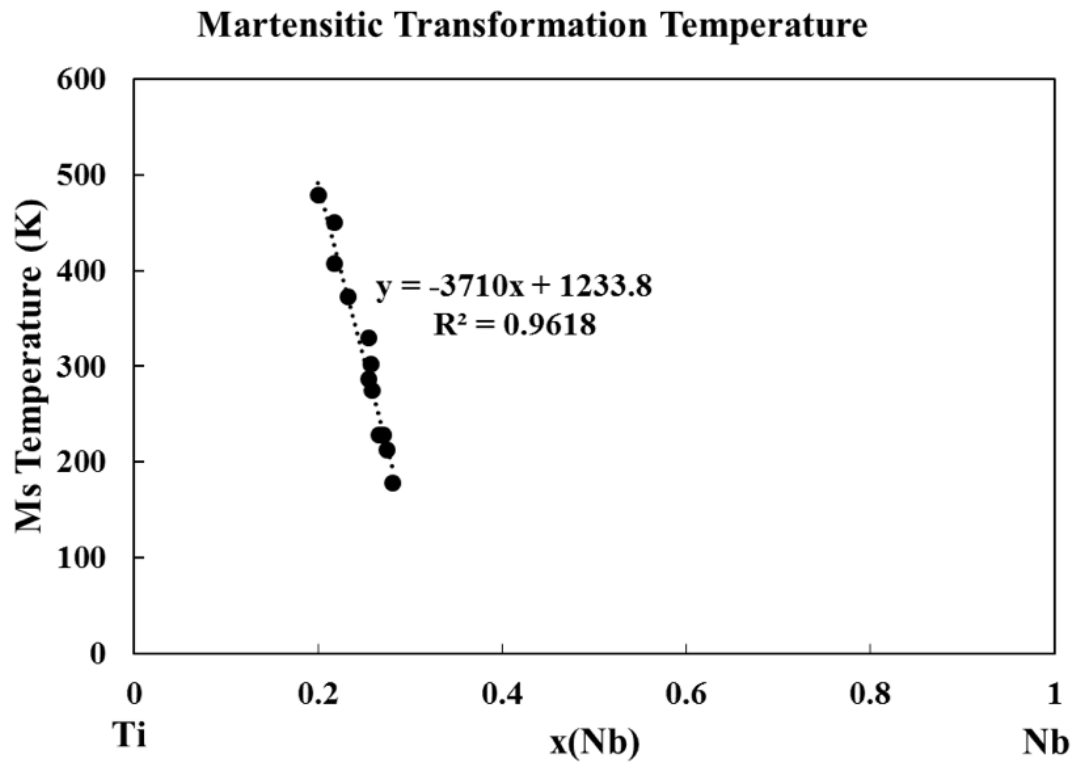


Figure 7.3. Martensitic transformation temperature is plotted versus the Ti-Nb composition.

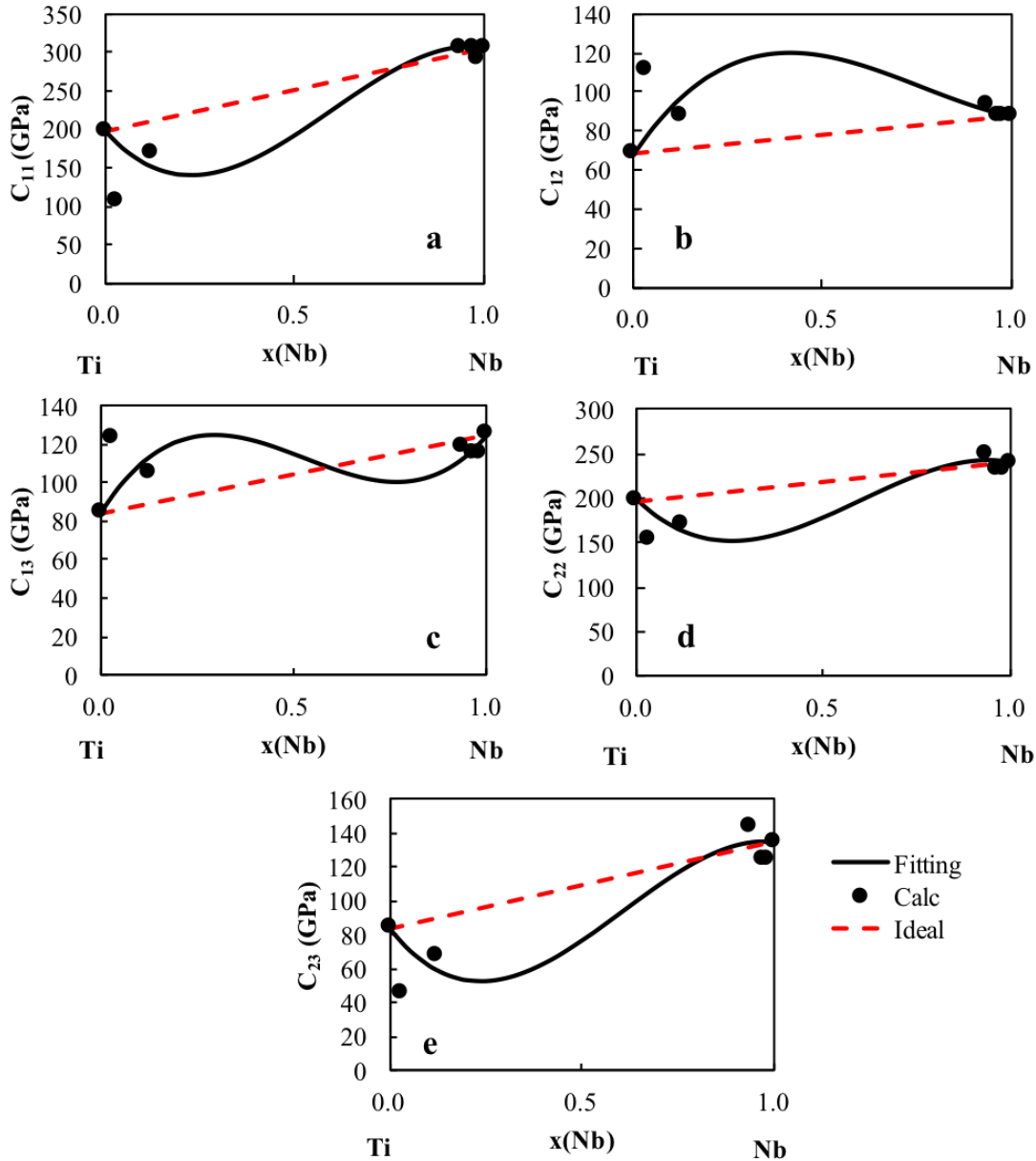


Figure 7.4. Calculated C_{11} , C_{12} , C_{13} , and C_{22} values (circles) plotted as well as the pure element extrapolation (red dashed line) and the present modeling (black dashed line) for five of the elastic stiffness constants of Ti-Nb in the α'' phase.

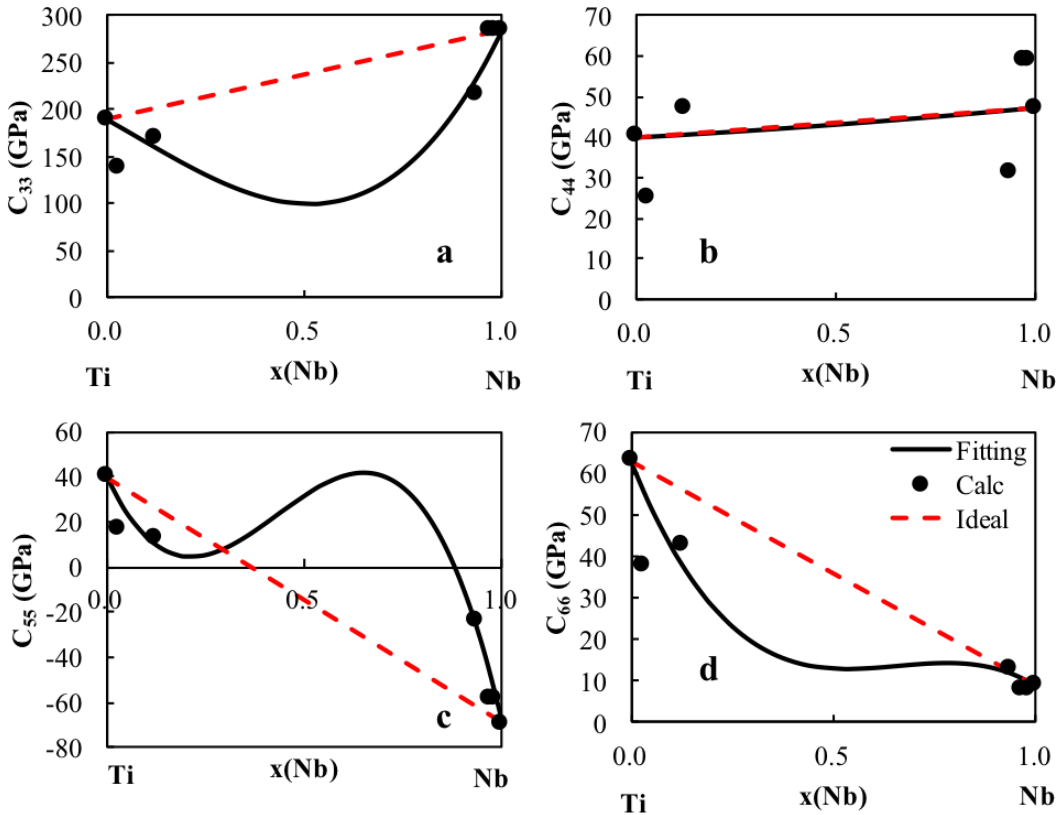


Figure 7.5. Calculated C_{23} , C_{33} , C_{44} , C_{55} , and C_{66} values (circles) plotted as well as the pure element extrapolation (red dashed line) and the present modeling (black dashed line) for four of the elastic stiffness constants of Ti-Nb in the α'' phase.

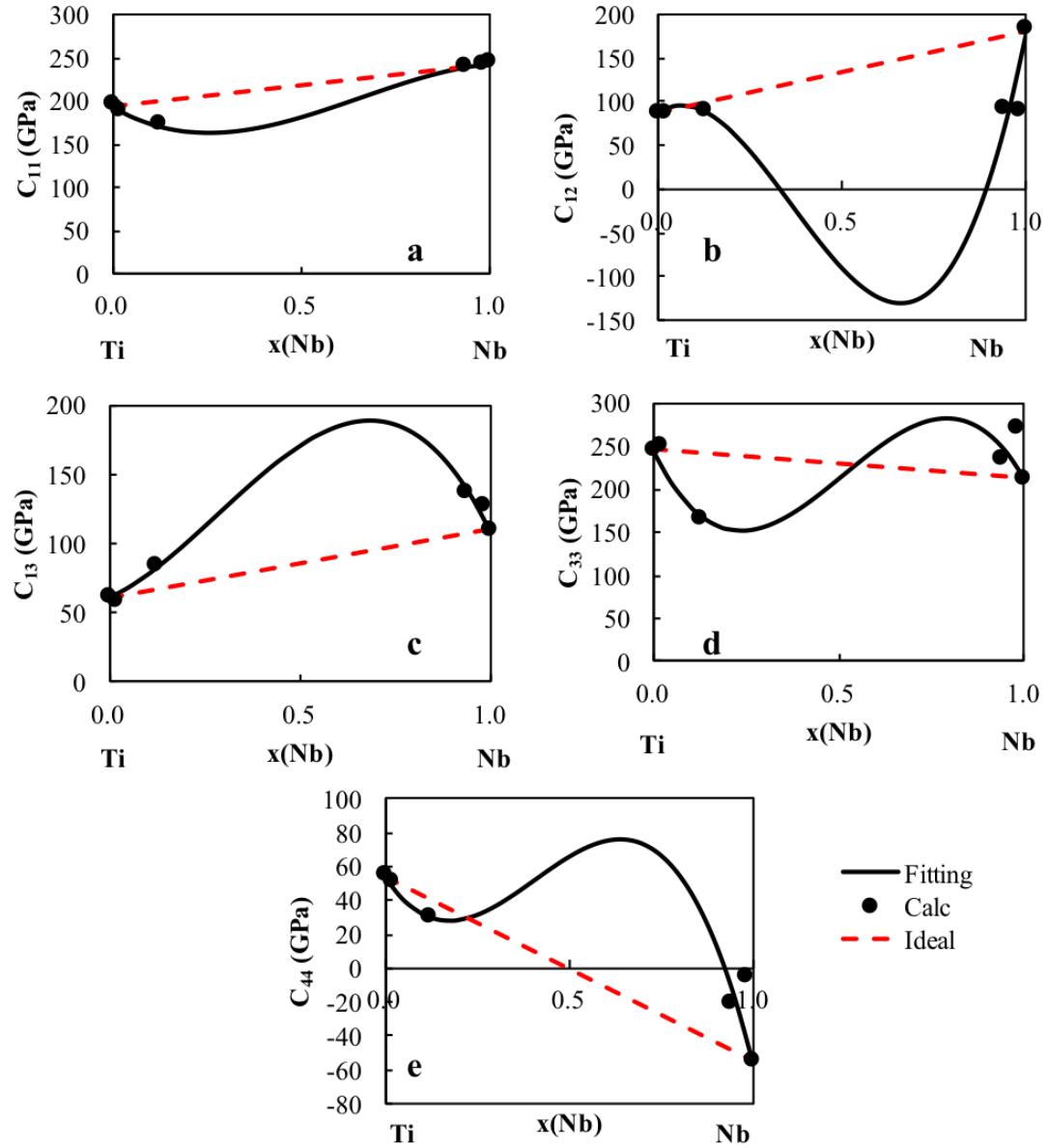


Figure 7.6. Calculated C_{11} , C_{12} , C_{13} , C_{33} , and C_{44} values (circles) plotted as well as the pure element extrapolation (red dashed line) and the present modeling (black dashed line) for the elastic stiffness constants of Ti-Nb in the ω phase.

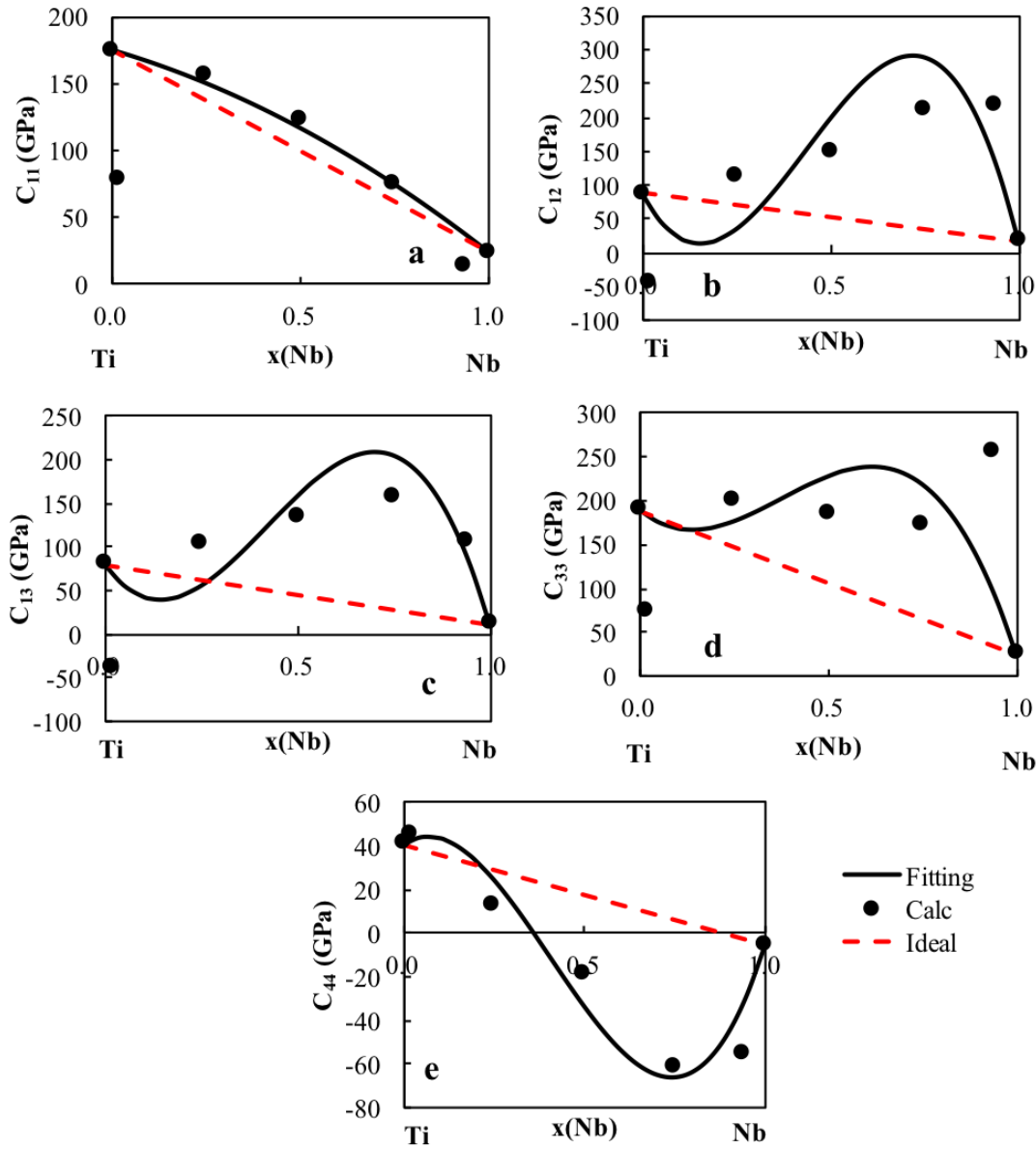


Figure 7.7. Calculated C_{11} , C_{12} , C_{13} , C_{33} , and C_{44} values (circles) plotted as well as the pure element extrapolation (red dashed line) and the present modeling (black dashed line) for the elastic stiffness constants of Ti-Nb in the hcp phase.

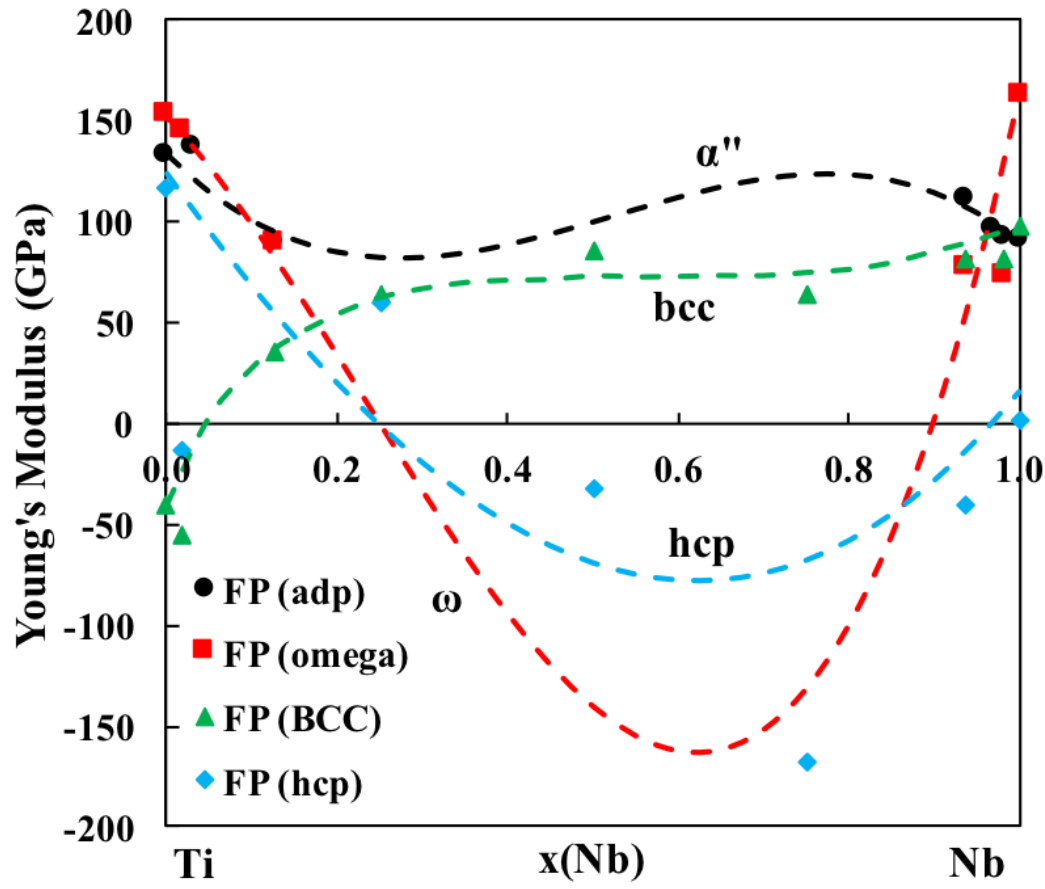


Figure 7.8. Elastic properties of the bcc, hcp, ω , α'' phases in the Ti-Nb system calculated from first-principles based on DFT are plotted as symbols. The CALPHAD fitting are plotted as the dashed lines. The figure is plotted from 100 at. % Ti to 100 at. % Nb.

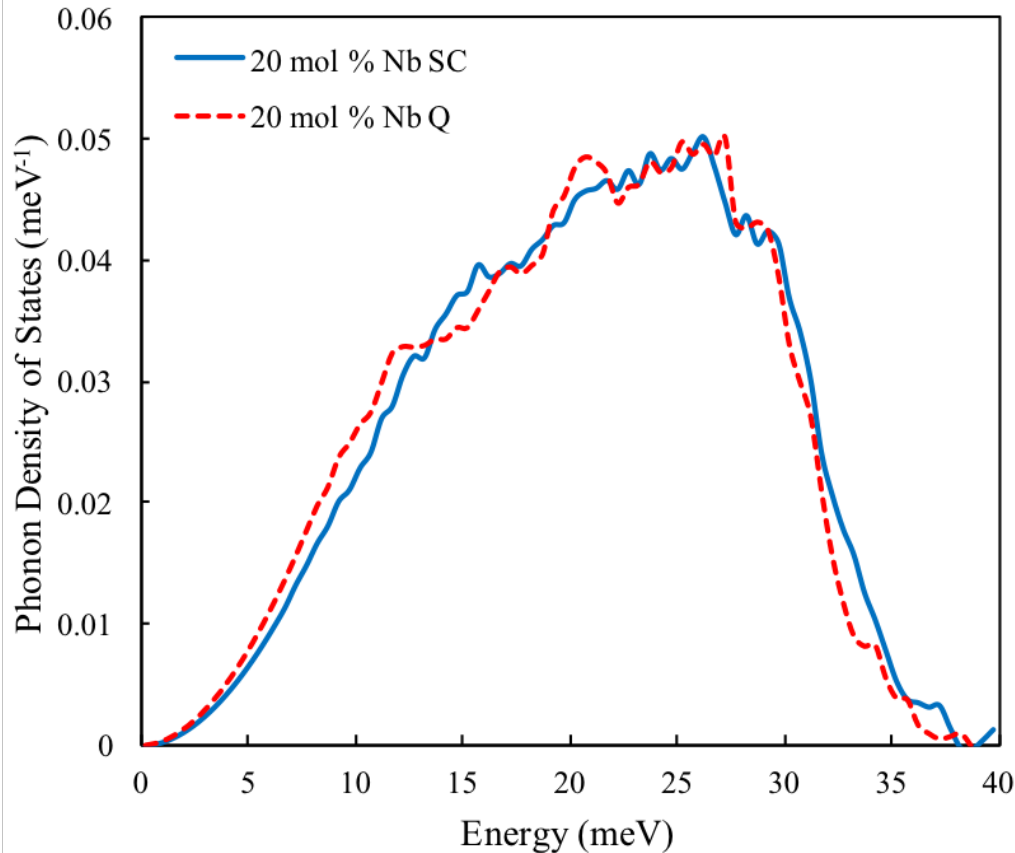


Figure 7.9. Phonon density of states is plotted for the TiNb alloy at 20 at. % Nb. The dashed line represents the slow cooled sample while the solid line represents the quenched sample.

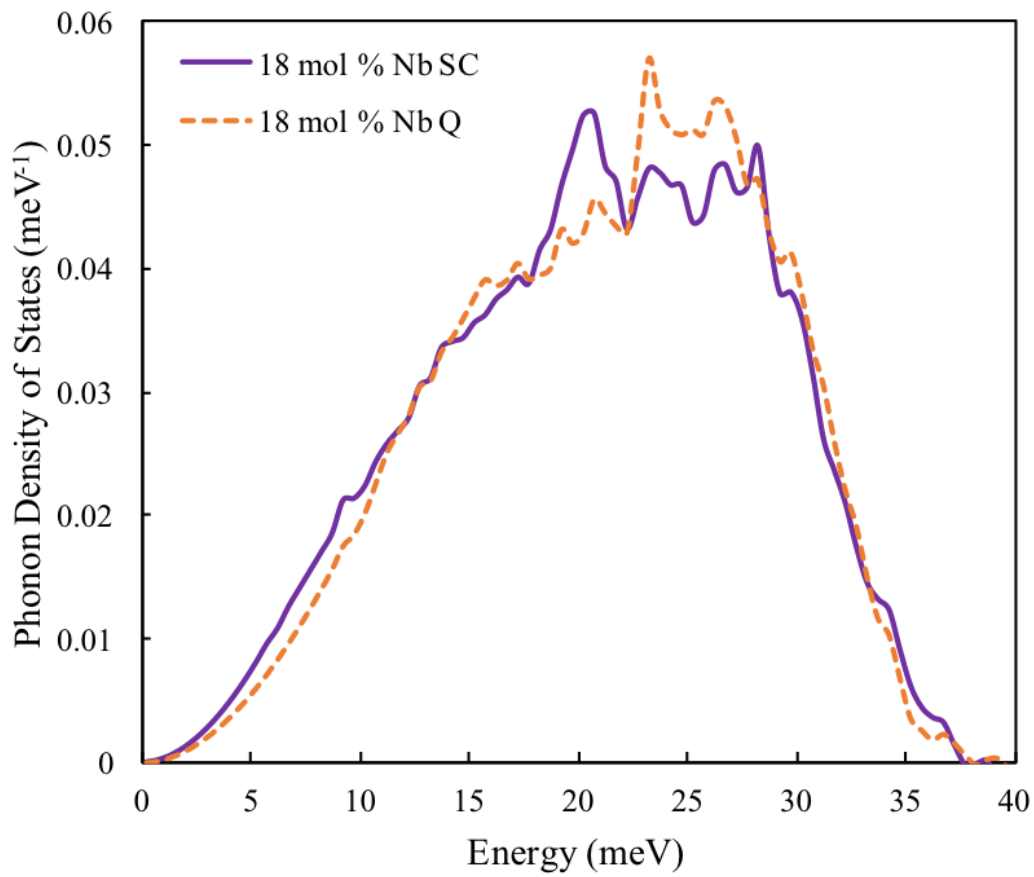


Figure 7.10. Phonon density of states is plotted for the TiNb alloy at 18 at. % Nb. The dashed line represents the slow cooled sample while the solid line represents the quenched sample.

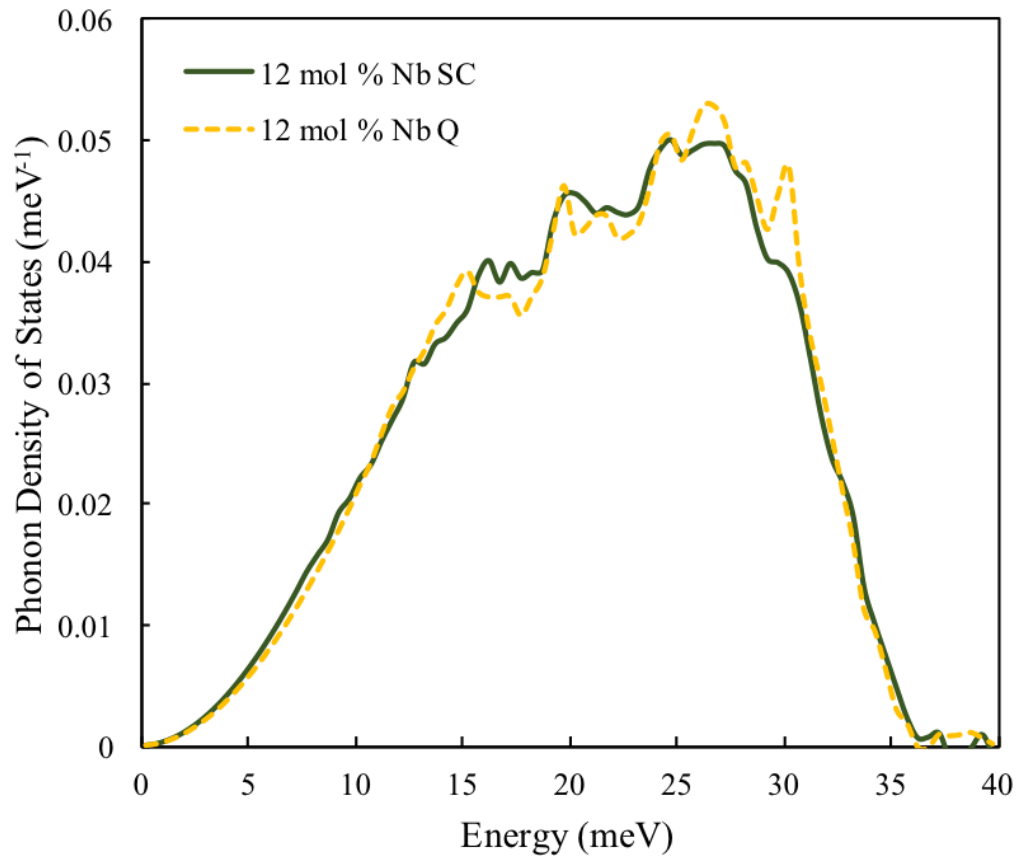


Figure 7.11. Phonon density of states is plotted for the TiNb alloy at 12 at. % Nb. The dashed line represents the slow cooled sample while the solid line represents the quenched sample.

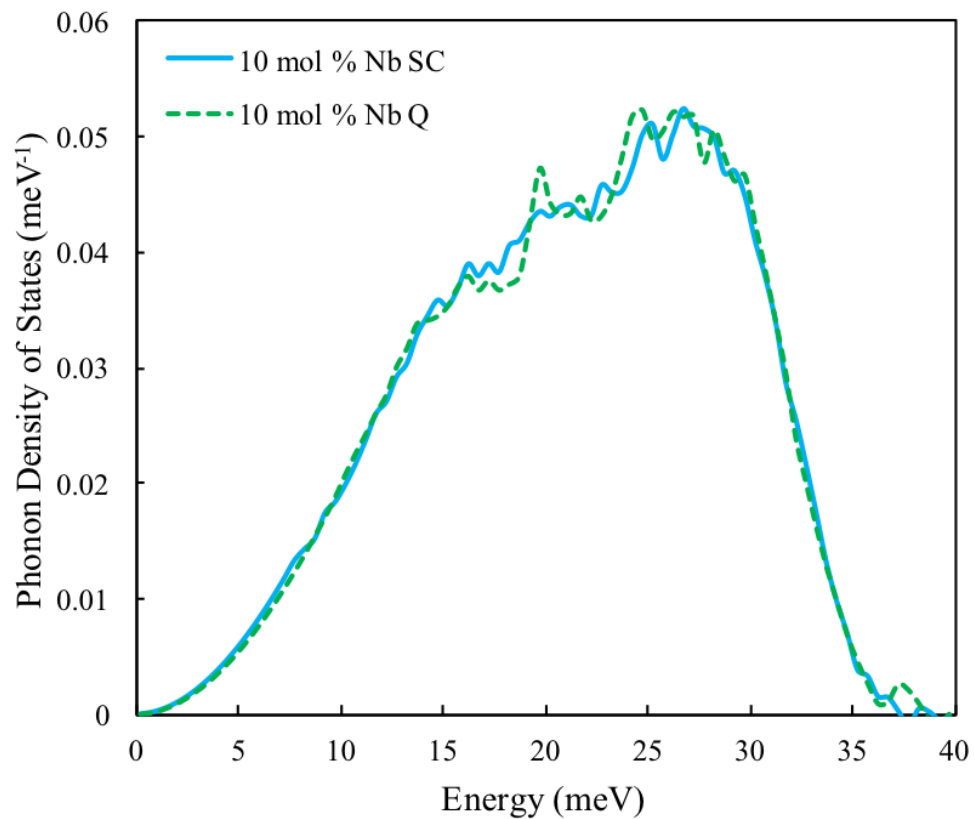


Figure 7.12. Phonon density of states is plotted for the TiNb alloy at 10 at. % Nb. The dashed line represents the slow cooled sample while the solid line represents the quenched sample.

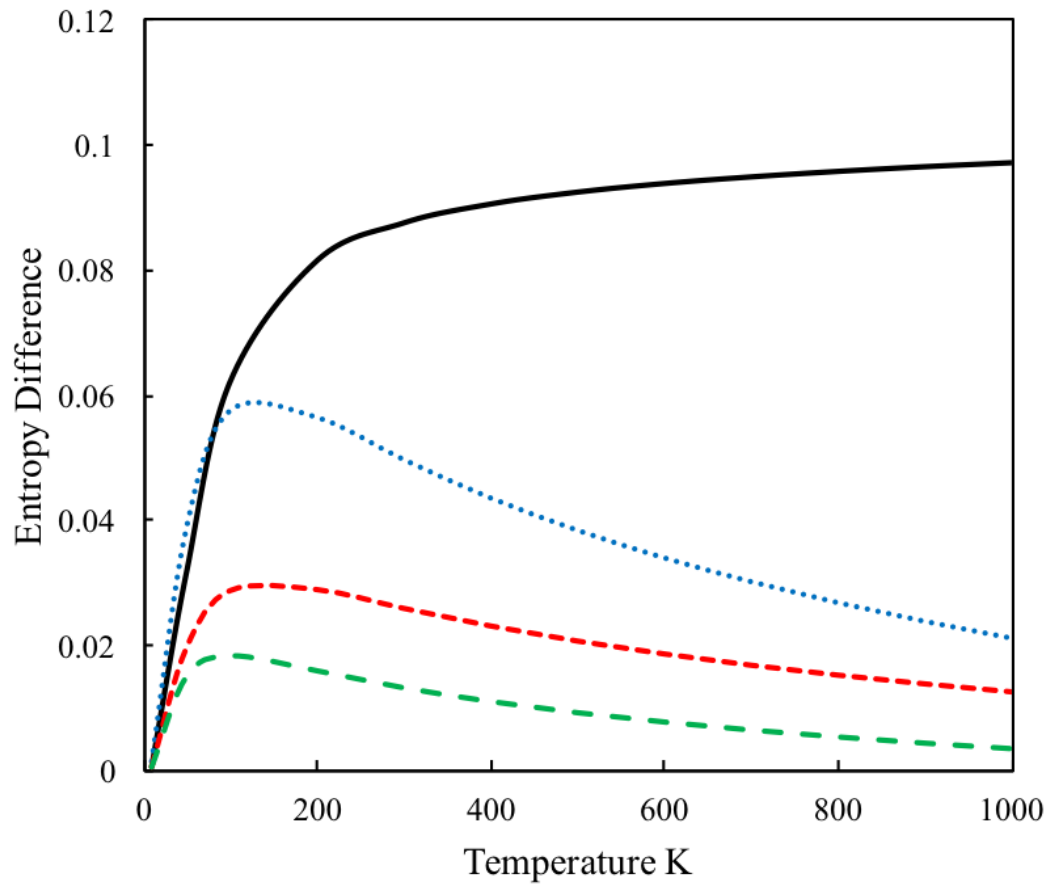


Figure 7.13. Entropy difference between the Ti-Nb alloys with the same alloy composition is plotted as a function of temperature.

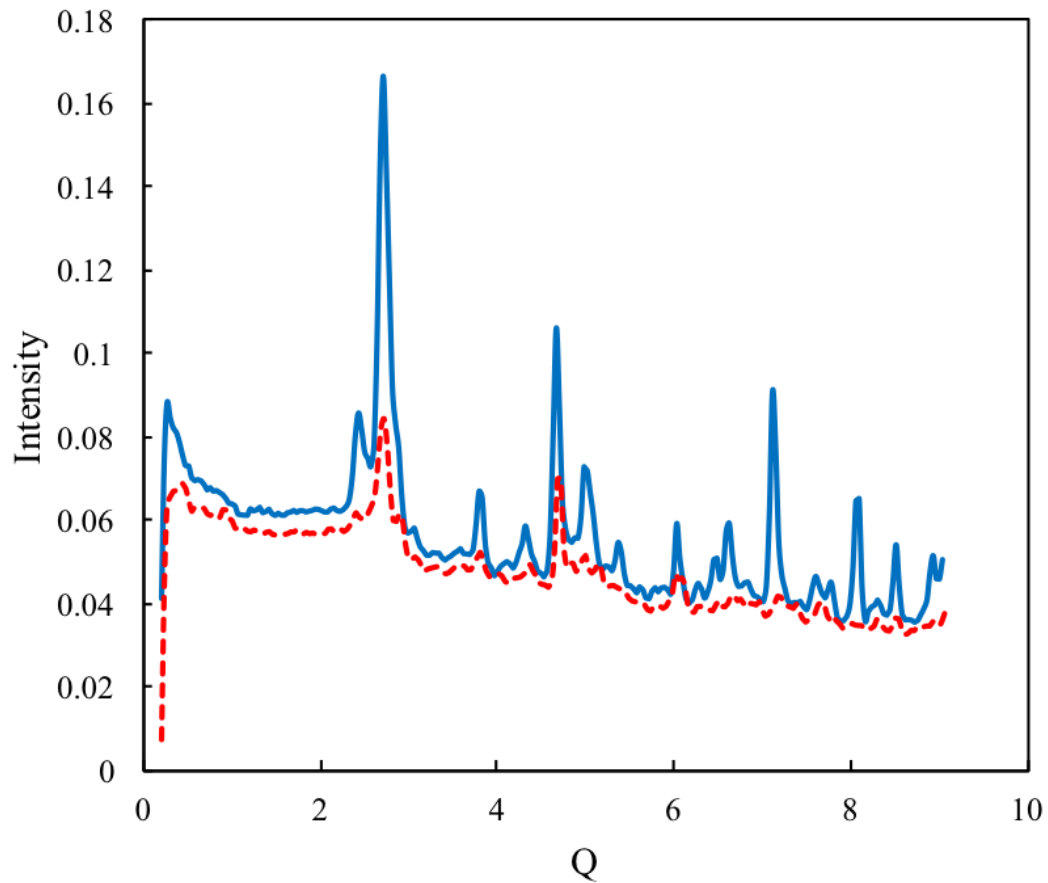


Figure 7.14. Diffraction pattern of the Ti-Nb alloy at 20 at. % Nb. The dashed line represents the slow cooled sample while the solid line represents the quenched sample.

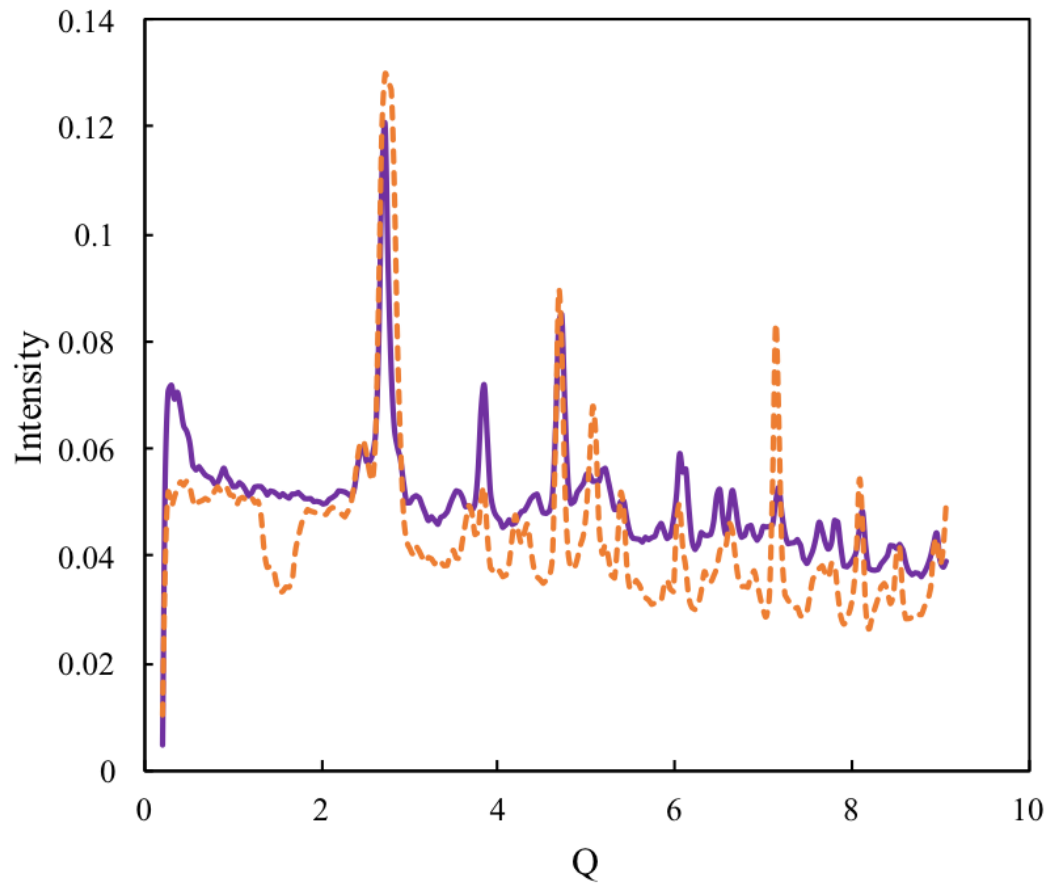


Figure 7.15. Diffraction pattern of the Ti-Nb alloy at 18 at. % Nb. The dashed line represents the slow cooled sample while the solid line represents the quenched sample.

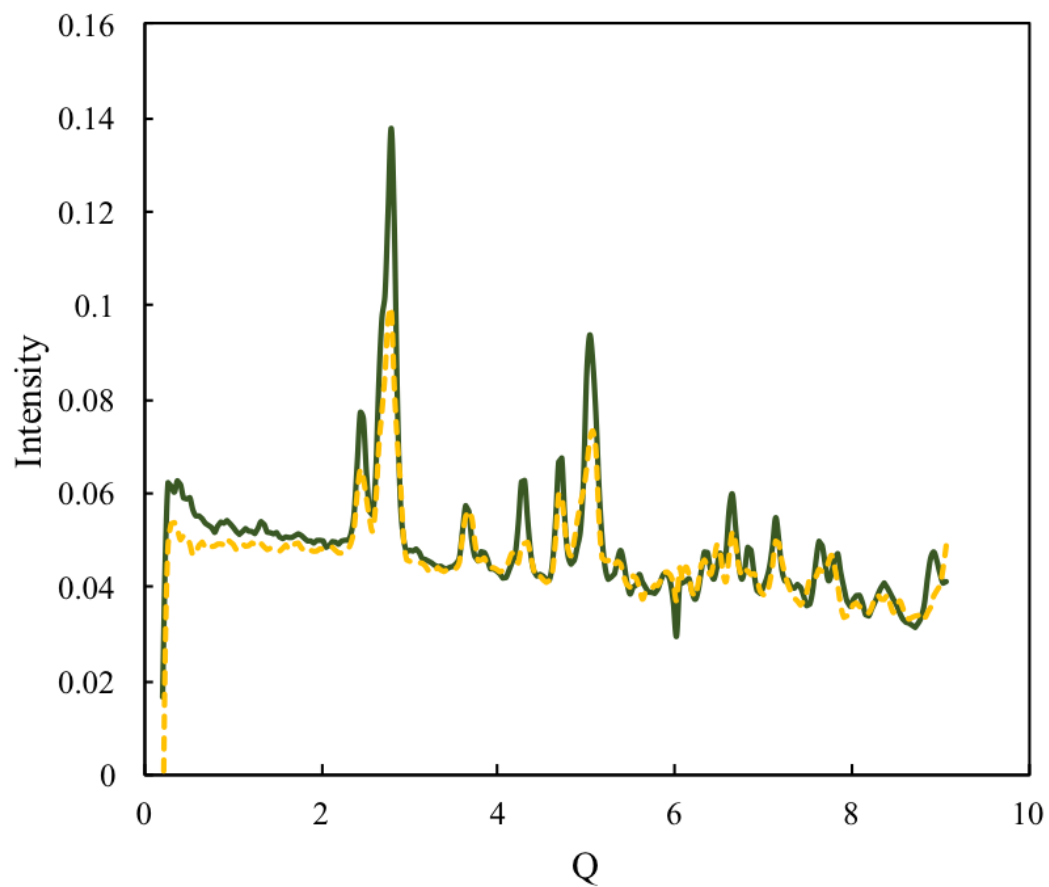


Figure 7.16. Diffraction pattern of the Ti-Nb alloy at 12 at. % Nb. The dashed line represents the slow cooled sample while the solid line represents the quenched sample.

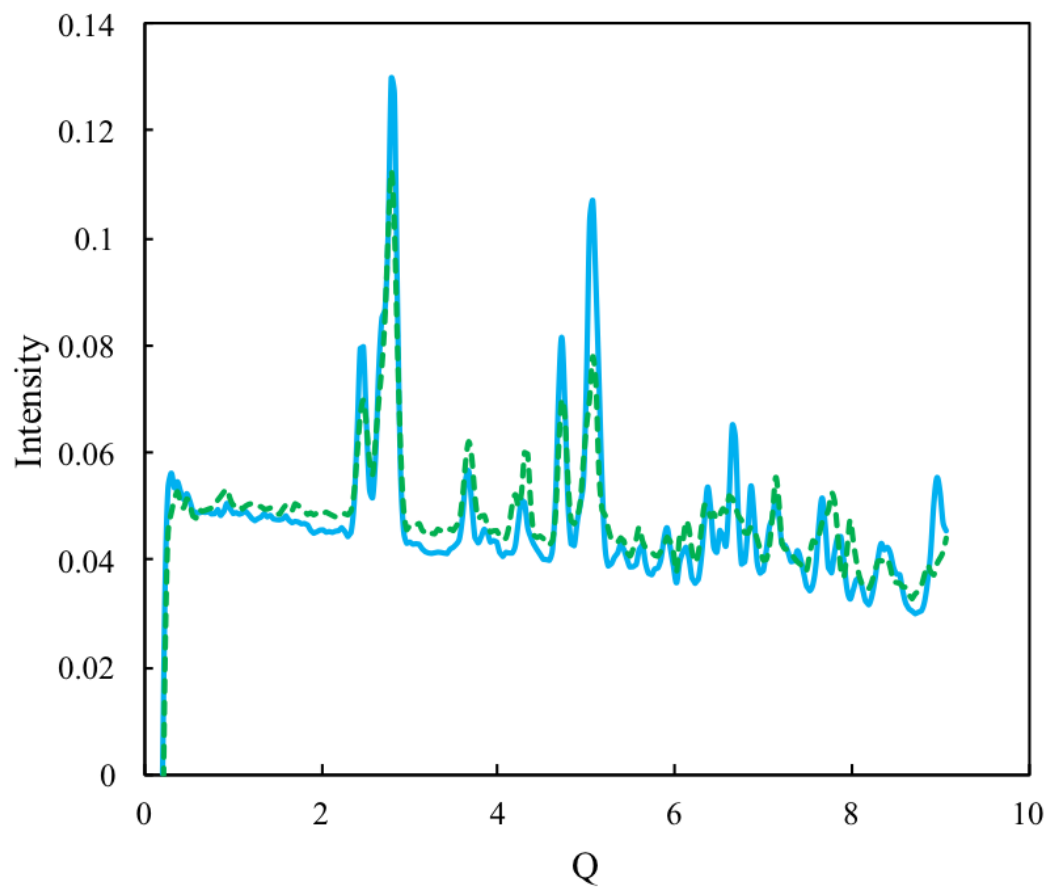


Figure 7.17. Diffraction pattern of the Ti-Nb alloy at 10 at. % Nb. The dashed line represents the slow cooled sample while the solid line represents the quenched sample.

Chapter 8 |

Conclusions and Future Work

8.1 Conclusions

In this dissertation, the effect of alloying elements on Ti-based alloys are systematically studied. The work begins by using first-principles based DFT calculations and the CALPHAD method to study the effect that the alloying elements Mo, Nb, Sn, Ta and Zr have on the equilibrium phase stability, thermodynamics, and elastic properties. The work uses the equation of states fitting of the energy vs. volume curves to get the ground state equilibrium properties. The Debye-Grüneisen model and phonon quasiharmonic approach are used to study the effect of temperature on the phase stability. A new theoretic framework is proposed to study the formation of the metastable phases. The accuracy of the theoretic framework and the transformation that occurs when these metastable phases form is studied using neutron scattering experiments. The compilation of the work develops a knowledge base for Ti-based alloys and will help to guide the future design of biocompatible implants. The main conclusions from this work are included below:

1. The thermodynamic descriptions were all incorporated into a complete database that accurately predicts the phase stability of the Ti-Mo-Nb-Sn-Ta-Zr systems. The thermodynamic descriptions of the pure elements are adopted from the SGTE database. All of the binary systems had previous thermodynamic descriptions available in literature except the Mo-Sn and Ta-Sn systems. All of the binary systems had previous thermodynamic descriptions available in literature except Mo-Sn and Ta-Sn. A previous model was evaluated for accuracy when available for the binary systems. The Sn-

Ta system was modeled in chapter 4. After evaluation the thermodynamic descriptions were incorporated into the present database. The binary interpolations of the Ti-containing ternary systems were plotted and compared with the available experimental data as well as the enthalpy of formation of the bcc phase calculated from first-principles based on DFT. The Ti-Sn-X systems ($X = \text{Mo, Nb, Ta, Zr}$) will be modeled in the future work with a thermodynamci description of the Mo-Sn system. The binary interpolations of the Ti-Nb-Zr and Ti-Ta-Zr systems had previously been plotted but no interaction parameters had been introduced. The present evaluation agreed with the previous evaluations and no ternary interaction parameters were introduced. The Ti-Mo-Zr system had previously been modeled and the present work agreed with the evaluation. The Ti-Mo-Nb, Ti-Mo-Ta and Ti-Nb-Ta systems had never previously been modeled. The present work evaluated interaction parameters for the Ti-Mo-Ta and Ti-Nb-Ta systems but didn't introduce any interaction parameters for the Ti-Mo-Nb system. The completed database is in appendix b.

2. Sn-Ta modeling was completed using data from DFT-based first-principles calculations and the available experimental data in the literature to model the Gibbs energies for the bcc and liquid solution phases and the stoichiometric Ta_3Sn and TaSn_2 phases of the Sn-Ta system. First-principles calculations were used to predict the enthalpy of formation of the bcc phase for the evaluation of interaction parameters in the phase. The decomposition temperature of Ta_3Sn was predicted to be 2884 °K. The completed thermodynamic description was complied into a tdb file in appendix b.
3. The effects of five alloying elements on the elastic properties of bcc Ti-X ($X = \text{Mo, Nb, Sn, Ta, Zr}$) alloys, including the elastic stiffness constants, bulk modulus, shear modulus, and Young's modulus, were systematically studied using first-principles calculations. The CALPAHD methodology was used to evaluate interaction parameters to predict the elastic properties as a function of composition. The calculations showed that 5.5, 11.5, 51.5, 9.5, and 4.0 at. % of Mo, Nb, Sn, Ta and Zr, respectively, were required to stabilize the bcc phase according to the Born criteria. The trends observed were summarized for each Ti-X ($X = \text{Mo, Nb, Sn, Ta, Zr}$) binary system. Alloying

with Mo, Nb, and Ta results in similar trends, which is probably because Mo, Nb, and Ta are strong bcc stabilizers and stable in the bcc structure at room temperature. The interaction parameters determined in the current work were used to predict the elastic properties of higher order alloys. The accuracy of database predictions of the Young's modulus was evaluated by comparing the calculated and experimental Young's moduli. Overall, the database provides good predictions of the elastic properties of Ti-alloys in the bcc phase as a function of composition.

4. The elastic properties of the bcc Ti-X-Y ternary alloys ($X \neq Y = \text{Mo, Nb, Sn, Ta, Zr}$), including the elastic stiffness constants, bulk modulus, shear modulus, and Young's modulus. The general CALPHAD modeling approach was used to fit ternary interaction parameters. From the elastic stiffness constant data, the Ti-X-Y ($X \neq Y = \text{Mo, Nb, Ta}$) show the same trends in the data. This is to be expected because Mo, Nb, and Ta are similar elements that are strong β -stabilizers and stable in the bcc phase at low temperatures. It was also seen that the Ti-X-Sn ($X = \text{Mo, Nb, Ta}$) alloys showed similar trends in the data for most of the elastic stiffness constants, so do the Ti-X-Zr ($X = \text{Mo, Nb, Ta}$) alloys. The present calculations showed that the bcc Ti-alloy was mechanically stabilized at compositions less than 91, 92, 95, 93, 91, 94, 87, 77, 89, and 80 at % Ti for the Ti-Mo-Nb, Ti-Mo-Ta, Ti-Mo-Zr, Ti-Nb-Zr, Ti-Sn-Zr, Ti-Ta-Zr, Ti-Mo-Sn, Ti-Nb-Sn, Ti-Nb-Ta and Ti-Sn-Ta alloys, respectively. As discussed above, Mo, Nb and Ta are strong β -stabilizers and thus the Ti-Mo-Nb, Ti-Mo-Ta, and Ti-Nb-Ta systems stabilize the bcc phase similarly. Also, discussed previously, Zr is a weak β -stabilizer alone but when alloyed with other elements it acts a strong β -stabilizer. This is observed with these results with the Ti-Mo-Zr, Ti-Nb-Zr, Ti-Ta-Zr systems all stabilizing the bcc phase at high Ti concentrations (95, 93, and 94 at.% respectively). Zr is even able to stabilize the Ti-Sn-Zr system at a high Ti concentration of 91 at.% Ti, even with Sn. Sn is not stable in the bcc phase and is not a β -stabilizer. So, when alloyed with Sn, a higher concentration of other alloying elements is needed to stabilize the bcc phase. The ternary interaction parameters were combined with the previously determined pure elements and binary interaction parameters to map some of the possible alloy compositions to find potential materials with a Young's modulus in the target

range for biomedical load-bearing implants. Overall, the introduction of the ternary interaction parameters improved the database's ability to predict the E of higher order alloys by a small amount. The complete database, however, satisfactorily predicts the elastic properties of higher order Ti-alloys.

5. The elastic stiffness constants and Young's moduli of the Ti-Nb system in the bcc, hcp, ω , and α'' phases. The E values were similar for the hcp and ω phase which makes sense since they both have hexagonal symmetry. The α'' phase has E values that are higher than the other three phase which explains why when formed the E increases. Experiments showed that up to 10 at. % Nb the samples formed solely the hcp phase and the database predicts the E values by an average variance of 8 GPa from the experimental E . The samples from 10 at. % Nb to 30 at. % Nb formed both the bcc and α'' or ω phases. If the samples are slow cooled then the samples form the bcc and ω phases. If the samples are quenched they form the bcc and α'' phases. Using experimentally determined phase fractions and the rule of mixtures, the database accurately predicts the E values by an average variance of 0.52 GPa when compared with the experimental E values. At Nb concentrations greater than 30 at. % Nb form solely the bcc phase and the database predicts the E values by an average variance of 7 GPa from the experimental E values. The phonon DOS at 300 °K differences between the slow cooled and quenched samples especially when looking at the entropy difference between the samples. Diffraction patterns from ARCS are difficult to fit but the phase fractions are approximated. The implementation of the new theoretic framework is ongoing but from the results here, if the phase fractions of the metastable phases can be predicted then the elastic database can accurately assess the Young's moduli and elastic stiffness constants.

8.2 Future Work

The following are presented as future work to be able to improve this thesis work:

1. Focusing on the modeling of the Sn binary and Ti-Sn-X ($X = Mo, Nb, Ta, Zr$) and incorporating them into this database would further improve the knowledge base of Ti-alloys that this thesis presents. As discussed, Sn is

being added due to its low cost and the fact that at low concentrations it doesn't effect the alloys biocompatibility. But even at low compositions having a better understanding of how Sn effects the phase stability would be helpful.

2. As discussed, introducing interaction parameters to describe the elastic properties for the non Ti-containing binary and ternary systems would improve the databases accuracy
3. The work on using the partition function approach will be continued. The next steps will be to calculate the helmholtz energies of all of the pure elements and to extend this to calculate better helmholtz energies for the metastable and unstable phases. The ability of the partition function approach to calculate more accurate entropies would be a great advancement in the field.

Appendix A | Ti-Mo-Nb-Ta-Zr Database

```
$*****  
$ The definition of the pure elements, vacancy and species  
$-----  
TEMPERATURE_LIMIT 0 6000.00 !  
ELEMENT /- ELECTRON_GAS 0.0000E+00 0.0000E+00 0.0000E+00!  
ELEMENT MO BCC_A2 95.94 4589.0 28.56 !  
ELEMENT NB BCC_A2 92.9064 5220.0 36.27 !  
ELEMENT TA BCC_A2 180.9479 5681.872 41.4718 !  
ELEMENT TI HCP_A3 4.7880E+01 4.8100E+03 3.0648E+01!  
ELEMENT ZR HCP_A3 9.1224E+01 5.5663E+03 3.9181E+01!  
ELEMENT VA VACUUM 0.0 0.0 0.0 !
```

```
$*****
```

```
$ The Gibbs energies of the elements  
$ in the stable and metastable forms from SGTE  
$-----  
$-----
```

```
* TI *
```

```
$-----  
$-----
```

```
FUNCTION GBCCTI
```

```
2.98150E+02 -1272.064+134.71418*T-25.5768*T*LN(T)
```

$-6.63845 \times 10^{-4} T^2 - 2.78803 \times 10^{-7} T^3 + 7208 T^*(-1); 1.15500 \times 10^3 Y$
 $+ 6667.385 + 105.366379 T - 22.3771 T \ln(T) + .00121707 T^2 - 8.4534 \times 10^{-7} T^3$
 $- 2002750 T^*(-1); 1.94100 \times 10^3 Y$
 $+ 26483.26 - 182.426471 T + 19.0900905 T \ln(T) - .02200832 T^2$
 $+ 1.228863 \times 10^{-6} T^3 + 1400501 T^*(-1); 4.00000 \times 10^3 N$ REF:20 !

FUNCTION GHSERTI

$2.98150 \times 10^2 - 8059.921 + 133.615208 T - 23.9933 T \ln(T)$
 $- .004777975 T^2 + 1.06716 \times 10^{-7} T^3 + 72636 T^*(-1); 9.00000 \times 10^2 Y$
 $- 7811.815 + 132.988068 T - 23.9887 T \ln(T) - .0042033 T^2 - 9.0876 \times 10^{-8} T^3$
 $+ 42680 T^*(-1); 1.15500 \times 10^3 Y$
 $+ 908.837 + 66.976538 T - 14.9466 T \ln(T) - .0081465 T^2 + 2.02715 \times 10^{-7} T^3$
 $- 1477660 T^*(-1); 1.94100 \times 10^3 Y$
 $- 124526.786 + 638.806871 T - 87.2182461 T \ln(T) + .008204849 T^2$
 $- 3.04747 \times 10^{-7} T^3 + 36699805 T^*(-1); 4.00000 \times 10^3 N$ REF:20 !

FUNCTION GFCCTI

$2.98150 \times 10^2 + 6000.1 T + GHSERTI; 6.00000 \times 10^3 N$ REF:20 !

FUNCTION GLIQTI

$2.98150 \times 10^2 + 12194.415 - 6.980938 T + GHSERTI; 1.30000 \times 10^3 Y$
 $+ 368610.36 - 2620.99904 T + 357.005867 T \ln(T) - .155262855 T^2$
 $+ 1.2254402 \times 10^{-5} T^3 - 65556856 T^*(-1) + GHSERTI; 1.94100 \times 10^3 Y$
 $+ 104639.72 - 340.070171 T + 40.9282461 T \ln(T) - .008204849 T^2$
 $+ 3.04747 \times 10^{-7} T^3 - 36699805 T^*(-1) + GHSERTI; 6.00000 \times 10^3 N$ REF:20 !

\$

\$

* MO *

\$

\$

FUNCTION GHSEMO

$298.15 - 7746.302 + 131.9197 T - 23.56414 T \ln(T)$
 $- .003443396 T^2 + 5.662834 \times 10^{-7} T^3 + 65812.39 T^*(-1)$
 $- 1.309265 \times 10^{-10} T^4; 2896.00 Y$
 $- 30556.41 + 283.559746 T - 42.63829 T \ln(T)$
 $- 4.849315 \times 10^{-9} T^3 + 33 T^*(-9); 4000.00 N$ REF:20 !

FUNCTION GLIQMO
298.15 41831.347-14.694912*T+4.24519E-22*T**7
+GHSERMO; 2896.00 Y
34095.373-11.890046*T+4.849315E33*T**(-9)+GHSERMO;
4000.00 N REF:20 !

FUNCTION GFCCMO
298.15 15200+0.63*T+GHSERMO; 4000.00 N REF:20 !

FUNCTION GHCPMO
298.15 11550+GHSERMO; 4000.00 N REF:20 !

\$_____

\$_____

* NB *

\$_____

\$_____

FUNCTION GHSERNB
2.98140E+02 -8519.353+142.045475*T
-26.4711*T*LN(T)+2.03475E-04*T**2-3.5012E-07*T**3
+93399*T**(-1); 2.75000E+03 Y
-37669.3+271.720843*T-41.77*T*LN(T)+1.528238E+32*T**(-9);
6.00000E+03 N REF:20 !

FUNCTION GHEXTNB
2.98150E+02 -8519.35+142.048*T
-26.4711*T*LN(T)+2.03475E-04*T**2-3.50119E-07*T**3
+93398.8*T**(-1); 6.00000E+03 N REF:23 !

FUNCTION GLIQNB
298.15 29781.555-10.816417*T
-3.06098E-23*T**7+GHSERNB; 2750.00 Y
+30169.901-10.964695*T-1.52824E32*T**(-9)+GHSERNB;
6000.00 N REF:20 !

FUNCTION GFCCNB
298.15 +13500+1.7*T+GHSERNB; 6000.00 N REF:20 !

FUNCTION GHCPNB
298.15 +10000+2.4*T+GHSERNB; 6000.00 N REF:20 !

\$

\$

* TA *

\$

\$

FUNCTION GHSERTA

2.98150E+02 -7285.889+119.139858*T
-23.7592624*T*LN(T)-.002623033*T**2+1.70109E-07*T**3
-3293*T**(-1); 1.30000E+03 Y
-22389.955+243.88676*T-41.137088*T*LN(T)+.006167572*T**2
-6.55136E-07*T**3+2429586*T**(-1); 2.50000E+03 Y
+229382.886-722.59722*T+78.5244752*T*LN(T)-.017983376*T**2
+1.95033E-07*T**3-93813648*T**(-1); 3.25800E+03 Y
-963392.734+2773.7774*T-337.227976*T*LN(T)+.039791303*T**2
-9.74251E-07*T**3+5.09949511E+08*T**(-1); 6.00000E+03 N REF:20 !

FUNCTION GFCCTA

2.98150E+02 +16000+1.7*T+GHSERTA; 6.00000E+03 N REF:20 !

FUNCTION GHCPTA

2.98150E+02 +12000+2.4*T+GHSERTA; 6.00000E+03 N REF:20 !

FUNCTION GLIQTA

2.98150E+02 +29160.975-7.578729*T+GHSERTA; 1.00000E+03 Y
+51170.228-181.121652*T+23.7872147*T*LN(T)-.009707033*T**2
+4.4449E-07*T**3-3520045*T**(-1)+GHSERTA; 1.30000E+03 Y
+66274.294-305.868555*T+41.1650403*T*LN(T)-.018497638*T**2
+1.269735E-06*T**3-5952924*T**(-1)+GHSERTA; 2.50000E+03 Y
-185498.547+660.615425*T-78.4965229*T*LN(T)+.00565331*T**2
+4.19566E-07*T**3+90290310*T**(-1)+GHSERTA; 3.29000E+03 Y
+1036069.47-2727.38037*T+320.319132*T*LN(T)-.043117795*T**2
+1.055148E-06*T**3-5.54714342E+08*T**(-1)+GHSERTA;
6.00000E+03 N REF:20 !

FUNCTION TATIB2

2.98150E+02 2500; 6.00000E+03 N REF:25 !

\$

\$
* ZR *
\$
\$
FUNCTION GLIQZR
2.98140E+02 +18147.69-9.080812*T
+1.6275E-22*T**7+GHSERZR; 2.12800E+03 Y
+17804.661-8.911574*T+1.342895E+31*T**(-9)+GHSERZR;
6.00000E+03 N REF:20 !
FUNCTION GBCCZR
2.98140E+02 -525.539+124.9457*T
-25.607406*T*LN(T)-3.40084E-04*T**2-9.729E-09*T**3
+25233*T**(-1)-7.6143E-11*T**4; 2.12800E+03 Y
-30705.955+264.284163*T-42.144*T*LN(T)+1.276058E+32*T**(-9);
6.00000E+03 N REF:20 !
FUNCTION GHSERZR
1.30000E+02 -7827.595+125.64905*T
-24.1618*T*LN(T)-.00437791*T**2+34971*T**(-1); 2.12800E+03 Y
-26085.921+262.724183*T-42.144*T*LN(T)-1.342895E+31*T**(-9);
6.00000E+03 N REF:20 !
\$
FUNCTION UN_ASS 298.15 0; 300 N !
\$

TYPE_DEFINITION % SEQ * !
TYPE_DEFINITION G SEQ * !
DEFINE_SYSTEM_DEFAULT SPECIE 5 !
DEFAULT_COMMAND DEF_SYS_ELEMENT VA !
\$

\$
PHASE LIQUID % 1 1.0 !

CONSTITUENT LIQUID :MO,TA,NB,TI,ZR: !

PARAMETER G(LIQUID, TI;0)
298.15 GLIQTI; 6000.00 N REF:20 !
PARAMETER G(LIQUID, MO;0)
298.15 GLIQMO; 6000.00 N REF:20 !
PARAMETER G(LIQUID, NB;0)
298.15 GLIQNB; 6000.00 N REF:20
PARAMETER G(LIQUID, TA;0)
298.15 GLIQT A; 6000.00 N REF:20 !
PARAMETER G(LIQUID, ZR;0)
298.15 +GLIQZR; 6000.00 N REF:20 !
PARAMETER G(LIQUID, MO, TI;0)
298.15 -9000.0+2*T; 6000.00 N REF:25 !
PARAMETER G(LIQUID, NB, TI;0)
298.15 +7406.1; 6000.00 N REF:23 !
PARAMETER G(LIQUID, TA, TI;0)
298.15 +1000; 6000.00 N REF:25 !
PARAMETER G(LIQUID, TA, TI;1)
298.15 -7000; 6000.00 N REF:25 !
PARAMETER G(LIQUID, TI, ZR;0)
298.15 -967.66; 6000.00 N REF:22 !
PARAMETER G(LIQUID, MO, NB;0) *
298.15 15253.7; 6000.00 N REF:21 !
PARAMETER G(LIQUID, MO, NB;1)
298.15 10594.2; 6000.00 N REF:21 !
PARAMETER G(LIQUID, MO, TA;0)
298.15 13978.9; 6000.00 N REF:21 !
PARAMETER G(LIQUID, MO, TA;1)
298.15 577.5; 6000.00 N REF:21 !
PARAMETER G(LIQUID, MO, ZR;0)
298.15 -24055.120+8.146158*T; 6000.00 N REF:26 !
PARAMETER G(LIQUID, MO, ZR;1)

298.15 -5132.1665+4.8041224*T; 6000.00 N REF:26 !

PARAMETER G(LIQUID,NB,TA;0)

298.15 0; 6000.00 N REF:21 !

PARAMETER G(LIQUID,NB,ZR;0)

298.15 10311; 6000.00 N REF:28 !

PARAMETER G(LIQUID,NB,ZR;1)

298.15 6709; 6000.00 N REF:28 !

PARAMETER G(LIQUID,TA,ZR;0)

298.15 13832.1; 6000.00 N REF:27 !

PARAMETER G(LIQUID,TA,ZR;1)

298.15 -7150; 6000.00 N REF:27 !

\$

PHASE BCC_A2 % 2 1 3 !

CONSTITUENT BCC_A2 :MO,TA,NB,TI,ZR:VA: !

PARAMETER G(BCC_A2,TI:VA;0)

298.15 +GBCCTI; 6000.0 N REF:20 !

PARAMETER G(BCC_A2,MO:VA;0)

298.15 +GHSERMO; 6000.00 N REF:20 !

PARAMETER G(BCC_A2,NB:VA;0)

298.15 +GHSERNB; 6000.00 N REF:20 !

PARAMETER G(BCC_A2,TA:VA;0)

298.15 +GHSERTA; 6000.00 N REF:20 !

PARAMETER G(BCC_A2,ZR:VA;0)

298.15 +GBCCZR; 6000.00 N REF:20 !

PARAMETER G(BCC_A2,MO,TI:VA;0)

298.15 2000.0; 6000.00 N REF:25 !

PARAMETER G(BCC_A2,MO,TI:VA;1)

298.15 -2000.0; 6000.00 N REF:25 !

PARAMETER G(BCC_A2,NB,TI:VA;0)

298.15 +13045.3; 6000.00 N REF:23 !

PARAMETER G(BCC_A2,TA,TI:VA;0)

298.15 12000; 6000.00 N REF:25 !

PARAMETER G(BCC_A2,TA,TI:VA;1)
298.15 -2500; 6000.00 N REF:25 !

PARAMETER G(BCC_A2,TI,ZR:VA;0)
298.15 -4346.16+5.48903*T; 6000.00 N REF:22 !

PARAMETER G(BCC_A2,MO,NB:VA;0)
298.15 -68202.6+29.85596*T; 6000.00 N REF:21 !

PARAMETER G(BCC_A2,MO,NB:VA;1)
298.15 8201.3; 6000.00 N REF:21 !

PARAMETER G(BCC_A2,MO,TA:VA;0)
298.15 -75129.2+30*T; 6000.00 N REF:21 !

PARAMETER G(BCC_A2,MO,TA:VA;1)
298.15 6039.24; 6000.00 N REF:21 !

PARAMETER G(BCC_A2,MO,ZR:VA;0)
298.15 +17935.985+3.102*T; 6000.00 N REF:26 !

PARAMETER G(BCC_A2,MO,ZR:VA;1)
298.15 -990.9911+4.299*T; 6000.00 N REF:26 !

PARAMETER G(BCC_A2,NB,TA:VA;0)
298.15 1298.02870; 6000.00 N REF:21 !

PARAMETER G(BCC_A2,NB,ZR:VA;0)
298.15 +15911+3.35*T; 6000.00 N REF:28 !

PARAMETER G(BCC_A2,NB,ZR:VA;1)
298.15 +3919-1.091*T; 6000.00 N REF:28 !

PARAMETER G(BCC_A2,ZR,TA:VA;0)
298.15 29499.6+2.6723*T; 6000.00 N REF:27 !

PARAMETER G(BCC_A2,ZR,TA:VA;1)
298.15 -4396.2+4.4302*T; 6000.00 N REF:27 !

PARAMETER G(BCC_A2,ZR,TA:VA;2)
298.15 -6353.3+4.9066*T; 6000.00 N REF:27 !

PARAMETER G(BCC_A2,MO,TA,TI:VA;0) 298.15 0; 6000.00 N !

PARAMETER G(BCC_A2,MO,TA,TI:VA;1) 298.15 0; 6000.00 N !

PARAMETER G(BCC_A2,MO,TA,TI:VA;2)
298.15 -1.5473118E+05; 6000.00 N !

PARAMETER G(BCC_A2,NB,TA,TI:VA;0)

2.98150E+02 -1.3660332E+05; 6.00000E+03 N !
PARAMETER G(BCC_A2,NB,TA,TI:VA;1)
2.98150E+02 -1.3660269E+05; 6.00000E+03 N !
PARAMETER G(BCC_A2,NB,TA,TI:VA;2)
2.98150E+02 0; 6.00000E+03 N !
\$
PHASE HCP_A3 % 2 1 .5 !
CONSTITUENT HCP_A3 :NB,TI%,ZR,TA,MO : VA% : !

PARAMETER G(HCP_A3, TI:VA;0)
298.15 +GHSERTI; 4000.00 N REF:20 !
PARAMETER G(HCP_A3, MO:VA;0)
298.15 +GHCPMO; 5000.00 N REF:20 !
PARAMETER G(HCP_A3, NB:VA;0)
298.15 +GHCPNB; 6000.00 N REF:20 !
PARAMETER G(HCP_A3, TA:VA;0)
298.15 +GHCPTA; 6000.00 N REF:20 !
PARAMETER G(HCP_A3, ZR:VA;0)
298.15 +GHSERZR; 6000.00 N REF:20 !
PARAMETER G(HCP_A3, MO, TI:VA;0)
298.15 22760-6*T; 6000.00 N REF:25 !
PARAMETER G(HCP_A3, NB, TI:VA;0)
298.15 +11742.4; 6000.00 N REF:23 !
PARAMETER G(HCP_A3, TA, TI:VA;0)
298.15 8500; 6000.00 N REF:25 !
PARAMETER G(HCP_A3, TI, ZR:VA;0)
298.15 +5133.02; 6000.00 N REF:22 !
PARAMETER G(HCP_A3, MO, ZR:VA;0)
298.15 +26753.79+4.556*T; 6000.00 N REF:26 !
PARAMETER G(HCP_A3, NB, ZR:VA;0)
298.15 24411; 6000.00 N REF:28 !
PARAMETER G(HCP_A3, ZR, TA:VA;0)
298.15 +30051.7; 6000.00 N REF:27 !

\$
TYPE_DEFINITION * GES A_P_D FCC_A1 MAGNETIC -3.0 2.80000E-01 !
PHASE FCC_A1 %* 2 1 1 !
CONSTITUENT FCC_A1 :MO,TA,ZR,NB : VA% : !

PARAMETER G(FCC_A1,TA:VA;0)
298.15 +GFCCTI; 4000.00 N REF:20 !
PARAMETER G(FCC_A1,MO:VA;0)
298.15 +GFCCMO; 5000.00 N REF:20 !
PARAMETER G(FCC_A1,NB:VA;0)
298.15 +GFCCNB; 6000.00 N REF:20 !
PARAMETER G(FCC_A1,TA:VA;0)
298.15 +GFCCTA; 6000.00 N REF:20 !
PARAMETER G(FCC_A1,MO,TA:VA;0)
298.15 16500.0; 6000.00 N REF:25 !
PARAMETER G(FCC_A1,TA,TI:VA;0)
298.15 8500; 6000.00 N REF:25 !

\$
PHASE AL3M_D022 % 2 3 1 !
CONSTITUENT AL3M_D022 :TI,MO : TA,TI,MO : !

PARAMETER G(AL3M_D022,TA:TI;0)
298.15 +4*GFCCTI; 6000.00 N REF:25 !
PARAMETER G(AL3M_D022,MO:MO;0)
298.15 +4*GFCCMO; 6000.00 N REF:25 !
PARAMETER G(AL3M_D022,TI:MO;0)
298.15 GFCCMO+3.0*GFCCTI; 6000.00 N REF:25 !
PARAMETER G(AL3M_D022,MO:TI;0)
298.15 3*GFCCMO+GFCCTI; 6000.00 N REF:25 !
PARAMETER G(AL3M_D022,TA:TA;0)
298.15 +3*GFCCTI+GFCCTA; 6000.00 N REF:25 !

TYPE_DEFINITION & GES A_P_D ALM_D019 MAGNETIC -3.0 2.80000E-01 !

PHASE ALM_D019 %& 2 3 1 !

CONSTITUENT ALM_D019 :MO,TA,TI% : MO,TA,TI : !

PARAMETER G(ALM_D019,TA:TI;0)
298.15 +4.0+4.0*GHSERTI; 6000.00 N REF:25 !
PARAMETER G(ALM_D019,TA:MO;0) 298.15 0; 6000 N!
PARAMETER G(ALM_D019,MO:TA;0) 298.15 0; 6000 N!
PARAMETER G(ALM_D019,MO:MO;0)
298.15 +4.0*GHCPMO; 6000.00 N REF:25 !
PARAMETER G(ALM_D019,TA:TA;0)
298.15 +4.0*GHCPTA; 6000.00 N REF:25 !
PARAMETER G(ALM_D019,TI:MO;0)
298.15 +17072.0-4.5*T+GHCPMO+3.0*GHSERTI; 6000.00 N REF:25 !
PARAMETER G(ALM_D019,MO:TI;0)
298.15 +17072.0-4.5*T+3.0*GHCPMO+GHSERTI; 6000.00 N REF:25 !
PARAMETER G(ALM_D019,TI:TA;0)
298.15 +6376+3.0*GHSERTI+GHCPTA; 6000.00 N REF:25 !
PARAMETER G(ALM_D019,TA:TI;0)
298.15 +6376+3.0*GHCPTA+GHSERTI; 6000.00 N REF:25 !
PARAMETER G(ALM_D019,MO,TI:MO;0)
298.15 +51212-13.5*T; 6000.00 N REF:25 !
PARAMETER G(ALM_D019,MO,TI:TI;0)
298.15 +51212-13.5*T; 6000.00 N REF:25 !
PARAMETER G(ALM_D019,MO:MO,TI;0)
298.15 +5692-1.5*T; 6000.00 N REF:25 !
PARAMETER G(ALM_D019,TI:MO,TI;0)
298.15 +5692-1.5*T; 6000.00 N REF:25 !
PARAMETER G(ALM_D019,TA,TI:TA;0)
298.15 +19128; 6000.00 N REF:25 !
PARAMETER G(ALM_D019,TA,TI:TI;0)
298.15 +19128; 6000.00 N REF:25 !
PARAMETER G(ALM_D019,TA:TA,TI;0)
298.15 2128; 6000.00 N REF:25 !

```
PARAMETER G(ALM_D019, TI:TA, TI;0)
298.15 +2128; 6000.00 N REF:25 !
$-----
TYPE_DEFINITION ' GES A_P_D ALTI MAGNETIC -1.0 4.00000E-01 !
PHASE ALTI %' 2 1 1 !
CONSTITUENT ALTI :MO,TA,TI : MO,TA,TI% : !
```

```
PARAMETER G(ALTI, TI:TI;0)
298.15 +2*GFCCTI; 6000.00 N REF:25 !
PARAMETER G(ALTI, MO:MO;0)
298.15 +2*GFCCMO; 6000.00 N REF:25 !
PARAMETER G(ALTI, TA:TA;0)
298.15 +2*GFCCTA; 6000.00 N REF:25 !
PARAMETER G(ALTI, TI:MO;0)
298.15 8250+GFCCMO+GFCCTI; 6000.00 N REF:25 !
PARAMETER G(ALTI, MO:TI;0)
298.15 8250+GFCCMO+GFCCTI; 6000.00 N REF:25 !
PARAMETER G(ALTI, TI:TA;0)
298.15 +4250+GFCCTI+GFCCTA; 6000.00 N REF:25 !
PARAMETER G(ALTI, TA:TI;0)
298.15 +4250+GFCCTA+GFCCTI; 6000.00 N REF:25 !
PARAMETER G(ALTI, MO, TI:MO;0)
298.15 8250; 6000.00 N REF:25 !
PARAMETER G(ALTI, MO, TI:TI;0)
298.15 8250; 6000.00 N REF:25 !
PARAMETER G(ALTI, MO:MO, TI;0)
298.15 8250; 6000.00 N REF:25 !
PARAMETER G(ALTI, TI:MO, TI;0)
298.15 8250; 6000.00 N REF:25 !
PARAMETER G(ALTI, TA, TI:TA;0)
298.15 4250; 6000.00 N REF:25 !
PARAMETER G(ALTI, TA, TI:TI;0)
298.15 4250; 6000.00 N REF:25 !
```

PARAMETER G(ALTI,TA:TA,TI;0)
298.15 4250; 6000.00 N REF:25 !
PARAMETER G(ALTI,TI:TA,TI;0)
298.15 4250; 6000.00 N REF:25 !
\$-----
TYPE_DEFINITION) GES AMEND_PHASE_DESCRIPTION
BCC_B2 DIS_PART BCC_A2,,,!
PHASE BCC_B2 %) 3 .5 .5 3 !
CONSTITUENT BCC_B2 :MO,NB,TA,TI,ZR : MO,NB,TA,TI%,ZR : VA : !

PARAMETER G(BCC_B2,MO:MO:VA;0) 298.15 0; 6000 N REF:25!
PARAMETER G(BCC_B2,TA:TA:VA;0) 298.15 0; 6000 N REF:25 !
PARAMETER G(BCC_B2,TI:TI:VA;0) 298.15 0; 6000 N REF:25 !
PARAMETER G(BCC_B2,TI:MO:VA;0)
298.15 10000.0; 6000.00 N REF:25 !
PARAMETER G(BCC_B2,MO:TI:VA;0)
298.15 10000.0; 6000.00 N REF:25 !
PARAMETER G(BCC_B2,TI:TA:VA;0)
298.15 +5000.0; 6000.00 N REF:25 !
PARAMETER G(BCC_B2,TA:TI:VA;0)
298.15 +5000.0; 6000.00 N REF:25 !
\$-----
PHASE BCT_A5 % 1 1.0 !
CONSTITUENT BCT_A5 :TI : !

PARAMETER G(BCT_A5,TI;0)
298.15 +4602.2+GHserti; 3000.00 N REF:20 !
\$-----
PHASE CBCC_A12 % 2 1 1 !
CONSTITUENT CBCC_A12 :TI : VA : !

PARAMETER G(CBCC_A12,TI:VA;0)
298.15 +4602.2+GHserti; 6000.00 N REF:20 !

\$

PHASE CUB_A13 % 2 1 1 !
CONSTITUENT CUB_A13 :TI : VA : !

PARAMETER G(CUB_A13, TI:VA;0)
298.15 +7531.2+GHserti; 6000.00 N REF:20 !

\$

PHASE DIAMOND_A4 % 1 1.0 !
CONSTITUENT DIAMOND_A4 :TI : !

PARAMETER G(DIAMOND_A4, TI;0)
298.15 +25000+GHserti; 6000.00 N REF:20 !

\$

PHASE LAVES_C14 % 2 2 1 !
CONSTITUENT LAVES_C14 :TI : TI% : !

PARAMETER G(LAVES_C14, TI:TI;0)
298.15 +15000+3*GHserti; 6000.00 N REF:20 !

\$

PHASE LAVES_C15 % 2 2 1 !
CONSTITUENT LAVES_C15 :TI,MO,ZR : TI,MO,ZR : !

PARAMETER G(LAVES_C15, TI:TI;0)

298.15 +15000+3*GHserti; 6.00000E+03 N REF:24!

PARAMETER G(LAVES_C15, MO:MO;0)

298.15 +3*GHSERMO+15000; 6000 N REF:26 !

PARAMETER G(LAVES_C15, ZR:ZR;0)

298.15 +3*GHSERZR+15000; 6000 N REF:26 !

PARAMETER G(LAVES_C15, TI:MO;0)

298.15 +GHSERMO+2*GHserti+15000; 6000 N REF:24 !

PARAMETER G(LAVES_C15, MO:TI;0)

298.15 +2*GHSERMO+GHserti+15000; 6000 N REF:24 !

PARAMETER G(LAVES_C15, TI:ZR;0)

298.15 +2*GHSERTI+GHSERZR+9000; 6000 N REF:24 !
PARAMETER G(LAVES_C15,ZR:TI;0)
298.15 +GHSERTI+2*GHSERZR+15000; 6000 N REF:24 !
PARAMETER G(LAVES_C15,MO:ZR;0)
298.15 +2*GHSERMO+GHSERZR-21734.78+0.1441789*T; 6000 N REF:26 !
PARAMETER G(LAVES_C15,ZR:MO;0)
298.15 +GHSERMO+2*GHSERZR+21734.78-0.1441789*T; 6000 N REF:26 !
PARAMETER G(LAVES_C15,MO:MO,ZR;0) 298.15 +60000; 6000 N REF:26 !
PARAMETER G(LAVES_C15,ZR:MO,ZR;0) 298.15 +60000; 6000 N REF:26 !
PARAMETER G(LAVES_C15,MO,ZR:MO;0) 298.15 +100000; 6000 N REF:26 !
PARAMETER G(LAVES_C15,MO,ZR:ZR;0) 298.15 +100000; 6000 N REF:26 !
PARAMETER G(LAVES_C15,TI:MO,ZR;0) 298.15 +60000; 6000 N REF:27 !
PARAMETER G(LAVES_C15,MO,ZR:TI;0) 298.15 +100000; 6000 N REF:27 !
\$

PHASE OMEGA % 2 1 .5 !
CONSTITUENT OMEGA :NB,TI% : VA% : !

PARAMETER G(OMEGA,ZR;0)
298.15 -8878.082+144.432234*T
-26.8556*T*LN(T)-.002799446*T**2+38376*T**(-1); 2128 Y
-29500.524+265.290858*T-42.144*T*LN(T)
+7.17445E+31*T**(-9); 6000 N REF:20 !
PARAMETER G(OMEGA,TI:VA;0)
298.15 1886.7-0.15161*T+GHSERTI; 4.00000E+03 N REF:23 !
PARAMETER G(OMEGA,NB:VA;0)
2.98150E+02 15000+2.4*T++GHSERNB; 6.00000E+03 N REF:23 !
PARAMETER G(OMEGA,NB,TI:VA;0)
298.15 -3775.9; 6000.00 N REF:23 !
\$

PHASE SI3TI5 % 3 2 3 3 !
CONSTITUENT SI3TI5 :TI : TI : TI : !

PARAMETER G(SI3TI5,TI:TI:TI;0)

298.15 +40000+20*T+8*GHSERTI; 6000.00 N REF:20 !

\$-----

PHASE SNTI3 % 2 1 3 !

CONSTITUENT SNTI3 :TI : TI% : !

PARAMETER G(SNTI3,TI:TI;0)

298.15 +4*GHSERTI+4; 6000.00 N REF:20 !

\$-----

PHASE ORTHORHOMBIC_A20 % 1 1.0 !

CONSTITUENT ORTHORHOMBIC_A20 :ZR : !

PARAMETER G(ORTHORHOMBIC_A20,ZR;0)

298.15 +4474.461+124.9457*T

-25.607406*T*LN(T)-3.40084E-04*T**2-9.729E-09*T**3

+25233*T**(-1)-7.6143E-11*T**4; 2128 Y

-25705.955+264.284163*T-42.144*T*LN(T)

+1.276058E+32*T**(-9); 6000 N REF:20 !

\$-----

PHASE TETRAGONAL_U % 1 1.0 !

CONSTITUENT TETRAGONAL_U :ZR : !

PARAMETER G(TETRAGONAL_U,ZR;0)

298.15 +4474.461+124.9457*T

-25.607406*T*LN(T)-3.40084E-04*T**2-9.729E-09*T**3

+25233*T**(-1)-7.6143E-11*T**4; 2128 Y

-25705.955+264.284163*T-42.144*T*LN(T)

+1.276058E+32*T**(-9); 6000 N REF:20 !

\$-----

DATABASE_INFO 'FOR THE TI_MO_NB_TA_ZR SYSTEM' !

LIST_OF_REFERENCES

NUMBER SOURCE

20 'A.T. Dinsdale, SGTE Data for Pure Elements, CALPHAD.

-
- 15 (1991) 317-425.'
- 21 'W. Xiong, Y. Du, Y. Liu, B.Y. Huang, H.H. Xu, H.L. Chen, et al., Thermodynamic assessment of the Mo-Nb-Ta system, Calphad-Computer Coupling Phase Diagrams Thermochem. 28 (2004) 133-140.'
- 22 'K.C.H. Kumar, P. Wollants, L. Delaey, Thermodynamic assessment of the Ti-Zr system and calculation of the Nb-Ti-Zr phase-diagram, J. Alloys Compd. 206 (1994) 121-127.'
- 23 'Y.L. Zhang, H.S. Liu, Z.P. Jin, Thermodynamic assessment of the Nb-Ti system, Calphad-Computer Coupling Phase Diagrams Thermochem. 25 (2001) 305-317.'
- 24 'S. Kar, D.M. Lipkin, A CALPHAD-based phase equilibrium model of Mo-Ti-Zr-C, in: TMS 2008 Annu. Meet. Suppl. Proceedings, Vol 2 Mater. Charact. Comput. Model., Minerals, Metals & Materials Soc, Warrendale, 2008: pp. 237-243.'
- 25 'I. Ansara, A.T. Dinsdale, M.H. Rand, COST 507: thermochemical database for light metal alloys, European Communities, Brussels and Luxembourg, 1998.'
- 26 'R.J. Perez, B. Sundman, Thermodynamic assessment of the Mo-Zr binary phase diagram, Calphad-Computer Coupling Phase Diagrams Thermochem. 27 (2003) 253-262.'
- 27 'A.F. Guillermet, Phase-diagram and thermochemical properties of the Zr-Ta system - an assessment based on Gibbs energy modeling, J. Alloys Compd. 226 (1995) 174-184.'
- 28 'A.F. Guillermet, Thermodynamic analysis of the stable phases in the Zr-Nb system and calculation of the phase-diagram, Zeitschrift Fur Met. 82 (1991) 478-487.'
- !
-

Appendix B |

Sn-Ta Database

```
$*****  
$ The definition of the pure elements, vacancy and species  
$-----  
ELEMENT /- ELECTRON_GAS 0.0000E+00 0.0000E+00 0.0000E+00!  
ELEMENT VA VACUUM 0.0000E+00 0.0000E+00 0.0000E+00!  
ELEMENT SN BCT_A5 1.1871E+02 6.3220E+03 5.1195E+01!  
ELEMENT TA BCC_A2 1.8095E+02 5.6819E+03 4.1472E+01!
```

```
$*****
```

```
$ The Gibbs energies of the elements  
$ in the stable and metastable forms from SGTE  
$-----  
$-----
```

* TA *

```
$-----  
$-----
```

FUNCTION GHSERTA

```
298.15 -7285.889+119.139857*T-23.7592624*T*LN(T)  
.002623033*T**2+1.70109E-07*T**3-3293*T**(-1); 1300 Y  
-22389.955+243.88676*T-41.137088*T*LN(T)+.006167572*T**2  
-6.55136E-07*T**3+2429586*T**(-1); 2500 Y  
+229382.886-722.59722*T+78.5244752*T*LN(T)-.017983376*T**2
```

+1.95033E-07*T**3-93813648*T**(-1); 3290 Y
-1042384.01+2985.49125*T-362.159132*T*LN(T)+.043117795*T**2
-1.055148E-06*T**3+5.54714342E+08*T**(-1); 6000 N REF20 !

FUNCTION GFCCTA

298.15 +8714.111+120.839857*T-23.7592624*T*LN(T)
.002623033*T**2+1.70109E-07*T**3-3293*T**(-1); 1300 Y
-6389.955+245.58676*T-41.137088*T*LN(T)+.006167572*T**2
-6.55136E-07*T**3+2429586*T**(-1); 2500 Y
+245382.886-720.89722*T+78.5244752*T*LN(T)-.017983376*T**2
+1.95033E-07*T**3-93813648*T**(-1); 3290 Y
-1026384.01+2987.19125*T-362.159132*T*LN(T)+.043117795*T**2
-1.055148E-06*T**3+5.54714342E+08*T**(-1); 6000 N REF20 !

FUNCTION GHCPTA

298.15 +4714.111+121.539857*T-23.7592624*T*LN(T)
.002623033*T**2+1.70109E-07*T**3-3293*T**(-1); 1300 Y
-10389.955+246.28676*T-41.137088*T*LN(T)+.006167572*T**2
-6.55136E-07*T**3+2429586*T**(-1); 2500 Y
+241382.886-720.19722*T+78.5244752*T*LN(T)-.017983376*T**2
+1.95033E-07*T**3-93813648*T**(-1); 3290 Y
-1030384.01+2987.89125*T-362.159132*T*LN(T)+.043117795*T**2
-1.055148E-06*T**3+5.54714342E+08*T**(-1); 6000 N REF20 !

FUNCTION GLIQTA

298.15 +21875.086+111.561128*T-23.7592624*T*LN(T)
.002623033*T**2+1.70109E-07*T**3-3293*T**(-1); 1000 Y
+43884.339-61.981795*T+.0279523*T*LN(T)-.012330066*T**2
+6.14599E-07*T**3-3523338*T**(-1); 3290 Y
-6314.543+258.110873*T-41.84*T*LN(T); 6000 N REF20 !

\$_____

\$_____

* SN *

\$_____

\$_____

FUNCTION GHSERSN

100 -7958.517+122.765451*T-25.858*T*LN(T)
+5.1185E-04*T**2-3.192767E-06*T**3+18440*T**(-1); 250 Y
-5855.135+65.443315*T-15.961*T*LN(T)-.0188702*T**2+3.121167E-06*T**3
-61960*T**(-1); 505.08 Y
+2524.724+4.005269*T-8.2590486*T*LN(T)-.016814429*T**2
+2.623131E-06*T**3-1081244*T**(-1)-1.2307E+25*T**(-9); 800 Y
-8256.959+138.99688*T-28.4512*T*LN(T)-1.2307E+25*T**(-9); 3000 N REF20 !

FUNCTION GBCCSN

100 -3558.517+116.765451*T-25.858*T*LN(T)
+5.1185E-04*T**2-3.192767E-06*T**3+18440*T**(-1); 250 Y
-1455.135+59.443315*T-15.961*T*LN(T)-.0188702*T**2+3.121167E-06*T**3
-61960*T**(-1); 505.08 Y
+6924.724-1.994731*T-8.2590486*T*LN(T)-.016814429*T**2
+2.623131E-06*T**3-1081244*T**(-1)-1.2307E+25*T**(-9); 800 Y
-3856.959+132.99688*T-28.4512*T*LN(T)-1.2307E+25*T**(-9); 3000 N REF20 !

FUNCTION GA12SN

100 -5958.517+122.765451*T-25.858*T*LN(T)
+5.1185E-04*T**2-3.192767E-06*T**3+18440*T**(-1); 250 Y
-3855.135+65.443315*T-15.961*T*LN(T)-.0188702*T**2+3.121167E-06*T**3
-61960*T**(-1); 505.08 Y+4524.724+4.005269*T-8.2590486*T*LN(T)
-.016814429*T**2+2.623131E-06*T**3-1081244*T**(-1)-1.2307E+25*T**(-9); 800 Y
-6256.959+138.99688*T-28.4512*T*LN(T)-1.2307E+25*T**(-9); 3000 N REF20 !

FUNCTION GA13SN

100 -5958.517+122.765451*T-25.858*T*LN(T)
+5.1185E-04*T**2-3.192767E-06*T**3+18440*T**(-1); 250 Y
-3855.135+65.443315*T-15.961*T*LN(T)-.0188702*T**2+3.121167E-06*T**3
-61960*T**(-1); 505.08 Y
+4524.724+4.005269*T-8.2590486*T*LN(T)-.016814429*T**2
+2.623131E-06*T**3-1081244*T**(-1)-1.2307E+25*T**(-9); 800 Y
-6256.959+138.99688*T-28.4512*T*LN(T)-1.2307E+25*T**(-9); 3000 N REF20 !

FUNCTION GDIAMOND

100 -9579.608+114.007785*T-22.972*T*LN(T)-.00813975*T**2
+2.7288E-06*T**3+25615*T**(-1); 298.15 Y

$-9063.001 + 104.84654T - 21.5750771T\ln(T) - .008575282T^{**2}$
 $+ 1.784447E-06T^{**3} - 2544T^{**(-1)}; 800 Y$
 $-10909.351 + 147.396535T - 28.4512T\ln(T); 3000 N \text{ REF20 !}$
FUNCTION GFCCSN
 $298.15 - 345.135 + 56.983315T - 15.961T\ln(T) - .0188702T^{**2}$
 $+ 3.121167E-06T^{**3} - 61960T^{**(-1)}; 505.08 Y$
 $+ 8034.724 - 4.454731T - 8.2590486T\ln(T) - .016814429T^{**2}$
 $+ 2.623131E-06T^{**3} - 1081244T^{**(-1)} - 1.2307E + 25T^{**(-9)}; 800 Y$
 $-2746.959 + 130.53688T - 28.4512T\ln(T) - 1.2307E + 25T^{**(-9)}; 3000 N \text{ REF20 !}$
FUNCTION GHCPSN
 $298.15 - 1955.135 + 57.797315T - 15.961T\ln(T)$
 $- .0188702T^{**2} + 3.121167E-06T^{**3} - 61960T^{**(-1)}; 505.08 Y$
 $+ 6424.724 - 3.640731T - 8.2590486T\ln(T) - .016814429T^{**2}$
 $+ 2.623131E-06T^{**3} - 1081244T^{**(-1)} - 1.2307E + 25T^{**(-9)}; 800 Y$
 $-4356.959 + 131.35088T - 28.4512T\ln(T) - 1.2307E + 25T^{**(-9)}; 3000 N \text{ REF20 !}$
FUNCTION GHCPZN_S
 $298.15 - 1950.135 + 57.797315T - 15.961T\ln(T)$
 $- .0188702T^{**2} + 3.121167E-06T^{**3} - 61960T^{**(-1)}; 505.08 Y$
 $+ 6429.724 - 3.640731T - 8.2590486T\ln(T) - .016814429T^{**2}$
 $+ 2.623131E-06T^{**3} - 1081244T^{**(-1)} - 1.2307E + 25T^{**(-9)}; 800 Y$
 $-4351.959 + 131.35088T - 28.4512T\ln(T) - 1.2307E + 25T^{**(-9)}; 3000 N \text{ REF20 !}$
FUNCTION GLIQSN
 $100 - 855.425 + 108.677684T - 25.858T\ln(T) + 5.1185E-04T^{**2}$
 $- 3.192767E-06T^{**3} + 18440T^{**(-1)} + 1.47031E-18T^{**7}; 250 Y$
 $+ 1247.957 + 51.355548T - 15.961T\ln(T) - .0188702T^{**2} + 3.121167E-06T^{**3}$
 $- 61960T^{**(-1)} + 1.47031E-18T^{**7}; 505.08 Y$
 $+ 9496.31 - 9.809114T - 8.2590486T\ln(T) - .016814429T^{**2}$
 $+ 2.623131E-06T^{**3} - 1081244T^{**(-1)}; 800 Y$
 $-1285.372 + 125.182498T - 28.4512T\ln(T); 3000 N \text{ REF20 !}$
FUNCTION GA7SN
 $100 - 5923.517 + 122.765451T - 25.858T\ln(T)$
 $+ 5.1185E-04T^{**2} - 3.192767E-06T^{**3} + 18440T^{**(-1)}; 250 Y$
 $- 3820.135 + 65.443315T - 15.961T\ln(T) - .0188702T^{**2} + 3.121167E-06T^{**3}$

-61960*T**(-1); 505.08 Y
+4559.724+4.005269*T-8.2590486*T*LN(T)-.016814429*T**2
+2.623131E-06*T**3-1081244*T**(-1)-1.2307E+25*T**(-9); 800 Y
-6221.959+138.99688*T-28.4512*T*LN(T)-1.2307E+25*T**(-9); 3000 N REF20 !

FUNCTION GA6SN

298.15 -468.135+57.181195*T-15.961*T*LN(T)-.0188702*T**2
+3.121167E-06*T**3-61960*T**(-1); 505.08 Y
+7911.724-4.256851*T-8.2590486*T*LN(T)-.016814429*T**2
+2.623131E-06*T**3-1081244*T**(-1)-1.2307E+25*T**(-9); 800 Y
-2869.959+130.73476*T-28.4512*T*LN(T)-1.2307E+25*T**(-9); 3000 N REF20 !
\$

FUNCTION UN_ASS 298.15 +0.0; 300 N !

\$

TYPE_DEFINITION % SEQ *!

DEFINE_SYSTEM_DEFAULT ELEMENT 2 !

DEFAULT_COMMAND DEF_SYS_ELEMENT VA /- !

\$

\$

TYPE_DEFINITION & GES A_P_D BCC_A2 MAGNETIC -1.0 4.00000E-01 !

PHASE BCC_A2 %& 2 1 3 !

CONSTITUENT BCC_A2 :SN,TA : VA : !

PARAMETER G(BCC_A2,SN:VA;0)

100 +GBCCSN; 3000 N REF20 !

PARAMETER G(BCC_A2,TA:VA;0)

298.15 +GHSERTA; 6000 N REF20 !

PARAMETER G(BCC_A2,SN,TA:VA;0)

298.15 7.0451375E+04; 6000 N !

PARAMETER G(BCC_A2,SN,TA:VA;1)

298.15 1.1223739E+05; 6000 N !

\$

PHASE BCT_A5 % 1 1.0 !

CONSTITUENT BCT_A5 :SN : !

PARAMETER G(BCT_A5,SN;0)

100 +GHSERSN; 3000 N REF20 !

\$

TYPE_DEFINITION ' GES A_P_D CBCC_A12 MAGNETIC -3.0 2.80000E-01 !
 PHASE CBCC_A12 %' 2 1 1 !
 CONSTITUENT CBCC_A12 :SN : VA : !

PARAMETER G(CBCC_A12,SN:VA;0) 100 +GA12SN; 3000 N REF20 !

\$

PHASE CUB_A13 % 2 1 1 !
 CONSTITUENT CUB_A13 :SN : VA : !

PARAMETER G(CUB_A13,SN:VA;0) 100 +GA13SN; 3000 N REF20 !

\$

PHASE DIAMOND_A4 % 1 1.0 !
 CONSTITUENT DIAMOND_A4 :SN : !

PARAMETER G(DIAMOND_A4,SN;0) 100 +GDIAMOND; 3000 N REF20 !

\$

TYPE_DEFINITION (GES A_P_D FCC_A1 MAGNETIC -3.0 2.80000E-01 !
 PHASE FCC_A1 %(2 1 1 !
 CONSTITUENT FCC_A1 :SN,TA : VA : !

PARAMETER G(FCC_A1,SN:VA;0) 298.15 +GFCCSN; 3000 N REF20 !
 PARAMETER G(FCC_A1,TA:VA;0) 298.15 +GFCCTA; 6000 N REF20 !

\$

TYPE_DEFINITION) GES A_P_D HCP_A3 MAGNETIC -3.0 2.80000E-01 !
 PHASE HCP_A3 %) 2 1 .5 !
 CONSTITUENT HCP_A3 :SN,TA : VA : !

PARAMETER G(HCP_A3,SN:VA;0) 298.15 +GHCPSEN; 3000 N REF20 !
 PARAMETER G(HCP_A3,TA:VA;0) 298.15 +GHCPATA; 6000 N REF20 !

\$

PHASE HCP_ZN % 2 1 .5 !
 CONSTITUENT HCP_ZN :SN : VA : !

PARAMETER G(HCP_ZN,SN:VA;0) 298.15 +GHCPZN_S; 3000 N REF20 !
\$-----

PHASE LIQUID % 1 1.0 !
CONSTITUENT LIQUID :SN,TA : !

PARAMETER G(LIQUID,SN;0) 100 +GLIQSN; 3000 N REF20 !
PARAMETER G(LIQUID,TA;0) 298.15 +GLIQT; 6000 N REF20 !
PARAMETER G(LIQUID,SN,TA;0) 298.15 -1.7117919E+04; 6000 N !
\$-----

PHASE RHOMBOHEDRAL_A7 % 1 1.0 !
CONSTITUENT RHOMBOHEDRAL_A7 :SN : !

PARAMETER G(RHOMBOHEDRAL_A7,SN;0) 100 +GA7SN; 3000 N REF20 !
\$-----

PHASE TA3SN % 2 3 1 !
CONSTITUENT TA3SN :TA : SN : !

PARAMETER G(TA3SN,TA:SN;0)
298.15 -68843.951-6.00E+00*T+3*GHSERTA+GHSERSN; 3000 N !
\$-----

PHASE TASN2 % 2 1 2 !
CONSTITUENT TASN2 :TA : SN : !

PARAMETER G(TASN2,TA:SN;0)
298.15 -29678.180-4.202*T+GHSERTA+2*GHSERSN; 3000 N !
\$-----

PHASE TETRAGONAL_A6 % 1 1.0 !
CONSTITUENT TETRAGONAL_A6 :SN : !

PARAMETER G(TETRAGONAL_A6,SN;0) 298.15 +GA6SN; 3000 N REF20 !
\$-----

\$*****

LIST_OF_REFERENCES

NUMBER SOURCE

20 'A.T. Dinsdale, SGTE Data for Pure Elements,
CALPHAD.15 (1991) 317-425. '

!

Appendix C | Mathematica Interaction Parameter Fitting

input: $n = 0, 0, 0.019, -2.81, 0.019, -2.81, 0.019, -2.81, 0.019, -2.81, 0.019, -2.81, 0.019, -2.81, 0.125, 4.00, 0.125, 4.00, 0.125, 4.00, 0.125, 4.00, 0.125, 4.00, 0.125, 4.00, 0.125, 4.00, 0.25, 8.67, 0.25, 8.67, 0.25, 8.67, 0.25, 8.67, 0.25, 8.67, 0.25, 8.67, 0.50, 12.00, 0.75, 1.00, 0.938, 6.42, 0.981, -0.11, 1, 0$

output: $0, 0, 0.019, -2.81, 0.019, -2.81, 0.019, -2.81, 0.019, -2.81, 0.019, -2.81, 0.125, 4., 0.125, 4., 0.125, 4., 0.125, 4., 0.125, 4., 0.25, 8.67, 0.25, 8.67, 0.25, 8.67, 0.25, 8.67, 0.5, 12., 0.75, 1., 0.938, 6.42, 0.981, -0.11, 1, 0$

input: $gp = \text{ListPlot}[n, \text{PlotMarkers} \rightarrow \square, 10, \text{PlotStyle} \rightarrow \text{Blue}]$ input: $\text{Fit}[n, (x^*(1 - x)), ((x^*(1 - x))^*(x - (1 - x))), x]$ (For a two parameter fit) input: $\text{Fit}[n, (x^*(1 - x)), x]$ (For a one parameter fit) input: $\text{Plot}[\%, x, 0, 1, \text{PlotRange} \rightarrow -100, 100]$ input: $\text{Show}[\%, gp]$

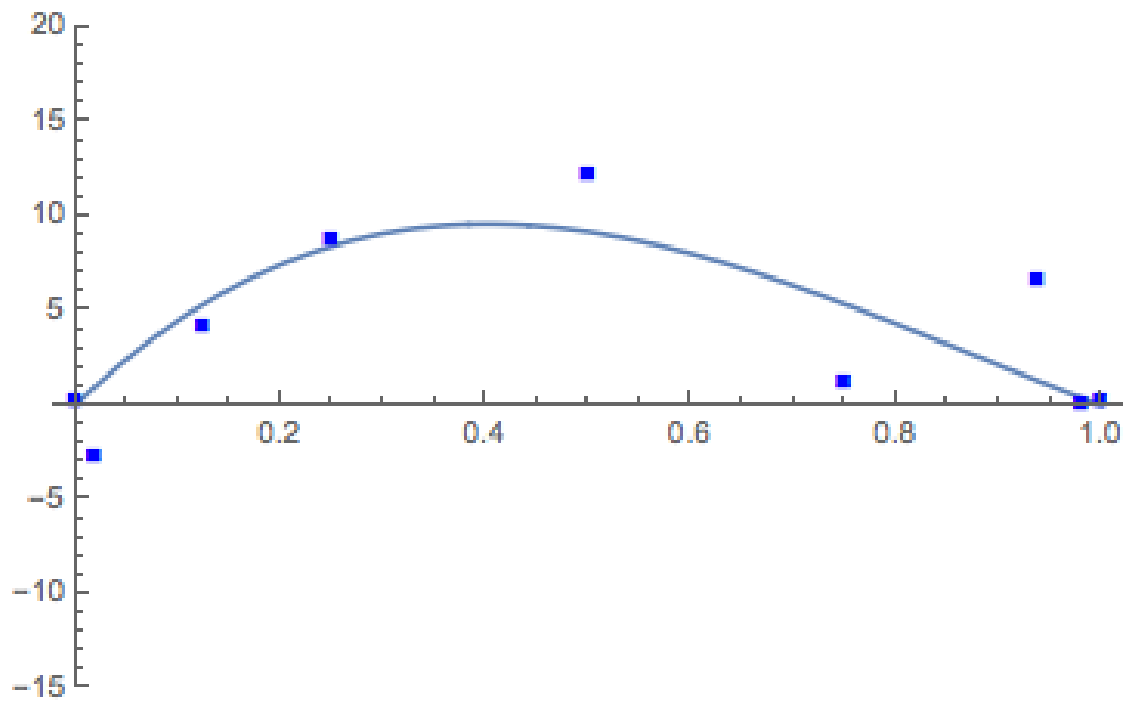


Figure C.1.

Appendix D | Ti Elastic Database

```
$*****  
$ The definition of the pure elements, vacancy and species  
$-----  
TEMPERATURE_LIMIT 0 6000.00 !  
ELEMENT /- ELECTRON_GAS 0.0000E+00 0.0000E+00 0.0000E+00!  
ELEMENT VA VACUUM 0.0 0.0 0.0 !  
ELEMENT TI BCC_A2 !  
ELEMENT MO BCT_A5 !  
ELEMENT NB BCC_A2 !  
ELEMENT SN BCT_A5 !  
ELEMENT TA BCC_A2 !  
ELEMENT ZR BCT_A5 !
```

```
$*****  
$-----  
FUNCTION C11BCCTI 298.15 +93; 6000 N !  
FUNCTION C12BCCTI 298.15 +115; 6000 N !  
FUNCTION C44BCCTI 298.15 +41; 6000 N !  
FUNCTION C11BCCMO 298.15 +475; 6000 N !  
FUNCTION C12BCCMO 298.15 +164; 6000 N !  
FUNCTION C44BCCMO 298.15 +108; 6000 N !
```

FUNCTION C11BCCNB	298.15 +245;	6000 N !
FUNCTION C12BCCNB	298.15 +144;	6000 N !
FUNCTION C44BCCNB	298.15 +27;	6000 N !
FUNCTION C11BCCSN	298.15 +50;	6000 N !
FUNCTION C12BCCSN	298.15 +52;	6000 N !
FUNCTION C44BCCSN	298.15 +29;	6000 N !
FUNCTION C11BCCTA	298.15 +278;	6000 N !
FUNCTION C12BCCTA	298.15 +164;	6000 N !
FUNCTION C44BCCTA	298.15 +81;	6000 N !
FUNCTION C11BCCZR	298.15 +86;	6000 N !
FUNCTION C12BCCZR	298.15 +91;	6000 N !
FUNCTION C44BCCZR	298.15 +32;	6000 N !
FUNCTION UN_ASS	298.15 +0;	300 N !
\$		
FUNCTION UN_ASS	298.15 0;	300 N !
\$		
\$*****		
TYPE_DEFINITION % SEQ *		!
TYPE_DEFINITION G SEQ *		!
DEFINE_SYSTEM_DEFAULT SPECIE 5		!
DEFAULT_COMMAND DEF_SYS_ELEMENT VA		!
\$		
\$*****		
\$*****		
\$		
TYPE_DEFINITION & GES A_P_D BCC_A2 MAGNETIC -1.0 4.00000E-01		!
PHASE BCC_A2 %& 2 1 3		!
CONSTITUENT BCC_A2 :TI,MO,NB,SN,TA,ZR : VA :		!
PARAMETER C11(BCC_A2, TI:VA;0)		
298.15 +C11BCCTI;	6000 N !	
PARAMETER C11(BCC_A2, MO:VA;0)		
298.15 +C11BCCMO;	6000 N !	

PARAMETER C11(BCC_A2,NB:VA;0)
298.15 +C11BCCNB; 6000 N !

PARAMETER C11(BCC_A2,SN:VA;0)
298.15 +C11BCCSN; 6000 N !

PARAMETER C11(BCC_A2,TA:VA;0)
298.15 +C11BCCTA; 6000 N !

PARAMETER C11(BCC_A2,ZR:VA;0)
298.15 +C11BCCZR; 6000 N !

PARAMETER C11(BCC_A2,TI,MO:VA;0)
298.15 -22.16; 6000 N !

PARAMETER C11(BCC_A2,TI,NB:VA;0)
298.15 +40.46; 6000 N !

PARAMETER C11(BCC_A2,TI,SN:VA;0)
298.15 +119.46; 6000 N !

PARAMETER C11(BCC_A2,TI,TA:VA;0)
298.15 +83.65; 6000 N !

PARAMETER C11(BCC_A2,TI,TA:VA;1)
298.15 -67.76; 6000 N !

PARAMETER C11(BCC_A2,TI,ZR:VA;0)
298.15 +246.97; 6000 N !

PARAMETER C11(BCC_A2,TI,ZR:VA;1)
298.15 -135.95; 6000 N !

PARAMETER C11(BCC_A2,TI,MO,NB:VA;0)
298.15 -29.97; 6000 N !

PARAMETER C11(BCC_A2,TI,MO,SN:VA;0)
298.15 -83.85; 6000 N !

PARAMETER C11(BCC_A2,TI,MO,TA:VA;0)
298.15 -106.53; 6000 N !

PARAMETER C11(BCC_A2,TI,MO,ZR:VA;0)
298.15 -245.27; 6000 N !

PARAMETER C11(BCC_A2,TI,NB,SN:VA;0)
298.15 -41.52; 6000 N !

PARAMETER C11(BCC_A2,TI,NB,TA:VA;0)

298.15 -93.77; 6000 N !
PARAMETER C11(BCC_A2, TI, NB, ZR:VA;0)
298.15 -220.35; 6000 N !
PARAMETER C11(BCC_A2, TI, SN, TA:VA;0)
298.15 -95.39; 6000 N !
PARAMETER C11(BCC_A2, TI, SN, ZR:VA;0)
298.15 -155.34; 6000 N !
PARAMETER C11(BCC_A2, TI, TA, ZR:VA;0)
298.15 -149.67; 6000 N !
\$—————
PARAMETER C12(BCC_A2, TI:VA;0)
298.15 +C12BCCTI; 6000 N !
PARAMETER C12(BCC_A2, MO:VA;0)
298.15 +C12BCCMO; 6000 N !
PARAMETER C12(BCC_A2, NB:VA;0)
298.15 +C12BCCNB; 6000 N !
PARAMETER C12(BCC_A2, SN:VA;0)
298.15 +C12BCCSN; 6000 N !
PARAMETER C12(BCC_A2, TA:VA;0)
298.15 +C12BCCTA; 6000 N !
PARAMETER C12(BCC_A2, ZR:VA;0)
298.15 +C12BCCZR; 6000 N !
PARAMETER C12(BCC_A2, TI, MO:VA;0)
298.15 -36.40; 6000 N !
PARAMETER C12(BCC_A2, TI, NB:VA;0)
298.15 -32.39; 6000 N !
PARAMETER C12(BCC_A2, TI, SN:VA;0)
298.15 +15.90; 6000 N !
PARAMETER C12(BCC_A2, TI, SN:VA;1)
298.15 -146.80; 6000 N !
PARAMETER C12(BCC_A2, TI, TA:VA;0)
298.15 +38.05; 6000 N !
PARAMETER C12(BCC_A2, TI, ZR:VA;0)

298.15 -110.53; 6000 N !
PARAMETER C12(BCC_A2, TI, ZR:VA;1)
298.15 +78.00; 6000 N !
PARAMETER C12(BCC_A2, TI, MO, NB:VA;0)
298.15 +13.97; 6000 N !
PARAMETER C12(BCC_A2, TI, MO, SN:VA;0)
298.15 +31.80; 6000 N !
PARAMETER C12(BCC_A2, TI, MO, TA:VA;0)
298.15 -12.35; 6000 N !
PARAMETER C12(BCC_A2, TI, MO, ZR:VA;0)
298.15 +50.43; 6000 N !
PARAMETER C12(BCC_A2, TI, NB, SN:VA;0)
298.15 +25.52; 6000 N !
PARAMETER C12(BCC_A2, TI, NB, TA:VA;0)
298.15 -15.80; 6000 N !
PARAMETER C12(BCC_A2, TI, NB, ZR:VA;0)
298.15 +72.10; 6000 N !
PARAMETER C12(BCC_A2, TI, SN, TA:VA;0)
298.15 -10.94; 6000 N !
PARAMETER C12(BCC_A2, TI, SN, ZR:VA;0)
298.15 +68.86; 6000 N !
PARAMETER C12(BCC_A2, TI, TA, ZR:VA;0)
298.15 -8.91; 6000 N !
\$

PARAMETER C44(BCC_A2, TI:VA;0)
298.15 +C44BCCTI; 6000 N !
PARAMETER C44(BCC_A2, MO:VA;0)
298.15 +C44BCCMO; 6000 N !
PARAMETER C44(BCC_A2, NB:VA;0)
298.15 +C44BCCNB; 6000 N !
PARAMETER C44(BCC_A2, SN:VA;0)
298.15 +C44BCCSN; 6000 N !
PARAMETER C44(BCC_A2, TA:VA;0)

298.15 +C44BCCTA; 6000 N !
PARAMETER C44(BCC_A2,ZR:VA;0)
298.15 +C44BCCZR; 6000 N !
PARAMETER C44(BCC_A2,TI,MO:VA;0)
298.15 -142.90; 6000 N !
PARAMETER C44(BCC_A2,TI,NB:VA;0)
298.15 -41.54; 6000 N !
PARAMETER C44(BCC_A2,TI,NB:VA;1)
298.15 -41.95; 6000 N !
PARAMETER C44(BCC_A2,TI,SN:VA;0)
298.15 +59.75; 6000 N !
PARAMETER C44(BCC_A2,TI,SN:VA;1)
298.15 -94.38; 6000 N !
PARAMETER C44(BCC_A2,TI,TA:VA;0)
298.15 -51.96; 6000 N !
PARAMETER C44(BCC_A2,TI,ZR:VA;0)
298.15 +70.06; 6000 N !
PARAMETER C44(BCC_A2,TI,MO,NB:VA;0)
298.15 +9.72; 6000 N !
PARAMETER C44(BCC_A2,TI,MO,SN:VA;0)
298.15 +74.73; 6000 N !
PARAMETER C44(BCC_A2,TI,MO,TA:VA;0)
298.15 +5.27; 6000 N !
PARAMETER C44(BCC_A2,TI,MO,ZR:VA;0)
298.15 -44.96; 6000 N !
PARAMETER C44(BCC_A2,TI,NB,SN:VA;0)
298.15 +67.85; 6000 N !
PARAMETER C44(BCC_A2,TI,NB,TA:VA;0)
298.15 +4.25; 6000 N !
PARAMETER C44(BCC_A2,TI,NB,ZR:VA;0)
298.15 -55.29; 6000 N !
PARAMETER C44(BCC_A2,TI,SN,TA:VA;0)
298.15 +67.85; 6000 N !

```
PARAMETER C44(BCC_A2, TI, SN, ZR:VA;0)
298.15 +3.85; 6000 N !
PARAMETER C44(BCC_A2, TI, TA, ZR:VA;0)
298.15 -23.70; 6000 N !
$*****
*****LIST_OF_REFERENCES
NUMBER SOURCE
!
```

Appendix E | Pycalphad script

This code is used in pycalphad to plot the elastic moduli and elastic properites as a function of composition. A tdb file must be loaded into the script. In the present work the tdb file in Appendix D is used.

```
import matplotlib
from matplotlib.axes import Axes
from matplotlib.patches import Polygon
from matplotlib.path import Path
from matplotlib.ticker import NullLocator, Formatter, FixedLocator
from matplotlib.transforms import Affine2D, BboxTransformTo, IdentityTransform
from matplotlib.projections import register_projection
import matplotlib.spines as mspines
import matplotlib.axis as maxis
import matplotlib.pyplot as plt

import numpy as np

class TriangularAxes(Axes):
    """
    A custom class for triangular projections.
    """

    name = 'triangular'

    def __init__(self, *args, **kwargs):
        Axes.__init__(self, *args, **kwargs)
        self.set_aspect(1, adjustable='box', anchor='SW')
        self.cla()
```

```

def __init__(self):
    self.xaxis = maxis.XAxis(self)
    self.yaxis = maxis.YAxis(self)
    self._update_transScale()

def cla(self):
    """
    Override to set up some reasonable defaults.
    """
    # Don't forget to call the base class
    Axes.cla(self)

    x_min = 0
    y_min = 0
    x_max = 1
    y_max = 1
    x_spacing = 0.1
    y_spacing = 0.1
    self.xaxis.set_minor_locator(NullLocator())
    self.yaxis.set_minor_locator(NullLocator())
    self.xaxis.set_ticks_position('bottom')
    self.yaxis.set_ticks_position('left')
    Axes.set_xlim(self, x_min, x_max)
    Axes.set_ylim(self, y_min, y_max)
    self.xaxis.set_ticks(np.arange(x_min, x_max+x_spacing, x_spacing))
    self.yaxis.set_ticks(np.arange(y_min, y_max+y_spacing, y_spacing))

def __set__lim_and__transforms(self):
    """
    This is called once when the plot is created to set up all the
    transforms for the data, text and grids.
    """
    # There are three important coordinate spaces going on here:
    #
    # 1. Data space: The space of the data itself
    #
    # 2. Axes space: The unit rectangle (0, 0) to (1, 1)
    # covering the entire plot area.
    #
    # 3. Display space: The coordinates of the resulting image,
    # often in pixels or dpi/inch.

```

```

# This function makes heavy use of the Transform classes in
# ``lib/matplotlib/transforms.py``. For more information, see
# the inline documentation there.

# The goal of the first two transformations is to get from the
# data space (in this case longitude and latitude) to axes
# space. It is separated into a non-affine and affine part so
# that the non-affine part does not have to be recomputed when
# a simple affine change to the figure has been made (such as
# resizing the window or changing the dpi).

# 1) The core transformation from data space into
# rectilinear space defined in the HammerTransform class.
self.transProjection = IdentityTransform()
# 2) The above has an output range that is not in the unit
# rectangle, so scale and translate it so it fits correctly
# within the axes. The peculiar calculations of xscale and
#yscale are specific to a Aitoff-Hammer projection, so don't
# worry about them too much.
self.transAffine = Affine2D.from_values(
    1., 0, 0.5, np.sqrt(3)/2., 0, 0)
self.transAffinedep = Affine2D.from_values(
    1., 0, -0.5, np.sqrt(3)/2., 0, 0)
#self.transAffine = IdentityTransform()

# 3) This is the transformation from axes space to display
# space.
self.transAxes = BboxTransformTo(self.bbox)

# Now put these 3 transforms together -- from data all the way
# to display coordinates. Using the '+' operator, these
# transforms will be applied "in order". The transforms are
# automatically simplified, if possible, by the underlying
# transformation framework.
self.transData = \
    self.transProjection + \
    self.transAffine + \
    self.transAxes

# The main data transformation is set up. Now deal with

```

```

# gridlines and tick labels.

# Longitude gridlines and ticklabels. The input to these
# transforms are in display space in x and axes space in y.
# Therefore, the input values will be in range (-xmin, 0),
# (xmax, 1). The goal of these transforms is to go from that
# space to display space. The tick labels will be offset 4
# pixels from the equator.

self._xaxis._pretransform = IdentityTransform()
self._xaxis._transform = \
    self._xaxis._pretransform + \
    self.transData
self._xaxis._text1._transform = \
    Affine2D().scale(1.0, 0.0) + \
    self.transData + \
    Affine2D().translate(0.0, -20.0)
self._xaxis._text2._transform = \
    Affine2D().scale(1.0, 0.0) + \
    self.transData + \
    Affine2D().translate(0.0, -4.0)

# Now set up the transforms for the latitude ticks. The input to
# these transforms are in axes space in x and display space in
# y. Therefore, the input values will be in range (0, -ymin),
# (1, ymax). The goal of these transforms is to go from that
# space to display space. The tick labels will be offset 4
# pixels from the edge of the axes ellipse.

self._yaxis._transform = self.transData
yaxis_text_base = \
    self.transProjection + \
    (self.transAffine + \
    self.transAxes)
self._yaxis._text1._transform = \
    yaxis_text_base + \
    Affine2D().translate(-8.0, 0.0)
self._yaxis._text2._transform = \
    yaxis_text_base + \
    Affine2D().translate(8.0, 0.0)

```

```

def get_xaxis_transform(self, which='grid'):
    assert which in ['tick1', 'tick2', 'grid']
    return self._xaxis_transform

def get_xaxis_text1_transform(self, pad):
    return self._xaxis_text1_transform, 'bottom', 'center'

def get_xaxis_text2_transform(self, pad):
    return self._xaxis_text2_transform, 'top', 'center'

def get_yaxis_transform(self, which='grid'):
    assert which in ['tick1', 'tick2', 'grid']
    return self._yaxis_transform

def get_yaxis_text1_transform(self, pad):
    return self._yaxis_text1_transform, 'center', 'right'

def get_yaxis_text2_transform(self, pad):
    return self._yaxis_text2_transform, 'center', 'left'

def _gen_axes_spines(self):
    dep_spine = mspines.Spine.linear_spine(self,
                                             'right')
    # Fix dependent axis to be transformed the correct way
    dep_spine.set_transform(self.transAffinedep + self.transAxes)
    return {'left': mspines.Spine.linear_spine(self,
                                                'left'),
            'bottom': mspines.Spine.linear_spine(self,
                                                 'bottom'),
            'right': dep_spine}

def _gen_axes_patch(self):
    """
    Override this method to define the shape that is used for the
    background of the plot. It should be a subclass of Patch.
    Any data and gridlines will be clipped to this shape.
    """
    return Polygon([[0, 0], [0.5, np.sqrt(3)/2], [1, 0]], closed=True)

# Interactive panning and zooming is not supported with this projection,

```

```

# so we override all of the following methods to disable it.
def can_zoom(self):
    """
    Return True if this axes support the zoom box
    """
    return False

def start_pan(self, x, y, button):
    pass

def end_pan(self):
    pass

def drag_pan(self, button, key, x, y):
    pass

# Now register the projection with matplotlib so the user can select
# it.
register_projection(TriangularAxes)

import pycalphad.io.tdb_keywords
pycalphad.io.tdb_keywords.TDB_PARAM_TYPES.extend\
([ 'EM', 'BULK', 'SHEAR', 'C11', 'C12', 'C44' ])
from pycalphad import Database, Model, equilibrium, calculate
import numpy as np
import pycalphad.variables as v
import sympy
from tinydb import where

class ElasticModel(Model):
    def build_phase(self, dbe):
        phase = dbe.phases[self.phase_name]
        param_search = dbe.search
        # EM, BULK, SHEAR, C11, C12, C44
        for prop in [ 'EM', 'BULK', 'SHEAR', 'C11', 'C12', 'C44' ]:
            prop_param_query = (
                (where('phase_name') == phase.name) & \
                (where('parameter_type') == prop) & \
                (where('constituent_array').test(self._array_validity)))

```

```

)
prop_val = self.redlich_kister_sum \
(phase, param_search, prop_param_query).subs(dbe.symbols)
setattr(self, prop, prop_val)

dbf = Database('ElasticTi.tdb')
mod = ElasticModel(dbf, ['TI', 'SN', 'ZR', 'VA'], 'BCC_A2')
symbols = dict([(sympy.Symbol(s), val) for s, val in dbf.symbols.items()])
mod.C11 = mod.C11.xreplace(symbols)
mod.C12 = mod.C12.xreplace(symbols)
mod.C44 = mod.C44.xreplace(symbols)
x1 = np.linspace(0,1, num=100)
x2 = np.linspace(0,1, num=100)
mesh = np.meshgrid(x1, x2)
X = mesh[0]
Y = mesh[1]
mesh_arr = np.array(mesh)
mesh_arr = np.moveaxis(mesh_arr, 0, 2)
dep_col = 1 - np.sum(mesh_arr, axis=-1, keepdims=True)
mesh_arr = np.concatenate((mesh_arr, dep_col), axis=-1)
mesh_arr = np.concatenate((mesh_arr, np.ones(mesh_arr.shape[:-1] + (1,))), axis=-1)
orig_shape = tuple(mesh_arr.shape[:-1])
mesh_arr = mesh_arr.reshape(-1, mesh_arr.shape[-1])
mesh_arr[np.any(mesh_arr < 0, axis=-1), :] = np.nan
res_c11 = calculate(dbf, ['TI', 'SN', 'TA', 'VA'], 'BCC_A2', T=300, P=101325,
    model=mod, output='C11', points=mesh_arr)
res_c11 = res_c11.C11.values.reshape(orig_shape)
res_c12 = calculate(dbf, ['TI', 'SN', 'TA', 'VA'], 'BCC_A2', T=300, P=101325,
    model=mod, output='C12', points=mesh_arr)
res_c12 = res_c12.C12.values.reshape(orig_shape)
res_c44 = calculate(dbf, ['TI', 'SN', 'TA', 'VA'], 'BCC_A2', T=300, P=101325,
    model=mod, output='C44', points=mesh_arr)
res_c44 = res_c44.C44.values.reshape(orig_shape)

```

```

import numpy as np
def compute_moduli(c11, c12, c44):
    """Consume elastic stiffness constants and, under symmetry assumptions, compute
    bulk modulus, shear modulus, and Young's modulus.

```

Parameters

c11: float64 array-like
c12: float64 array-like
c44: float64 array-like

Returns

```

B, G, Y : tuple of float64 array-likes """
# Ported from a matlab code
c11 = np.array(c11)
c12 = np.array(c12)
c44 = np.array(c44)
cij = np.zeros(c11.shape + (6,6))
cij [..., 0, 0] = cij [..., 1, 1] = cij [..., 2, 2] = c11
cij [..., 0, 1] = cij [..., 1, 0] = cij [..., 0, 2] = \
cij [..., 2, 0] = cij [..., 1, 2] = cij [..., 2, 1] = c12
cij [..., 3, 3] = cij [..., 4, 4] = cij [..., 5, 5] = c44
sij = np.linalg.inv(cij)
A_c = (cij [..., 0, 0] + cij [..., 1, 1] + cij [..., 2, 2]) / 3.
B_c = (cij [..., 0, 1] + cij [..., 0, 2] + cij [..., 1, 2]) / 3.
C_c = (cij [..., 3, 3] + cij [..., 4, 4] + cij [..., 5, 5]) / 3.
A_s = (sij [..., 0, 0] + sijs [..., 1, 1] + sijs [..., 2, 2]) / 3.
B_s = (sij [..., 0, 1] + sijs [..., 0, 2] + sijs [..., 1, 2]) / 3.
C_s = (sij [..., 3, 3] + sijs [..., 4, 4] + sijs [..., 5, 5]) / 3.
Bv = (A_c + 2*B_c) / 3.
Gv = (A_c - B_c + 3*C_c) / 5.
Br = 1. / (3*A_s + 6*B_s)
Gr = 5. / (4*A_s - 4*B_s + 3*C_s)
Bvrh = (Br + Bv) / 2.
Gvrh = (Gr + Gv) / 2.
Yvrh = (9*Bvrh*Gvrh) / (Gvrh + 3*Bvrh)
return Bvrh, Gvrh, Yvrh

```

bulk_modulus, shear_modulus, young_modulus = \

```

compute_moduli(res_c11, res_c12, res_c44)

%matplotlib inline
import matplotlib.pyplot as plt

fig = plt.figure(figsize=(12,12))
ax = fig.gca(projection='triangular')
CS = ax.contour(X, Y, bulk_modulus, linewidths=4, \
levels=list(range(100, 300, 10)), cmap='cool')
ax.clabel(CS, inline=1, fontsize=13, fmt='%1.0f')
#PCM=ax.get_children()[0] #get the mappable,
#the 1st and the 2nd are the x and y axes
#plt.colorbar(PCM, ax=ax)
ax.set_xlabel('x(Mo)', fontsize=18)
ax.set_ylabel('x(Nb)', fontsize=18, rotation=60, labelpad=-180)
ax.tick_params(axis='both', which='major', labelsize=18)
ax.tick_params(axis='both', which='minor', labelsize=18)
ax.set_title('Bulk modulus')
#fig.savefig('TiMoNb-Bulk.pdf')

%matplotlib inline
import matplotlib.pyplot as plt

fig = plt.figure(figsize=(12,12))
ax = fig.gca(projection='triangular')
CS = ax.contour(X, Y, shear_modulus, linewidths=4, \
levels=list(range(0, 150, 5)), cmap='cool')
ax.clabel(CS, inline=1, fontsize=13, fmt='%1.0f')
#PCM=ax.get_children()[0] #get the mappable,
#the 1st and the 2nd are the x and y axes
#plt.colorbar(PCM, ax=ax)
ax.set_xlabel('x(Mo)', fontsize=18)
ax.set_ylabel('x(Nb)', fontsize=18, rotation=60, labelpad=-180)

```

```

ax.tick_params(axis='both', which='major', labelsize=18)
ax.tick_params(axis='both', which='minor', labelsize=18)
ax.set_title('Shear_modulus')
#fig.savefig('TiMoNb-Shear.pdf')

%matplotlib inline
import matplotlib.pyplot as plt

fig = plt.figure(figsize=(12,12))
ax = fig.gca(projection='triangular')
CS = ax.contour(X, Y, young_modulus, linewidths=4, \
levels=list(range(0, 350, 10)), cmap='cool')
ax.clabel(CS, inline=1, fontsize=13, fmt='%1.0f')
#PCM=ax.get_children()[0] #get the mappable,
#the 1st and the 2nd are the x and y axes
#plt.colorbar(PCM, ax=ax)
ax.set_xlabel('x(Mo)', fontsize=18)
ax.set_ylabel('x(Nb)', fontsize=18, rotation=60, labelpad=-180)
ax.tick_params(axis='both', which='major', labelsize=18)
ax.tick_params(axis='both', which='minor', labelsize=18)
ax.set_title('Young\s_modulus')
#fig.savefig('TiMoNb-Young.pdf')

```

Appendix F |

Ti-Nb Experimental Elastic Data

Table F.1: The experimentally determined E values for the Ti-Nb system reviewed and averaged for chapter 7 are listed here [6–9].

x(Nb)	x(Ti)	E (GPa)	Reference
0.00	1.00	117.16	[6]
0	1.00	132	[8]
0.00	1.00	115.77	[7]
0.00	1.00	108.30	[9]
0.01	0.99	112.30	[6]
0.01	0.99	112.74	[7]
0.02	0.98	109.05	[6]
0.02	0.98	107.61	[7]
0.05	0.95	79.46	[6]
0.05	0.95	78.69	[7]
0.05	0.95	80.27	[6]
0.08	0.92	66.49	[6]
0.08	0.92	66.33	[7]
0.09	0.91	66.89	[6]
0.09	0.91	70.58	[9]
0.10	0.90	66.49	[6]
0.10	0.90	115	[8]
0.10	0.90	91	[8]
0.10	0.90	66.09	[7]

Table F.1: The experimentally determined E values for the Ti-Nb system reviewed and averaged for chapter 7 are listed here [6–9].

x(Nb)	x(Ti)	E (GPa)	Reference
0.11	0.89	77.99	[7]
0.11	0.89	79.46	[6]
0.18	0.82	92.43	[6]
0.18	0.82	93.62	[7]
0.19	0.81	65.27	[6]
0.19	0.81	63.24	[6]
0.20	0.80	75	[8]
0.20	0.80	89	[8]
0.20	0.80	68.85	[9]
0.22	0.78	71.46	[7]
0.22	0.78	72.63	[9]
0.22	0.78	68.62	[9]
0.23	0.77	72.16	[6]
0.23	0.77	103.64	[7]
0.23	0.77	60.34	[9]
0.23	0.77	67.24	[9]
0.24	0.76	65.16	[9]
0.24	0.76	57.07	[9]
0.25	0.75	71.76	[6]
0.25	0.75	74	[8]
0.25	0.75	78	[8]
0.25	0.75	66.33	[7]
0.26	0.74	61.85	[9]
0.26	0.74	73.09	[9]
0.26	0.74	82.19	[7]
0.26	0.74	60.50	[7]
0.26	0.74	67.70	[6]
0.26	0.74	54.31	[9]
0.27	0.73	56.46	[9]
0.27	0.73	52.76	[9]

Table F.1: The experimentally determined E values for the Ti-Nb system reviewed and averaged for chapter 7 are listed here [6–9].

x(Nb)	x(Ti)	E (GPa)	Reference
0.29	0.71	62.83	[7]
0.29	0.71	61.43	[7]
0.30	0.70	67.70	[6]
0.30	0.70	62.69	[9]
0.30	0.70	72	[8]
0.30	0.70	69	[8]
0.30	0.70	69.31	[9]
0.30	0.70	67.96	[7]
0.34	0.66	76.21	[9]
0.34	0.66	86.02	[9]
0.34	0.66	74.26	[7]
0.34	0.66	75.84	[9]
0.34	0.66	75.00	[6]
0.36	0.64	73.78	[6]
0.39	0.61	76.62	[6]
0.43	0.57	84.0	[7]

Bibliography

- [1] WU, C., Y. XIN, X. WANG, and J. LIN (2010) “Effects of Ta content on the phase stability and elastic properties of β Ti-Ta alloys from first-principles calculations,” *Solid State Sciences*, **12**(12), pp. 2120–2124.
- [2] IKEHATA, H., N. NAGASAKO, T. FURUTA, A. FUKUMOTO, K. MIWA, and T. SAITO (2004) “First-principles calculations for development of low elastic modulus Ti alloys,” *Physical Review B*, **70**(17), p. 174113.
- [3] ZHOU, Y. L., M. NIINOMI, and T. AKAHORI (2004) “Effects of Ta content on Young’s modulus and tensile properties of binary Ti-Ta alloys for biomedical applications,” *Materials Science and Engineering: A*, **371**(1-2), pp. 283–290.
- [4] ZHOU, Y.-L. and M. NIINOMI (2009) “Ti₆₂Ta alloy with the best mechanical compatibility in Ti-Ta alloys for biomedical applications,” *Materials Science and Engineering: C*, **29**(3), pp. 1061–1065.
- [5] FEDOTOV, S., T. CHELIDZE, Y. KOVNERISTYY, and V. SANADZE (1985) “Phase structure, critical points MS and AS of martensitic transformations and elastic properties of metastable alloys of the Ti-Ta system,” *Phys. Met. Metall.*, **60**(3), pp. 139–143.
- [6] TIMOSHEVSKII, A., S. YABLONOVSKII, and O. IVASHIN (2011) “First-principles calculations atomic structure and elastic properties of Ti-Nb alloys,” *arXiv preprint arXiv:1111.7182*.
- [7] OZAKI, T., H. MATSUMOTO, S. WATANABE, and S. HANADA (2004) “Beta Ti Alloys with Low Young’s Modulus,” *MATERIALS TRANSACTIONS*, **45**(8), pp. 2776–2779.
- [8] FRIÁK, M., W. COUNTS, D. MA, B. SANDER, D. HOLEC, D. RAABE, and J. NEUGEBAUER (2012) “Theory-guided materials design of multi-phase Ti-Nb alloys with bone-matching elastic properties,” *Materials*, **5**(10), pp. 1853–1872.

- [9] KARRE, R., M. NIRANJAN, and S. DEY (2015) “First principles theoretical investigations of low Young’s modulus beta Ti_xNb and Ti_xNb_{1-x}Zr alloys compositions for biomedical applications,” *Materials Science and Engineering: C*, **50**, pp. 52–58.
 URL <http://www.sciencedirect.com/science/article/pii/S0928493115000715>
- [10] MATSUMOTO, H., S. WATANABE, N. MASAHASHI, and S. HANADA (2006) “Composition dependence of Young’s modulus in Ti-V, Ti-Nb, and Ti-V-Sn alloys,” *Metallurgical and Materials Transactions A*, **37**(11), pp. 3239–3249.
- [11] XIONG, W., Y. DU, Y. LIU, B. HUANG, H. XU, H. CHEN, and Z. PAN (2004) “Thermodynamic assessment of the Mo-Nb-Ta system,” *Calphad-Computer Coupling of Phase Diagrams and Thermochemistry*, **28**(2), pp. 133–140.
- [12] PEREZ, R. and B. SUNDMAN (2003) “Thermodynamic assessment of the Mo-Zr binary phase diagram,” *Calphad-Computer Coupling of Phase Diagrams and Thermochemistry*, **27**(3), pp. 253–262.
- [13] GUILLERMET, A. (1991) “Thermodynamic analysis of the stable phases in the Zr-Nb system and calculation of the phase-diagram,” *Zeitschrift Fur Metallkunde*, **82**(6), pp. 478–487.
- [14] ABRIATA, J. P. and J. C. BOLCICH (1982) “The Nb-Zr (Niobium-Zirconium) system,” *Bulletin of alloy phase diagrams*, **3**(1), pp. 34–44.
- [15] GUILLERMET, A. (1995) “Phase-diagram and thermochemical properties of the Zr-Ta system - an assessment based on Gibbs energy modeling,” *Journal of Alloys and Compounds*, **226**(1-2), pp. 174–184.
- [16] ANSARA, I., A. DINSDALE, and M. RAND (1998) *COST 507: thermochemical database for light metal alloys*, vol. 2, European Communities, Brussels and Luxembourg.
- [17] MURRAY, J. (1981) “The Mo-Ti (Molybdenum-Titanium) system,” *Bulletin of Alloy Phase Diagrams*, **2**(2), pp. 185–192.
- [18] UESUGI, T., S. MIYAMAE, and K. HIGASHI (2013) “Enthalpies of Solution in Ti_xX (X= Mo, Nb, V and W) Alloys from First-Principles Calculations,” *Materials Transactions*, **54**(4), pp. 484–492.
- [19] ZHANG, Y., H. LIU, and Z. JIN (2001) “Thermodynamic assessment of the Nb-Ti system,” *Calphad-Computer Coupling of Phase Diagrams and Thermochemistry*, **25**(2), pp. 305–317.

- [20] KUMAR, K., P. WOLLANTS, and L. DELAEY (1994) “Thermodynamic calculation of Nb-Ti-V phase diagram,” *CALPHAD*, **18**(1), pp. 71–79.
- [21] ——— (1994) “Thermodynamic assessment of the Ti-Zr system and calculation of the Nb-Ti-Zr phase-diagram,” *Journal of Alloys and Compounds*, **206**(1), pp. 121–127.
- [22] MURRAY, J. L. (1987) “Phase diagrams of binary titanium alloys,” *ASM International, 1987*, p. 354.
- [23] NIKITIN, P. and V. MIKHEYEV (1971) “Examination of titanium corner of Ti-Ta-Mo equilibrium diagram,” *Russian Metallurgy-Metally-USSR*, (1), pp. 144–147.
- [24] KAR, S. and D. LIPKIN (2008) “A CALPHAD-based phase equilibrium model of Mo-Ti-Zr-C,” in *TMS 2008 Annual Meeting Supplemental Proceedings, Vol 2: Materials Characterization, Computation and Modeling*, Minerals, Metals & Materials Soc, Warrendale, pp. 237–243.
- [25] PROKOSHKIN, D. A. and M. I. ZAKHAROVA (1967) “Phase equilibrium in the molybdenum-titanium-zirconium system(Ternary phase diagram of Mo-Ti-Zr system from eleven isothermal cross sections),” in *AKADEMIIA NAUK SSSR, DOKLADY*, vol. 172, pp. 1382–1384.
- [26] NA, L. and W. WARNE (2001) “Estimation of the Nb-Ti-Ta phase diagram,” *Ieee Transactions on Applied Superconductivity*, **11**(1), pp. 3800–3803.
- [27] TOKUNAGA, T., S. MATSUMOTO, H. OHTANI, and M. HASEBE (2007) “Thermodynamic calculation of phase equilibria in the Nb-Ni-Ti-Zr quaternary system,” *Materials transactions*, **48**(2), pp. 89–96.
- [28] LIN, L., L. DELAEY, O. VANDERBIEST, and P. WOLLANTS (1996) “Calculation of isothermal sections of three ternary Ti-Zr-X systems,” *Scripta Materialia*, **34**(9), pp. 1411–1416.
- [29] HOCH, M. and D. BUTRYMOW (1964) “System tantalum-titanium-zirconium-oxygen at 1500 degrees C,” *Transactions of the Metallurgical Society of AIME*, **230**(1), pp. 186–192.
- [30] TAIOLI, S., C. CAZORLA, M. J. GILLAN, and D. ALFÈ (2007) “Melting curve of tantalum from first principles,” *Physical Review B*, **75**(21), p. 214103.
- [31] OLIJNYK, H. (1992) “Pressure dependence of Raman phonons of metallic β -Sn,” *Physical Review B*, **46**(10).
- [32] DINSDALE, A. (1991) “SGTE Data for Pure Elements,” *CALPHAD*, **15**(4), pp. 317–425.

- [33] TOFFOLON, C., C. SERVANT, and B. SUNDMAN (1998) “Thermodynamic assessment of the Nb-Sn system,” *Journal of Phase Equilibria*, **19**(5), pp. 479–485.
- [34] ZHANG, W.-D., Y. LIU, H. WU, M. SONG, T.-Y. ZHANG, X.-D. LAN, and T.-H. YAO (2015) “Elastic modulus of phases in Ti_xMo alloys,” *Materials Characterization*, **106**, pp. 302–307.
- [35] BOYER, R., G. WELSCH, and E. COLLINGS (1994) “Materials Properties Handbook: Titanium Alloys,” *ASM International, Materials Park, OH*.
- [36] SUNG, B.-S., T.-E. PARK, and Y.-H. YUN (2015) “Microstructures and electrochemical behavior of Ti-Mo alloys for biomaterials,” *Advances in Materials Science and Engineering*, **2015**(Article ID 872730), pp. 1–7.
- [37] TANE, M., S. AKITA, T. NAKANO, K. HAGIHARA, Y. UMAKOSHI, M. NIINOMI, H. MORI, and H. NAKAJIMA (2010) “Low Young’s modulus of Ti_xNb_yTa_zZr alloys caused by softening in shear moduli c₄₄ and c₁₁ near lower limit of body-centered cubic phase stability,” *Acta Materialia*, **58**(20), pp. 6790–6798.
- [38] GEETHA, M., A. SINGH, R. ASOKAMANI, and A. GOGIA (2009) “Ti based biomaterials, the ultimate choice for orthopaedic implants – A review,” *Progress in Materials Science*, **54**(3), pp. 397–425.
- [39] MOHAMMED, M., Z. KHAN, and A. SIDDIQUEE (2014) “Beta titanium alloys: the lowest elastic modulus for biomedical applications: a review,” *International Journal of Chemical, Molecular, Nuclear, Materials and Metallurgical Engineering*, **8**(8), pp. 788–793.
- [40] NIINOMI, M., M. NAKAI, and J. HIEDA (2012) “Development of new metallic alloys for biomedical applications,” *Acta Biomaterialia*, **8**(11), pp. 3888–3903.
- [41] NOZOE, F., H. MATSUMOTO, T. K. JUNG, S. WATANABE, T. SABURI, and S. HANADA (2007) “Effect of low temperature aging on superelastic behavior in biocompatible beta TiNbSn Alloy,” *Materials transactions*, **48**(11), pp. 3007–3013.
- [42] OTIS, R. and Z.-K. LIU (2017) “pycalphad: CALPHAD-based computational thermodynamics in Python,” *Journal of Open Research Software*, **5**(1), pp. 1–11.
- [43] LONG, M. and H. RACK (1998) “Titanium alloys in total joint replacement materials science perspective,” *Biomaterials*, **19**(18), pp. 1621–1639.

- [44] KURTZ, S. (2007) “Projections of primary and revision hip and knee arthroplasty in the United States from 2005 to 2030,” *The Journal of Bone and Joint Surgery (American)*, **89**(4), pp. 780–785.
- [45] KRISHNA, B., S. BOSE, and A. BANDYOPADHYAY (2007) “Low stiffness porous Ti structures for load-bearing implants,” *Acta biomaterialia*, **3**(6), pp. 997–1006.
- [46] NIINOMI, M. (2003) “Recent research and development in titanium alloys for biomedical applications and healthcare goods,” *Science and Technology of Advanced Materials*, **4**(5), pp. 445–454.
- [47] ITO, A., Y. OKAZAKI, T. TATEISHI, and Y. ITO (1995) “In vitro biocompatibility, mechanical properties, and corrosion resistance of Ti-Zr-Nb-Ta-Pd and Ti-Sn-Nb-Ta-Pd alloys,” *Journal of Biomedical Materials Research*, **29**(7), pp. 893–899.
- [48] JAIN, A., S. ONG, G. HAUTIER, W. CHEN, W. RICHARDS, S. DACEK, S. CHOLIA, D. GUNTER, D. SKINNER, and G. CEDER (2013) “The Materials Project: A materials genome approach to accelerating materials innovation,” *Apl Materials*, **1**(1), p. 11002.
- [49] ANTOLIN, N., O. RESTREPO, and W. WINDL (2012) “Fast free-energy calculations for unstable high-temperature phases,” *Physical Review B*, **86**(5), p. 54119.
- [50] MEI, Z. Z. G. (2011) *First-principles Thermodynamics of Phase Transition: from Metal to Oxide*, Ph.D. thesis.
- [51] BRAILOVSKI, V., S. PROKOSHIN, M. GAUTHIER, K. INAEKYAN, S. DUBINSKIY, M. PETRZHIK, and M. FILONOV (2011) “Bulk and porous metastable beta $Ti_{x}Nb_{y}Zr$ (Ta) alloys for biomedical applications,” *Materials Science and Engineering: C*, **31**(3), pp. 643–657.
- [52] TANE, M., S. AKITA, T. NAKANO, K. HAGIHARA, Y. UMAKOSHI, M. NIINOMI, and H. NAKAJIMA (2008) “Peculiar elastic behavior of $Ti_{x}Nb_{y}Zr$ single crystals,” *Acta Materialia*, **56**(12), pp. 2856–2863.
- [53] KHACHATURYAN, A. (1985) “Theory of structural transformations in solids. 1983,” *Wiley, New York, Jacobs AE, Phys. Rev. B*, **31**, p. 5984.
- [54] SALJE, E. (1990) “Phase transitions in ferroelastic and co-elastic crystals,” *Ferroelectrics*, **104**(1), pp. 111–120.
- [55] HOHENBERG, P. and W. KOHN (1964) “Inhomogeneous Electron Gas,” *Physical Review*, **136**(3B), pp. B864–B871.
URL <http://link.aps.org/doi/10.1103/PhysRev.136.B864>

- [56] KOHN, W. and L. SHAM (1965) “Self-Consistent Equations Including Exchange and Correlation Effects,” *Phys. Rev.*, **140**, pp. 1133–1138.
- [57] PERDEW, J. and Y. WANG (1992) “Accurate and simple analytic representation of the electron-gas correlation energy,” *Physical Review B*, **45**(23), p. 13244.
- [58] PERDEW, J., K. BURKE, and M. ERNZERHOF (1996) “Generalized gradient approximation made simple,” *Physical Review Letters*, **77**(18), pp. 3865–3868.
- [59] CUPERLEY, D. M. and B. J. ALDER (1980) “Ground state of the electron gas by a stochastic method,” *Physical Review Letters*, **45**(7), p. 566.
- [60] SHANG, S., Y. WANG, D. KIM, and Z.-K. LIU (2010) “First-principles thermodynamics from phonon and Debye model: Application to Ni and Ni₃Al,” *Computational Materials Science*, **47**(4), pp. 1040–1048.
- [61] KRESSE, G. and J. FURTHMÜLLER (1996) “Efficiency of ab-initio total energy calculations for metals and semiconductors using a plane-wave basis set,” *Computational Materials Science*, **6**(1), pp. 15–50.
- [62] KRESSE, G. and D. JOUBERT (1999) “From ultrasoft pseudopotentials to the projector augmented-wave method,” *Physical Review B*, **59**(3), pp. 1758–1775.
- [63] WANG, A., S. SHANG, D. ZHAO, J. WANG, L. CHEN, Y. DU, Z.-K. LIU, T. XU, and S. WANG (2012) “Structural, phonon and thermodynamic properties of fcc-based metal nitrides from first-principles calculations,” *Calphad*, **37**, pp. 126–131.
- [64] MORUZZI, V. L., J. F. JANAK, and K. SCHWARZ (1988) “Calculated thermal properties of metals,” *Physical Review B*, **37**(2), pp. 790–799.
- [65] LIU, X. L., B. K. VANLEEUWEN, S. SHANG, Y. DU, and Z.-K. LIU (2015) “On the scaling factor in Debye–Grüneisen model: A case study of the Mg–Zn binary system,” *Computational Materials Science*, **98**, pp. 34–41.
- [66] WANG, Y., Z.-K. LIU, and L.-Q. CHEN (2004) “Thermodynamic properties of Al, Ni, NiAl, and Ni₃Al from first-principles calculations,” *Acta Materialia*, **52**(9), pp. 2665–2671.
- [67] SHANG, S., Y. WANG, and Z.-K. LIU (2007) “First-principles elastic constants of alpha- and theta-Al₂O₃,” *Applied Physics Letters*, **90**(10), pp. 101909–1–101909–3.
- [68] SIMMONS, G. and H. WANG (1971) *Single Crystal Elastic Constants and Calculated Aggregate Properties: A Handbook*, M.I.T. Press, Cambridge.

- [69] ZUO, Y. and Y. CHANG (1993) “Thermodynamic calculation of the Mg-Cu phase diagram,” *Zeit. Metall.*, **84**(10), pp. 662–667.
- [70] CHUNG, D. H. and W. R. BUSSSEM (1967) “The VoigtâĂŖReussâĂŖHill approximation and elastic moduli of Polycrystalline MgO, CaF₂, β -ZnS, ZnSe, and CdTe,” *Journal of Applied Physics*, **38**(6), pp. 2535–2540.
- [71] BORN, M. and K. HUANG (1998) *Dynamical Theory of Crystal Lattices*, Oxford University Press.
- [72] NYE, J. (1985) *Physical Properties of Crystals: Their Representation by Tensors and Matrices*, Oxford University Press.
- [73] JIANG, C., C. WOLVERTON, J. SOFO, L.-Q. CHEN, and Z.-K. LIU (2004) “First-principles study of binary bcc alloys using special quasirandom structures,” *Physical Review B*, **69**(21), pp. 214202–1–214202–10.
- [74] JIANG, C. (2009) “First-principles study of ternary bcc alloys using special quasi-random structures,” *Acta Materialia*, **57**(16), pp. 4716–4726.
- [75] TOGO, A., F. OBA, and I. TANAKA (2008) “First-principles calculations of the ferroelastic transition between rutile-type and CaCl₂-type SiO₂ at high pressures,” *Physical Review B*, **78**(13), p. 134106.
- [76] LIU, Z. K. and Y. WANG (2016) *Computational Thermodynamics of Materials*, Cambridge University Press.
- [77] ANDERSSON, J.-O., T. HELANDER, L. HÖGLUND, P. SHI, and B. SUNDMAN (2002) “Thermo-Calc & DICTRA, computational tools for materials science,” *Calphad*, **26**(2), pp. 273–312.
- [78] REDLICH, O. and A. T. KISTER (1948) “Algebraic representation of thermodynamic properties and the classification of solutions,” *Industrial & Engineering Chemistry*, **40**(2), pp. 345–348.
- [79] ZACHERL, C., S. SHANG, A. SAENGDEEJING, and Z.-K. LIU (2012) “Phase stability and thermodynamic modeling of the Re–Ti system supplemented by first-principles calculations,” *Calphad*, **38**, pp. 71–80.
- [80] SHANG, S., J. SAAL, Z. MEI, Y. WANG, and Z.-K. LIU (2010) “Magnetic thermodynamics of fcc Ni from first-principles partition function approach,” *Journal of Applied Physics*, **108**(12), p. 123514.
- [81] LIU, Z.-K. (2009) “First-principles calculations and CALPHAD modeling of thermodynamics,” *Journal of Phase Equilibria and Diffusion*, **30**(5), pp. 517–534.

- [82] SAUNDERS, N. and A. MIODOWNIK (1998) *CALPHAD (Calculation of Phase Diagrams): A Comprehensive Guide: A Comprehensive Guide*, vol. 1, Elsevier.
- [83] LUKAS, H., S. FRIES, and B. SUNDMAN (2007) *Computational Thermodynamics: the CALPHAD Method*, vol. 131, Cambridge University Press, Cambridge.
- [84] YOUNG, R. and A. LARSON (1998) “Rietveld analysis of X-ray and neutron powder diffraction patterns,” *Atlanta (GA): School of*.
URL <http://debian.ccp14.ac.uk/ccp/web-mirrors/dbws/downloads/young/guide99.pdf>
- [85] TORAYA, H. (1986) “Whole-Powder-Pattern Fitting Without Reference to a Structural Model: Application to X-ray Powder Diffractometer Data,” *J. Appl. Cryst.*, **19**, pp. 440–447.
- [86] FULTZ, B., T. KELLEY, M. MCKERNIS, J. LIN, J. LEE, O. DELAIRE, M. KRESCH, and M. AIVAZIS (2009), “Experimental inelastic neutron scattering,” .
- [87] SQUIRES, G. L. (2012) *Introduction to the theory of thermal neutron scattering*, Cambridge university press.
- [88] MANLEY, M. E. (2001) *From elementary excitations to microstructures: The thermodynamics of metals and alloys across length scales*.
- [89] MANLEY, M. E., R. J. MCQUEENEY, B. FULTZ, R. OSBORN, G. H. KWEI, and P. D. BOGDANOFF (2002) “Vibrational and electronic entropy of β -cerium and γ -cerium measured by inelastic neutron scattering,” *Physical Review B*, **65**(14), p. 144111.
URL <http://link.aps.org/doi/10.1103/PhysRevB.65.144111>
- [90] BLÖCHL, P. (1994) “Projector augmented-wave method,” *Physical Review B*, **50**(24), p. 17953.
- [91] MONKHORST, H. and J. PACK (1976) “Special points for Brillouin-zone integrations,” *Physical Review B*, **13**(12), pp. 5188–5192.
- [92] PREDEL, B. (1997) “Mo-Ti (Molybdenum-Titanium) BT - Li-Mg Å Nd-Zr,” Springer Berlin Heidelberg, Berlin, Heidelberg, pp. 1–3.
- [93] HOFFMAN, J. R., E. RUDY, S. T. WINDISCH, and A. J. STOSICK (1967) “The constitution of binary molybdenum-carbon alloys(Binary molybdenum-carbon system investigated using X-ray, metallographic, thermoanalytical and melting-point techniques),” *AIME, TRANSACTIONS*, **239**, pp. 1247–1267.

- [94] ENGLISH, J. (1961) *Binary and Ternary Phase Diagrams of Columbium, Molybdenum, Tantalum, and Tungsten*, Tech. rep.
- [95] SCHMITZ-PRANGHE, N. and P. DUENNER (1968) “Gitterstruktur und thermische Ausdehnung der Uebergangsmetalle Scandium, Titan, Vanadin und Mangan,” *Zeitschrift fuer Metallkunde*, **59**, pp. 377–382.
- [96] “Materials Project,” .
URL <http://www.materialsproject.org>
- [97] WOLFRAM RESEARCH, I., “Matematica,” .
- [98] YI, C., S. JIANG, and C. NANXIAN (2009) “The effect of Mo atoms in ternary nitrides with eta-type structure,” *Solid State Communications*, **149**, pp. 121–125.
- [99] BOLEF, D. (1961) “Elastic constants of single crystals of the bcc transition elements V, Nb, and Ta,” *Journal of Applied Physics*, **32**(1), pp. 100–105.
- [100] NEUBURGER, M. C. (1936) “Praezisionsmessung der Gitterkonstante von sehr reinem Niob,” *Zeitschrift fuer Kristallographie, Kristallgeometrie, Kristallphysik, Kristallchemie (-144,1977)*, **93**, pp. 158–159.
- [101] ——— (1936) “Praezisionsmessung der Gitterkonstante von sehr reinem Tantal,” *Zeitschrift fuer Kristallographie, Kristallgeometrie, Kristallphysik, Kristallchemie (-144,1977)*, **93**, pp. 312–313.
- [102] TRECO, R. M. (1953) “Effect of small additions of oxygen on lattice constants and hardness of zirconium,” *Transactions of the American Institute of Mining, Metallurgical and Petroleum Engineers*, **197**, pp. 344–348.
- [103] BERGERHOFF, G., R. HUNDT, R. SIEVERS, and I. D. BROWN (1983) “The inorganic crystal structure data base,” *Journal of Chemical Information and Computer Sciences*, **23**(2), pp. 66–69.
- [104] KARLSRUHE, F. I. Z., “Inorganic Crystal Structure Database,” .
- [105] KURODA, D., M. NIINOMI, M. MORINAGA, Y. KATO, and T. YASHIRO (1998) “Design and mechanical properties of new β type titanium alloys for implant materials,” *Materials Science and Engineering: A*, **243**(1), pp. 244–249.
- [106] HE, G. and M. HAGIWARA (2004) “Ti-Cu-Ni (Fe, Cr, Co)-Sn-Ta (Nb) alloys with potential for biomedical applications,” *Materials Transactions*, **45**(4), pp. 1120–1123.

- [107] ——— (2006) “Ti alloy design strategy for biomedical applications,” *Materials Science and Engineering: C*, **26**(1), pp. 14–19.
- [108] OKAMOTO, H. (2003) “Sn-Ta (Tin-Tantalum),” *Journal of Phase Equilibria*, **24**(5), p. 484.
- [109] STUDNITZKY, T. and R. SCHMID-FETZER (2002) “Phase Formation and reaction Kinetics in M-Sn systems (M=Zr, Hf, Nb, Ta, Mo),” *Zeitschrift Fur Metallkunde*, **93**(9), pp. 894–903.
- [110] BASILE, F. (1971) “Cristallographic study and supraconductive properties of compounds V₃Sn and Ta₂Sn₃,” in *Annales de chimie*, vol. 6, pp. 241–244.
- [111] YUE, Q., Y. LIU, M. CHU, and J. SHEN (2009) “Thermodynamic modeling of the Sn–V binary system,” *Calphad*, **33**(3), pp. 539–544.
- [112] TOFFOLON, C., C. SERVANT, J. GACHON, and B. SUNDMAN (2002) “Re-assessment of the Nb-Sn system,” *Journal of Phase Equilibria*, **23**(2), pp. 134–139.
- [113] COURTNEY, T., G. PEARSALL, and J. WULFF (1965) “Effect of Processing History on the Superconducting Properties and Long-Range Order of Ta₃Sn,” *Journal of Applied Physics*, **36**(10), pp. 3256–3260.
- [114] PREDMORE, R. and R. ARSENAULT (1970) “Short range order of Ta-Mo B.C.C. alloys,” *Scripta Metallurgica*, **4**(3), pp. 213–217.
- [115] SHANG, S., A. SAENGDEEJING, Z. MEI, D. KIM, H. ZHANG, S. GANESHAN, Y. WANG, and Z.-K. LIU (2010) “First-principles calculations of pure elements: Equations of state and elastic stiffness constants,” *Computational Materials Science*, **48**(4), pp. 813–826.
- [116] ALLEN, W. and J. PEREPEZKO (1991) “Solidification of undercooled Sn-Sb peritectic alloys: Part I. Microstructural evolution,” *Metallurgical Transactions A*, **22**(3), pp. 753–764.
- [117] ARROYAVE, R. and Z.-K. LIU (2006) “Intermetallics in the Mg-Ca-Sn ternary system: Structural, vibrational, and thermodynamic properties from first principles,” *Physical Review B*, **74**(17), p. 174118.
- [118] CALVERT, L. and P. VILLARS (1991) “Pearson’s Handbook of Crystallographic Data for Intermetallic Phases,” *ASM, Materials Park, OH*.
- [119] PELTZER Y BLANCÁ, E. L., A. SVANE, N. E. CHRISTENSEN, C. O. RODRÍGUEZ, O. M. CAPPANNINI, and M. S. MORENO (1993) “Calculated static and dynamic properties of β -Sn and Sn-O compounds,” *Physical Review B*, **48**(21), pp. 15712–15718.

- [120] JOUAULT, F. and P. LECOCQ (1967) “Etude comparee des trois diagrammes V-Sn, Nb-Sn, Ta-Sn,” *Colloques Internationaux du Centre National de la Recherche Scientifique*, **157**, pp. 229–235.
- [121] GELLER, S., B. T. MATTHIAS, and R. GOLDSTEIN (1955) “Some new intermetallic compounds with the beta.-wolfram structure,” *Journal of the American Chemical Society*, **77**, pp. 1502–1504.
- [122] WANG, Y., S. CURTAROLO, C. JIANG, R. ARROYAVE, T. WANG, G. CEDER, L.-Q. CHEN, and Z.-K. LIU (2004) “Ab initio lattice stability in comparison with CALPHAD lattice stability,” *Calphad*, **28**(1), pp. 79–90.
- [123] ARROYAVE, R. and Z.-K. LIU (2006) “Thermodynamic modelling of the Zn–Zr system,” *Calphad*, **30**(1), pp. 1–13.
- [124] DICKINSON, J. and P. ARMSTRONG (1967) “Temperature dependence of the elastic constants of molybdenum,” *Journal of Applied Physics*, **38**(2), pp. 602–606.
- [125] KIM, H., Y. IKEHARA, J. KIM, H. HOSODA, and S. MIYAZAKI (2006) “Martensitic transformation, shape memory effect and superelasticity of Ti–Nb binary alloys,” *Acta Materialia*, **54**(9), pp. 2419–2429.
- [126] BUDAI, J. D., J. HONG, M. E. MANLEY, E. D. SPECHT, C. W. LI, J. Z. TISCHLER, D. L. ABERNATHY, A. H. SAID, B. M. LEU, L. A. BOATNER, R. J. MCQUEENEY, and O. DELAIRE (2014) “Metallization of vanadium dioxide driven by large phonon entropy,” *Nature*, **515**(7528), pp. 535–539.
URL <http://dx.doi.org/10.1038/nature13865> <http://www.nature.com/nature/journal/v515/n7528/abs/nature13865.html>{#}supplementary-information

Vita
Cassie Marker

The details of my childhood are inconsequential.